FY24 Laboratory Directed Research & Development Annual Report

Savannah River National Laboratory ®

Disclaimer

This work was prepared as an account of work sponsored by an agency of the United States Government. Neither the United States Government nor any agency thereof, nor any of their employees, nor any of their contractors, subcontractors or their employees, makes any warranty, express or implied, or assumes any legal liability or responsibility for the accuracy, completeness, or any third partys use or the results of such use of any information, apparatus, product, or process disclosed, or represents that its use would not infringe privately owned rights. Reference herein to any specific commercial product, process, or service by trade name, trademark, manufacturer, or otherwise, does not necessarily constitute or imply its endorsement, recommendation, or favoring by the United States Government or any agency thereof or its contractors or subcontractors. The views and opinions of authors expressed herein do not necessarily state or reflect those of the United States Government or any agency thereof, its contractors or subcontractors.

Message from the Deputy Lab Director for Science and Technology and Director of Innovation and University Engagement

At Savannah River National Laboratory (SRNL), we put science to work to provide solutions for the Department of Energy (DOE) and the National Nuclear Security Administration (NNSA). As the need for technical solutions to complex problems continues to evolve, SRNL is rising to meet the challenge.

Investments through SRNL's Laboratory Directed Research and Development (LDRD) program drive exploratory research foundational to advancing mission critical technologies for the Office of Environmental Management (EM), NNSA and other offices of DOE. A skilled technical workforce is central to yielding high quality solutions to real world challenges. In FY24, the LDRD program invested in workforce development by supporting postdoctoral researchers and graduate students.

Leveraging the joint appointment program was a focus for the FY24 LDRD program with the first co-advised postdoctoral researcher onboarded at the laboratory, supported by an SRNL research advisor and a joint appointee. The FY24 program also advanced research collaborations with joint appointees supporting LDRD research success by building upon their unique resources and capabilities to further LDRD supported projects.

Enjoy reading this Annual Report which summarizes the innovative science and engineering contributions of SRNL staff supported by the LDRD Program.

Dr. Sue Clark
Deputy Laboratory Director,
Science and Technology

Dr. Elizabeth Hoffman
Director, Innovation and University
Engagement

Contents

FY24 Reports

Overview

The Laboratory Directed Research and Development (LDRD) program yields foundational scientific research and development (R&D) essential to growing SRNL's core competencies, in alignment with SRNL's Strategic Plan to provide long-term benefits to the Department of Energy (DOE), the National Nuclear Security Administration (NNSA), and other customers and stakeholders. Five strategic goals are outlined in SRNL's strategic plan:

1) Provide applied science and engineering for EM's active clean-up sites and LM's post closure management sites
2) Provide science-based solutions for gaps identified in nonproliferation strategic vision and support the government in activities impacting national security
3) Lead Science, Technology & Engineering as the central technical authority for processing tritium loaded reservoirs and support production of plutonium pits
4) Align science and energy security programs by focusing modern modeling, simulation, and data analytics tools on materials engineering and performance applications
5) Build a workforce for the future

To fully achieve these strategic goals, SRNL must build upon its technical core competencies. SRNL's six core competencies underpinning the laboratory's strategic goals include:

- Accelerating remediation, minimizing waste, and reducing risk
- Enabling next-generation nuclear material processing and disposition
- Creating Manufacturing and energy solutions for EM, NNSA, and other sponsors
- Assuring production and supply of strategic materials and components
- Sensing, characterizing, and assessing materials production and environmental impacts
- Securing connected control systems and associated data

SRNL has focused LDRD Program investments to expand and strengthen the SRNL core competencies. Each project aligns with one or more of the technical core competencies. In addition to supporting SRNL's core competencies, each LDRD investment aligns with one or more of three overall program objectives:

The Three Main Objectives of the LDRD Program

Mission Agility

Enable agile responses to national scientific and security challenges

Scientific & Technical Vitality

Advance the frontiers of science, technology, and engineering

Workforce Development

Attract, develop, and retain tomorrow's technical workforce
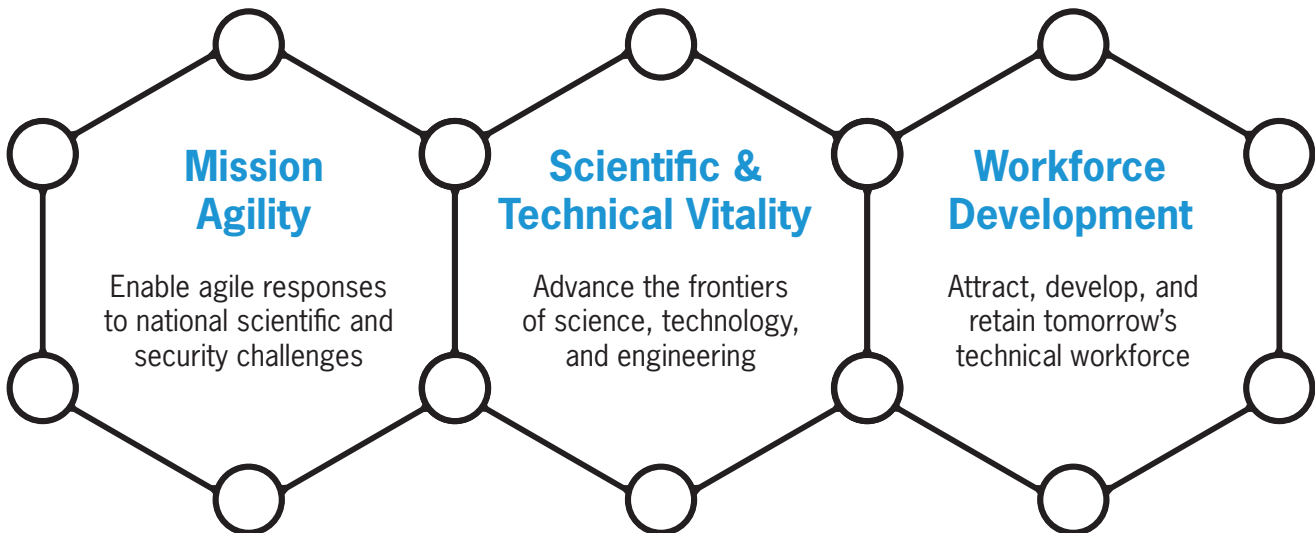
LDRD FY24 by the Numbers

54
Total Projects

$8.38M
Total Program Cost
Fully Burdened

Universities Engaged
- Augusta University
- Clemson University
- Georgia Institute of Technology
- Univeristy of South Carolina, Columbia
- University of Flordia
- University of Georgia
- University of Kansas
- University of Mississippi
- University of South Carolina, Aiken
- University of Tennessee, Martin
- Virginia Polytechnic Institute & State University

27
Peer-Reviewed Publications

Manuscripts are evaluated in an independent review where experts assess the research for quality and accuracy prior to publication acceptance.

2
Patents Issued

3
Patent Applications

3
Invention Disclosures

28
Postdocs Funded
over 10% of total hours

11
Postdocs Converted to Staff Hires

36
Projects Involving Postdocs

22
Projects Led by Early Career Staff

Early career: within 5 years of terminal degree

7
Projects Involving Interns

Advancing Optimization Theory for Agile Solutions

Savannah River National Laboratory's (SRNL) Laboratory Directed Research and Development (LDRD) Program empowers researchers, and the Lab, to address complex challenges with cutting edge solutions – often before mission sponsors are even aware of them as a need they have.

For example, most scientists and engineers are familiar with design of experiment and Analysis of Variance (ANOVA), even if they don't use them very often. Most scientists and engineers have at least one piece of equipment that's specialized enough that it takes an expert to tune it properly or wring the most out of it. But what if there was a way to apply the first thing to the second thing – a way to make those complex or finnicky instruments easier to use well and more approachable to the broader scientific community?

Enter Dr. Stephanie Gamble. Her work – including her LDRD project Multivariate Optimization Theory for Sampling Instrumentation – is a great example of cross-disciplinary pollination gone right.

Dr. Gamble's work in this area didn't begin with instrument tuning or calibration - it began with a request for assistance with analyzing data from the Lab's 2D gas chromatograph (GCxGC). Like most theoreticians, one of the first things she did was start learning about what calibration was done when collecting the data, and what post-measurement corrections had been performed and why. She quickly realized that, with the number of parameters in play with a GCxGC, calibrating the instrument one setting at a time was almost certainly leaving performance on the table. She also had an idea of how to get at that extra performance.

Mission Agility

Enable agile responses to national scientific and security challenges

With her collaborator's encouragement, she submitted an LDRD proposal to develop her methodology, which is based around using Karush-Kuhn-Tucker (KKT) conditions – an extension of Lagrange multipliers that bounds parameters instead of fixing them. In this case, they're used to bound instrument settings within the physical limits of any given machine, in order to find the best possible settings within them, whether that be something like best all-around tunings, highest sensitivity to a particular stimulus, or a more traditional calibration against a known standard. Dr. Gamble tied her optimization method to a foundation informed by ANOVA analysis of an instrument's settings, making it pre-eminently generalizable to any other instrument or process one might care to look at. In other words, her flexible approach is robust, device-agnostic, and has a broad range of applications, from environmental monitoring to medical technologies.

"I enjoy teaching scientists in other fields math knowledge that is applicable to them, that they might not have otherwise thought to look into," says Gamble. "Optimization is broadly applicable and still heavily researched in math fields – it's constantly evolving and improving with new techniques and methods that are applicable across scientific domains." Her project is a prime example of how SRNL's LDRD program fosters mission agility, allowing researchers to pivot and expand their work to address new needs as they emerge.

This adaptability is central to Gamble's work, which after it's success with gas chromatography is now being applied to other efforts in the NNSA portfolio, such as the NA-22 funded cooling tower initiative, where her methods are being used to optimize sample collection for environmental measurements. Additionally, she is exploring how her methods can be applied to particle analysis, also within NA-22, where her methods could help offer new insights into other complex systems. By expanding her work into diverse scientific domains, Gamble is further exemplifying how SRNL's research can evolve to meet the challenges of a rapidly changing technological landscape.

Through her innovative work, Dr. Gamble is not only advancing optimization theory but also making a lasting impact on how scientific instruments are used to solve pressing problems across industries. This project highlights SRNL's ongoing commitment to scientific discovery and its ability to adapt to the evolving needs of national security, technology, and environmental sustainability.

"I enjoy teaching scientists in other fields math knowledge that is applicable to them, that they might not have otherwise thought to look into."

- Stephanie Gamble

Securing Healthcare Through Cybersecurity Research

The Laboratory Directed Research and Development (LDRD) Program at Savannah River National Laboratory (SRNL) is a key driver of scientific and technical vitality, a core objective aimed at advancing innovative and high-risk research that strengthens the lab's scientific expertise. Through initiatives like David Baldwin's project, *Reverse Engineering of Medical Devices for Innovation and Advancement in Healthcare*, SRNL is making significant strides in the field of cybersecurity. This cutting-edge research addresses critical vulnerabilities in medical devices, as healthcare technologies increasingly rely on interconnected digital systems, creating new opportunities to advance cybersecurity expertise at SRNL.

Baldwin's project exemplifies how the LDRD program fosters scientific vitality by tackling emerging cybersecurity challenges in a rapidly evolving sector. As the medical device industry expands, with an increasing reliance on wireless and Internet of Things (IoT) technologies, vulnerabilities are emerging that could jeopardize patient safety and sensitive healthcare data. Baldwin's team is addressing these risks by reverse engineering medical devices, including ultrasound equipment, to uncover hidden cybersecurity flaws and mitigate potential threats before they can be exploited.

"The medical device market, much like home IoT, is a rapidly expanding field that exponentially introduces new technologies," Baldwin explains. "While these devices are providing consumers and patients with expanded information and an increasingly seamless user experience, the prioritization of convenience and readily available information often overlooks the significance of securing these devices."

Scientific & Technical Vitality

Advance the frontiers of science, technology, and engineering
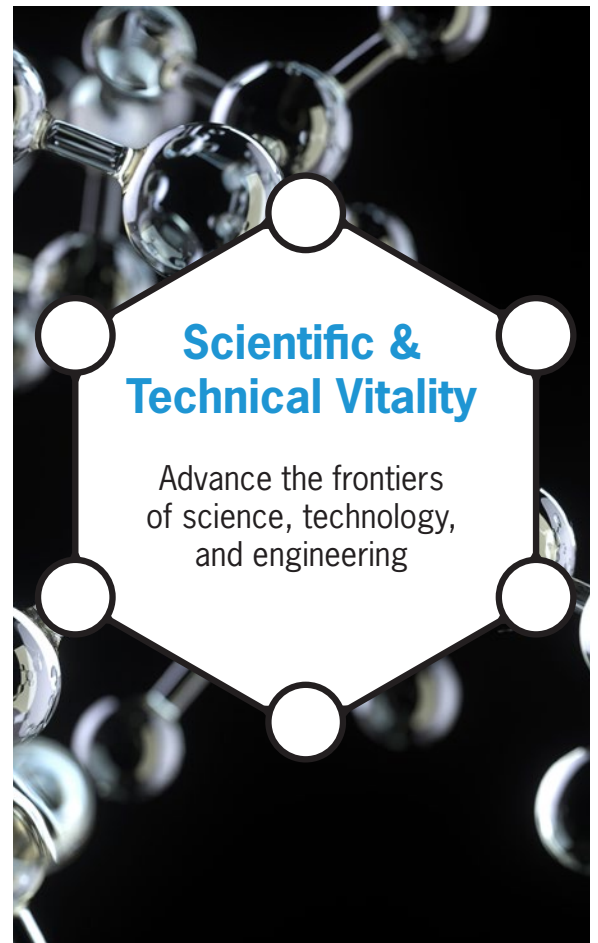
This gap in security fuels the motivation behind Baldwin's research to identify and secure these technological vulnerabilities, ensuring both patient safety and the integrity of healthcare systems.

Collaborating with Augusta University (AU), Baldwin's team has established a comprehensive testing framework to evaluate the cybersecurity of medical devices in realistic environments. Dr. Jeff Morris, a key collaborator at Augusta University, notes, "AU and SRNL are engaged in a research project to create a framework to test the cybersecurity of IoT medical devices. A team consisting of AU faculty, graduate students, and SRNL scientists are creating a testing framework that uses a combination of software, hardware, and communication tests to determine how example medical devices interact in use cases that represent hospital, home, and business environments." This partnership is crucial for expanding SRNL's capabilities and deepening its involvement in cybersecurity, particularly in securing embedded systems critical to healthcare.

Traditionally known for its expertise in chemical and nuclear science, SRNL is now leveraging its skills to tackle complex cybersecurity challenges in new areas. By reverse engineering medical devices and securing the networks they rely on, SRNL is strengthening its competencies in areas such as securing connected control systems, embedded systems, and data integrity.

As part of this initiative, SRNL is also developing capabilities in different areas including firmware reverse engineering, cryptography, red team testing, and threat-hunting techniques. These skills are essential for understanding and mitigating the risks posed by cyber threats to critical healthcare systems and national security. Baldwin underscores the significance of this work: "Identifying and securing these gaps in security is the motivation for conducting this research," ensuring that SRNL's contributions will have a lasting impact on healthcare technology security.

Looking ahead, Baldwin's project is positioning SRNL as a leader in cybersecurity research for medical devices, with the potential to shape national healthcare security standards and contribute to broader cybersecurity advancements. Through continued collaboration with Augusta University, SRNL is poised to make meaningful contributions to securing the nation's healthcare infrastructure while advancing scientific knowledge in the field of cybersecurity.
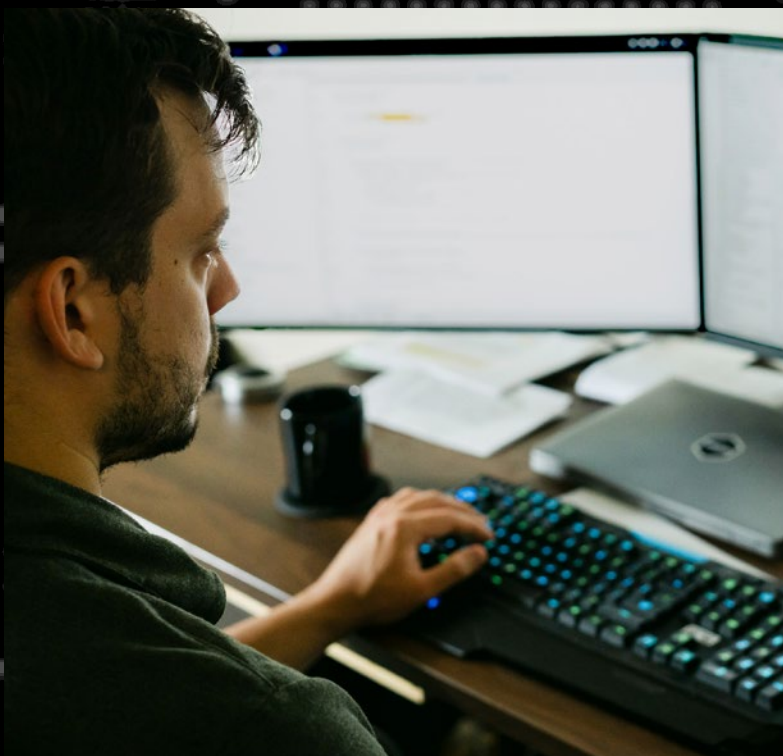
"Identifying and securing these gaps in security is the motivation for conducting this research."

- David Baldwin
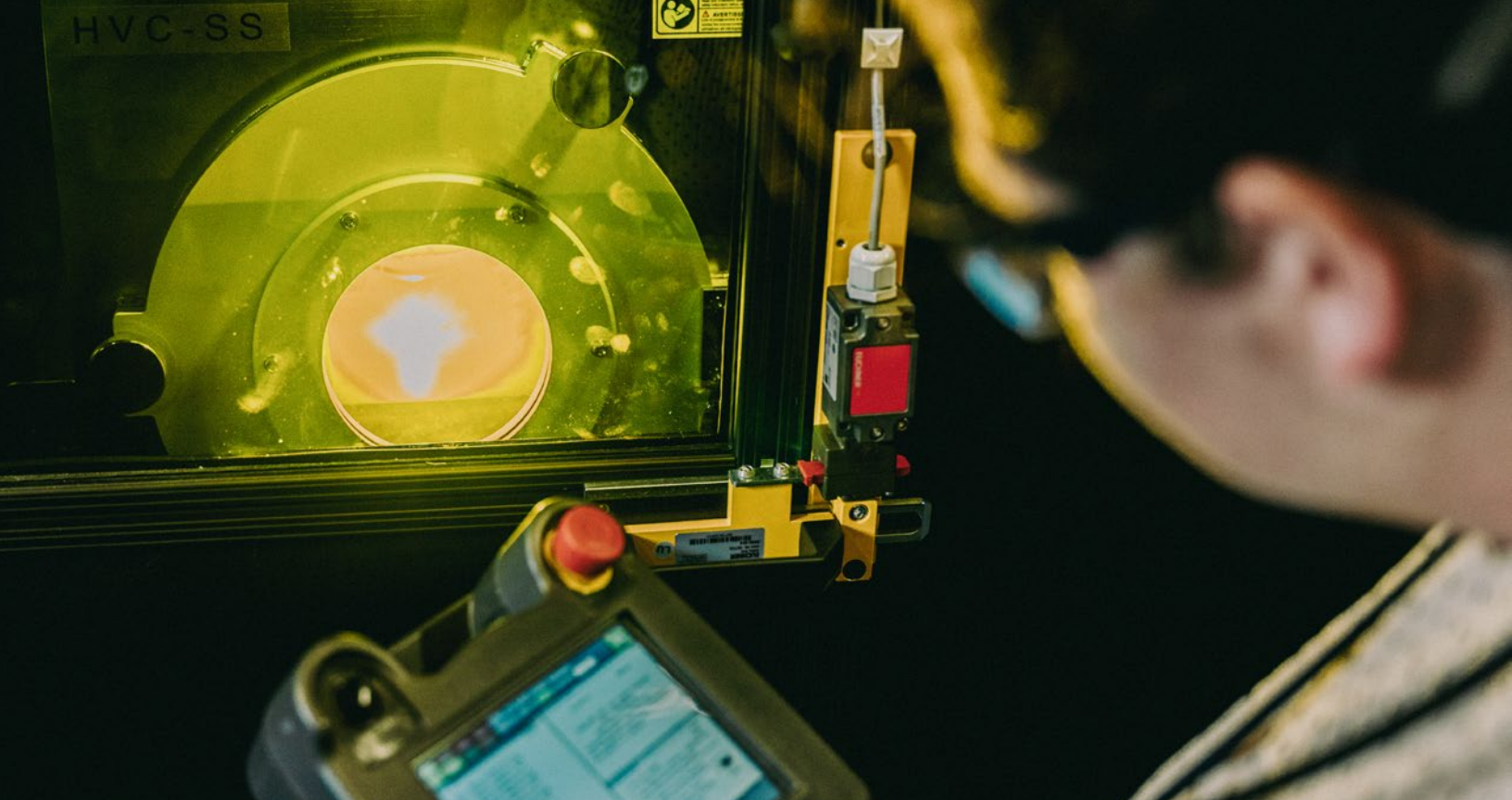
Fostering the Next Generation of Scientists: SRNL's Eisenhower Postdoctoral Fellowship

Workforce Development

Attract, develop, and retain tomorrow's technical workforce

The Laboratory Directed Research and Development (LDRD) program at Savannah River National Laboratory (SRNL) plays a critical role in strengthening the laboratory's workforce by cultivating emerging talent through opportunities like the Dwight D. Eisenhower Postdoctoral Fellowship. This distinguished program is designed to attract top-tier scientists at the beginning of their careers, providing them with the resources and mentorship needed to advance their expertise while contributing to high-impact research at SRNL.

Since its inception, the Eisenhower Fellowship has become a key component of SRNL's workforce development strategy, with a select group of fellows pursuing independent research initiatives supported by LDRD funding. These postdoctoral researchers are chosen through a highly competitive process that encourages innovative thinking and scientific exploration. Their projects are aligned with SRNL's core mission areas, offering them the opportunity to address complex technical challenges while advancing the laboratory's capabilities.

In FY24, three outstanding researchers Eisenhower Fellows were funded, each bringing a unique perspective and skillset to SRNL's research efforts. The fellows are working on high-priority projects across various scientific domains, applying their expertise to solve complex problems and make lasting contributions to SRNL's mission. Through their work, they will not only enhance SRNL's research portfolio but also develop professionally, gaining invaluable experience that will prepare them for future leadership roles in the scientific community.

The LDRD program supports these fellows by providing them with

the freedom to conduct independent research while being guided by experienced SRNL mentors. This dynamic combination of autonomy and mentorship fosters the development of critical thinking, problem-solving, and technical skills, allowing the fellows to grow as independent researchers. The opportunity to publish their findings in peer-reviewed journals further strengthens their professional reputation and builds their networks within the broader scientific community.

The Eisenhower Fellowship serves as an incubator for talent, preparing the next generation of researchers to address the evolving needs of national security, energy, and environmental challenges. Since its inception, five fellows have been selected for the fellowship, with two successfully transitioning into full-time staff positions at SRNL. This transition underscores the long-term impact of the program,

which not only enhances SRNL's immediate research capabilities but also strengthens its future workforce by bringing top-tier scientific talent into the fold.

Through the Eisenhower Postdoctoral Fellowship, SRNL is investing in the future of scientific research, ensuring that the laboratory remains at the forefront of technological innovation. By supporting postdoctoral researchers and giving them the opportunity to solve complex challenges while building their careers, the LDRD program is helping to shape the next generation of scientific leaders who will continue to advance SRNL's mission and contribute to national security and scientific discovery.

Meet the Current Eisenhower Fellows

Colleen Hilla, Ph.D.

Joined SRNL in May 2023

Ohio State University, Department of Materials Science

"The Eisenhower postdoc position has allowed me to take full ownership over my research at SRNL. This has allowed me to interface with more people throughout the lab and seek out additional engaging research opportunities. Focusing on a single research project has allowed me to build upon my research focus area and discover how this work can best integrate into the lab as I continue my career."

Jennifer Naglic, Ph.D.

Joined SRNL in June 2024

University of South Carolina - Columbia, Department of Chemical Engineering

"I pursued the Eisenhower Postdoctoral Research Fellowship as this position provides me the ability to investigate the work that I am passionate about while establishing myself at SRNL. Beginning my career with a project that I designed allows me the opportunity to grow as a researcher while figuring out the ins and outs of funding my work."

Stephen Vicchio. Ph.D.

Joined SRNL in January 2024

Clemson University, Department of Chemical Engineering

"The ability to focus solely on my own project, stemming from an idea I had during the last six months of my PhD, has challenged me to grow outside of my comfort zone through the addition of new skills. The Eisenhower Fellowship is the perfect opportunity for me to conduct cutting-edge research while also gaining more project management skills, so that I can be a successful Principal Investigator."

FY24 PROJECTS

CORE COMPETENCY:

Accelerating remediation, minimizing waste and reducing risk

Validation of Organics in Tank Waste by Stir-Bar Sorptive Extraction

Andrew Boggess

Current analysis performed on radioactive samples for the quantitation of organic compounds consumes large volumes of hazardous chlorinated solvent. A solventless method was explored in this work for its applicability to liquid waste samples. This new analytical method may accelerate remediation, minimize hazardous solvent waste, and reduce exposure risk to workers.

Introduction

SRNL performs analysis for organic compounds in Liquid Waste System (LWS) tank samples, flammability study samples, tritium hydrocarbon analysis submissions, off-gas analysis studies, and many other non-routine and R&D samples. SRNL performs volatile and semi-volatile organics analysis by gas chromatography – mass spectrometry, following one of several solvent extraction and preparation techniques involving (most often) dichloromethane. However, environmental regulators have begun to phase out the use of chlorinated solvents (including dichloromethane) in industrial labs for public health and environmental stewardship. Novel methods of sample extraction and preparation will be required in the near future. Detection and quantitation of organics in liquid waste is difficult due to high radioactivity, pH, and other matrix effects. These challenges are magnified by the need for increased sensitivity and high precision. Solid-phase extractions, such as stir-bar sorptive extraction (SBSE), have been effective in past studies[1] at solving poor reporting limits stemming from matrix effects. Building upon successful non-rad investigation[2] at Hanford, this work simultaneously eliminated dichloromethane extractions while improving analytical capabilities (sensitivity, accuracy, precision, and range of target analytes) in radioactive samples by use of SBSE. Implementation of SBSE may allow SRNL to accelerate remediation by matching the aggressive tank closure schedule with improved sampling efficiency: with SBSE, up to 20 samples can be extracted simultaneously, compared to three currently possible. SBSE may eliminate the use of solvents almost entirely, minimizing waste and reducing one of the largest risks of contamination: sample spillage during prep work. Likewise, worker exposure time may be significantly reduced by eliminating the laborious hands-on liquid extraction.

Approach

This research used SRNL-owned assets to investigate the feasibility of SBSE to improve method reporting limits, increase accuracy/precision, decrease or eliminate the use of problematic chlorinated solvents, and decrease analytical method runtime (thereby freeing up analyst manhours and decreasing exposure). These goals were accomplished by:

1. Building upon proof-of-concept work performed at Hanford Labs using SBSE in non-radioactive environments.
2. Investigating the interactions between the sorptive media and common tank waste radionuclides.
3. Validating extraction efficacy in the complex environment of simulated and real tank samples.

This work conducted fundamental experiments investigating SBSE in real-world pH ranges and tank waste, interactions between the sorbent material and LWS radionuclides (specifically, the ability to selectively leave behind the radionuclides), the ability for SBSE to extract both volatile and non-volatile compounds in waste simultaneously, and the use-reuse lifetime of each stir bar in this environment. These are fundamental questions (with no answers currently in literature) that will be necessary for any lab working with radioactive samples to address transition to SBSE. Target compounds vital for analysis at SRNL (i.e., Next Generation Solvent components, tritium hydrocarbons contaminants, off-gas flammability compounds, etc.) are uncommon outside of the DOE complex, creating a marked gap in the literature. For this reason, LWS-specific compounds were prioritized.

Accomplishments

- Method optimization was performed in aqueous and simulated tank waste for determination of SBSE extraction time, extraction temperature, desorption solvent, desorption time, matrix additives, and pH. An example of parameter optimization can be found in **Figure 1**: SBSE extraction time optimization.
- Analytical performance was determined in simulated and real tank samples to determine analytical variance, sensitivity, accuracy, and precision. **Figure 2** shows a comparison between SBSE and liquid-liquid extraction in buffered waste tank simulant.
- Final method performance validation was performed using optimized method parameters in simulated and real tank waste for polyaromatic hydrocarbons, common volatile hydrocarbons, and phenolic LWS solvent breakdown products.
- In total, SBSE marked improvement over existing analytical methods for semi-volatile and volatile analysis in the following areas (reporting means):
- Reporting limit: The SBSE method produced a standard quantitative limit (defined as the concentration capable of producing a 5:1 signal to noise ratio) of 0.01 mg/L, 0.04 mg/L, and 0.07 mg/L for phenolic breakdown products. This quantitative limit represents a 100x improvement over the existing solvent extraction method for polyaromatic hydrocarbons, a 20x improvement for phenolic LWS

breakdown product, and a 14x improvement for chlorinated hydrocarbons.
- Accuracy: The tank-specific organic surrogates were recovered from aqueous samples at 99.2% mean recovery. These surrogates include polyaromatic hydrocarbons and volatile chlorinated hydrocarbons of known and sufficient extraction efficiency that may be of interest to LWS and R&D customers.
- Precision: The relative standard deviation on replicate measurements (n=10) at the optimized parameters produced a mean relative standard deviation of 13.6%. This mean includes all polyaromatic hydrocarbons, volatile chlorinated hydrocarbons, and phenolic breakdown products (of undetermined extraction efficiency).
- Method prep time: The SBSE prep method resulted in a 13x reduction in sample prep time: six samples per 8-hour shift using the standard method vs. 20 samples per 2-hour prep method time using SBSE.
- Solvent consumption: The SBSE method reduced total solvent consumption by 99.3%, and a 100% reduction in hazardous chlorinated solvent usage.

Peer-reviewed Publication

- Boggess, A. J.; White, T.L. Analytical Efficacy of SBSE in Liquid Nuclear Waste: Optimization and Validation. *J. Radioanal. Nucl. Chem.* **2024**, (In preparation) *
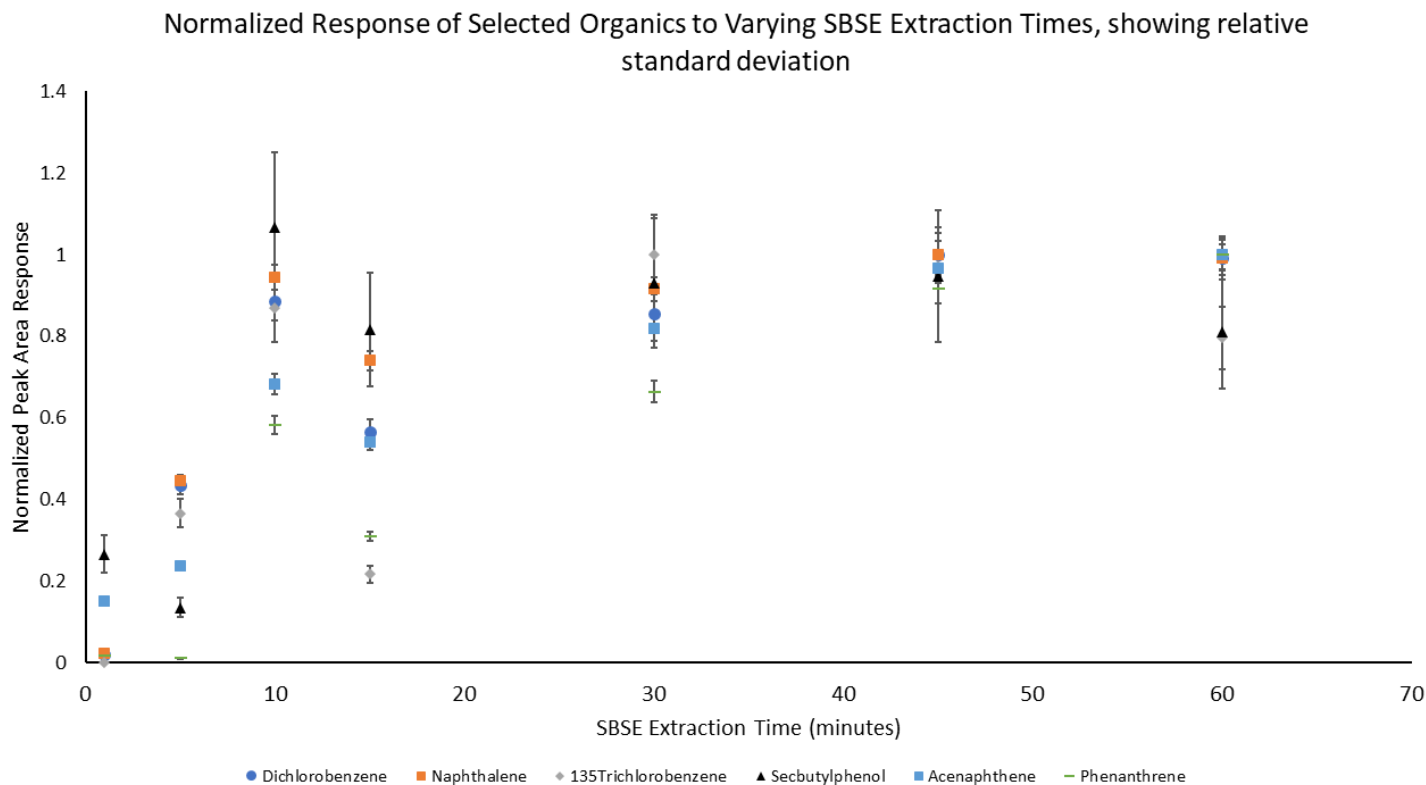
Figure 1. Optimization of SBSE extraction time to achieve equilibration among all selected analyte types in deionized water.

Analyte Recovery from Buffered Simulated Tank Waste using Liquid-Liquid Extraction and SBSE, showing 1 standard deviation
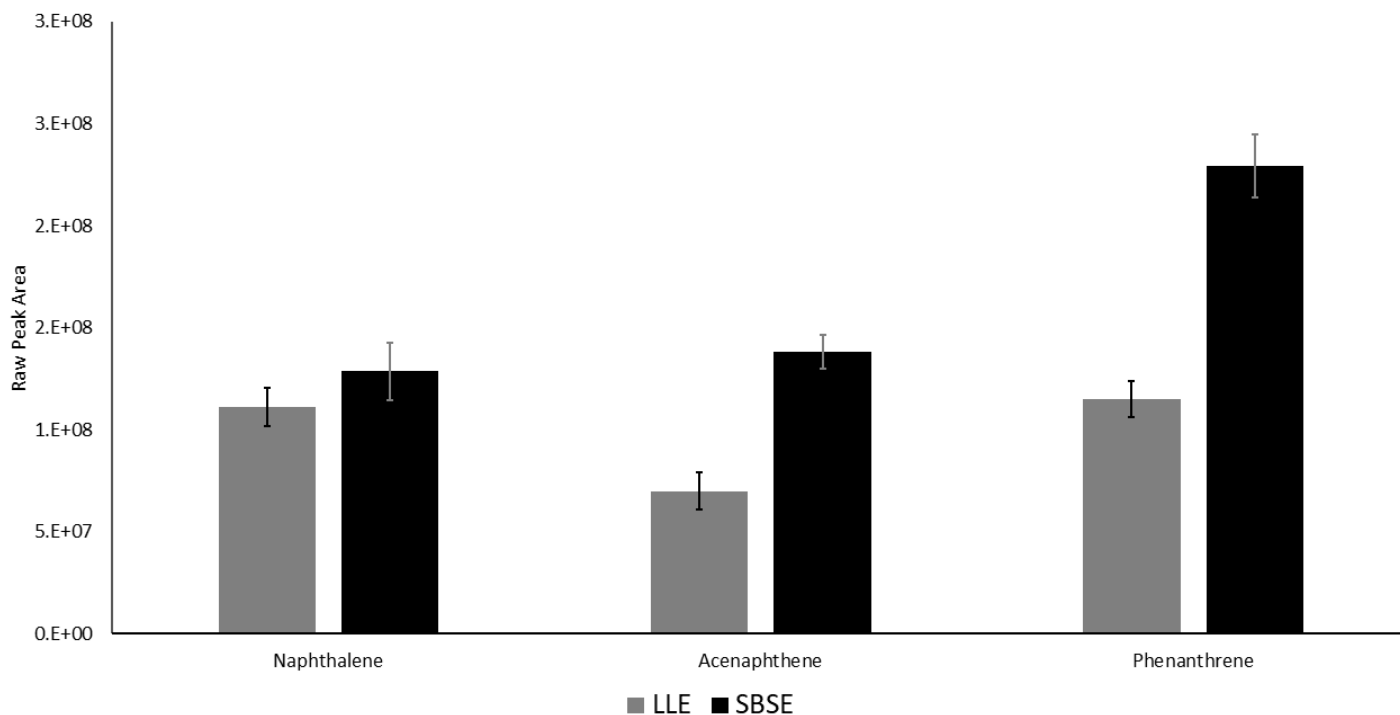
Figure 2. Performance of SBSE relative to liquid-liquid extraction (LLE) in buffered (pH 5) waste tank simulant for applicable selected organics.

Team Members

Thomas White, Schavon Johnson, Mark Field

References

1. David, F.; Sandra. P. Stir Bar Sorptive Extraction for Trace Analysis. *J. Chrom. A.* 2006**,** 1152 (1-2), 54-69. DOI: 10.1016/j.chroma.2007.01.032
2. Bairai, S. T.; Lindberg, M. J. *Analysis of Organic Chemicals in Hanford Tank Waste Simulant by Stir Bar Sorptive Extraction;* RPP-RPT-63952, Hanford 222-S Laboratory Facilities, Washington River Protection Solutions, LLC, Hanford, WA, 2022

Improving Radon Risk Mapping Using Advanced Data Analytics and AI/ML

Thomas Danielson

Chronic exposure to radon is the leading cause of lung cancer in non-smokers. Radon risk maps are often provided at county-wide scales, lacking resolution for higher risk areas in otherwise low risk counties. This effort applies data analytics to increase the resolution of radon risk maps to the neighborhood/property scale.

Introduction

Chronic exposure to radon is the leading cause of lung cancer among non-smokers and more than one third of the United States is estimated to have a high geologic radon potential.[1] In Aiken County, SC, radon potential is generally low. However, approximately 10% of homes have measured concentrations above the recommended action level. Elevated radon concentrations found in Aiken County are attributed to sparse and naturally occurring uranium-containing mineral deposits (e.g., gorceixite)[2]. However, limited data are available to describe the precise locations, presenting a unique opportunity to overcome challenges associated with using limited data to make predictions for a sparse target output.

"Big data" approaches have been increasingly applied to radon risk modeling, especially in European countries.[3] However, most studies have explored applications across large regions (e.g., country-wide) or have access to large sampling datasets. Here, ArcGIS has been used to merge datasets containing the geologic formations and topography in Aiken County, limited at-home radon sampling, and flyover spectral gamma readings from the NURE[4] program (**Figure 1**). Notably, all data are coarse resolution when considering localized subsurface mineral formations, hence limited soil gas sampling has been performed as well. By applying machine learning approaches, the correlated features within the data guide sampling efforts, and the data/models are updated as new information is gained until sufficient resolution and predictive capability is achieved. In this way, we can better inform policymakers of where to sample and the required data needed to gain adequate resolution while minimizing cost.

Approach

The four datasets have been merged together using ArcGIS and subsequently processed using Python to a grid with a resolution of 1 km^2. The correlations between geologic formations and elevated uranium resource potential (as measured by NURE) were explored using Pearson correlations and principal component analysis on sub-region scale within the county, as illustrated in **Figure 2**. Additionally, the random forest algorithm was used to identify if the features that have been introduced to the data model (e.g., topographic and geologic formations) can be used to predict the NURE data. A preliminary sampling plan was created using the locations of the geologic features that have the strongest correlation with the NURE uranium resource potential within a subregion.
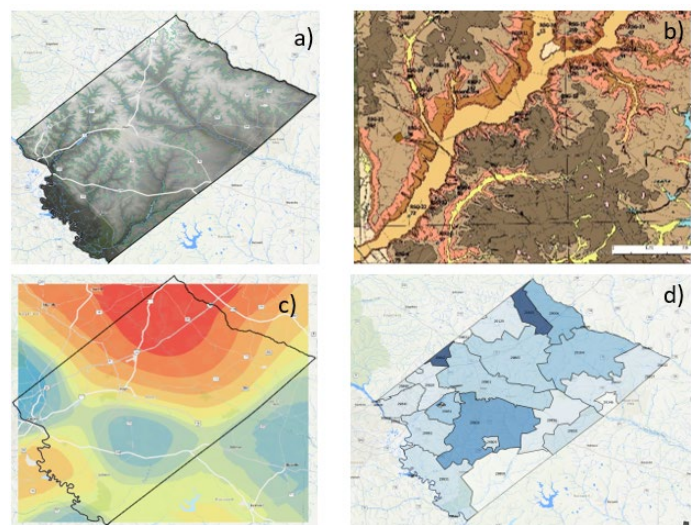

Figure 1. ArcGIS mapping of a) digital elevation, b) zoomed in geologic formations, c) spectral gamma flyover (NURE), and d) mean at-home sampling value across zip code regions in Aiken County.
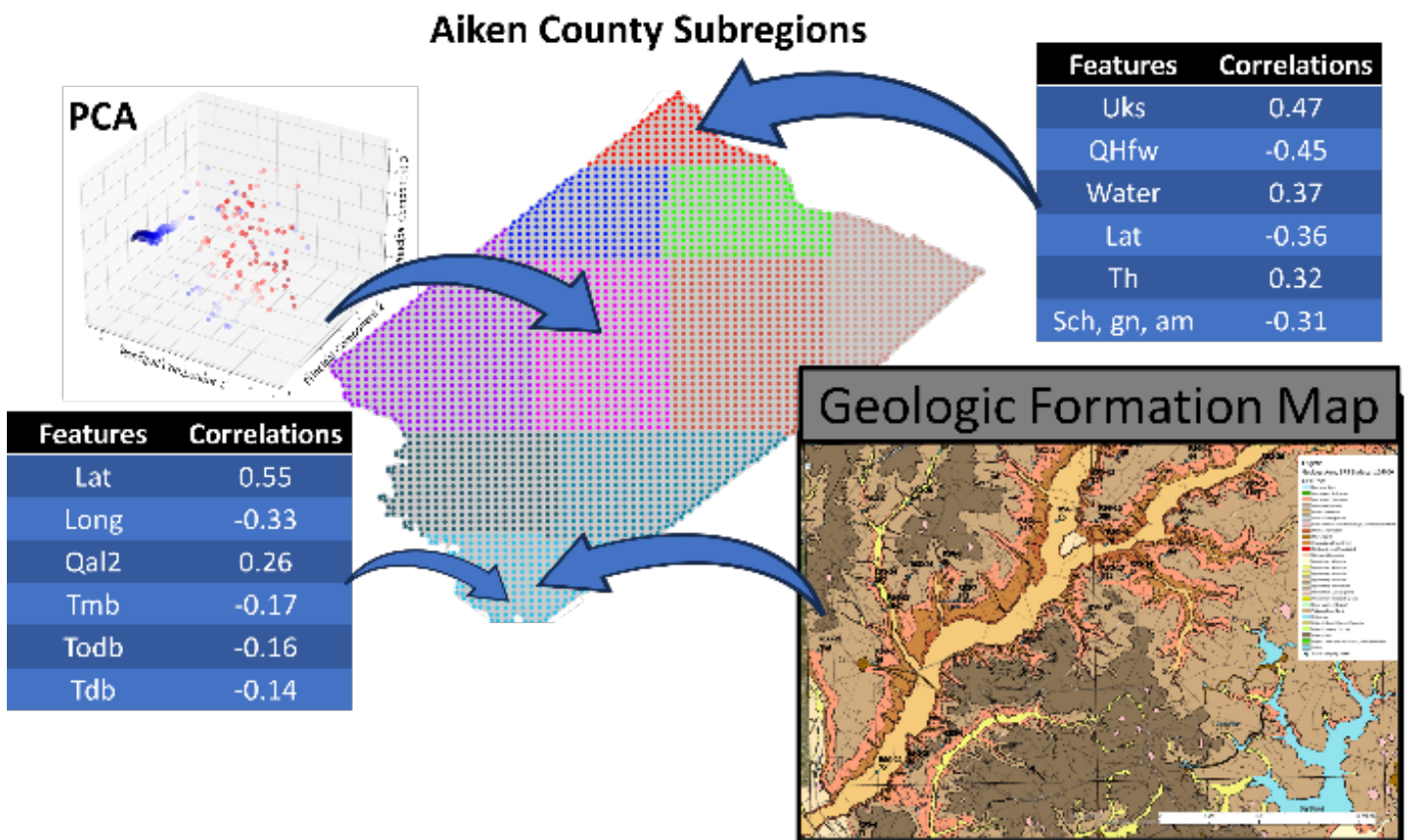
Figure 2. Illustration of data analytics workflow, after all data from Figure 1 were merged into ArcGIS.

Sampling was carried out by extracting soil gas, transferring the soil gas to a scintillation cell, and measuring the number of decays across a 15-minute time interval. Initially, all sampling has been performed within the Savannah River Site boundary. In this area, formations surrounding the Dry Branch and Tobacco Road Sand formations have been identified as features of interest where uranium-containing mineral formations may exist. On the first round of sampling, samples are collected near presumed positive locations and away from presumed positive locations to provide additional positive/negative information context to the coarse preliminary datasets that were used. As sampling occurs, this additional information is incorporated to the data model and findings are updated.

Accomplishments

- Data have been incorporated to ArcGIS to create the preliminary data model and preliminary correlations were explored across Aiken County. The Undifferentiated Cretaceous Sediments, Dry Branch, Tobacco Road, and Piedmont Undivided formations, along with latitude and longitude and elevation are among the strongest correlated features with elevated uranium resource potential readings from the NURE dataset.

- Approximately 60 soil gas samples were collected from within the Savannah River Site boundary and a map were created to show the variability in the radon concentration in soil gas across the area (**Figure 3**). Samples were collected at high and low spatial resolutions to explore trends in the concentration when a higher reading is identified. All concentrations within the SRS site boundary were relatively low and further sampling is merited to capture a broader range of variability.

- Random forest models were trained across the Aiken County subregions to determine if the NURE concentration map can be reproduced using the geologic information that was incorporated in **Figure 4**. While R^2 values are low, mean squared error values tend to be low as well and the actual versus predicted interpolated maps tend to be in qualitative agreement, indicating that the random forest may be a good tool for guiding preliminary sampling even with the spatially coarse datasets that were used here. Refinement of the models is underway.
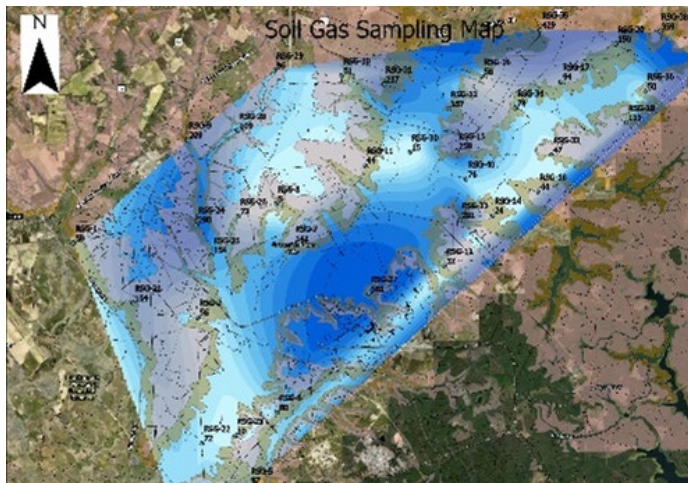
Figure 3. Interpolated map of soil gas concentrations at approximately 60 locations on the Savannah River Site. Darker blue indicates higher concentration.
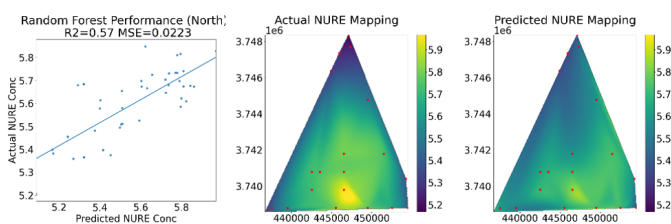
Team Members

Jordan Floyd, Fabiola Rivera-Noriega[+], Brian Looney, Elizabeth LaBone

[+]*SRNL Intern*

References

1. Gundersen, L.C.S., Schumann, R. R„ Otton, J. K., Dubiel, R. F., Owen, D. E„ and Dickinson, K. A. *Geology of radon in the United States*, Geological Society of America Special Paper 271, 1992.
2. Michel, J., Cole, K. H., and Moor, W. S. *Uraniferous gorceixite in the South Carolina coastal plain (USA),* Chem. Geol., 35: 227-245, 1982.
3. Bena, E., Ciotoli, G., Petermann, E., Bossew, P., Ruggiero, L., Verdi, L., Huber, P., Mori, F., Mazzoli, C., Sassi, R. *A New Perspective in Radon Risk Assessment: Mapping the Geological Hazard as a First Step to Define the Collective Radon Risk Exposure*, Science of the Total Environment 912, 2024.
4. Duval, J. S., Carson, J. M., Holman, P. B., and Darnley, A. G. *Terrestrial Radioactivity and Gamma-Ray Exposure in the United States and Canada: US Geological Survey Open-File Report* 2005-1413, 2005.
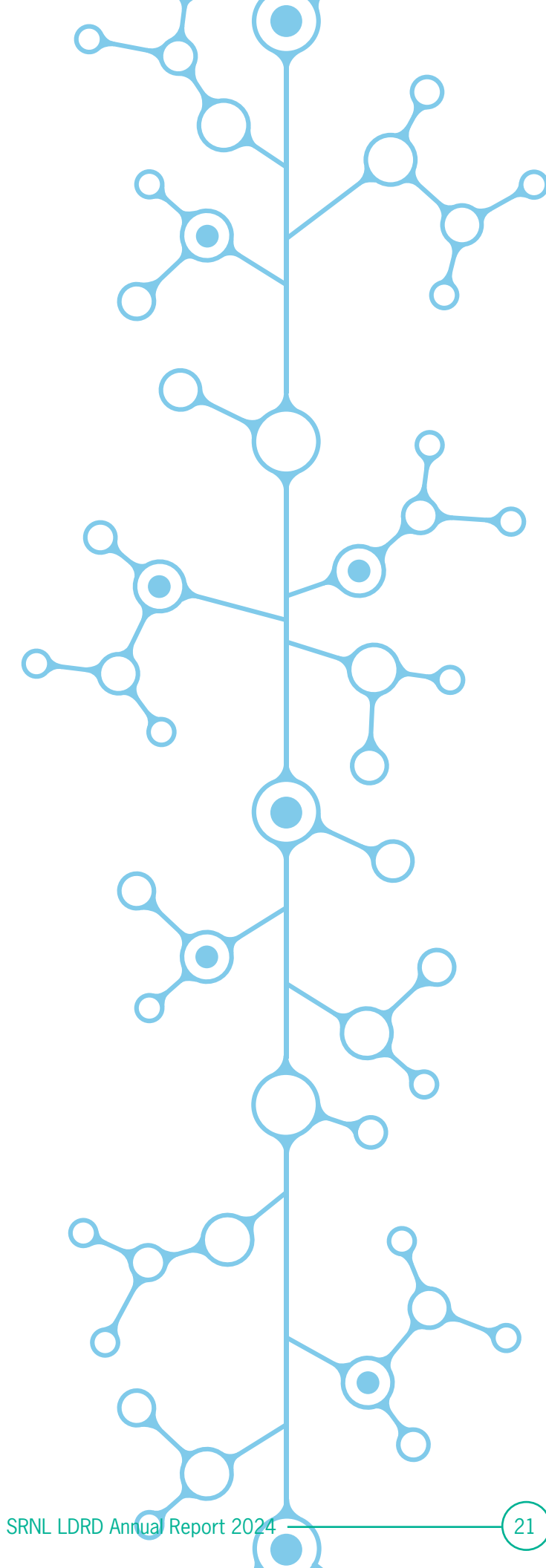
Valorization of Nuclear Waste Through Computational Actinide Catalyst Development

Megan Hoover

The investigation of an actinide-based catalyst for chlorine production was accomplished by simulating different reaction mechanisms using density functional theory with the SRNL's high-performance computer. Based on this study, a deeper understanding of how actinide-based catalysts can be engineered for other key industrial processes was elucidated.

Introduction

Ammonia synthesis, one of the most important industrial reactions for global agriculture, consumes approximately 2% of the total energy consumption.[1] One such catalyst for ammonia synthesis, which Haber and Le Rossignol patented in 1910, makes use of uranium.[2] This approach of using uranium and other actinide elements is not novel but compared to non-radioactive transition metal d-block catalysts, the use of actinides has been significantly underutilized by the scientific catalysis community for industrial applications. The actinides represent a unique group of heavy metal elements with interesting chemical properties that could make them attractive for catalytic applications. In this work, an industrially relevant reaction called the Deacon process, or the thermochemical oxidation of HCl, was modeled to determine the efficacy of using uranium for wider catalytic applications. The Deacon process is typically operated with an expensive RuO_2-based catalyst, but researchers from Bayer indicated a unique uranium-oxide U_3O_8 catalyst is thermodynamically stable and catalytically active for HCl oxidation.[3] Experimentally, only key macroscopic observables can be reported such as the apparent activation energy, reaction orders, and the overall rate of reaction. However, experimental studies struggle to both deconvolute specific reaction mechanisms and determine reaction steps that could be rate limiting for the catalytic conversion. Therefore, computational work elucidates reaction pathways that can guide future catalyst design.

Approach

The approach was a combination of density functional theory, chemical reaction engineering, and statistical mechanics to directly model the catalytic behavior of a uranium single atom catalyst on a ZrO_2 support or with a Zr-based metal-organic framework (MOF). From the literature, a uranium-based single atom catalyst is active for the thermochemical oxidation of HCl to Cl_2 (i.e., the Deacon process). Using the ZrO_2 support, the first objective was to determine the catalyst morphology at operating conditions with direct insight from experimental evidence. The optimized catalyst model is presented in **Figure 1**.
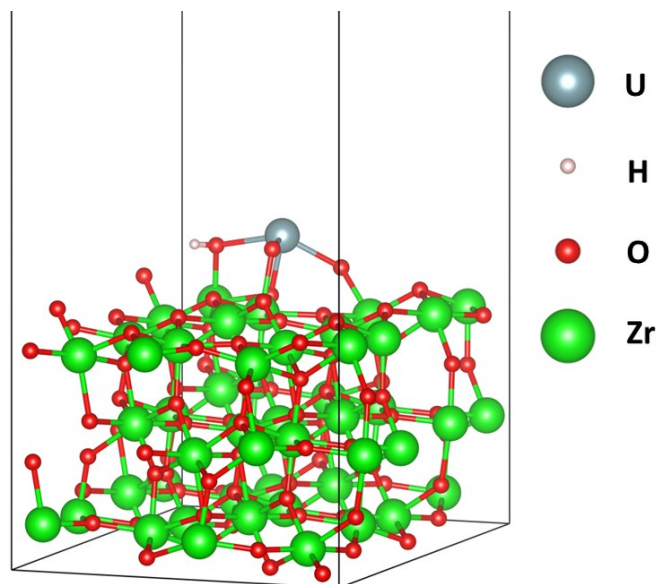

Figure 1. Reference (-111) ZrO_2 slab with a structurally optimized uranium (U) single atom catalyst. This configuration of atomic species serves as the Reaction Coordinate State 0 for all following figures.

The second objective was to model elementary reactions on the optimized catalyst by modeling as many elementary reactions as possible for HCl oxidation. These reactions include adsorption, desorption, and structural rearrangement processes. Some pathways were explored that yielded possible energy barriers that were deemed unlikely to occur at operating conditions. The most viable pathways from the analysis are outlined in **Figures 2 and 4**. The last step of catalyst modeling was to compute forward rate constants for all elementary steps and to compute a global system of species balances for all surface states. The project is currently expanding upon the Cl work to compute the reaction pathways for HBr and HI oxidation to develop trends regarding general halogen oxidation. Using a metal-organic framework (**Figure 6**), a similar methodology to the ZrO_2 work followed to compare the thermodynamics of the Deacon process relative to the ZrO_2 work.

Accomplishments

- The completion of an *ab initio* thermodynamic analysis for a single atom catalyst under experimental reaction conditions using the HCl, HBr, HI, and O_2 feed streams (e.g., **Figure 1**).
- This work is essential to catalyst first principles modeling. The model qualitatively matches the experimental catalyst as determined by high-angle annular dark-field imaging-scanning transmission electron microscopy (HAADF-STEM).[4]
- Gathered a direct understanding of the relative stability of uranium-based single atom catalyst in a highly oxidizing environment.
- Completed two unique and feasible thermodynamic reaction pathways at experimental operating temperatures - "O_2 on ZrO_2 Mechanism" (**Figures 2 and 3**) and "U-OCl Complex Mechanism" (**Figures 4 and 5**).
- This work is one of the only studies performed on the Deacon process (e.g., HCl thermochemical oxidation) using *ab initio* methods with an actinide-based catalyst. In the literature, *ab initio* studies focus on expensive RuO_2 and other transition-metal oxides.
- Developed a microkinetic model of both pathways, the "O_2 on ZrO_2 Mechanism" and the "U-OCl Complex Mechanism" using the COMSOL Multiphysics software, under the assumption of barrierless elementary reactions.
- Established the rate limiting behavior in the Deacon process, which is associated with HCl adsorption after the initial water formation and the formation of diatomic Cl_2.

- Generated of a cluster model with U(III) cation anchored to the NU-1000 (called U-NU-1000) metal-organic framework (**Figure 6**), and corresponding initial mechanistic study of the Deacon process.
- Added Stephen Vicchio to the VASP license.
- Targeting a journal publication for the project by Jan 2025.

Team Members

Nicholas Szaro*, Stephen Vicchio*, Megan Hoover,

*Postdoctoral Researcher
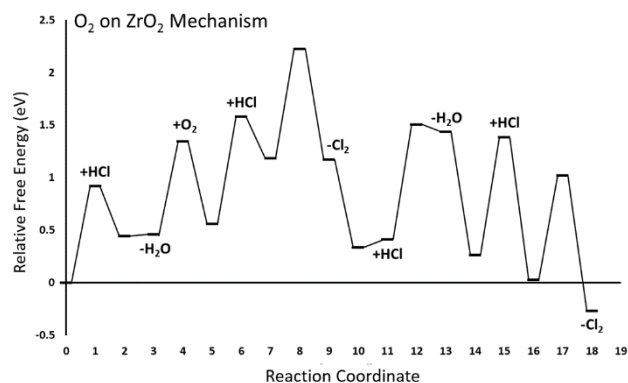
Figure 2. Thermodynamic free energy reaction diagram of the 'O_2 on ZrO_2 support' pathway for the $4HCl + O_2 \rightarrow 2Cl_2 + 2H_2O$ reaction with U on a (-111) ZrO_2 catalyst modeled at 773 K, where all gas species are computed at 1 bar pressure.

Figure 3. Pictorial reaction diagram of the 'O_2 on ZrO_2 support' pathway as outlined in Figure 2. The blue numbers refer to the reaction coordinate states in Figure 2.

References

1. IEA *Ammonia Technology Roadmap*; Paris 2021.
2. Haber, F.; Rossignol, R. L. Process of Making Ammonia. 1910.
3. Amrute, A. P.; Krumeich, F.; Mondelli, C.; Pérez-Ramírez, J., Depleted uranium catalysts for chlorine production. *Chemical Science* **2013,** *4* (5), 2209-2217.
4. Krumeich, F.; Amrute, A. P.; Mondelli, C.; Pérez-Ramírez, J., Structural Changes of a U3O8/ZrO2 Catalyst During HCl Oxidation – a HAADF-STEM Study. *Zeitschrift für anorganische und allgemeine Chemie* **2014,** *640* (5), 768-773.
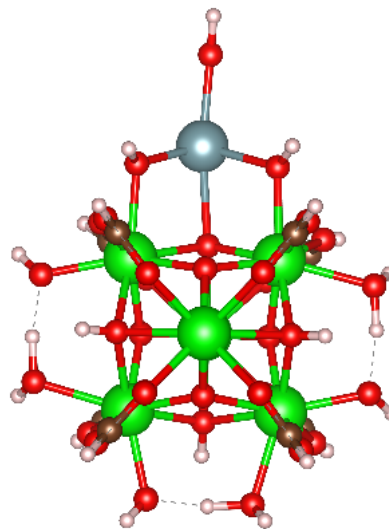
Figure 6. The initial reference structure for a uranium (U) single atom catalyst anchored to the NU-1000 metal-organic framework (MOF). The same atomic color scheme as Figure 1 is adopted.
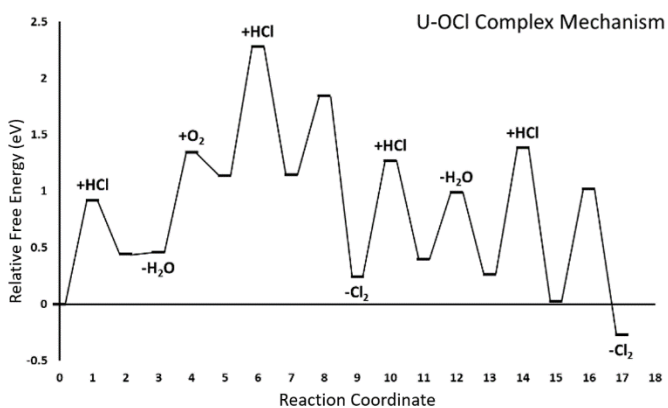
Figure 4. Thermodynamic free energy reaction diagram of the 'U-OCl Complex' pathway for the 4HCl + O$_2$ → 2Cl$_2$ + 2H$_2$O reaction with U on a (-111) ZrO$_2$ catalyst modeled at 773 K, where all gas species are computed at 1 bar pressure.
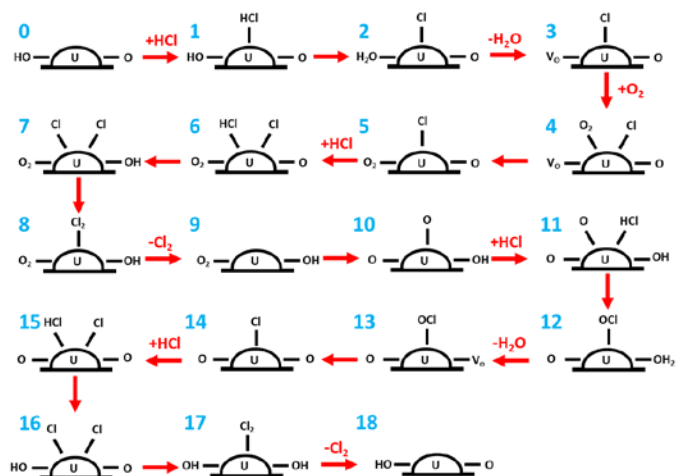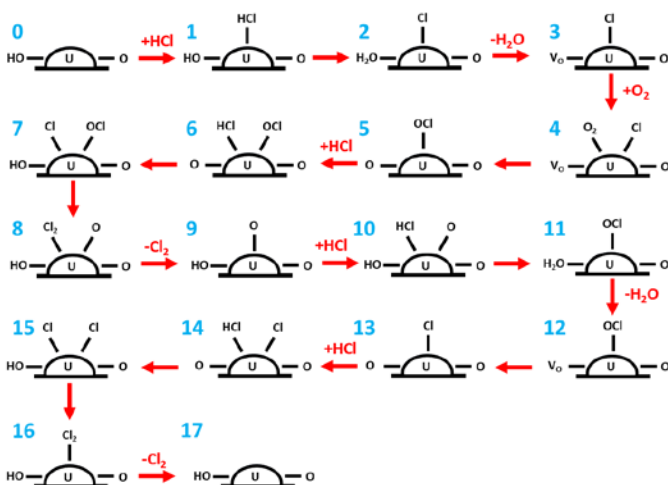

Figure 5. Pictorial reaction diagram of the 'U-OCl Complex' pathway as outlined in Figure 4. The blue numbers refer to the reaction coordinate states in Figure 4.
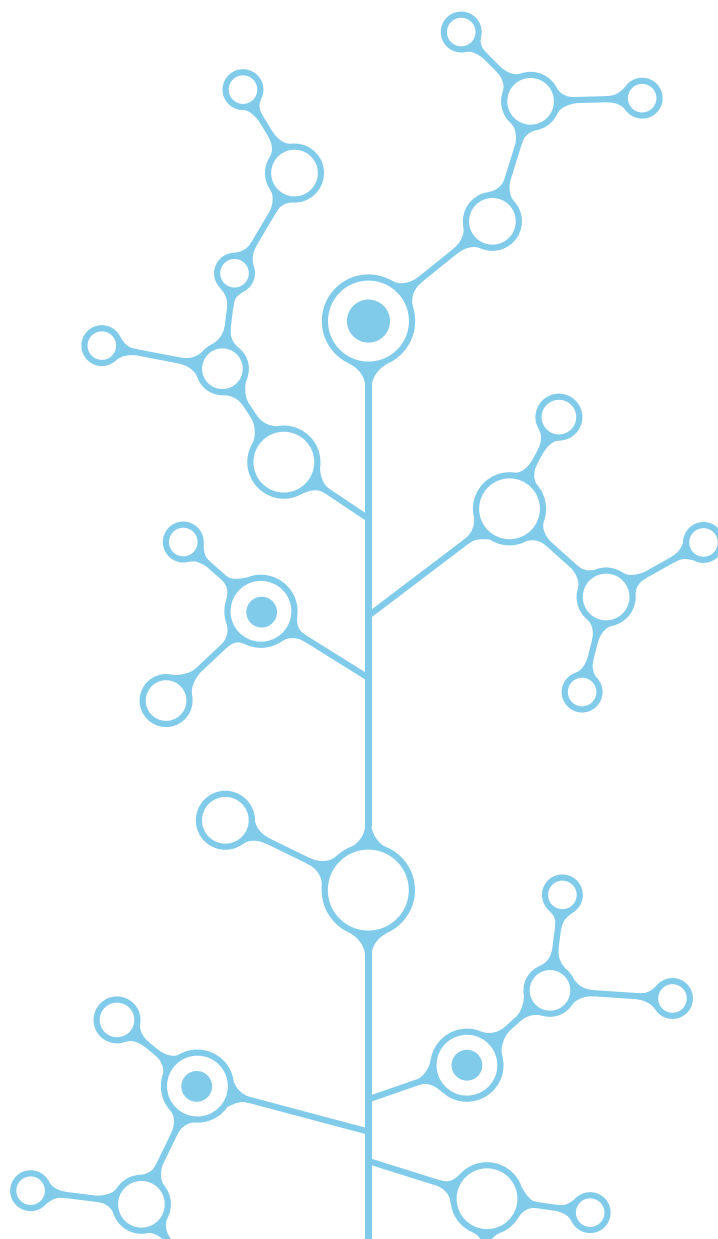
Modified Carbon Engineered Cellular Magmatics

Will Jolin

Engineered Cellular Magmatics, upcycled from post-consumer waste glass, can provide a porous scaffold to support activated carbon. The activated carbon can be used to sequester organic contaminants and then be modified by attaching a chelator to remove metals from solution with increased efficacy, creating a tunable solution for contaminant removal.

Introduction

Engineered Cellular Magmatics (ECMs) are synthetic, engineered pumice traditionally used as insulation or as geotechnical fill. To generate ECMs, source glass material (typically commercial soda-lime-silica container glass) is mixed with a foaming agent. The mixture is subjected to thermal treatment at temperatures much lower than traditional glass recycling, where the foaming agent decomposes and creates pores in the ECM structure. The foaming agent, often calcium carbonate, can be modified to other sources of carbon leading to variations in the product structure.[1] Activated carbon, in conjunction with other agents (e.g., calcium carbonate), can be used to foam ECMs that leaves behind a portion of oxidized carbon on the surface of the ECM pores.[2] This oxidized carbon can be used to target and sequester organic contaminants and other molecules of concern (e.g., PFAS). Further modification of the surface-bound activated carbon with chelators (e.g., ethylenediaminetetraacetic acid (EDTA)) can modify the material to sequester metals. Finally, the ECMs can be remelted to isolate the contaminants from the environment in a durable waste form.

Approach

The objective of the proposed work is to test the ability of carbon-containing ECMs to capture organics and then to modify the carbon-containing ECMs to capture various metals. ECMs with 1-5 wt% activated carbon were fabricated. Sorption of methylene blue, crystal violet, and rose Bengal to 3 materials (carbon-containing ECMs, activated carbon alone, and non-carbon ECMs) was tested through batch experiments. The carbon-containing ECMs were further modified by attaching functional groups that target specific contaminants of concern. Two modification methods were tested (**Figure 1**): 1) zinc (or nickel) impregnation, where positively charged zinc sorbs to the negatively charged carboxyl group and, 2) the attachment of EDTA through a silica cross link. Zinc, a weak Lewis acid, can act as a complexation site to bind nitrates, iodates, and other oxyanions, while EDTA is a robust chelator of cationic metals and radionuclides. Finally, the ability of these ECMs to be remelted, sealing the contaminants inside a glass waste form, was established (**Figure 2**).
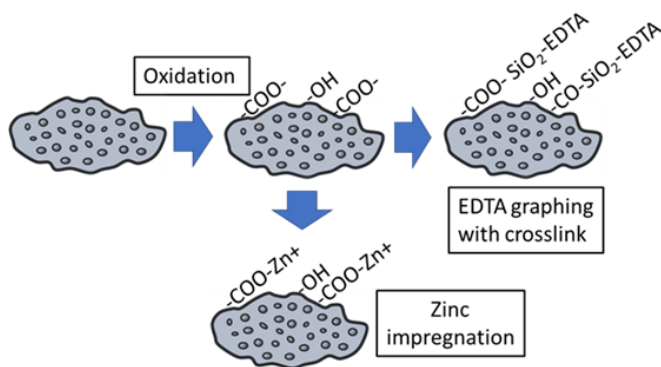

Figure 1. ECM modification process

Figure 2. Carbon-containing ECMs and non-Carbon ECMs prior to remelt (left) and after remelting at various temperatures (right)

Accomplishments

- ECMs with 1-5 wt% activated carbon were fabricated at SRNL at the lab scale. One percent carbon provided the best balance between reproducibility, porosity/surface area, and carbon content.
- The foaming process was reversed by remelting the foam glass, establishing a disposition method for foam glass after sequestering contaminants (**Figure 2**).
- Carbon-containing ECMs were able to remove 99% of organic dyes at 0.01 mM in solution, showing marked improvements over activated carbon or non-carbon ECMs alone (**Figure 3**).
- Diminishing returns at higher concentration further emphasized the increased ability of carbon-containing ECM over activated carbon and non-carbon ECMs to remove the organic dyes (**Figure 3**).
- A method for EDTA attachment to ECMs was developed. EDTA was attached to the surface of the activated carbon-containing ECMs through a silica cross link where Tetraethyl orthosilicate (TEOS) and N-(Trimethoxysilpropyl)ethylenediamine tetraacetic acid (TMS-EDTA) were added stepwise to a hydrochloric acid solution containing the carbon ECMs. This seemingly permanent attachment overcame the interferences of the glass matrix for attachment and modification.
- The modified material was characterized by thermogravimetric analysis (TGA). TGA results revealed approximate 1% coverage of EDTA by mass on the surface of the ECMs.

- Sorption of Fe, Ni, and Pb was then tested to the modified and unmodified ECMS through batch isotherm experiments.
- An 80% uptake of Fe was evident onto EDTA modified carbon ECMs in acidic conditions. Minimal uptake was seen for unmodified ECMs, carbon-containing or otherwise, under similar conditions (**Figure 4**). The modification of carbon-containing ECMs was therefore determined to be successful.
- Sorption of Pb was high to all forms of ECMs (modified and unmodified), suggesting the use of the material as a multi-mechanism sorbent.
- Under alkaline conditions, sorption of all metals to unmodified ECMs was high, again showing the usefulness of ECMs as a means to sequester contaminants overall.
- Nitrate and chromate uptake onto zinc and nickel impregnated ECMs was minimal, likely due to the interference of counterions released from the glass structure or the formation of unreactive Zn or Ni oxides on the surface.
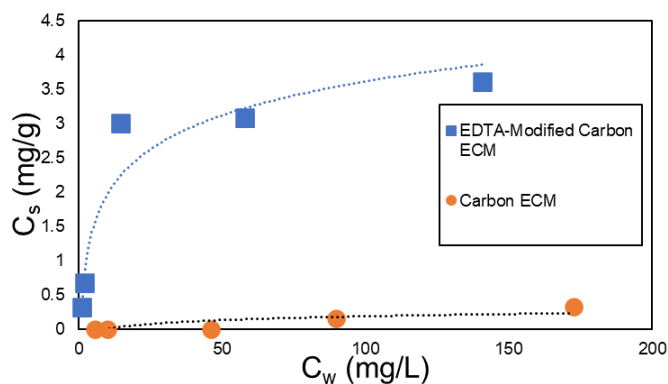
Figure 4. Sorption isotherms of Fe to EDTA modified carbon ECMs and unmodified carbon ECMs reveal the ability of modified to increase sorption.
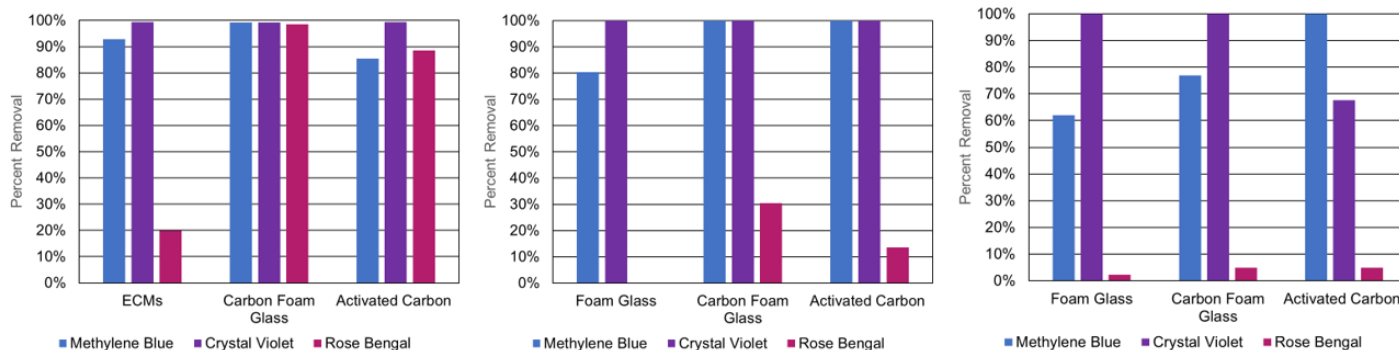
Figure 3. Removal percentages of methylene blue, crystal violet, and rose Bengal at 0.01 mM (left), 0.1 mM (center), and 1 mM (right) starting concentrations.

Intellectual Property

Invention Disclosures
- Carbon Foam Glass Ceramics for Contaminant Capture
- Functionalized Carbon Modified Foamed Glass Ceramics (Func-FGCs)

Patent Applications
- Functionalized Carbon-Modified Foamed Glass Ceramics (Provisional)
- Functionalized Carbon-Modified Foamed Glass Ceramics and PFAS Removal by Use of Carbon-Modified Foamed Glass Ceramics

Team Members

Austin Stanfield[*], Anna Stanfield, Eric McCaslin[*], Cory Trivelpiece, Alex Kugler, Courtney Burckhalter, Madison Hsieh, Robert Hausrath, Nicodemus Rod, Logan Howell[+], Kylie Manning[+]

[*]*Postdoctoral Researcher*
[+]SRNL Intern

References

1. König, J., R.R. Petersen, and Y. Yue, *Influence of the glass–calcium carbonate mixture's characteristics on the foaming process and the properties of the foam glass.* Journal of the European Ceramic Society, 2014. **34**(6): p. 1591-1598.
2. König, J., R.R. Petersen, and Y. Yue, *Fabrication of highly insulating foam glass made from CRT panel glass.* Ceramics International, 2015. **41**(8): p. 9793-9800.

Thiol-Functionalized Metal-Organic Frameworks for Mercury Removal from Waste Tanks

Ingrid Lehman-Andino

This project plans to accelerate waste remediation and reduce environmental risk by using metal organic framework materials as a deployable technology to remove mercury species from high-level waste stored at Savannah River Site facilities. This research is crucial for understanding the chemical properties of these porous materials.

Introduction

The Savannah River Site (SRS) Liquid Waste Stream (LWS) contains mercury that originated decades ago from canyon processing.[1] This mercury was used as a catalyst for the dissolution of the aluminum cladding on spent fuel rods to aid in the recovery of fission products. [1,2] The elevated levels of mercury in the tanks remains a concern due to its highly toxic properties. High levels of inorganic mercury and methylmercury are present at SRS facilities, such as the Defense Waste Processing Facility (DWPF)[1] and Salt Waste Processing Facility (SWPF)[1]. The mercury in the High Level Waste (HLW) can appear in many forms: elemental, organomercury, calomel (Hg_2Cl_2), and mercuric chloride ($HgCl_2$). Monitoring tank mercury levels has shown the recovery of mercury via sumps or mercury cells to be ineffective. Traditional adsorbents such as activated carbons[3,4] ion exchange resins[5], and zeolites[6] usually show low capacity, weak binding affinity, and poor selectivity for mercury.[3,7]

Due to the high toxicity of mercury, the efforts to accelerate remediation and reduce environmental risks are vital. The removal of mercury from waste tanks has become an emergent problem. Thiol-functionalized metal-organic frameworks (MOFs) have been shown to be efficient at selectively removing Hg^{2+} in the presence of metals such as Cu^{2+}, Ni^{2+}, Fe^{3+}, Ca^{2+}, Mg^{2+}, Cd^{2+}, Cr^{6+}, Mn^{2+}, Pb^{2+} and Zn^{2+}, over a broad pH range (1–10).[8-12] These MOFs have multiple thiols per organic ligand, while also maintaining ultrahigh porosity; therefore, they have the potential to remove more mercury per molecule than industry-standard adsorbents.[8] Developing new adsorbents as alternative materials for the highly alkaline HLW would support rapid response actions for future accumulation of mercury in the waste tanks.

Approach

The chemical behavior of mercury at SRS is complicated by the formation of high quantities of organomercury species, specifically methylmercury.[2] Our goal is to understand the chemistry and behavior of the MOFs toward the adsorption and sequestration of mercury species, beginning with Hg(II). The MOF candidates that show potential in initial testing will be selected for testing in tank waste samples. To achieve this goal, we designed and structurally characterized several isoreticular MOFs with thiol-functionalized linkers. Kinetic experiments for Hg(II) uptake and release at varying pH conditions are currently underway along with testing radiolytic stability of the MOFs. Direct Mercury Analysis is utilized to monitor the mercury kinetics with the synthesized MOFs. Additionally, we aim to test the MOFs' capacities to selectively extract Hg from tank waste simulation samples, competitive binding experiments, and test recyclability of the MOF at various pHs.

Accomplishments

- Isoreticular MOFs UiO-66-SH and UiO-67-(SH)$_2$ (**Figure 1**) were successfully synthesized and characterized by Powder X-ray Diffraction (P-XRD). This included design, materials procurement, hazard analysis, environmental evaluation planning, synthesis, and characterization.
- Stability studies under a series of alkaline conditions were completed for UiO-66-SH and UiO-67-(SH)$_2$. Their stability was evaluated under similar pH waste tank conditions, where UiO-67-(SH)$_2$ shows a higher stability to harsh pH condition such as pH 14.
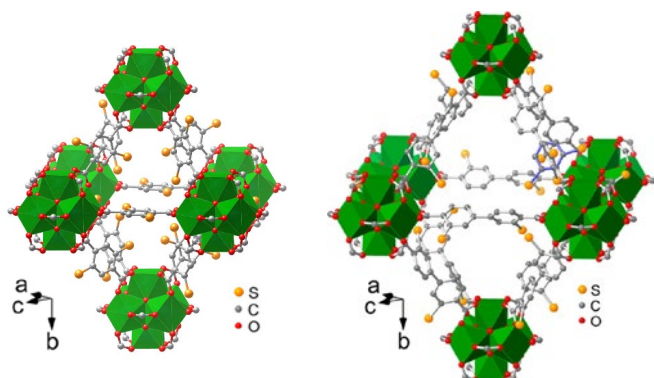
Figure 1. Octahedral cage from the single crystal structure of the UiO-67-SH[13] (left) UiO-67-(SH)$_2$ (right) framework[9].

- Radiolytic studies demonstrated stability of UiO-66-SH up to a 10 Mrad cumulative dose, while UiO-67-(SH)$_2$ shows stability up to 5.61×10^4 rad of cumulative dose. Studies were followed by P-XRD to confirm their crystallinity.
- Thiol-functionalized MOF UiO-66-SH demonstrated an optimal adsorption by the removal of 90% Hg(II) from a pH 10 solution at 24 hours, showing a higher affinity than UiO-67-(SH)$_2$.
- The kinetic data (**Figure 2**) show that the metal ions adsorption on UiO-66-SH increases sharply during the first 10 min and later plateaus. The higher initial adsorption rate is because these MOFs have sufficient number of adsorption sites and high metal ion affinity for the –SH groups. For UiO-67-(SH)$_2$ SRNL also observed an initial increase in the adsorption, but not as sharp as UiO-66-SH, which can be attributed to some instability at pH 10 conditions. Rapid mass transfer in the solution phase, the intraparticle diffusion, and adsorption of metal cations on the surface of the adsorbent binding sites (**Figure 2**) show the best performance for UiO-66-SH.
- A poster was presented at the Fall American Chemical Society (ACS) Conference in the Nuclear division, and it was honorably selected to be presented at the Sci-Mix during the same conference. *Thiol Functionalized Metal-Organic Frameworks (MOFs) for Mercury Removal from Waste Tanks* (SRNL-MS-2024-00453).
- Posters were presented at SRNL Day at Georgia Tech and at University of South Carolina Aiken during the Fall (SRNL-MS-2024-00453).
- Initial manuscript is beginning to be drafted. (Lehman-Andino, I., Cram, M., Pham, P., Martin, C. R., Dyer, S. Emerging Technologies for Mercury Removal adsorbents from High Level Radioactive Waste. *Technical Review. Chem. Soc. Rev*. in draft. **2024**.)

Team Members

Morgan Cram, Sonia Dyer, Corey Martin, Phuong Pham*

*Postdoctoral Researcher

References

1. Nguyen, V.Q. Literature Review Investigating Adsorbents for Mercury Removal from Salt Batch Feed Material. SRNL-STI-2024-00068, **2024**.
2. Bannochie, C. J.; Fellinger, T. L.; Garcia-Strickland, P.; Shah, H. B.; Jain, V.; Wilmarth, W. R. *Sep. Sci. Technol.* **2018**, *53*, 1935.
3. Stone, M. E., McCabe, D.J. Review of Mercury in the SRS Tank Waste Storage and Treatment Processes for Applicability to Hanford Waste Processing, SRNL, **2020**.
4. Ritter, J. A.; Bibler, J. P. Water *Sci. Technol*. **1992**, 25, 165.
5. Wilmarth, W.R.; DuoliteTM GT-73 Resin Testing in Support of the Salt Disposition Alternatives; WSRC-TR-98-00361, October, **1998**.
6. Sun, D. T.; Peng, L.; Reeder, W. S.; Moosavi, S. M.; Tiana, D.; Britt, D. K.; Oveisi, E.; Queen, W. L. *ACS Cent. Sci*. **2018**, 4, 349.
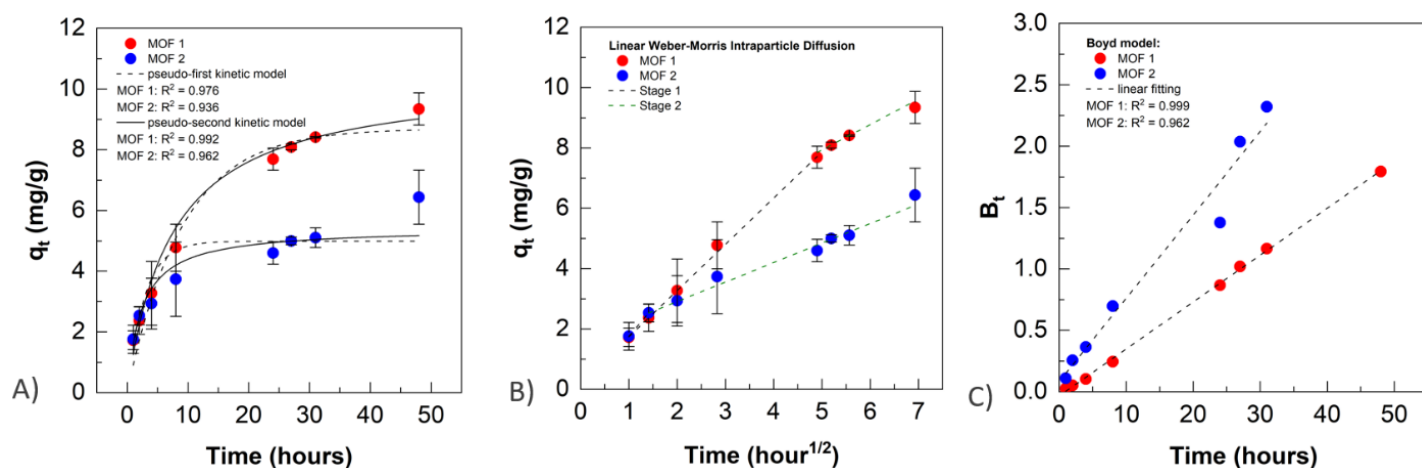
Figure 2. Kinetic data models base of adsorption experiments in pH 10: A) Pseudo-first/second models, B) Weber Morris intraparticle diffusion, and C) Boyd diffusion model. MOF 1 =UiO-66-SH, MOF 2= UiO-67-(SH)$_2$.

7. Inglezakis, V. J.; Kudarova, A.; Guney, A.; Kinayat, N.; Tauanov, Z. *Sustainable Chem. Pharm*. **2023**, 32, 101017.

8. Liang, L.; Chen, Q.; Jiang, F.; Yuan, D.; Qian, J.; Lv, G.; Xue, H.; Liu, L.; Jiang, H.-L.; Hong, M. *J. Mater. Chem. A* **2016**, 4, 15370.

9. Yan-Lung Wong, Yingxue Diao, Jun He, Matthias Zeller, and Zhengtao Xu. *Inorg. Chem*. **2019** 58 (2), 1462-1468.

10. Gao, J.; Li, Z.; Deng, Z.; Liu, M.; Wei, W.; Zheng, C.; Zhang, Y.; Chen, S.; Deng, P. *Nanomaterials* **2021**, *11*, 2488.

11. Ding, L., Luo, X., Shao, P., Yang, Y., Sun, D. *ACS Sustainable Chem. Eng.* **2018**, 6, 7, 8494–8502.

12. Yee, K., Reimer, N., Liu, J., Cheng, S., Yiu, S., Weber, J., Stock, N., Xu, Z. *J. Am. Chem. Soc*. **2013**, 135, 7795–7798.

13. Guo, B.; Cheng, X.; Tang, Y.; Guo, W.; Deng, S.; Wu, L.; Fu, X. *Angewandte Chemie International Edition.* **2022**, 61 (13), e202117244.

A Lightning Forecast System to Mitigate Risk at DOE-EM Sites

Stephen Noble

Lightning represents a safety hazard to outdoor workers and equipment at the Savannah River Site and at other Department of Energy sites. Our objective is to provide innovative site lightning forecasts using modeled cloud physics, typical of real-world lightning formation, that are derived from high resolution numerical weather prediction models.

Introduction

The Savannah River Site (SRS) experiences more than 3,000 lightning strikes per year, which poses a safety risk to workers. The current notification system for lightning strikes on SRS is based on the detection of previously occurring cloud-to-ground lightning strikes within the SRS boundaries or a small buffer area (~10 km) and does not provide advanced warning of lightning threat. This procedure has led to a handful of near misses in the last few years when thunderstorms have developed directly over SRS, allowing limited or no warning to workers in the field.

Lightning potential is created by strong vertical atmospheric motions separating charges within mixed phase clouds, an essential condition for the transfer of ions creating charge separation. Mesoscale numerical weather prediction models provide resolution of cloud properties such as the phase of water content as well as vertical velocities. Lightning indices, such as the Lightning Potential Index (LPI, 1), make use of information from these models to provide lightning potential forecasts in a realistic physical sense. The Atmospheric Technologies Group (ATG) operationally runs mesoscale models for use in site forecasts and emergency response, which can be also used to provide information for lightning forecasts. The project objective is to provide a robust lightning forecast system to reduce risk to DOE workers and property, especially in a changing climate where extreme weather events are likely to occur more often.

Approach

Forecast data were collected from implementing two tuned mesoscale models in 2023. Verification for predicted LPI was performed using the National Lightning Detection Network (NLDN) cloud-to-ground lightning strikes that occurred within each model domain. Original forecasts, as indicated in previous year, were overpredicting lightning events (Type 1 errors, false positives) in terms of a daily, binary 24-hour lightning forecast (**Table 1**). Analysis for this year was performed to identify a filter to limit the number of false positive forecasts while still preserving a low number of false negative (Type 2 error) forecasts. The filter was based on assuring that some the maximum LPI in a single grid box was above a given threshold, otherwise, the entire lightning potential forecast for that period was considered zero. By maximizing the equitable threat score for various thresholds and maintaining false negatives below 3%, SRNL identified the filter that provided the optimized forecast results (**Table 2**).

		validation	
		NDLN yes	NLDN no
forecast	LPI yes	87 (~27%)	106 (~33%)
	LPI no	2 (~1%)	122 (~39%)

Table 1. Original 24-hour binary forecast results.

		validation	
		NDLN yes	NLDN no
forecast	LPI yes	81 (~25.5%)	44 (~14%)
	LPI no	8 (~2.5%)	184 (~58%)

Table 2: Optimized filtered 24-hour binary forecast results.

Risk levels were determined by strike numbers converted to LPI values using a regression analysis of the sorted 15-minute values for each forecast. While the average timing difference between model peak LPI and peak NLDN lightning strike density was minimal, those differences varied greatly. Therefore, forecast implemented the maximum average LPI that occurred over 3 hours. The

final visualization products were developed for both the Regional Atmospheric Modeling System (RAMS) and the Weather Research and Forecasting (WRF) model; they are generated daily as a tool for SRS forecasters (**Figures 1 & 2**).

RAMS 3–hr max LPI Forecast 2024/7/15 6:00 UTC
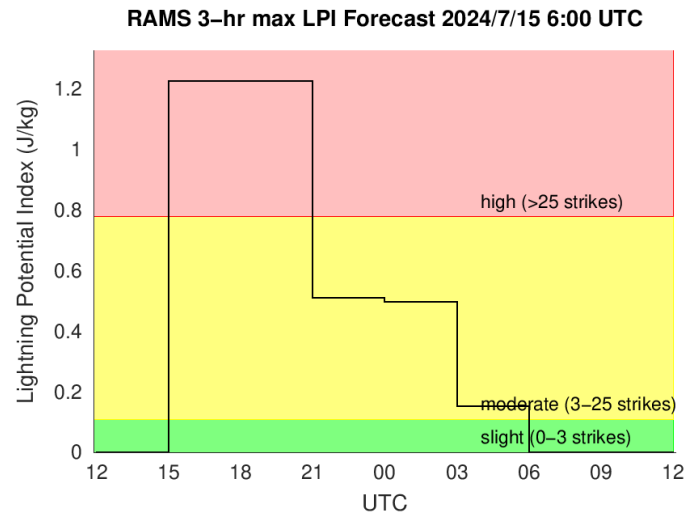
Figure 1. Lightning potential forecast timeseries product for RAMS model issued for 15 July 2024.
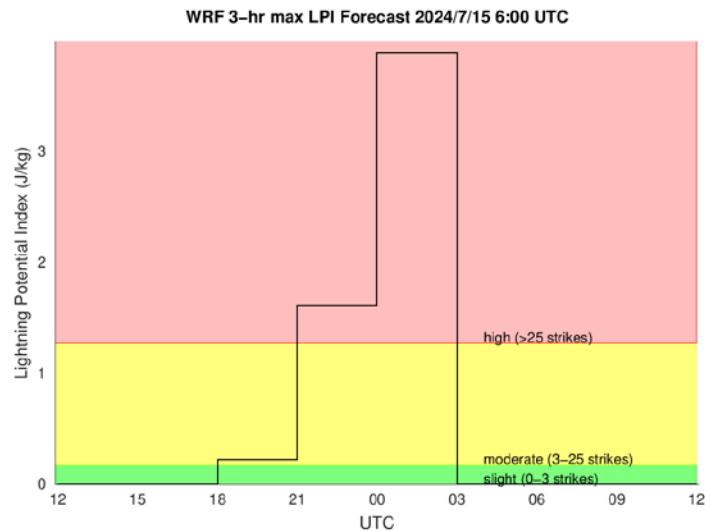
Figure 2. Lightning potential forecast timeseries product for WRF model issued for 15 July 2024.

Accomplishments

- Used 317 RAMS-verified forecasts to calculate the prediction threat score and identified a filter to remove erroneous lightning predictions caused by low predicted values of lightning potential.
- Performed regression analysis on sorted forecasted lightning potential and lightning strike density to identify lightning potential thresholds for risk categories.
- Calculated probabilities of lightning forecast accuracy based on risk categories (see **Figure 1**): 41% lightning occurrence when in the slight category, 78% chance of lightning in the moderate category, and 91% chance of lightning in the high category.
- Created a usable 3-hour maximum domain averaged LPI forecast product (**Figure 1**) and a 24-hour maximum LPI map for use by site forecasters.
- Performed the same analysis for 431 WRF forecasts and developed the same forecast products as comparison.

Peer-reviewed Publication

- Thomas, A.; Noble, S. A Physics-Based Ensemble Machine-Learning Approach to Identifying a Relationship Between Lightning Indices and Binary Lightning Hazard. *Frontiers in Earth Science* **2024**, under review

Team Members

Andrew Thomas, Steve Weinbeck, Steven Chiswell, Robert Buckley

Reference

1. Yair, Y.; Lynn, B.; Price, C.; Kotroni, V.; Lagouvardos, K.; Morin, E.; Mugnai, A.; Llasat, M. d. C. Predicting the potential for lightning activity in Mediterranean storms based on the Weather Research and Forecasting (WRF) model dynamic and microphysical fields. *J. Geophys. Res.* **2010**, 115, D04205. DOI: 10.1029/2008JD010868

Topological Magnetic Textures in Lanthanide- and Actinide-based Quantum Materials

Binod Rai

Quantum materials, governed by quantum behavior, exhibit emergent phenomena such as exotic magnetism and topological states of matter, making them promising candidates for future energy storage technologies. Understanding and engineering these materials is essential for their successful application in next-generation technologies.

Introduction

The design and development of new materials have historically driven the discovery of novel physical phenomena and technological advancements. Quantum materials, known for their exotic magnetism and topological states, hold significant potential for future energy storage applications. The unique phenomena associated with these materials have captivated scientists globally. However, exotic magnetism and topological states are only known for a few materials. Among these, f-electron-based compounds are particularly promising, as Ruderman–Kittel–Kasuya–Yosida (RKKY) interactions and spin-orbit coupling contribute to stabilizing these exotic states.

This research program has identified and synthesized several quantum materials with the potential to exhibit exotic magnetism. Through collaboration with universities, national labs, and DOE User Facilities, we investigated the relationship between structural, magnetic, and electronic properties. Our focus on the fundamental science of quantum materials has led to the discovery of complex magnetic structures. These findings are crucial for advancing our understanding and establishing a pathway from the discovery of topological materials to their practical application.

Approach

The crystal growth lab, established for the first time at SRNL, was utilized to synthesize several materials such as $PuCl_3 \cdot 6H_2O$, Np_2O_5, NpO_2, $NdCuGa_3$, $EuIr_3Si_7$, and $Ir_3(Si,Ga)_7$. Single crystal XRD at SRNL was crucial for discovery of new crystals such as $EuIr_3Si_7$ and $Ir_3(Si,Ga)_7$.

Magnetic and thermodynamic properties of these materials were measured at collaborating institutions Idaho National Laboratory (INL), Los Alamos National Laboratory (LANL), and Oak Ridge National Laboratory (ORNL). To explore their magnetic structures, neutron beamtime proposals were submitted and awarded through the DOE User Facility at ORNL, with seven neutron scattering experiments successfully completed between FY22 and FY24. Our research has revealed intriguing crystal structure details and complex magnetic structures. Additionally, since May 2024, the new Dynacool Physical Property Measurement System (PPMS) at SRNL has been fully operational, further helping to successfully complete this project.

Accomplishments

- **Publications and Manuscripts:** Published five peer-reviewed articles with two additional manuscripts in preparation.
- **Funding Success:** Submitted multiple DOE SC proposals between FY22 and FY24, resulting in one funded proposal in FY23 and another encouraged to submit a full proposal in FY24.
- **Invited Publications:** Authored an invited review on Actinide Oxides for the Institute of Physics (IOP), published in *Reports on Progress in Physics* (Impact Factor: 18.01) in May 2024. Additionally, published a topical review on RTX3 in *Journal of Physics: Condensed Matter* in May 2022.
- **Conference, National Labs and University Presentations:** Delivered seven invited talks and five contributed talks at INK, ORNL, Augusta University, University of Notre Dame, the American Physical Society. The Mineral Metals and Materials Society, American Vacuum Society, and Materials Research Society meetings in FY22, FY23 and FY24, showcasing results on materials like actinide oxides, $NdCuGa_3$ $EuIr_3Si_7$ and $Ir_3(Si,Ga)_7$.

- **Neutron Scattering Proposals:** Successfully secured seven neutron beamtime awards at ORNL from FY22 to FY24.
- **Lab Establishment:** Established a crystal growth lab at SRNL for intermetallic and oxide-based materials for the first time.
- **Material Synthesis:** Synthesized and characterized several candidate quantum materials, including $NdCuGa_3$, Np_2O_5, NpO_2, $PuCl_3$, $Ir_3(Ga,Si)_7$ and $EuIr_3Si_7$.
- **New Capabilities:** Installed an arc-melter at SRNL in FY23, enabling the alloying of metallic materials.

Peer-reviewed Publications

- **Binod K. Rai**, Shuxiang Zhou, Santosh KC, Luke R Sadergaski, "Physical properties of Np_2O_5 single crystals. (manuscript in preparation *2024)*.
- **Binod K. Rai**, Alex Bretaña, Gregory Morrison, Volodymyr B. Buturlim, Hanno zur Loye, Krzysztof Gofryk "Physical properties of $Ir_3(Ga,Si)_7$ single crystals. (manuscript in preparation *2024)*.
- **Binod K. Rai**, Alex Bretaña, Gregory Morrison, Ryan Greer, Krzysztof Gofryk, Hanno zur Loye, "Magnetism of Binary Actinide Oxides: A Review", Reports on Progress in Physics, **87** (2024) 066501 (Invited Review Article)

- **Binod K. Rai**, Patrick O'Rourke, Catherine Housley, Henry Ajo, Arjun Pathak, Narayan Poudel, Krzysztof Gofryk, Boris Maiorov, Qiang Zhang, Travis Williams, and Matthias Frontzek, "Magnetic properties of $NdCuGa_3$ single crystals", Journal of Magnetism of Magnetic Materials, **589** (2024)171515
- Matthias D. Frontzek, Luke R. Sadergaski, Samantha K. Cary, **Binod K. Rai**, "Search for octupolar ordering in NpO_2 by unpolarized neutron powder diffraction", J. Solid State Chemistry 321 (2023) 123875
- **Binod K. Rai**, Patrick O'Rourke, Utpal Roy, "Review on crystal structures and magnetic properties of *RTX*3 materials", *J. Physics: Cond. Matter.* **2022** 34 273002 (*Invited* Topical Review Article, SRNL publication spotlight)
- **Binod K. Rai**, Shang Gao, Matthias Frontzek, Yaohua Liu, A. D. Christianson, A. F. May, "Magnetic properties of Fe-substituted $NiBr_2$ single crystals", *J. Magn. & Magn. Mater.*, **2022** 557 169452

Team Members

Catherine Housley, Alex Bretaña[*], Henry Ajo, Bejamin Conner, Hanno zur Loye[a], Gregory Morrison[a], Krzysztof Gofryk[b], Boris A Maiorov[c], Luke R Sadergaski[d]

[*]*Postdoctoral Researcher*
[a]*University of South Carolina*
[b]*Idaho National Laboratory*
[c]*Los Alamos National Laboratory*
[d]*Oak Ridge National Laboratory*

Heat Waves and Extreme Rainfall at SRS

Andrew Michael Thomas

Heat waves are an ever-growing concern as average global temperatures rise. Extreme heat events are known to impact health but can also modify rain patterns. In the humid climate of the Southeast, while there is overall less rainfall during heat waves, there are increased short-term rainfall rates that increase flood risks.

Introduction

In coastal Australia, heat waves have recently been shown to de-stabilize the daytime boundary layer, while contributing to greater nocturnal stability (1). In severe weather forecasting, the presence of a stable surface layer has been known to inhibit convective cloud formation before a modest lifting mechanism – such as a weak cold front or "dry line" – allows for a more sudden release of convective energy, which may contribute to severe thunderstorms. With the observance of localized, heavy rainfall events during or after a series of hot days, and with weak cold/stationary fronts being a relatively common occurrence in the summertime in the Georgia/Carolinas region of the Southeast U.S., it is possible that the presence of a heat wave in a humid climate could serve as an enhancer to extreme rainfall events in the region.

Focusing on the CSRA region, this study examined the climatology and catalogued heat wave events in the 21st century. The study found that while heat waves show a decreased amount of rainfall, there are peaks in the early afternoon hours that indicate stronger "pulse" thunderstorm events occur during heat wave periods, which have a greater severity in impact and increase flooding risk.

Approach

Using the past 24 years (2000-2024?) of observations from the SRS N-area meteorological tower, along with local airport weather stations, days and the corresponding daily high temperatures that meet or exceed the 95th percentile of daily high temperatures were tabulated, with periods of three or more consecutive days exceeding the 95th percentile

categorized as a "heat wave." Precipitation on subsequent and constituent days was also noted. The team used the different 61 m and 2 m temperatures at the N-area climatology tower to calculate the surface lapse rates during the heat wave periods. During 95th-percentile heat waves, the surface inversion was stronger than the average summer day (June/July/August, or JJA) during the night (**Figure 1**), which matches preliminary model analysis (2).

Multi-Radar/Multi-Sensor (MRMS) gridded rainfall estimates were used to determine the onsite rainfall amounts, which are reasonably accurate for SRS and the CSRA (3). The surface lapse rates have some correlation to accumulated SRS rainfall within ~6 hours of lag time (**Figure 2**). Predictably, the rainfall values during heat wave days are low but do have spikes in the early afternoon, indicating some rainfall events, and there is increased rainfall in the days following heat wave days (**Figure 3**).
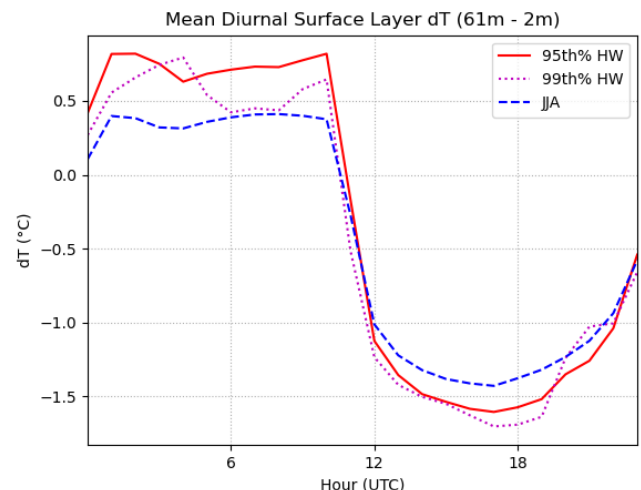
Figure 1. Difference in 61m and 2m temperatures from N-area Climatology 2000-2024.
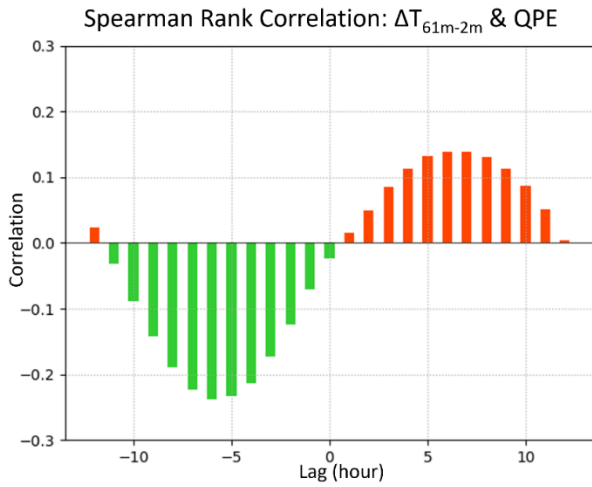
Figure 3. Spearman Rank Correlation between the "surface layer" temperature difference and the 1hr MRMS Quantitative Precipitation Estimate (QPE) at SRS for 2015-2023.

Figure 2. Hourly MRMS QPE summed over SRS for heat wave days, the days after heat waves, and the JJA average for 2015-2023.

A select number of these events were examined closer, using a meteorological model, with experiments conducted by the atmospheric state of the initial

conditions. Simulations show that increasing the stability of the surface layer (**Figure 4**) can produce enhanced rainfall within the model domain (**Figure 5**).
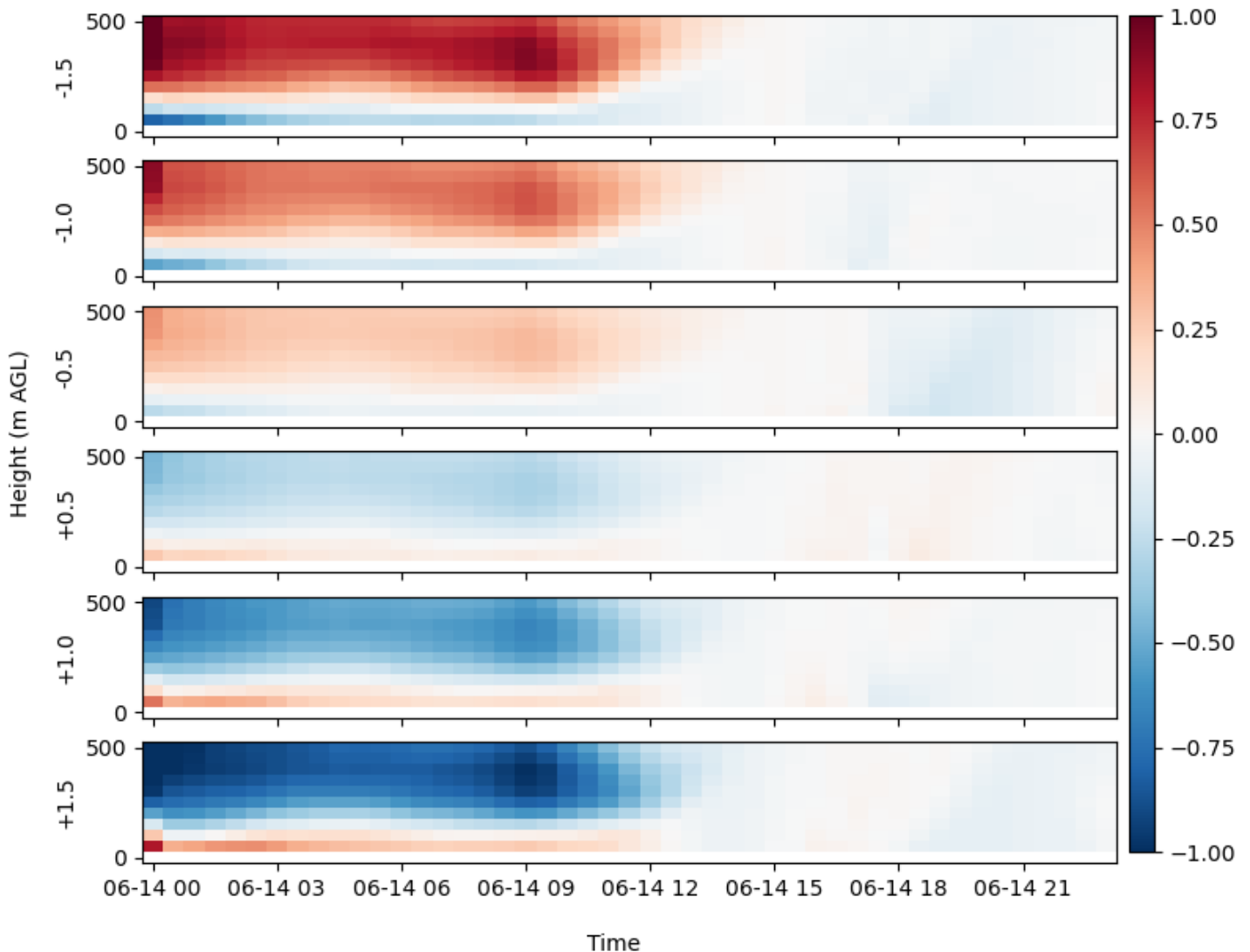
Figure 4. Vertical temperature deviations in the altered simulations against the control simulations.
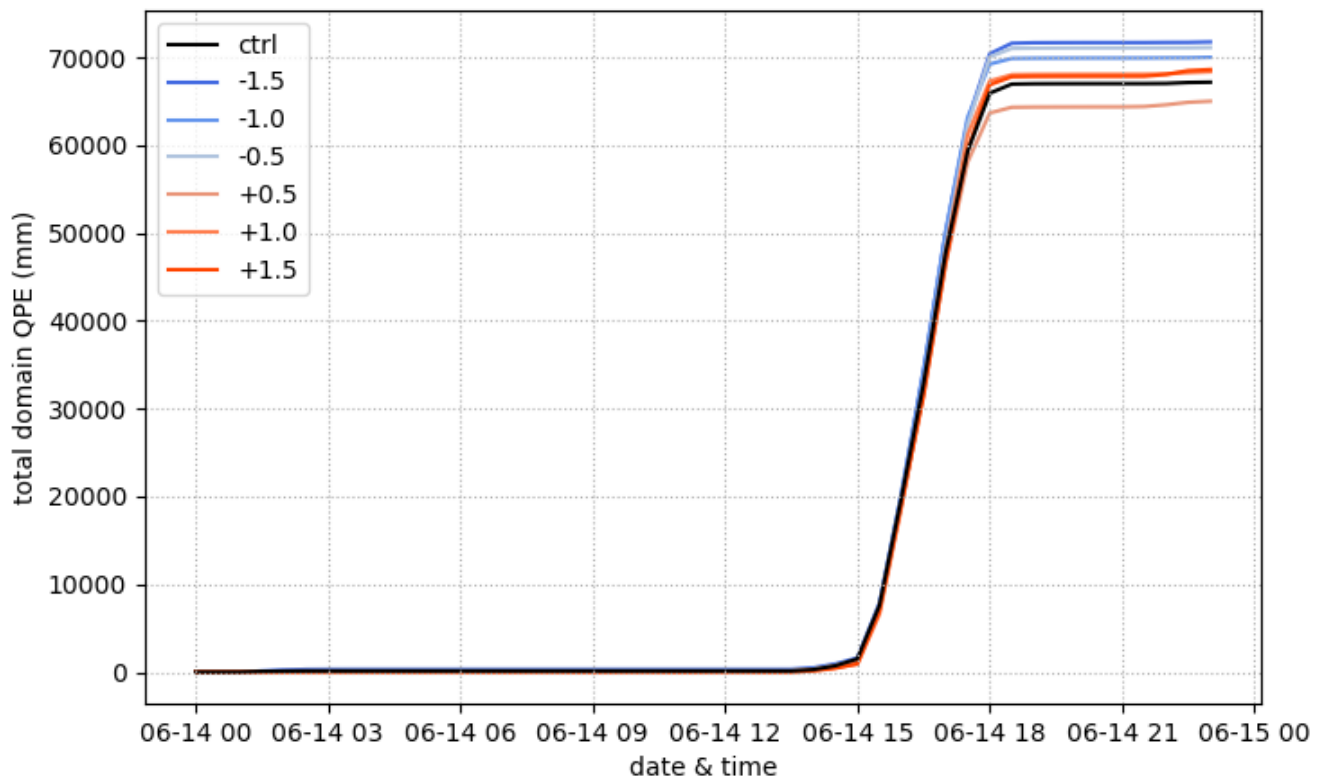
Figure 5. Accumulated precipitation for all seven WRF simulations (labelled)

Accomplishments

- Created a dataset of observed heat waves at SRS from 2000 to 2024.
- Analyzed climatology of precipitation, temperature, pressure, and humidity trends during the heat wave cases, the days after the heat wave, and comparison to summer trends.
- Made progress on a publication.
- Performed sensitivity experiments of heat waves.

Peer-reviewed Publication

- Heat Wave Enhancement of Nocturnal Stable Layers and Extreme Precipitation at the Savannah River Site* (in preparation)

Team Member

Joseph Wermter

References

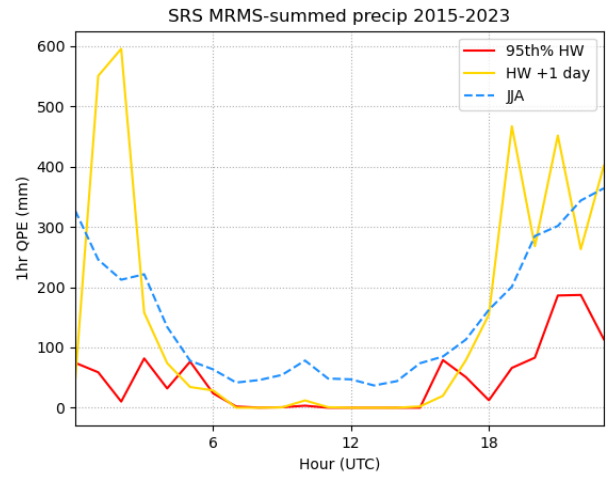1. Huang, Q.; Reeder, M. J.; Jakob, C.; King, M. J.; Su, C.-H. The life cycle of the heatwave boundary layer identified from commercial aircraft observations at Melbourne Airport (Australia). *Quarterly Journal of the Royal Meteorological Society,* **2023**, 149(757), 3440–3454. DOI: 10.1002/qj.4566
2. Gott, J. A. Boundary Layer Height Variation over the Savannah River Site during a Heat Wave. *N. p.,* **2023**. DOI: 10.2172/1993025
3. Rivera-Giboyeaux, A. M. Radar Derived Rainfall and Rain Gauge Measurements at SRS. *N. p.,* **2020**. DOI: 10.2172/1602977

Computationally-Guided Insights into the Influence of Ligands on Catalysis for Improved Waste-To-Energy Conversion

Stephen P. Vicchio

This study utilizes quantum chemical calculations to investigate how subtle changes in catalyst structure alter the catalytic performance of methane-to-methanol conversion. The findings demonstrate how coordinating ligands at the inactive metal centers impact the methane conversion at active metal centers. Potential reasons for these unique ligand-induced trends are considered.

Introduction

Metal-organic frameworks (MOFs) consist of inorganic nodes (i.e., containing metal atoms) that are interconnected by organic linkers (i.e., containing carbon and no metal atoms), as shown in **Figure 1**. For catalytic applications, MOFs are attractive because of their high active site densities and tunability.[1] Prior work on MOF-based catalysis using the Materials Institute Lavoisier 100 (MIL-100) MOF demonstrates the potential for the conversion of methane-to-methanol.[2-4] Developing catalysts capable of methane-to-methanol conversion is vital to methane valorization into a valued-added product (e.g., methanol), an important process for addressing anthropogenic methane emissions. Direct methane-to-methanol catalysis is inhibited by the unfavorable C-H bond dissociation of methane (~440 kJ/mol) and the favorable C-H bond dissociation of methanol (~400 kJ/mol),[5] thus leading to overoxidation products (i.e., CO and CO_2). Interestingly, Hall et al. observed differences in CO oxidation apparent activation energies as a function of MIL-100 node hydration, with higher activation temperatures leading to less H_2O ligands anchored to the inactive metal centers within MIL-100.[6] These results demonstrate a novel concept, called "indirect second sphere coordination effects," where ligands coordinated to the inactive metal centers alter the catalytically active metal center of MIL-100. These effects are worthy of further exploration, as insights into the structure-function relationships between the ligand environment and catalysis function are essential to rational catalyst design.

Approach

SRNL's high-performance computer enables the rapid screening of MIL-100 MOFs to investigate indirect second sphere coordination effects. Specifically, the work investigates methane-to-methanol (MTM) conversion using density functional theory; the MTM reaction mechanism is presented in **Figure 2**.
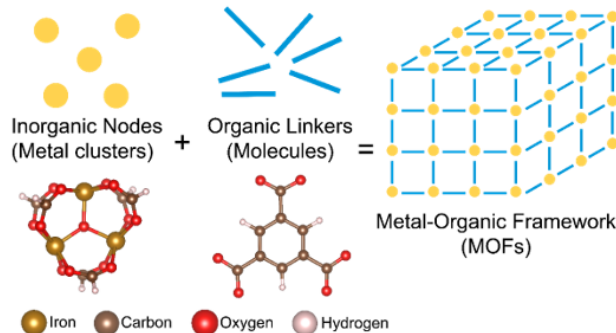
Figure 1. Metal-organic frameworks (MOFs) are comprised of inorganic nodes and organic linkers to generate 3D, porous, crystalline materials. These materials are useful for a variety of applications, including catalysis, where the metal centers of the inorganic nodes can convert waste methane into methanol. Herein, the node and linker for the Materials of Institut Lavoiser (MIL)-100 MOF are shown.
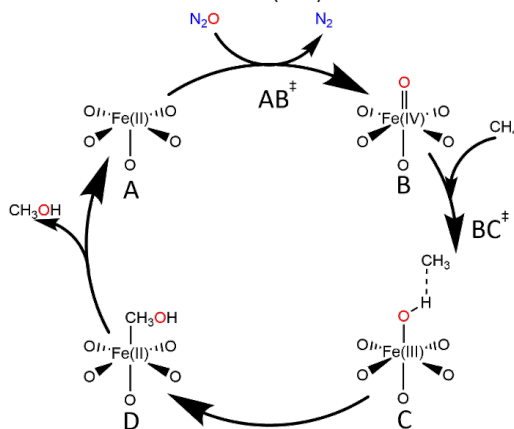
Figure 2. The reaction diagram illustrating the catalytic oxidation of methane (CH_4) to methanol (CH_3OH) using nitrous oxide (N_2O) as an oxidant. The MIL-100 node is truncated only showing the Fe active site. The reaction intermediate nomenclature is adopted herein, with the labeled intermediates considered within the model. The structures **AB‡** and **BC‡** are transition state intermediates, as indicated by the superscript '‡'. Each labeled intermediate (i.e., **A**, **AB‡**, **B**, **BC‡**, **C**, and **D**) are simulated using density functional theory (DFT) at the um06l/def2tzvp level of theory.

The key reaction steps considered are the oxo formation (ΔH_O^C), hydrogen atom transfer (ΔH_H^C), and methanol release ($\Delta H_{CH_3OH}^C$) enthalpies, as well as the oxo formation ($\Delta H_O^{C,\ddagger}$) and hydrogen atom transfer ($\Delta H_H^{C,\ddagger}$) transition state enthalpies. The different initial structures with various MOF variants, ligand compositions, and coordinating ligands are presented in **Figure 3**.
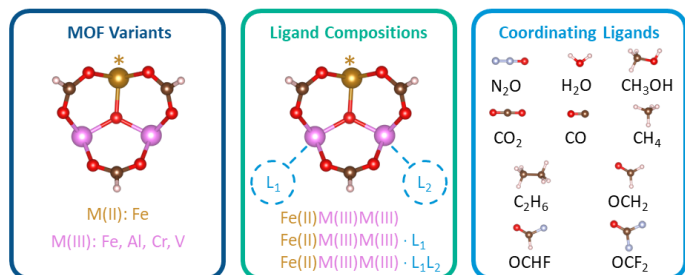
Figure 3. The different MOF Variants (4), Ligand Compositions (3) and Coordination Ligands (10) considered within the library. Different ligand environments at the inactive metal centers (pink) are considered to understand how the methane-to-methanol reaction mechanism (**Figure 2**) is influenced through indirect second sphere coordination effects. Color key: Nitrogen (Silver), Oxygen (Red), Hydrogen (White), Carbon (Bronze), Fe(II) Active Site (Brown), and M(III) Metal Center (Pink).

The different ligands are selected based on being a byproduct from synthesis (H_2O), initial reactants (N_2O and CH_4), desired rection intermediates (CH_3OH), undesired reaction intermediates (CO, CO_2, OCH_2), and other ligands either associated within natural gas (C_2H_6) or with unique chemical properties (OCH_2 and $OCHF$). By simulating these three reaction steps with different ligand environments, the analysis identifies how coordinating ligands at the M(III) inactive metal sites influence the catalysis at the Fe(II) active site. Specifically, **Figures 4-7** highlight the sensitivity of coordinating ligands on the different MOF variants (Objective 1.0).
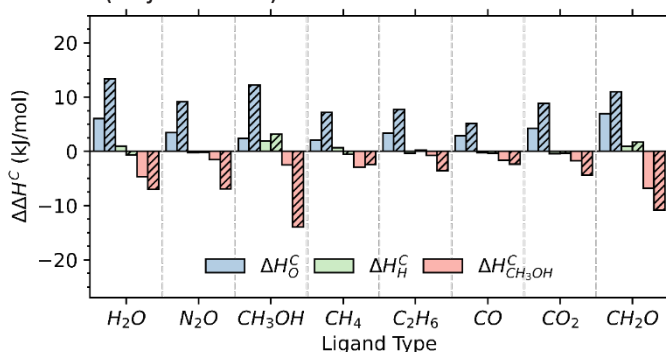

Figure 4. The FeFeFe reaction enthalpies for oxo formation (ΔH_O^C), hydrogen atom transfer (ΔH_H^C), and methanol release ($\Delta H_{CH_3OH}^C$) with different ligands coordinated to the inactive Fe sites. The reaction enthalpies for the ligand containing structures are referenced to the reaction enthalpies without any ligands (introducing the $\Delta\Delta H^C$ term). A $\Delta\Delta H^C > 0$ means that the ligand increased the reaction enthalpies relative to the enthalpy without any ligands, and a $\Delta\Delta H^C < 0$ means that the ligand decreased the reaction enthalpies relative to the enthalpy without any ligands. Solid bars indicate a single coordinating ligand at a single Fe site and marked bars and marked bars indicate a single coordinating ligand at two, different Fe sites.

Figure 5. The FeAlAl reaction enthalpies for oxo formation (ΔH_O^C), hydrogen atom transfer (ΔH_H^C), and methanol release ($\Delta H_{CH_3OH}^C$) with different ligands coordinated to the inactive Al sites. The reaction enthalpies for the ligand containing structures are referenced to the reaction enthalpies without any ligands (introducing the $\Delta\Delta H^C$ term). A $\Delta\Delta H^C > 0$ means that the ligand increased the reaction enthalpies relative to the enthalpy without any ligands, and a $\Delta\Delta H^C < 0$ means that the ligand decreased the reaction enthalpies relative to the enthalpy without any ligands. Solid bars indicate a single coordinating ligand at a single Al site and marked bars and marked bars indicate a single coordinating ligand at two, different Al sites.
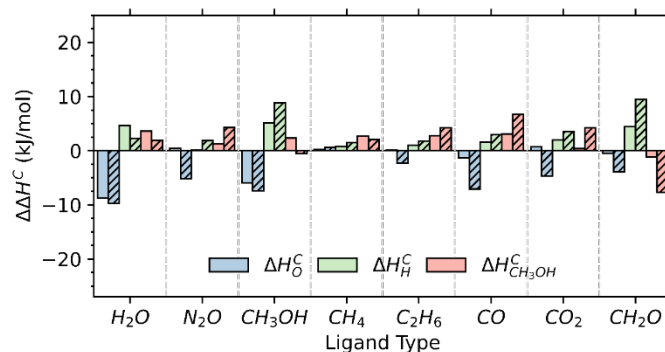
Figure 6. The FeCrCr reaction enthalpies for oxo formation (ΔH_O^C), hydrogen atom transfer (ΔH_H^C), and methanol release ($\Delta H_{CH_3OH}^C$) with different ligands coordinated to the inactive Cr sites. The reaction enthalpies for the ligand containing structures are referenced to the reaction enthalpies without any ligands (introducing the $\Delta\Delta H^C$ term). A $\Delta\Delta H^C > 0$ means that the ligand increased the reaction enthalpies relative to the enthalpy without any ligands, and a $\Delta\Delta H^C < 0$ means that the ligand decreased the reaction enthalpies relative to the enthalpy without any ligands. Solid bars indicate a single coordinating ligand at a single Cr site and marked bars and marked bars indicate a single coordinating ligand at two, different Cr sites.
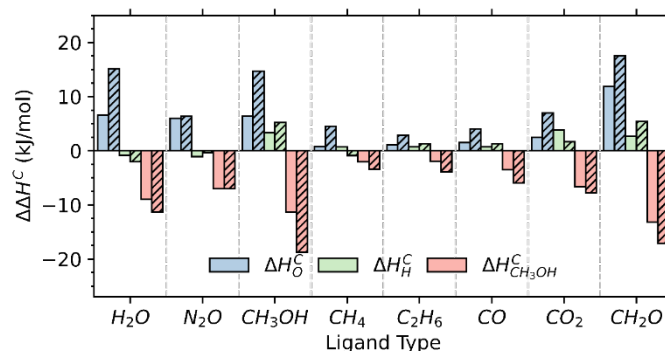
The oxo formation and methanol release enthalpies are sensitive to the indirect second sphere coordination effects, whereas the hydrogen atom transfer enthalpies are insensitive. Furthermore, the structure library enables investigations into chemical descriptors describing how a specific coordinating ligand anchored to the inactive metal center influences MTM (**Figure 8**). The current structural library provides the foundation for a detailed investigation into these indirect second coordination effects for methane-to-methanol conversion.
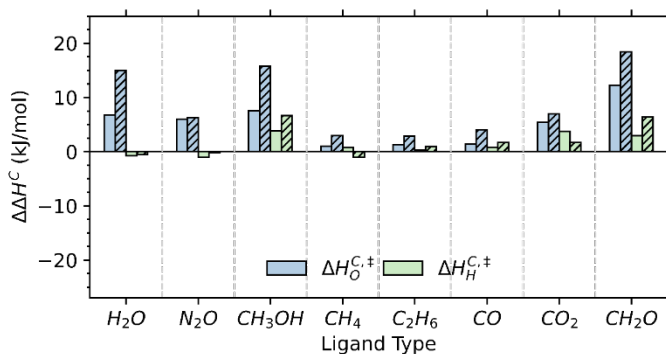
Figure 7. The FeAlAl transition state reaction enthalpies for oxo formation ($\Delta H_O^{C,\ddagger}$) and hydrogen atom transfer ($\Delta H_H^{C,\ddagger}$) with different ligands coordinated to the inactive Al sites. The transition state reaction enthalpies for the ligand containing structures are referenced to the reaction enthalpies without any ligands (introducing the $\Delta\Delta H^C$ term). A $\Delta\Delta H^C > 0$ means that the ligand increased the reaction enthalpies relative to the enthalpy without any ligands, and a $\Delta\Delta H^C < 0$ means that the ligand decreased the reaction enthalpies relative to the enthalpy without any ligands. Solid bars indicate a single coordinating ligand at a single Al site and marked bars and marked bars indicate a single coordinating ligand at two, different Al sites.
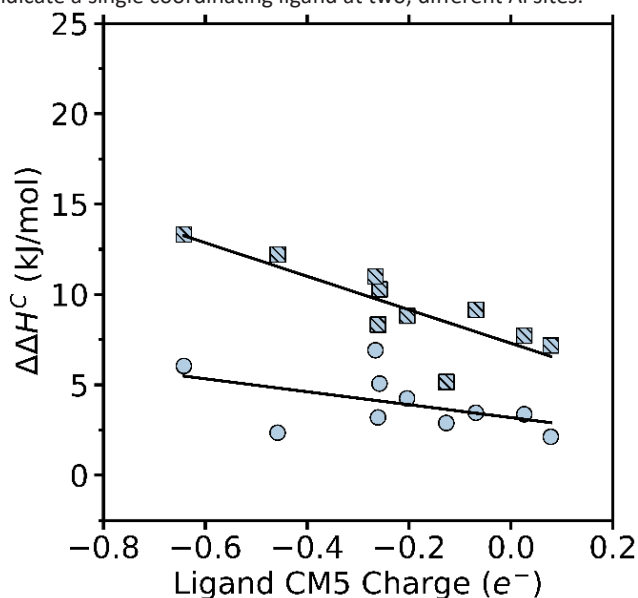

Figure 8. Investigating electronic potential descriptors for the sensitivities of oxo formation reaction enthalpies ($\Delta\Delta H^C$) with respect to the different ligand environments for the FeAlAl MIL-100 MOF. The ligand CM5 charges represent the partial charges of ligand binding atom computed from the charge model 5. The solid circles present a single coordinating ligand at a single Al site and the marked squares indicate a single coordination ligand at two, different Al sites.

Accomplishments

- Generated a structural library (~500 structures) consisting of FeFeFe, FeAlAl, FeCrCr, and FeVV MIL-100 MOFs with different ligand coordination environments (i.e., H_2O, N_2O, CH_3OH, CH_4, C_2H_6, CO, CO_2, CH_2O, CFHO, and CF_2O), as described by **Figure 3**.
- Simulated the entire structure library using density functional theory (DFT) in Gaussian16 (~2000 different calculations due to optimization, stability, frequency, and basis set super position error steps).

- Computed the oxo formation, hydrogen atom transfer, and methanol release reaction enthalpies and the oxo formation and hydrogen atom transfer transition state reaction enthalpies (reactions presented in **Figure 2**) for the entire structural library, as presented in **Figures 4-7**.
- Demonstrated how both the MOF composition (i.e., FeFeFe vs. FeCrCr) and the ligand composition at the inactive metal centers leads to unique deviations relative to the structure without any ligands.
- Identified preliminary descriptors linking the ligand properties (i.e., ligand partial charge) to the indirect second sphere coordination effects within the MIL-100 MOF (**Figure 8**).
- Established a computational framework for generating, submitting, and analyzing all the data generated, including both the energies (used to produce the reaction pathways) and the electronic/geometric properties of the optimized configurations (used to identify chemical descriptors).
- Presented findings at the SRNL Postdoc Poster Session, the ACS 2024 Annual Meeting (oral and poster), and the 2024 SRNL Research SLAM.

Team Members

Nicholas Szaro*, Megan Hoover, Jonathon Baker, Tilak Dhakal, Adrian Mistreanu, Richard Lewis, Evelyn Evans

*Postdoctoral Researcher

References

1. Yang, D.; Gates, B. C. Catalysis by Metal Organic Frameworks: Perspective and Suggestions for Future Research. *ACS Catalysis* **2019**, *9* (3), 1779-1798. DOI: 10.1021/acscatal.8b04515.
2. Vitillo, J. G.; Bhan, A.; Cramer, C. J.; Lu, C. C.; Gagliardi, L. Quantum Chemical Characterization of Structural Single Fe(II) Sites in MIL-Type Metal–Organic Frameworks for the Oxidation of Methane to Methanol and Ethane to Ethanol. *ACS Catalysis* **2019**, *9* (4), 2870-2879. DOI: 10.1021/acscatal.8b04813.
3. Vitillo, J. G.; Lu, C. C.; Cramer, C. J.; Bhan, A.; Gagliardi, L. Influence of First and Second Coordination Environment on Structural Fe(II) Sites in MIL-101 for C–H Bond Activation in Methane. *ACS Catalysis* **2020**, *11* (2), 579-589. DOI: 10.1021/acscatal.0c03906.
4. Simons, M. C.; Prinslow, S. D.; Babucci, M.; Hoffman, A. S.; Hong, J.; Vitillo, J. G.; Bare, S. R.; Gates, B. C.; Lu, C. C.; Gagliardi, L.; et al. Beyond Radical Rebound: Methane Oxidation to Methanol Catalyzed by Iron Species in Metal-Organic Framework Nodes. *J Am Chem Soc* **2021**, *143* (31), 12165-12174. DOI: 10.1021/jacs.1c04766

Understanding the Chemistry and Physics of the Pu Metal-Oxide Interface with Vibrational and LIBS Spectroscopy

Eliel Villa-Aleman

Bulk and surface spectroscopic properties of PuO_2 and the oxidation of Pu metal were studied in this research using laser-induced breakdown spectroscopy and deep ultraviolet Raman spectroscopy of PuO_2 pellets and Pu metal while contained in a double-walled cell. This work helped understand corrosion and oxides of metals.

Introduction

The stability of a plutonium (Pu) metal surface is highly dependent on the ambient environment and the intrinsic alpha decay from Pu. In the presence of air, Pu metal oxidizes to PuO_2. A thin layer of Pu_2O_3 can then form at the metal – PuO_2 interface (see **Figure 1**) and Pu_2O_3-catalyzed corrosion can occur at the metal surface. Under slightly elevated temperatures, Pu metal can react with moist air to form PuH_2 which is flammable and can react with O_2 and N_2 to generate Pu oxides. Ultimately, the growth of PuO_2, Pu_2O_3, and PuH_2 depends on atmospheric conditions, pressures, and temperatures.
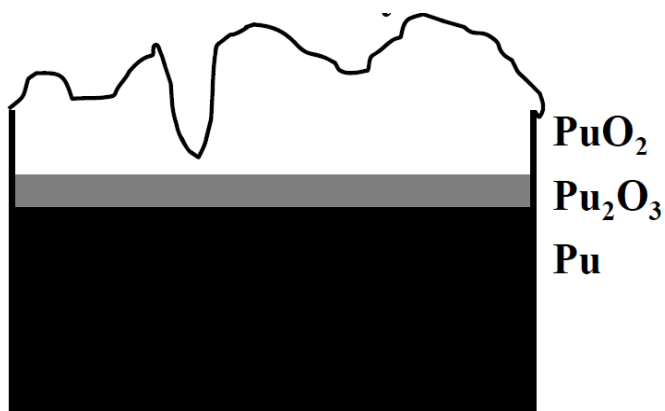

Figure 1. Depiction of surface oxide contaminants that form on the surface of Pu metal and impact metal integrity.

To date, reactions at the Pu metal surface have been studied almost exclusively with X-ray photoelectron spectroscopy (XPS) and X-ray diffraction (XRD). While XPS and XRD are useful tools for bulk analysis, their application towards interrogating very thin layers on a Pu metal surface is limited because the high penetration of highly energetic X-rays that exceed the thickness of very thin surface layers. In contrast to XPS and XRD, vibrational spectroscopic tools might enable the identification of different chemical species, layer thickness, oxide layer growth, and possibly radical reactions in very thin microscopic regions on the surface of Pu metal. The goal of this project is to use Raman spectroscopy and laser-induced breakdown spectroscopy to characterize Pu, Pu oxides and the molecular transition from bulk to surface.

Approach

Characterization of the surface of actinide compounds requires the development of unique tools to work with these difficult to handle materials. SRNL designed and developed double-walled cells for handling actinide materials. The concept revolutionized the spectroscopy research of Pu-bearing compounds. In this project, new cells were designed to enable the study of PuO_2 pellets with laser-induced breakdown spectroscopy and with deep ultraviolet Raman spectroscopy. The methodology of making PuO_2 pellets without a binder was perfected and the technology to conduct laser-induced breakdown spectroscopy with low peak power pulses was developed to monitor regions as small as 80 micrometers. The highly efficient setup design for light capture enabled the acquisition a spectrum with only 400 uJ/pulse. The ablation technique also enabled the clean-up of surface oxides from the Pu metal.

Different types of oxides are produced during the Pu metal oxidation. Surface versus bulk analysis with spectroscopy is extremely difficult due to the thin upper surface layer (<100 nanometers). In order to characterize the surface molecular structure using Raman spectroscopy, an in-depth study was conducted with different wavelengths. The high absorptivity of light towards short wavelengths (ultraviolet) by PuO_2 enabled the development of a penetration depth study and the characterization of the upper 10 nanometers. The Raman

spectra of PuO_2 was acquired with laser wavelengths at 785, 633, 561, 514, 488, 457, 405, 355, 325, and 244nm to investigate the penetration depth. The wavelength dependent Raman spectra shown in **Figure 2** demonstrate the differences between the bulk and the surface.
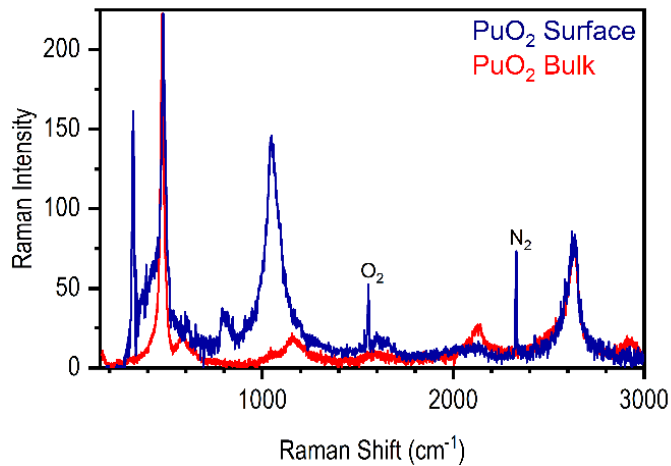

Figure 2. Typical Raman spectrum of PuO_2 in red showing the T_{2g} vibrational band, defect bands, and overtones and the Raman spectrum from the PuO_2 surface acquired with deep UV (244 nm).

Accomplishments

- Developed new double-walled cells for laser-induced breakdown spectroscopy research.
- Developed new metal double-walled cells to slow down oxygen into the cell and reduce metal oxidation.
- Developed a method for the fabrication of pellets for laser-induced breakdown spectroscopy using a 400-micrometer-thick paper mask.
- Developed a unique high efficiency throughput spectrometer to enhance signal to noise ratio by a factor of ~12x.
- Conducted for the first-time laser-induced breakdown spectroscopy of material (CeO_2, PuO_2, and Pu metal) in a double-walled cell.
- Extracted ablated particulates from cell and imaged with scanning electron microscopy to identify the morphologies of the particulates and identified the molten versus non-molten.
- Developed the methodology for the characterization of surfaces using deep ultraviolet Raman spectroscopy.
- Developed the methodology for removing surface oxides from a metal using laser ablation.

Peer-reviewed Publications

- Eliel Villa-Aleman*, Emily H. Kwapis, Bryan J. Foley, Thomas C. Shehee, Don D. Dick, Henry M. Ajo, and Kyle C. Hartig. Laser-Induced Plasmas of Plutonium Dioxide in a Double-Walled Cell. *Appl Spectrosc.*, 2024, 78(4), 412-422. DOI: 10.1177/00037028241226977
- Eliel Villa-Aleman*, Jason R. Darvin, Don D. Dick, Thomas C. Shehee, and Bryan J. Foley. Characterization of PuO_2 with Visible and UV Raman Spectroscopy: Discrimination between the Bulk, Surface, and an Intermediate Disordered Layer. Submitted to the *Journal of Raman Spectroscopy*

Team Members

Jason R. Darvin, Don D. Dick, Bryan J. Fowley, Thomas C. Shehee, Henry M. Ajo, Kyle C. Hartig[a], Emily H. Kwapis[a], Justin Borrero[a]

[a]University of Florida

References

1. L.N. Dihn, J.M. Haschke, C.K. Saw, P.G. Allen, W. McLean II, J. Nucl. Mater. 408 (2011) 171-175.
2. C.K. Saw, J.M. Haschke, P.G. Allen, W. McLean II, L.N. Dinh, J. Nucl. Mater. 429 (2012) 128-135.
3. Villa-Aleman E, Dick DD, Christian JH, Foley BJ. Journal of Raman Spectroscopy, 52, 1486.
4. Villa-Aleman E, Bridges NJ, Shehee TC, Houk AL Journal of Nuclear Materials 2019, 515, 140.
5. Villa-Aleman E, Houk AL, Shehee TC, Bridges NJ Journal of Nuclear Materials 2021, 551, 152969.
6. Villa-Aleman E, Houk AL, Bridges NJ, Shehee TC Journal of Raman Spectroscopy 2019, 50, 899.

FY24 PROJECTS

CORE COMPETENCY:

Enabling next generation nuclear materials processing and disposition

Technetium Management and Use through Novel Sulfides and Alloys

Jake Amoroso

This project explores chalcogenide (S, Se, Te) and metallic alloy materials as a means to control the chemical behavior of technetium, which is mobile in the environment. The research will enable development of novel material systems to immobilize waste constituents that are difficult to immobilize in conventional waste forms due to their physicochemical properties.

Introduction

Controlling behavior of technetium (Tc) and other RedOx-sensitive compounds is important for commercial applications as well as long-term disposal of radioactive waste. Tc in radioactive waste mostly exists as pertechnetate ($Tc^{(VII)}O_4^-$), which is highly soluble and mobile in the environment. Once reduced, Tc oxide ($Tc^{(IV)}O_2$) is sparingly soluble. Tc sulfide ($Tc^{(IV)}S_2$) is insoluble, making it an attractive material for Tc immobilization. However, the reoxidation mechanism(s) remain largely unknown. Greater understanding of the reoxidation mechanisms in technetium sulfide is critical to its long-term stability and application as a waste form and storage medium.[1] To prepare Tc sulfides for study, limited reported synthetic routes warranted new ways to prepare these materials, which was explored using the Boron-Chalcogen Mixture (BCM) method.[2, 3]

The exploration of extended structure Tc materials provides critical knowledge about the coordination environments of Tc especially due to the amorphous nature of the binary compounds that make characterization difficult. New Tc compounds can be synthesized from Tc oxides using the BCM method. Preparing single crystalline products will allow for facile characterization by single crystal X-ray diffraction (SXRD). The synthesis of extended structure Tc materials will give insight into stable Tc materials that could be used to sequester Tc from solution.

Bimetallic nanoparticles and alloys can be formed by the interatomic mixing of the monometallic components. These present a class of materials with tunable composition and properties.[4] Exploring the synthesis of rhenium (Re) and Tc alloy synthesis will generate materials that can be exploited for Tc waste management applications.

Approach

Investigation of the reoxidation mechanism and practicality of technetium chalcogenides requires bulk amounts of material. The BCM method allows for the synthesis of bulk chalcogenide materials starting from metal oxides. Utilizing the BCM method, ReS_2, $ReSe_2$, and Re_2Te_5 were synthesized starting from $NaReO_4$ (**Figure 1**).
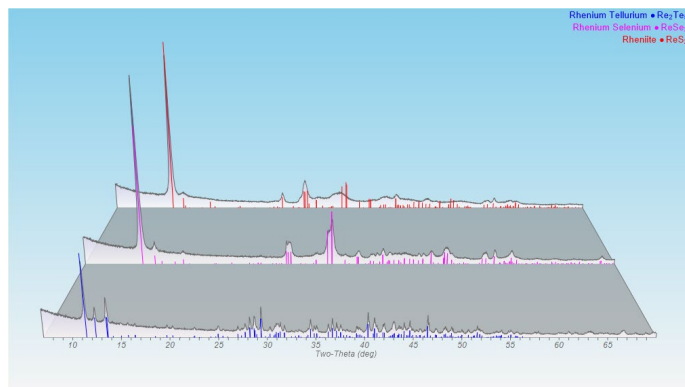
Figure 1. PXRD patters of ReS_2, $ReSe_2$, and Re_2Te_5 prepared using the BCM method.

The reoxidation mechanisms of these Re chalcogenides is being explored using differential scanning calorimetry (DSC) and thermogravimetric analysis (TGA). Additionally, the BCM method was used to synthesize crystals of $Na_2Re_3S_6$ allowing for the determination of its crystal structure, which has previously been poorly defined (**Figure 2**). To create Re and Re-precious metal core-shell nanoparticles, SRNL utilized an aqueous synthetic method to reduce $NaReO_4$ to Re^0 in an aqueous solution (**Figure 3A**). To prepare the core-shell nanoparticles, the galvanic replacement reaction was employed, which exploits the RedOx potential difference between Re and precious metal that causes the precious metal to plate itself on the Re nanoparticles (**Figure 3B**).
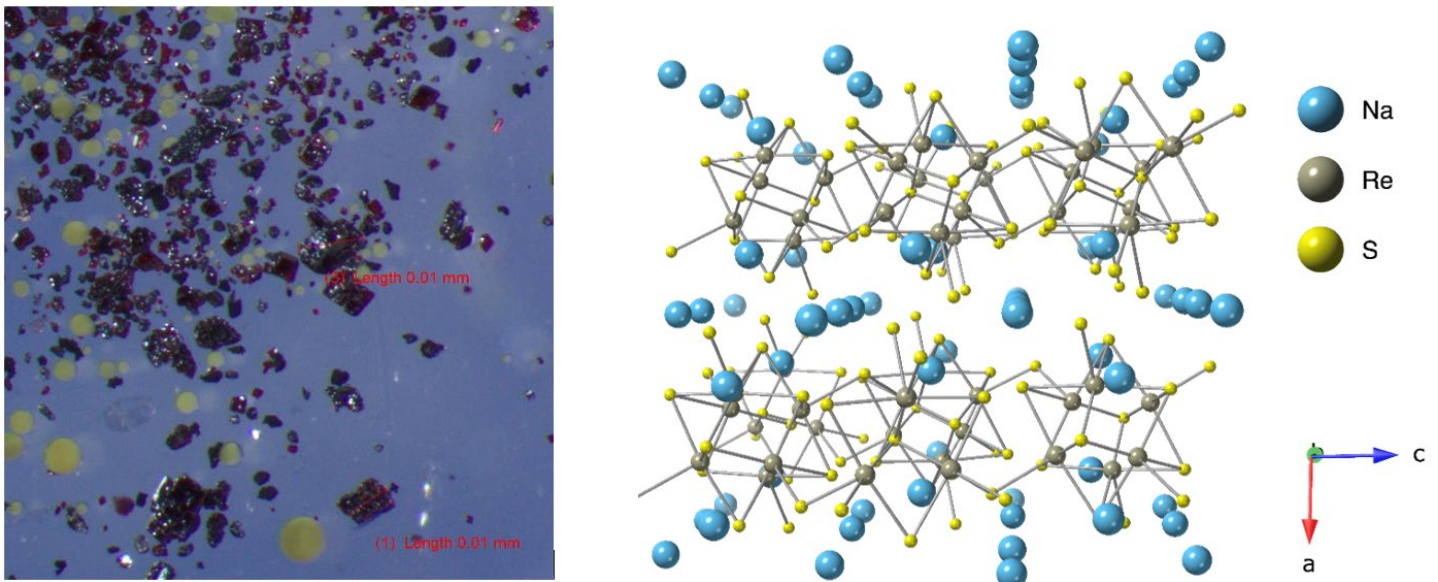
Figure 2. (Right) Optical image of synthesized $Na_2Re_3S_6$ crystals and (Left) the solved crystal structure.
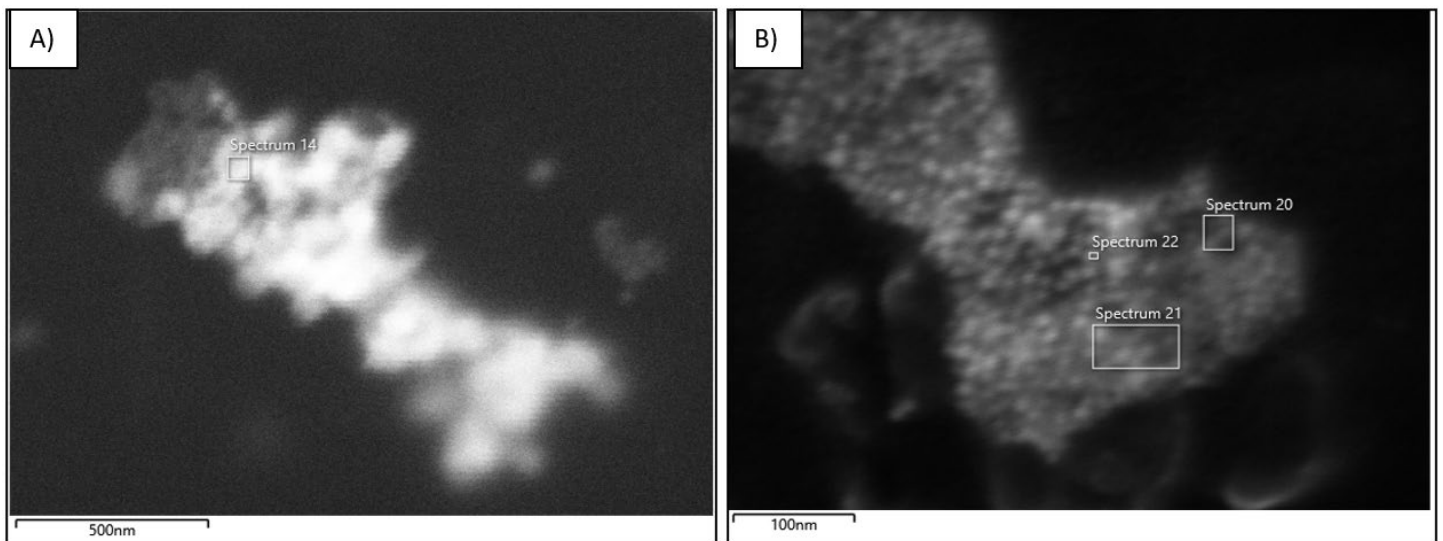
Figure 3. SEM images of the (A) Re nanoparticles and (B) Re-precious metal nanoparticles.

The Re nanoparticles have shown to crash out after being oxidized by air exposure while the Re-precious metal shows greater stability to air, staying in solution. To further test the stability differences between the monometallic and bimetallic Re and Re@precious metal nanoparticles, HNO_3 was added to the solution, which will oxidize Re unless protected by the shell of the precious metal. The preparation of Tc chalcogenides and nanoparticles used the synthetic procedures utilized for the Re analogues to exploit their properties for Tc waste management.

Accomplishments

- Synthesized ReS_2, $ReSe_2$, and Re_2Te_5 using the BCM method
- Investigated the reoxidation of ReS_2 using DSC
- Synthesized single crystalline $Na_2Re_3S_6$ using the BCM method
- Determined the crystal structure of $Na_2Re_3S_6$
- Synthesized Re, Re@Ag nanoparticles and novel Re-precious metal core-shell nanoparticles
- Began HNO_3 stability test of Re-precious metal nanoparticles

Team Members

Logan Breton[**], Kyle Brinkman[a], Abhaya Mishra[a*]

[a]*Clemson University*
[*]*Postdoctoral Researcher*
[**]*Laboratory Director's Postdoctoral Research Fellow*

References

1. Pearce, C. I.; Icenhower, J. P.; Asmussen, R. M.; Tratnyek, P. G.; Rosso, K. M.; Lukens, W. W.; Qafoku, N. P. Technetium Stabilization in Low-Solubility Sulfide Phases: A review. *ACS Earth and Space Chemistry* **2018**, *2* (6), 532–547. https://doi.org/10.1021/acsearthspacechem.8b00015.

2. Breton, L. S.; Klepov, V. V.; Loye, H.-C. Z. Facile oxide to chalcogenide conversion for actinides using the Boron–Chalcogen mixture method. *Journal of the American Chemical Society* **2020**, *142* (33), 14365–14373. https://doi.org/10.1021/jacs.0c06483.

3. Ferrier, M.; Kerlin, W. M.; Poineau, F.; Sattelberger, A. P.; Czerwinski, K. R. Recent developments in the synthetic chemistry of technetium disulfide. *Dalton Transactions* **2013**, *42* (44), 15540. https://doi.org/10.1039/c3dt52079j.

4. Pandey, S.; Koch, R. J.; Li, G.; Misture, S. T.; Wang, H.; Phillpot, S. R. Thermodynamics and kinetics of ordered and disordered Cu/Au alloys from first principles calculations. *Journal of Alloys and Compounds* **2019**, *809*, 151615. https://doi.org/10.1016/j.jallcom.2019.07.327.

Exploring Electron Probe Micro-Analysis for Nuclear Nonproliferation and Material Processing

Bryan Foley

Single particle analysis has become increasingly popular over the last decade; however, no currently available nondestructive analysis techniques can quantitatively measure the elemental composition of single particles. To remedy this, a proof-of-concept study comparing electron probe micro-analysis against gold-standard inductively coupled plasma–mass spectrometry measurements was conducted.

Introduction

Single particle analysis of adventitious particles originating in nuclear processes is becoming increasingly common.[1,2] However, a current gap in available analytical instrumentation is a rapid, high-throughput screening technique capable of providing quantitative elemental information on single particle analytes.[3,4] To this end, electron probe micro-analysis (EPMA) has been identified as a key technique that could fill this analytical gap. EPMA is an efficient, cost-effective, and nondestructive analytical tool[5] that can triage and prioritize samples for further conventional, resource-intensive analyses (e.g., Large Geometry-Secondary Ion Mass Spectrometry or Thermal Ionization Mass Spectrometry).[1,2,6] EPMA drastically outperforms nondestructive triage analysis by SEM/EDS by quantitatively resolving elemental variations of 10s-100s of parts per million at the nanometer scale; whereas, SEM and other similar Nondestructive Assay (NDA) methods are inherently qualitative and designed primarily for imaging applications.[3,4,5] Evaluation and acceptance of EPMA by the broader microanalytical community could drastically increase the speed and accuracy of triage measurements for single particle analysis campaigns. Despite the use of EPMA as a routine tool in other research areas[5], there are currently no open-literature, peer-reviewed publications detailing the use of EPMA technology in single particle analysis, especially for analytes of interest to the nuclear safeguards community. The EPMA particle analyses described in this work will be used to assess the viability of this technique for micrometer-scale, safeguards-oriented analytical applications and will form the basis of future proposals as well as the first open-literature, peer reviewed publication detailing use of EPMA technology in single particle analysis for nuclear safeguards applications.

Approach

Five compositions of mixed nickel/cerium particles were shipped to Japan Electron Optics Laboratory, Ltd. (JEOL) for analysis by EPMA. Two form factors of these particles were shipped: 1) microparticulate deposited onto 1" Si planchets and 2) bulk powders consisting of monodisperse particulate (2-3 mg). The CeO_2 samples contained a varying amount of nickel – ranging from 0% (pure CeO_2) to 10% nickel in cerium. The mixed nickel/cerium particles were judiciously selected for this proof-of-concept study as the EPMA detection crystal used for the analysis of cerium and nickel are the same detector crystals (PET and LiF), which can also be used for uranium and plutonium, albeit at different energies. The shipped particles were analyzed at the University of Minnesota by JEOL EPMA microscopists and internally at SRNL by traditional mass spectrometrists. The results of these analyses were compared to assess whether EPMA is a viable technique for quantitative triage measurements of single particle analytes.

Accomplishments

- Five compositions of monodisperse mixed nickel/cerium particles identified at SRNL were successfully shipped to JEOL. These materials were distributed both as a bulk powder (2-3 mg) and as particles on 1" silicon planchets.
- JEOL provided results of the EPMA analysis of these materials to SRNL, including imaging, energy dispersive x-ray spectroscopic analysis, and wave dispersive x-ray analysis.
- Q-ICP-MS measurements were also performed on particles extracted from the planchets.

- For EPMA measurements on single particles, the values returned by JEOL were within 10% of the elemental distribution predicted from mixing calculations. This is an encouraging result that may indicate EPMA is a viable screening technique for high-throughput, preliminary analysis of single particle materials.
- A peer-reviewed publication is in the final stages of preparation for submission to *Microscopy and Microanalysis*.

Team Members

Kyle Samperton, Alexis Riche[*], Shelby Bowden[*], Rachel Bergin[*]

[*]*Postdoctoral Researcher*

References

1. Naes, B.E.; Scott, S.; Waldron, A.; Lawson, S.; Bronikowki, M.G.; Gleaton, L.I.; Smith, R.J.; Wurth, K/J.; Tenner, T.J.; Wellons, M. Production of mixed element actinide reference particulates to support nuclear safeguards using THESEUS, an aerosol-based particulate synthetic method. *Analyst.* **2023**,*148*, 3226-3238.
2. Tenner, T. J., Naes, B. E., Wurth, K. N., Meininger, D., Wellons, M. S., Pope, T. R. New particle working standards for NWAL particle laboratory calibration and quality control—LANL LGSIMS characterization and evaluation. *Proceedings of the INMM & ESARDA Joint Annual Meeting*, **2023**, 1-10.
3. Ranebo, Y., Niagolova, N., Erdmann, N., Eriksson, M., Tamborini, G., & Betti, M.Production and Characterization of Monodisperse Plutonium, Uranium, and Mixed Uranium– Plutonium Particles for Nuclear Safeguard Applications. *Analytical chemistry*, **2010**, *82*(10), 4055-4062.
4. Wurth, K; Tenner, T., Naes., B. Detecting Pu in U-bearing Particles by SEM.EDS for Nuclear Safeguards Applications. *Microscopy and Microanalysis.* **2023**, *29*, 192-193.
5. Reed, S. J. B. *Electron microprobe analysis and scanning electron microscopy in geology.* , 2nd ed.; Cambridge University Press, 2005.
6. Diacre, A.; Fauré, A.-L.; Cornaton, M.; Pointurier, F.; Evrard, O. *Talanta* **2023**, *252*, 123848.
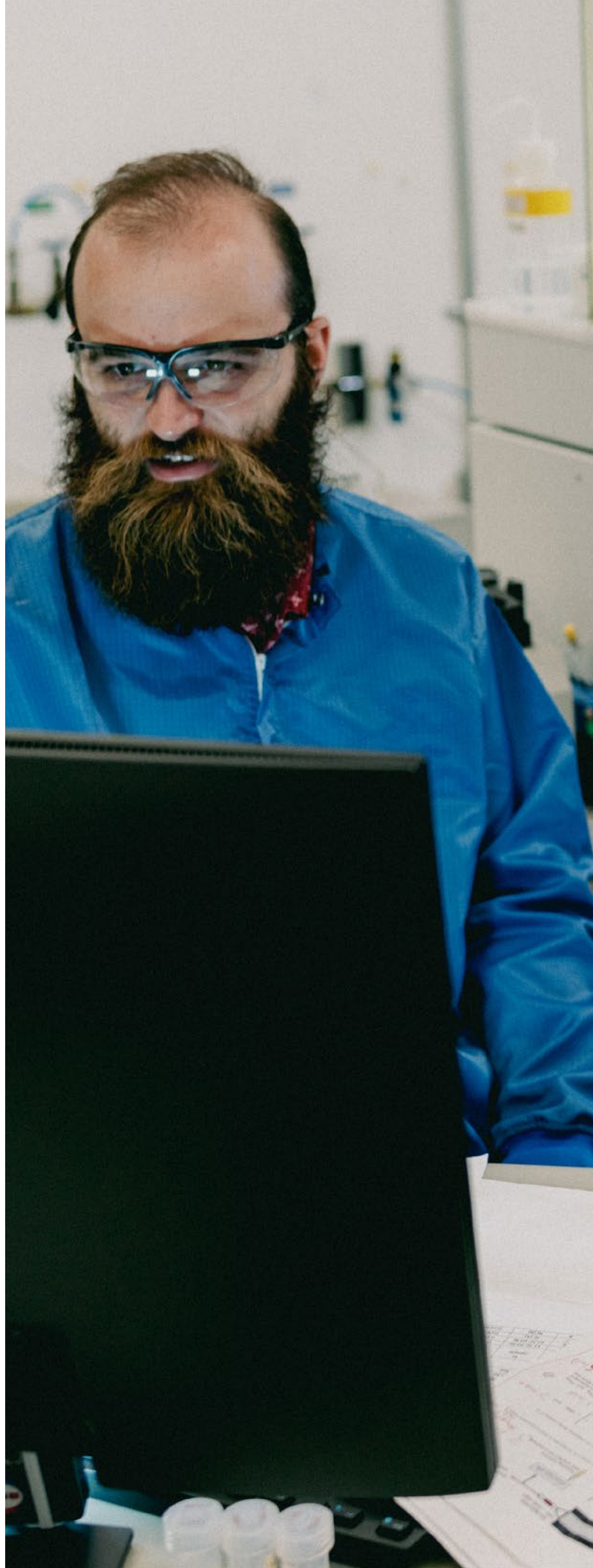
Enhancing Charge Injection in Polyoxometalate-based Dye-Sensitized Solar Cells

Lauren Hanna

A selected 3d-transition metal containing polyoxometalate and corresponding parent polyoxometalate was synthesized. These materials were successfully characterized using a variety of spectroscopic and electrochemical techniques. The polyoxometalates were sensitized with a porphyrin-based dye to permit for photoinduced charge transfer for solar energy applications.

Introduction

Solar energy technology, such as dye-sensitized solar cells, relies on light harvesting materials that optimize use of the solar spectrum for green energy applications. The overall efficiency of a photovoltaic cell is heavily dependent on the electron injection efficiency from the photosensitizer to the semiconductor[1]. Charge injection to the semiconductor is often limited by the intrinsic lifetime of the photoinduced, charge separated state of the sensitizer, which results in electron-hole recombination[1]. To address this issue, a class of materials known as polyoxometalates have been investigated as potential photoanode materials. Polyoxometalates (POMs) are a class of molecular metal oxide analogues that are composed of high valent transition metals (such as Mo, W, or V). Due to their chemical makeup, they are excellent electron acceptors and exhibit reversible redox activity[2, 3]. To efficiently tune the electronic structure of the POM, low valent 3d-transition metals can be integrated into the framework.

Recent studies have concluded that covalent linkages between the photosensitizer and polyoxometalate may generate hybrid products with unique charge transfer properties[4-6]. Despite these efforts, no fundamental systematic study has been conducted that investigates how the nature of the polyoxometalate affects the efficacy of charge transfer when covalently bound to a photosensitizer.

To understand the charge transfer dynamics of the hybrid material, our investigation designed a 3d-transition metal containing polyoxometalate covalently bound to a porphyrin photosensitizer (4Fe-POM-Zn-CTPP). The results of this study were compared to the analogous homogenous parent Wells-Dawson polyoxometalate, POM, and the corresponding hybrid material, POM-Zn-CTPP (**Figure 1**).
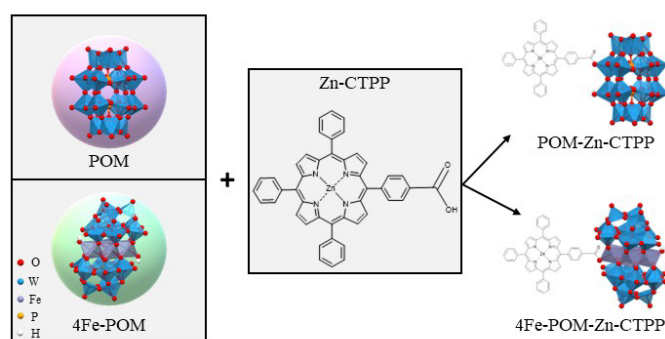
Figure 1. Depiction of the polyoxometalates (POM and 4Fe-POM), porphyrin (Zn-CTPP), and hybrid species (POM-Zn-CTPP and 4Fe-POM-Zn-CTPP) in this study

Approach

The purpose of this project is to understand how incorporation of a heterometal in a given polyoxometalate can affect photo-induced charge transfer from a photosensitizer to the POM. The approach of the project is to first, synthesize an iron-containing polyoxometalate, as well as the parent polyoxometalate containing no heterometal (iron). These POMs are then characterized using a series of spectroscopic and electrochemical techniques to confirm the identity and stoichiometry of each of the POMs **(Figures 2-5)**. Following, the POMs were covalently bound to a porphyrin photosensitizer, zinc (II) monocarboxyphenyl triphenyl porphyrin. These hybrid materials were deposited as thin films on conducting substrates to generate photoanodes.

The efficiency of charge transfer from porphyrin photosensitizer to polyoxometalate was evaluated for both materials through spectroscopic and electrochemical means to understand the effect of the heterometal. Fluorescence spectroscopy evaluated each POM-porphyrin hybrid material to determine

whether fluorescence quenching occurred. Quenching of the porphyrin fluorescence was a clear indication of successful charge transfer. Transient photocurrent measurements evaluated the current produced by materials when illuminated by white light; a key quality for successful dye-sensitized photoanode materials. Other electrochemical measurements, such as open circuit voltage and I-V curves, revealed the efficiency of the polyoxometalate-porphyrin material under visible light irradiation.

From these measurements, it was determined that the incorporation of the iron heterometal resulted in efficient charge transfer from the porphyrin moiety to polyoxometalate.
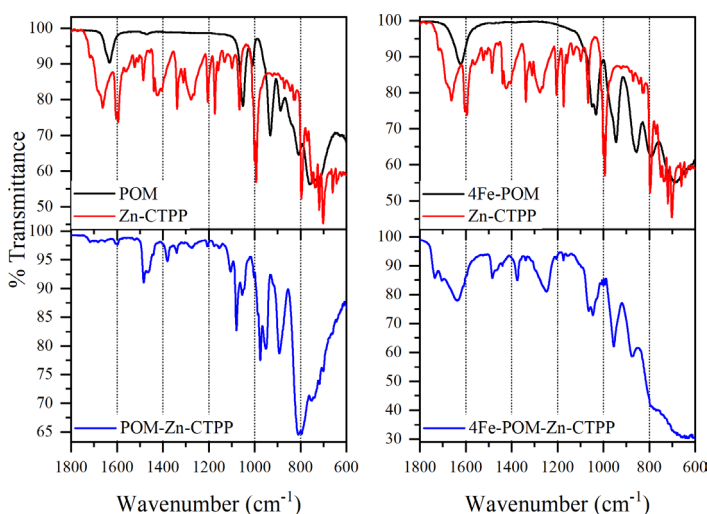

Figure 2. FT-IR spectra of left: POM (black), Zn-CTPP (red), and POM-Zn-CTPP (blue) and right: 4Fe-POM (black), Zn-CTPP (red), and 4Fe-POM-Zn- CTPP (blue)
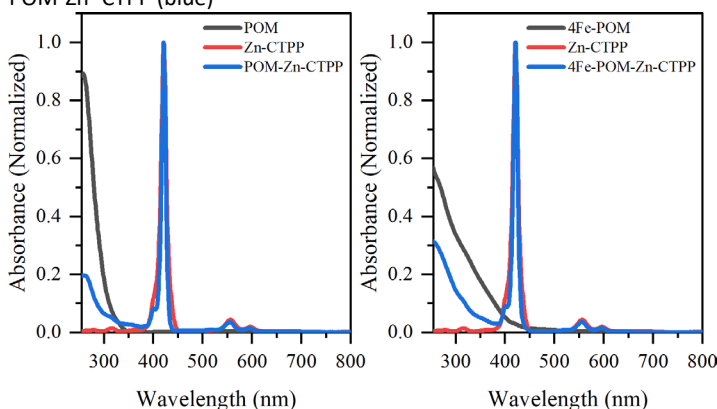
Figure 3. UV/Vis spectra of left: POM (black), Zn-CTPP (red), and POM-Zn-CTPP (blue) and right: 4Fe-POM (black), Zn-CTPP (red), and 4Fe-POM-Zn- CTPP (blue) measured in acetonitrile

Accomplishments

- Deposited films of hybrid polyoxometalate-porphyrin materials on conductive (ITO) substrates to generate photoelectrodes
- Carried out photoelectrochemical measurements under dark and illuminated conditions to reveal the production of photocurrent (**Figure 6-7**)

- Revised manuscript to submit to RSC Advances
- Abstract was submitted and accepted for a talk at SERMACS conference
- Presented at SERMACS conference in Durham, NC in October 2023
- Submitted samples for ICP-OES characterization to understand the ratio of porphyrin:polyoxometalate ratio
- Submitted samples for XPS characterization, data was analyzed (**Figures 8-10**) to reveal how the porphyrin was coordinated to the polyoxometalate

Peer-reviewed Publication

1. Hanna, L.; McDonald, K. D. Investigation of Heterometal Substitution in Polyoxometalate-Porphyrin Hybrid Materials for Efficient Charge Transfer. *RSC Advances* **2024**. (in progress)

Team Member

Kori McDonald[*]

[*]*Postdoctoral Researcher*
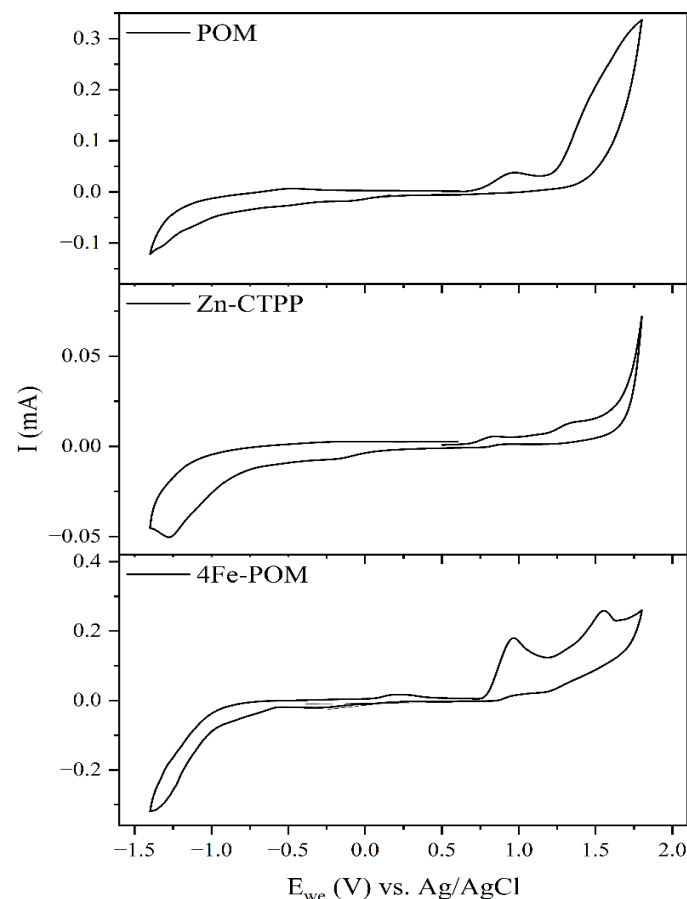
Figure 4. Cyclic Voltammograms of Left: POM (top), Zn-CTPP (middle), and 4Fe-POM (bottom) in 0.1 M TBAPF6 in acetonitrile with a 50 mV/s scan rate
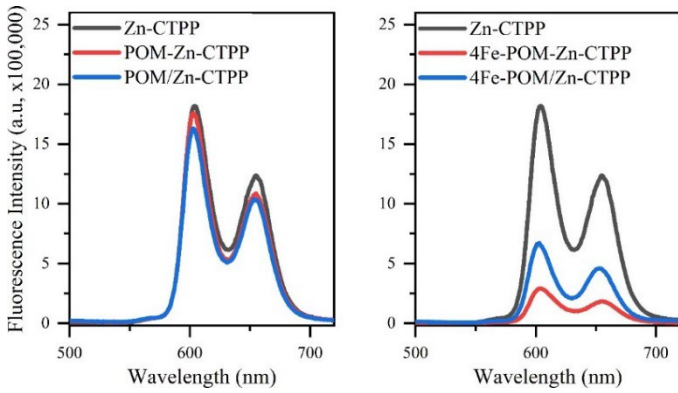
Figure 5. Fluorescence spectra upon 371 nm excitation of right: Zn-CTPP (black), POM-Zn-CTPP (red), and POM/Zn-CTPP (blue) and left: Zn-CTPP (black), 4Fe-POM-Zn-CTPP (red), and 4Fe-POM/Zn-CTPP (blue)

Figure 7. Photocurrent measurement set up with test vessel with optical window and white light source

Figure 6. Photoelectrochemical response of POM-Zn-CTPP (black) and 4Fe-POM-Zn-CTPP (red) with a +0.1 V bias upon irradiation in 0.1 M Na_2SO_4 with methanol as a sacrificial agent
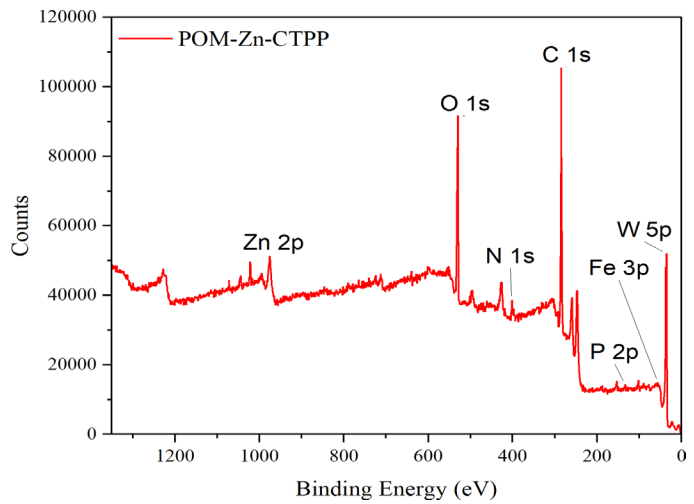
Figure 8. XPS survey scan of POM-Zn-CTPP
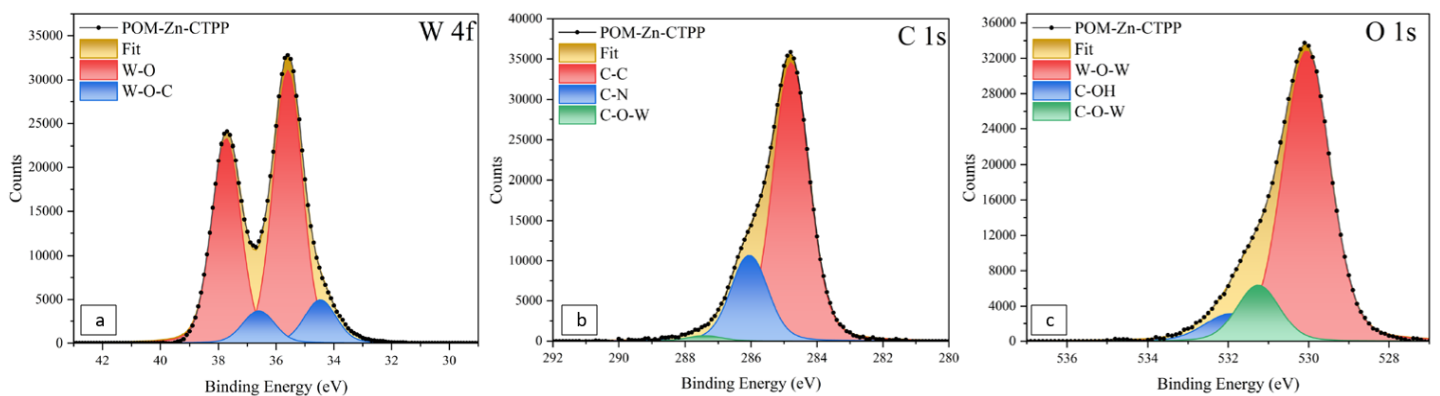
Figure 9. a) W 4f XPS spectrum of POM-Zn-CTPP b) 10 XPS C 1s spectrum of POM-Zn-CTPP c) XPS O 1s spectrum of POM-Zn-CTPP
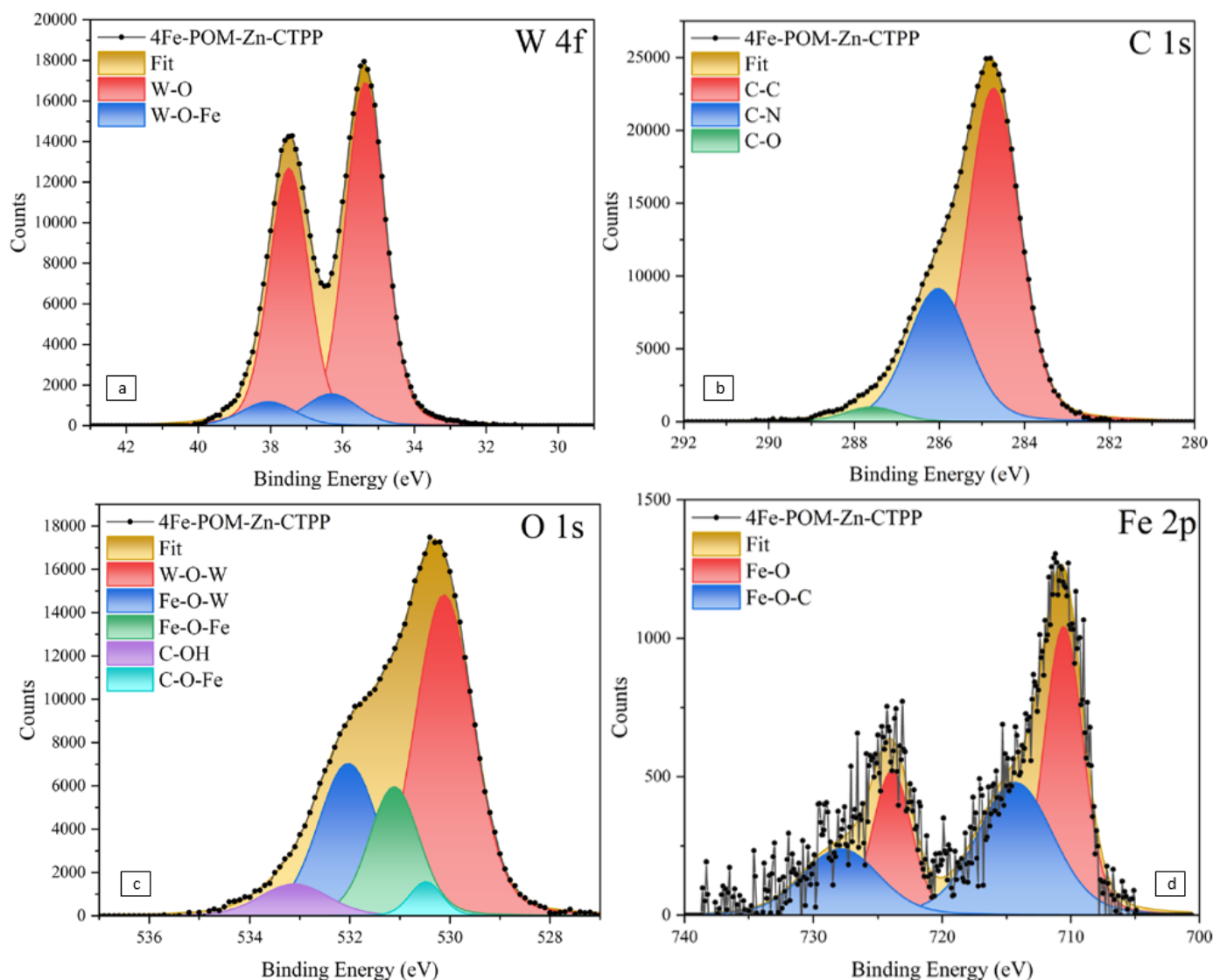
Figure 10. a) W 4f XPS of 4Fe-POM-Zn-CTPP b) C 1s XPS of 4Fe-POM-Zn-CTPP c) O 1s XPS of 4Fe-POM-Zn-CTPP d) Fe 2p XPS of 4Fe-POM-Zn-CTPP

References

1. Katoh, R.; Furube, A. Electron injection efficiency in dye-sensitized solar cells. *Journal of Photochemistry and Photobiology C: Photochemistry Reviews* **2014**, *20*, 1-16. DOI: https://doi.org/10.1016/j.jphotochemrev.2014.02.001.

2. Wang, Y.; Fu, X.; Wang, T.; Li, F.; Li, D.; Yang, Y.; Dong, X. Polyoxometalate electron acceptor incorporated improved properties of Cu2ZnSnS4-based room temperature NO2 gas sensor. *Sensors and Actuators B: Chemical* **2021**, *348*, 130683. DOI: https://doi.org/10.1016/j.snb.2021.130683.

3. Sun, X.; Lan, Q.; Geng, J.; Yu, M.; Li, Y.; Li, X.; Chen, L. Polyoxometalate as electron acceptor in dye/TiO2 films to accelerate room-temperature NO2 gas sensing. *Sensors and Actuators B: Chemical* **2023**, *374*, 132795. DOI: https://doi.org/10.1016/j.snb.2022.132795.
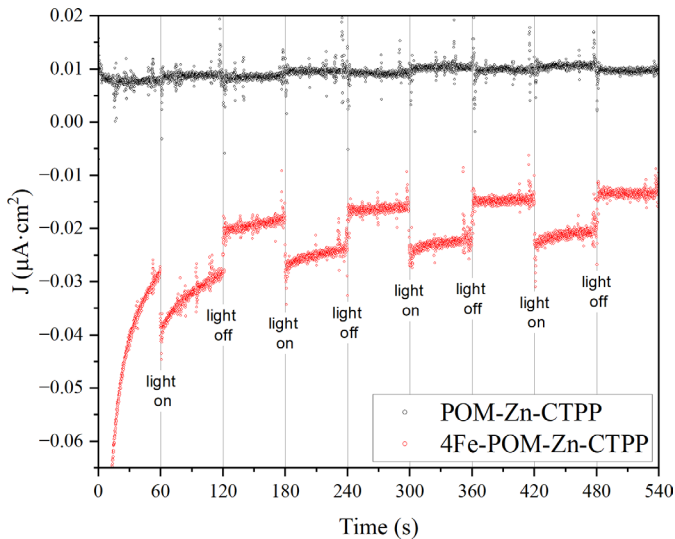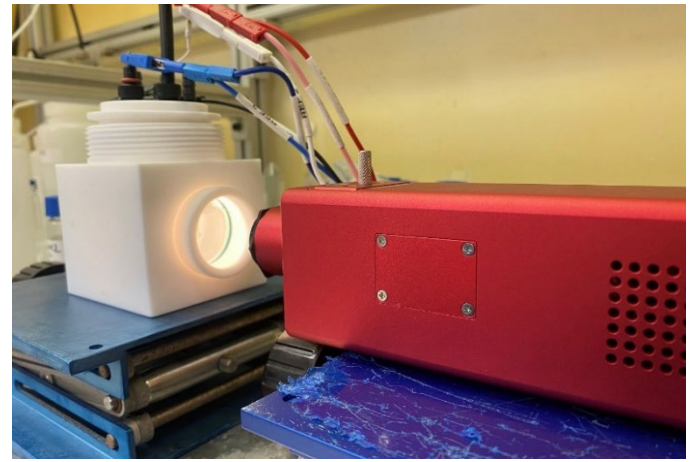
4. Winter, A.; Endres, P.; Schröter, E.; Jäger, M.; Görls, H.; Neumann, C.; Turchanin, A.; Schubert, U. S. Towards Covalent Photosensitizer-Polyoxometalate Dyads-Bipyridyl-Functionalized Polyoxometalates and Their Transition Metal Complexes. *Molecules* **2019**, *24* (24), 4446.

5. Ma, P.; Hu, F.; Wang, J.; Niu, J. Carboxylate covalently modified polyoxometalates: From synthesis, structural diversity to applications. *Coordination Chemistry Reviews* **2019**, *378*, 281-309. DOI: https://doi.org/10.1016/j.ccr.2018.02.010.

6. Zhu, Y.; Huang, Y.; Li, Q.; Zang, D.; Gu, J.; Tang, Y.; Wei, Y. Polyoxometalate-Based Photoactive Hybrid: Uncover the First Crystal Structure of Covalently Linked Hexavanadate-Porphyrin Molecule. *Inorganic Chemistry* **2020**, *59* (4), 2575-2583. DOI: 10.1021/acs.inorgchem.9b03540.

Light Isotope Separation Using Deep Eutectic Solvents

Kori D. McDonald

Lithium-6 enrichment has become an important research area within commercialized fusion development, with the only limitation being the lack of environmentally friendly, industrial scale purification methods. This project's goal was to investigate the use of cost and environmentally friendly Deep Eutectic Solvents for lithium-6 enrichment.

Introduction

Nuclear fusion is a phenomenon that is well known within the nuclear physics community as a viable option for alternative energy as many natural gases and fossil fuels are phased out of commercial use. Deuterium and tritium fusion reactions are currently the leading candidates for nuclear fusion, with the only limiting factor being a means to produce tritium at an industrial scale. Lithium-6 is a well-known isotope that can produce tritium and helium following a fission reaction. Unfortunately, lithium-6 enrichment methods are limited to the COLEX process, which leaves behind an alarming amount of mercury waste as an environmental contaminant. Deep eutectic solvents are believed to be a potential alternative to lithium isotope separations due to the ease of generation, in addition to the minimum environmental waste generated when these solvents are employed. Previous studies have suggested that deep eutectic solvents are capable of separating lithium isotopes by utilizing a 2-Thenoyltrifluoroacetone and trioctylphosphine oxide system that can biphasically react with a solution containing lithium chloride. This system displayed a separation factor of 1.068, which when compared to the 1.054 separation within the COLEX process, makes it a potential candidate for lithium-6/7 separation. In this study SRNL investigated this system in comparison to two newly-synthesized deep eutectic solvents and found that within these acetylacetone based systems, little isotopic separation is observed. SRNL investigated these systems both experimentally and computationally showing the different lithium cation affinities, in addition to proposing how different functional groups can influence these systems.

Approach

Experimentally, the first part of this project involved synthesizing previously published Deep Eutectic Solvents, which have shown selectivity towards extracting lithium from aqueous media. Upon synthesis, verification of results previously shown within the literature was completed investigating extraction efficiencies. Following extraction verification, experiments were completed and analyzed by mass spectrometry to investigate selectivity towards lithium-6 binding within these known systems. Upon verifying previously shown results, new Deep Eutectic Solvents were synthesized varying the functional groups surrounding the lithium binding site with the goal of establishing a trend for binding based on different substituents. These new solvents were then characterized and investigated in their ability to extract lithium-6 selectively over lithium-7. If a trend was shown within lithium-6 extraction efficiencies, lithium-6 cation affinities were calculated with these substituents, in addition to other potential candidates to guide future experiments (**Figure 1**).
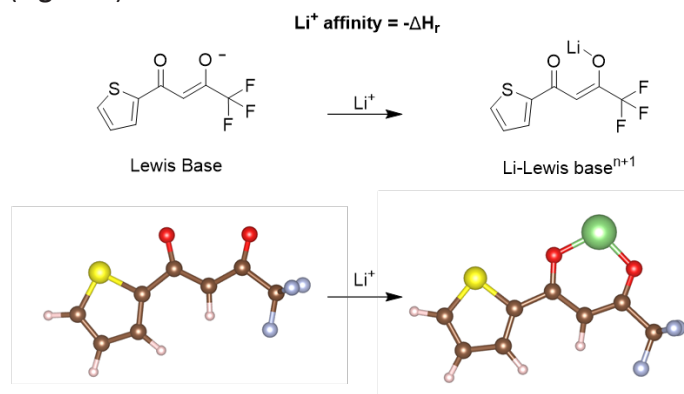

Figure 1. Schematic representing lithium cation affinity calculations (a.) and the associated structures following geometric optimization calculations as visualized through VESTA.

Accomplishments

- Biphasic experiments have been completed attempting to enrich Lithium-6 (**Figure 2**).
- Collaborations have been established with USC and UNC for ICP-MS services.
- Theoretical investigations have been completed to supplement experimental findings.
- Boron extractions from aqueous media have been shown, a feat that has little to no literature precedence.
- Presented research findings at Ionic Liquids Gordon Research Conference in August 2024.
- Manuscript submitted reporting findings of lithium separation experiments.
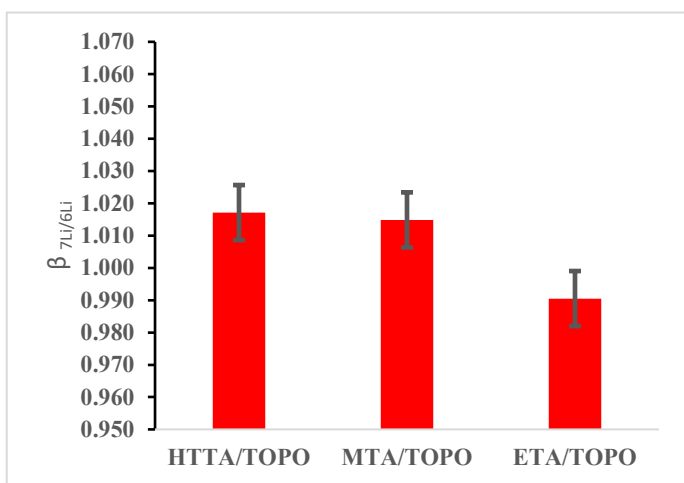
Figure 2. Results from 1,1,1-Trifluoro-2,4-pentanedione (MTA/TOPO) and Ethyl 4,4,4-trifluoroacetoacetate/TOPO (ETA/TOPO) system compared to previous methods of lithium isotope separation.

Peer-reviewed Publication

- Smith, J. E.; McDonald, K. D.; Hitchcock, D. A.; Garcia-Diaz, B. L., Isotopic Analysis of Aqueous Extractions of Lithium Using Deep Eutectic Solvents. *Submitted*.

Team Members

Jesse E. Smith *, Kori D. McDonald, Dale A. Hitchcock, Brenda L. Garcia Diaz

* Laboratory Director's Postdoctoral Researcher

References

1. Hansen, B. B.; Spittle, S.; Chen, B.; Poe, D.; Zhang, Y.; Klein, J. M.; Horton, A.; Adhikari, L.; Zelovich, T.; Doherty, B. W.; Gurkan, B.; Maginn, E. J.; Ragauskas, A.; Dadmun, M.; Zawodzinski, T. A.; Baker, G. A.; Tuckerman, M. E.; Savinell, R. F.; Sangoro, J. R., Deep Eutectic Solvents: A Review of Fundamentals and Applications. *Chemical Reviews* **2021,** *121* (3), 1232-1285.
2. Zhu, A.; Bian, X.; Han, W.; Cao, D.; Wen, Y.; Zhu, K.; Wang, S., The application of deep eutectic solvents in lithium-ion battery recycling: A comprehensive review. *Resources, Conservation and Recycling* **2023,** *188*, 106690.
3. Xie, Z.; Xie, M.; Tang, T.; Yang, F.; Xue, L.; Jiang, Z., β-Diketone-Driven Deep Eutectic Solvent for Ultra-Efficient Natural Stable Lithium-7 Isotope Separation. *Separations* **2023,** *10* (2), 111.
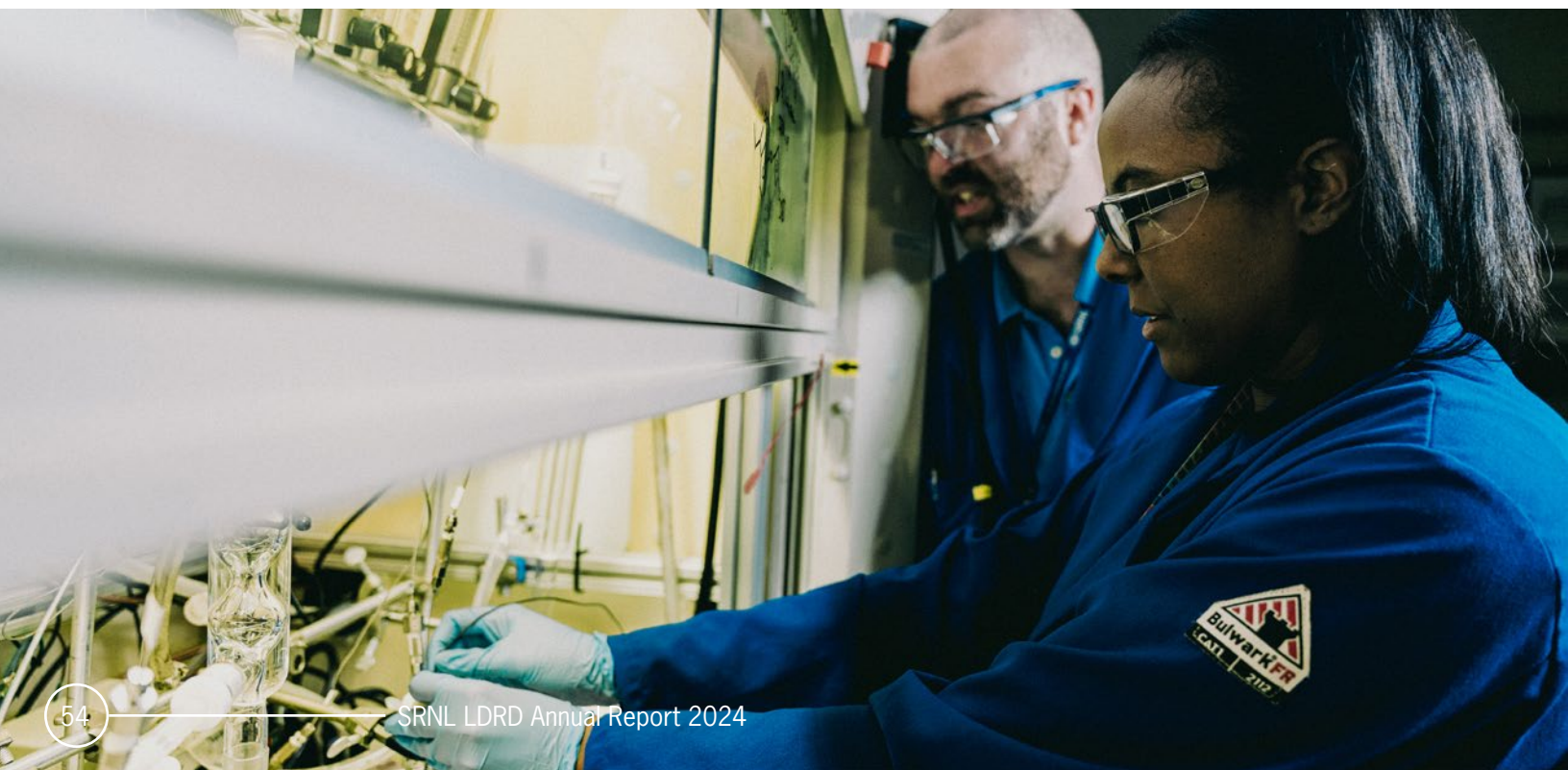
Urban Heat Island Impacts to Air and Water Quality in the Augusta Metropolitan Area

Joseph E. Wermter

Urban Heat Island effects describe warmer temperatures in urban regions. While they are often felt at the surface, they also impact upper-air and water temperatures. The goal of this project is to determine how the urban heat island of Augusta, Georgia impacts the surrounding weather and hydrology.

Introduction

The Urban Heat Island (UHI) is the longest-known anthropogenic impact on weather and climate but is one of the least understood[1]. UHI effects encompass increased heat over urban surfaces due to the prevalence of built structures instead of natural soil. Urbanization in the 21st century has led to an amplification in UHI effects, which poses environmental concerns as well as public health risks.

The heat anomalies over urban surfaces lead to increased convection, increased dispersion of pollution to areas outside of the urban centers[2], and influences on rainfall[3]. Urban heat also affects the hydrology of streams that run through the area. While the UHI is often observed in larger metropolitan areas, it is less studied in small- or moderately-sized cities that are still developing.

The population of the Augusta Metropolitan Area (AMA) has increased more than 10% in the last decade. Because of increasing urban sprawl in conjunction with overall increased anthropogenic warming, it is critical to define Augusta's UHI impact and model how it could change in the future. The objective of this project is to define the UHI effects of a moderately-sized city and to develop ways to forecast their impacts, with this year's goal to provide a comparison to larger cities in the Southeast U.S. (SEUS).

Approach

Building on the previous year's results, this year the project focused on characterizing and modeling the "boundary layer" – or urban boundary layer (UBL) – and "hydrological" UHI (HUHI). Two different sets of UBL simulations were done using the Weather Research and Forecasting (WRF) model. One set compared the AMA's UHI effects to those in the nearby Columbia Metropolitan Area (CMA); the other is a series of simulations comparing the AMA and CMA's UHI effects to the Atlanta area, encompassing an urban climate archipelago (a series of UHIs).

The second series accounted for urban growth, utilizing modeled urban growth projections for the Southeast curated by N.C. State for the years 2050 and 2100. These showed that the inclusion of urban projections increased the UHI effects seen both at the surface, and aloft in the atmosphere. Overall, the rigorous modeling and analysis of the urban boundary layer lays groundwork for future UHI studies, perhaps incorporating the use of aerial measurements (such as drones) to validate the models and provide further insight into urban turbulence.

In addition to the WRF simulations, hydrological model simulations were run using the ALGE3D model. Through this process, methods were developed to utilize WRF-simulated parameters in the HEC-HMS model – in addition to Multi-Radar/Multi-Sensor (MRMS) gridded precipitation values – which were ingested into ALGE3D to produce hydraulic and thermal calculations of the rainfall. This was a case study that showed how a full-scale atmospheric-to-hydrological model interface could operate, laying the groundwork for future projects that would improve onsite forecasting.

Accomplishments

- P.I. Wermter robustly modeled the diurnal urban boundary layer over different seasonal regimes over the AMA, and the potential relationships and boundary layer interactions with Columbia (**Figure 1**).
- P.I. Wermter and Co-I. Thomas compared the UHI and boundary layer dynamics of the AMA and CMA with Atlanta and surrounding cities; conducted sensitivity model runs on the impact of future urbanization.

- Simulated Atlanta UBL compared to aircraft soundings to/from the Hartsfield-Jackson Atlanta Airport (ATL) curated by David Rahn of KU.
- Results showed that increasing the urban impervious surfaces with the projected years 2050 and 2100 vastly increases the 2 m "canopy layer" UHI (**Figure 2**), as well as the mean boundary layer height over the urban regions (**Figure 3**).
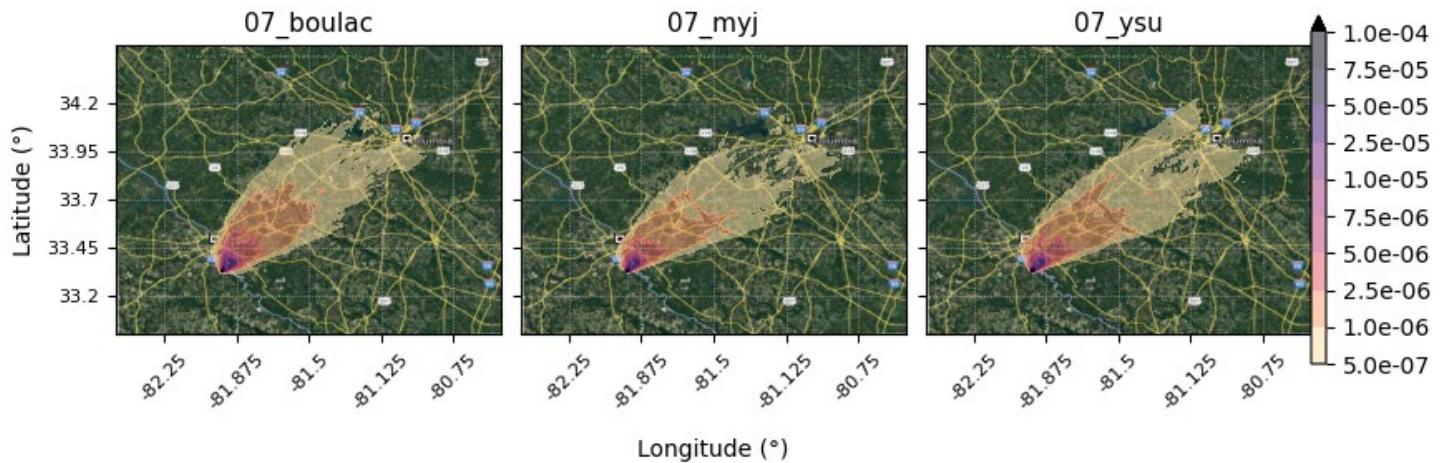
Figure 1. HYSPLIT Mean Nocturnal Plumes using WRF simulations over Augusta and Columbia for 24-30 July, 2022. Each panel represents a WRF simulation utilizing a different TKE closure scheme (BouLac, MYJ, and YSU, respectively from left-to-right).
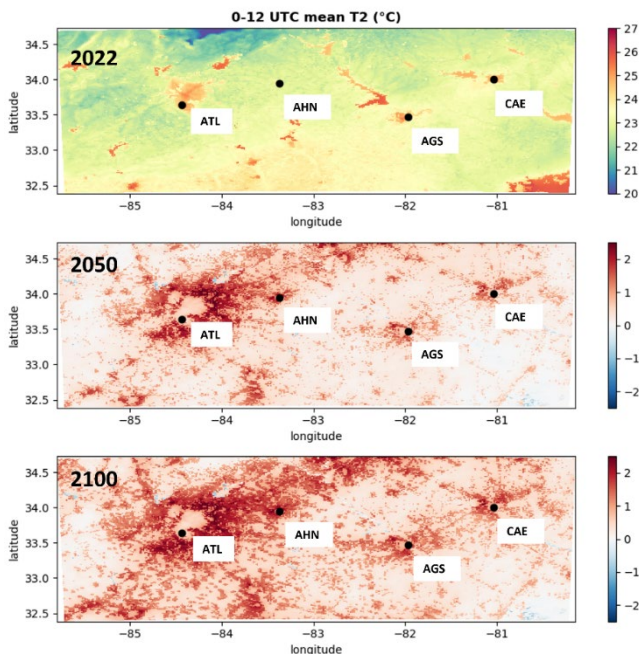
Figure 2. 0-12 UTC mean 2-m temperatures for WRF simulations spanning 1-30 June, 2022. Top panel shows mean temperatures from the 2022 "control" simulation, with the middle and bottom panels showing the differences in mean temperature with the control simulation from the 2050 and 2100 simulations, respectively.
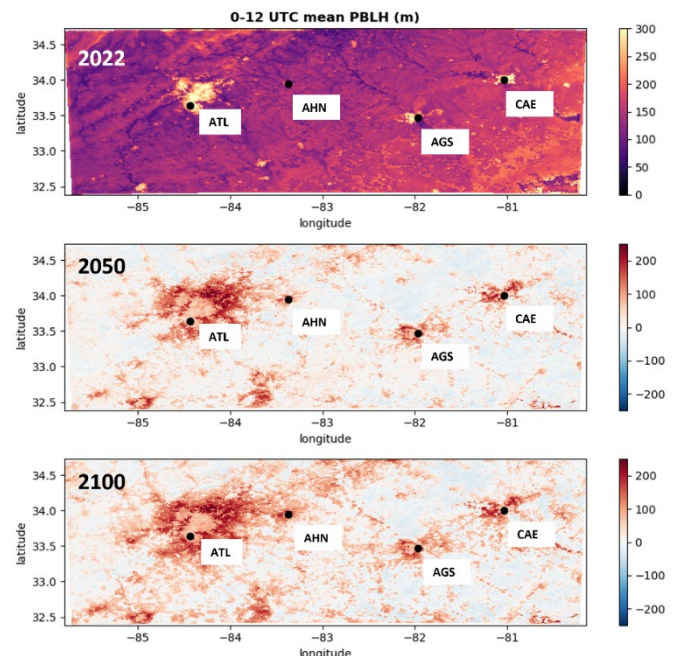
Figure 3. As in Figure 2 but with mean PBL height.

- Increases in boundary layer turbulence at night correspond to a decrease of nocturnal static stability and an enhancement to mean PBLH (**Figure 4**).
- These results show some of the clearest pictures of the urban heat impacts to the boundary layer, and can be utilized as a case-study for future projects, especially within the southeast U.S.
- P.I. Wermter and Co-I. Turner conducted analyses of the HUHI of the Savannah River near Augusta in comparison to Savannah.
- Stream temperature data at select locations of the Savannah River near Augusta were provided by the Phinizy Center for Water Sciences.

- Increases in temperature surges were found to be statistically significant within the Augusta urban center, suggesting that there is an increase in temperature following runoff from "pulse thunderstorms" over the urban region (**Figure 5**).
- HUHI research is a new area of study, and this study is one of the first to examine the timing and locality of HUHI surges.
- P.I. Wermter and Co-I. Turner developed scripts to read in WRF temperature data and MRMS rain data (**Figure 6**) to calculate runoff in HEC-HMS, which provides inputs into the ALGE3D model. Co-I. Turner conducted ALGE3D simulations that have shown temperature surges in response to recorded rain events at the Augusta urban surface (**Figure 7).**
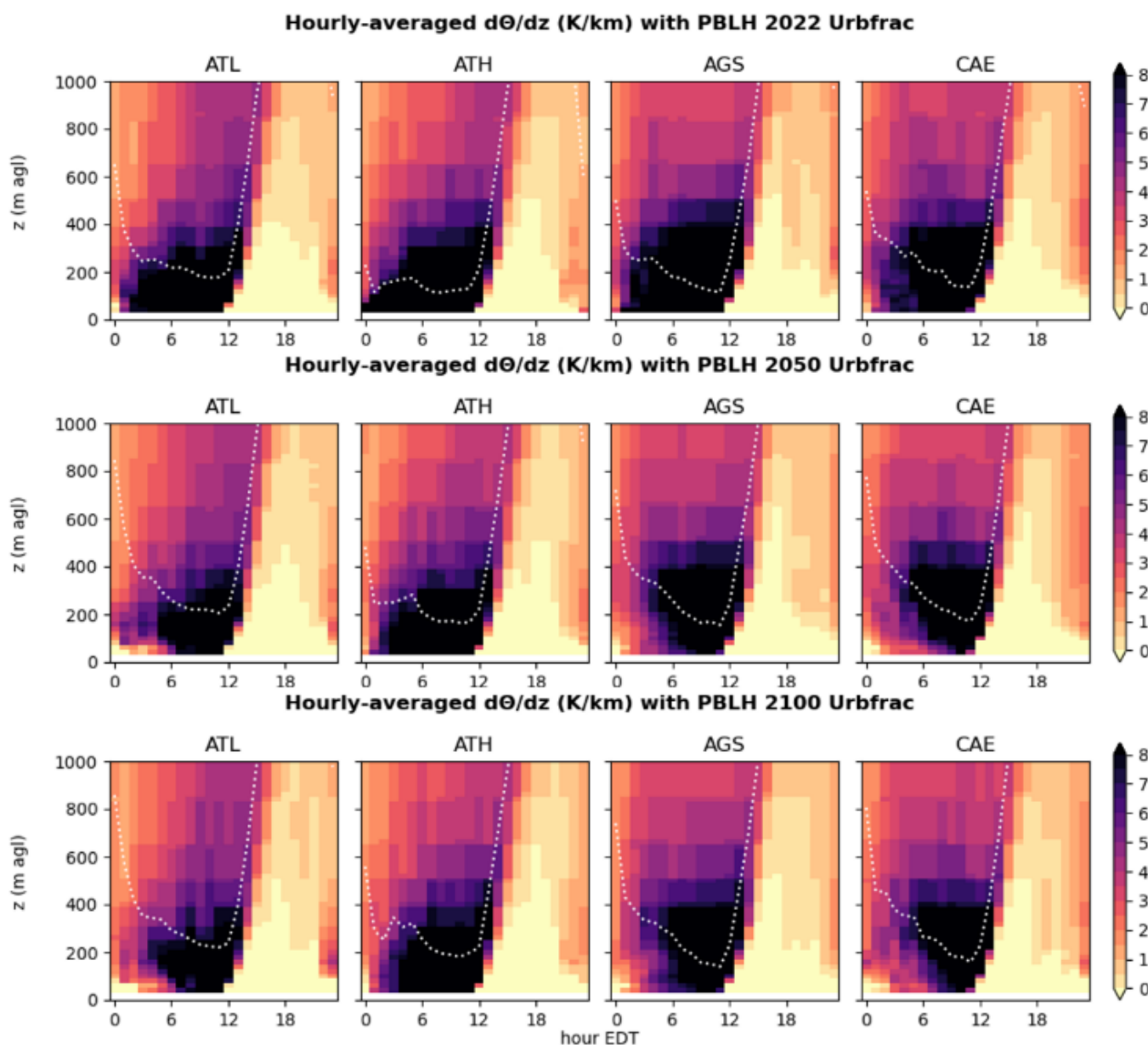
Figure 4. Static stability over the four urban regions for (top) 2022, (middle) 2050, and (bottom) 2100 urban surfaces.

Stream Temperature Deviations by Magnitude of Rain Hour
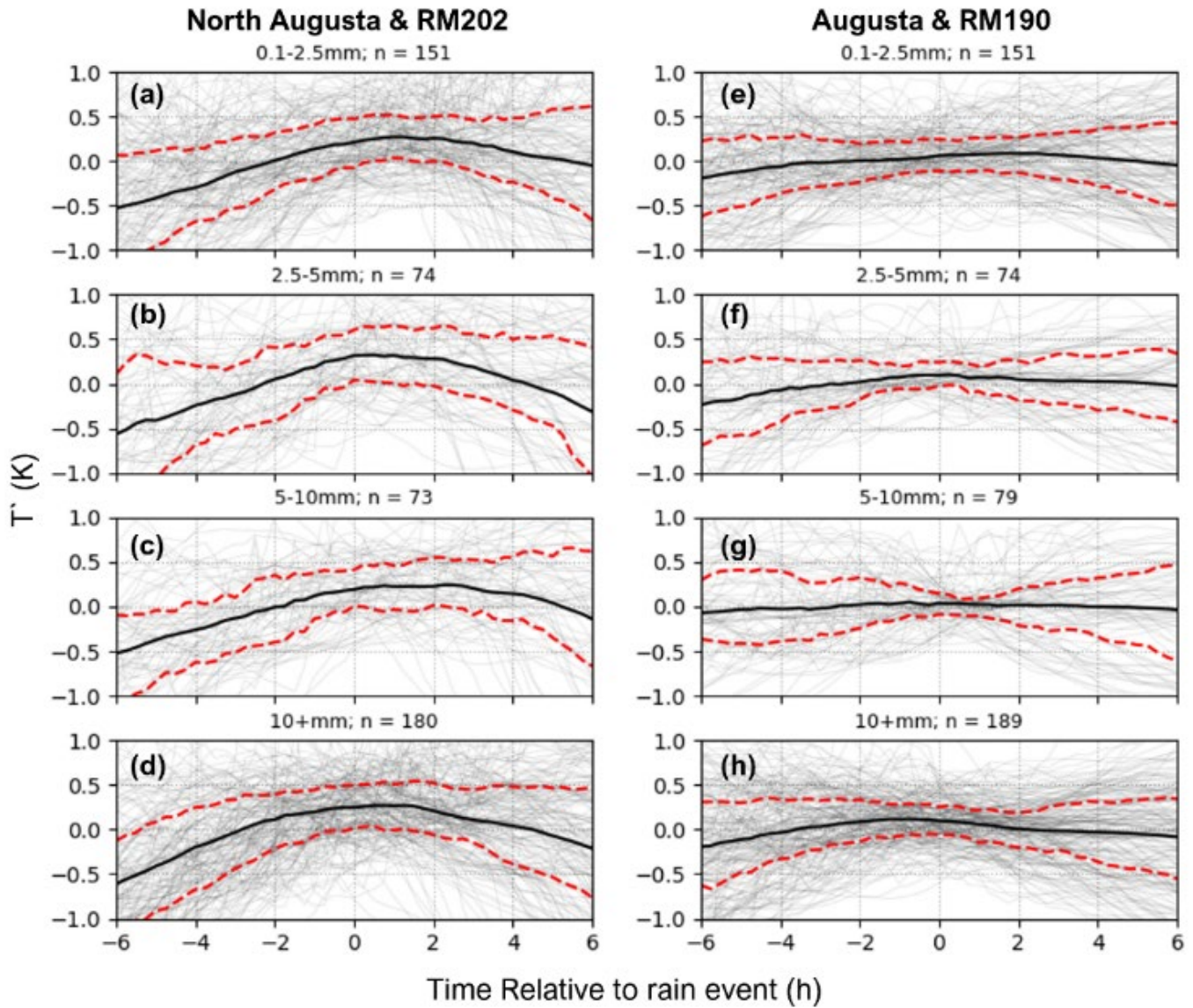
Figure 5. Temperature deviations at the Savannah River at (a-d) the Augusta/North Augusta urban center, and (e-h) the Savannah River Lock & Dam.
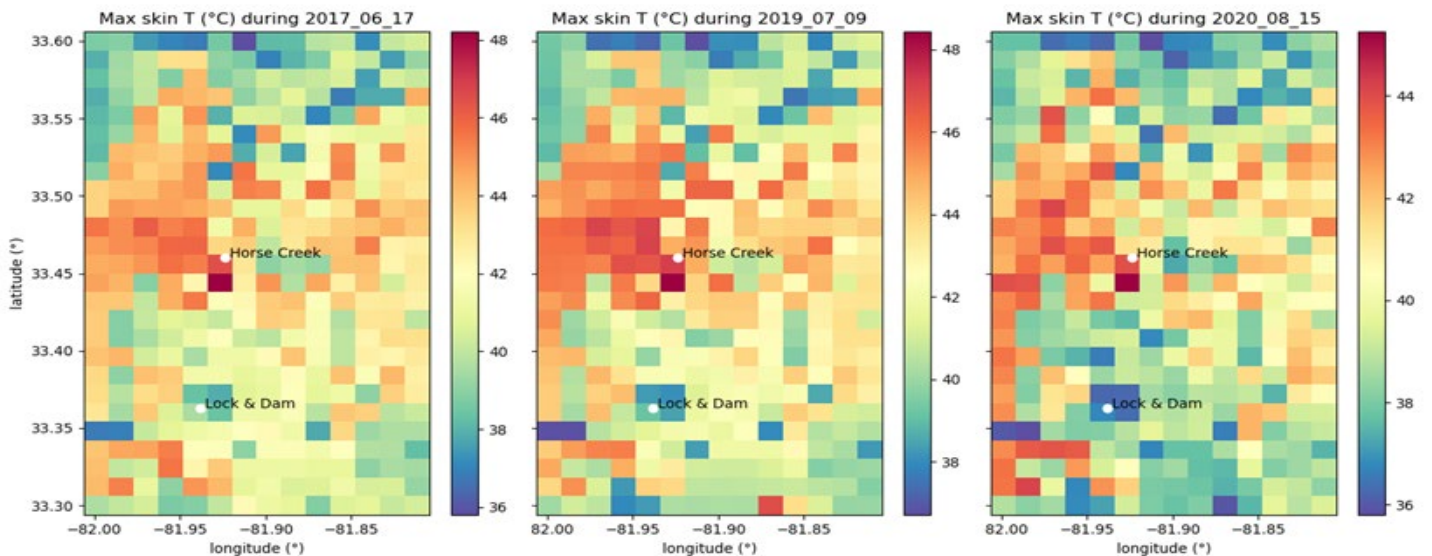
Figure 2. Skin Temperature maps for (left) 17 June 2017, (middle) 9 July 2019, and (right) 15 August 2020 produced by WRF used as input into ALGE.
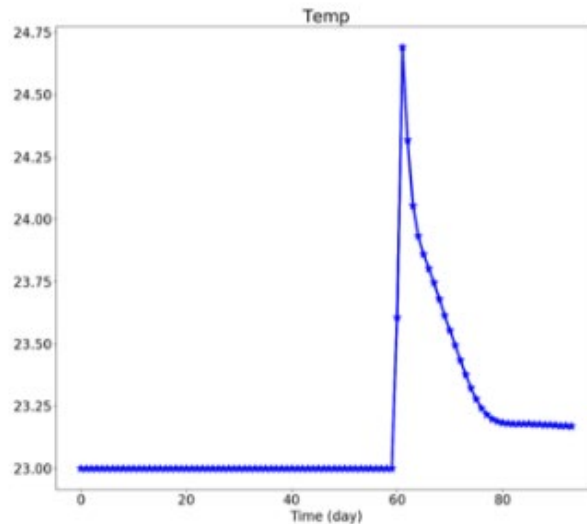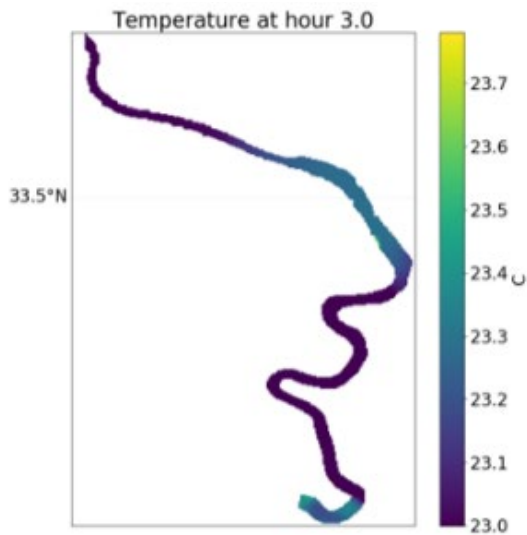
Figure 7. (left) Temperature map of the Savannah River and (right) corresponding time series for Savannah Bluff Lock and Dam for 15 August 2020.

- Bathymetry of the Savannah River near Augusta was curated by WDTS VFP Gregory Nail from UTM, who also provided guidance for running the HEC-HMS model.
- Further work could be done in this area, potentially with more hydrology-compatible builds of WRF (WRF-Hydro, NU-WRF & LIS, etc.).
- Co-I. Appelbaum defended his M.S. thesis under the guidance of Co-I. Shepherd.

Peer-reviewed Publications

- Mcleod, J.; Shepherd, J.M.; Appelbaum, M. Evidence of cloud and rainfall modification in a mid-sized urban area – A climatological analysis of Augusta, Georgia. *City and Environment Interactions.* **2024**. 21, 100141, DOI: 10.1016/j.cacint.2024.100141
- Wermter, J.; Turner, V.; Appelbaum, M.; Shepherd, J. M.; Lott, J. Stream Temperature Responses to Summer Urban Rain Events Along the Savannah River. *Submitted to the Journal of South Carolina Water Resources – Under Review*
- Wermter, J. E.; Shepherd, J. M. Sensitivity of Simulated Mid-Sized Urban Boundary Layers to Turbulence Parameterizations – Curious Atmospheric Interactions between Augusta and Columbia. *In preparation for submission to Geophysical Research Letters.*
- Wermter, J. E.; Thomas, A. M.; Appelbaum, M.; Shepherd, J. M.; Rahn, D. A.; Gott, J. A. Urban Boundary Layers in Georgia and South Carolina: Interactions and Future Urbanization. *In preparation for submission to Urban Climate*
- Nail, G.; Turner, V. GIS processing of publicly available fishing map data into a digital elevation model (DEM). *Submitted to ArcUser Magazine*

Team Members

Vivian Turner, Andrew Thomas**, J. Marshall Shepherd[a], Max Appelbaum*[a], Sergio Bernardes[a], Jordan Mcleod[b], Gregory Nail[c], David Rahn[d], Jacob Lott[e]

[a]*University of Georgia*
[b]*University of South Alabama*
[c]*University of Tennessee – Martin*
[d]*University of Kansas*
[e]*Phinizy Center for Water Sciences*
*Student Researcher
**Post-Doctoral Researcher

References

1. Barlow, J. F., Progress in observing and modelling the urban boundary layer. Urban Climate **2014**, 10, 216-240.
2. Cosgrove, A.; Berkelhammer, M., Downwind footprint of an urban heat island on air and lake temperatures (vol 1, 46, 2018). Npj Clim Atmos Sci **2019**, 2.
3. McLeod, J.; Shepherd, M.; Konrad, C. E., Spatio-temporal rainfall patterns around Atlanta, Georgia and possible relationships to urban land cover. Urban Climate **2017**, 21, 27-42.
4. Johnson, B.; Shepherd, J. M., An urban-based climatology of winter precipitation in the northeast United States. Urban Climate **2018**, 24, 205-220.
5. Zahn, E.; Welty, C.; Smith, J. A.; Kemp, S. J.; Baeck, M. L.; Bou-Zeid, E., The Hydrological Urban Heat Island: Determinants of Acute and Chronic Heat Stress in Urban Streams. Journal of the American Water Resources Association **2021**, 57 (6), 941-955.

FY24 PROJECTS

CORE COMPETENCY:

Creating manufacturing solutions for EM, NNSA, and energy security

Computational Investigation of CdTeSe Growth and Doping Strategies for PV Applications

Jonathon N. Baker

Theoretical calculations were employed to study gas-surface interactions in cadmium telluride-based thin films. SRNL evaluated possible thin film models, growth thermodynamics, and the role of lateral interactions between adsorbing atoms. These calculations further our understanding of thin film growth for better engineering.

Introduction

SRNL approached the problem of how to best optimize cadmium telluride (CdTe) thin film growth by first understanding the physics of adsorption with first principles simulations (e.g., density functional theory). CdTe thin film solar cells are a competitive rival technology to crystalline silicon (Si) for commercial photovoltaic adoption [1] and an attractive alternative due to a low environmental footprint, tunable electronic properties with alloying (e.g., Zn and Se introduction), and readily available precursors [2,3,4]. Despite these advantages, CdTe fabrication using physical vapor deposition technology (PVD) is outdated relative to the rest of the field (e.g., atomic layer deposition, chemical vapor deposition, PVD as applied to other materials). Core to those advances is the chemical potential- and vapor pressure-control during thin film growth. First principles have been successful in the group III-Vs [5], for example, in describing atomic adsorption interactions and surface diffusion, but is limited to a small number of atoms. A different approach to simulate crystal growth is the kinetic Monte Carlo (kMC) method, [6] which is based on modeling elementary processes like adsorption, desorption, and migration all at once for many more atoms than possible with density functional theory. The chemical potential and vapor pressures are key to the adsorption process. Therefore, the novelty of this work is to apply both approaches to the (111) surface plane of CdTe by coupling the chemical potential and vapor pressures. The intent of this work is to predict thin film growth behavior based on applied vapor pressure.

Approach

The approach was a combination of density functional theory, surface science, and statistical mechanics to directly model the growth of CdTe with Se and Zn dopants. From the literature, it is known that the (111) surface is the most dominantly observed facet for CdTe [7]; therefore, the first objective in this study was to determine the surface morphology of CdTe(111). Optimized surface models are presented in **Figure 1a and 1b**. The second objective was to model the adsorption of Cd, Zn, Te, and Se at both the dilute limit and with a neighboring secondary adsorbate (e.g., binary pairs). **Figure 1a** displays all tested adatom sites.
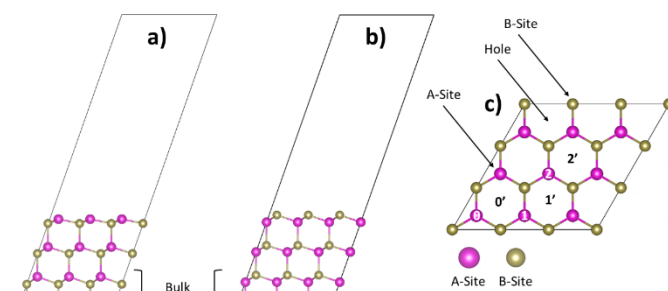
Figure 1. a) Side view of the Cd-terminated CdTe(111) surface with 4 atomic layers, b) side view of the Te-terminated CdTe(111) surface with 4 atomic layers, and c) top view of the CdTe(111) surface with a (3 × 3) supercell and three adsorption sites for adatoms: A-top, B-top, and Hole. The various binding sites for Cd, Te, Zn, and Se adatom pair calculations are displayed in white and black (*e.g.*, (0-0'), (0-1), (0-1'), (0-2), (0'-1'), and (0'-2') binary pairs). The bulk layers are fixed to the bulk CdTe lattice values for all simulations.

The dilute limit adsorption energies are displayed in **Figure 2**. Displayed in **Figures 3 and 4** are the binary interaction energies between adatoms. The third step in this study was to increase the concentration of the adsorbates from the dilute limit to full saturation to better understand lateral interactions at a variety of different coverages (**Figure 5**). Lastly, the surface migration barriers of adatom diffusion with example pathways were computed (**Figure 6**).

In combination with collision theory, the law of mass action, and transition state theory, elementary reaction rate constants for adsorption, desorption, and migration steps key to thin film growth were calculated. The predicted reaction rate constants can then be applied to a reactor model based on kMC, which simulates epitaxial growth for large systems by using random numbers in combination with the predicted elementary reaction rates.

Cd-Terminated (111)		Te-Terminated (111)	
Site	E_{ads} (eV)	Site	E_{ads} (eV)
A-Top (Te)	-4.29	A-Top (Cd)	-0.86
A-Top (Se)	-4.61	A-Top (Zn)	-0.88
Hole (Te)	-5.95	Hole (Cd)	-2.41
Hole (Se)	-6.31	Hole (Zn)	-2.52
Hole (Cd)	-1.77	Hole (Te)	-3.19
Hole (Zn)	-1.98	Hole (Se)	-3.18

Figure 2. Energy of adsorption (E_{ads} in eV) for Cd, Te, Se, and Zn adatoms in the dilute adsorption limit. Gas phase monoatomic Cd, Te, Se, and Zn atoms are used as the reference species for all adsorption energy calculations.

Accomplishments

- Wrote a Python-implementation of kMC for both CdTe(111) surface facets that supports Cd, Zn, Te, and Se adsorption, desorption, and migration; supports modularity for user directed migration pathways; and prints atomic structure of each predicted state.
- Dilute limit predictions of Cd, Zn, Te, and Se adsorption on both CdTe(111) facets (**Figure 2**). Results are comparable predictions that agree favorably with existing literature [7]. This is the first work to examine modeling of Zn and Se dilute limit adsorption.
- Predictions of the interaction energy between adsorbates on both terminations of CdTe(111) facets (**Figure 3**). This is the first work to examine treatments of the interactions between interaction energy between Cd-Cd, Cd-Zn, Cd-Te, Cd-Se, Te-Te, Te-Se, Te-Zn, Se-Zn, Se-Se, and Zn-Zn binary interactions.
- Predictions of the adsorbate energy with increasing surface coverage on both CdTe(111) facets (**Figure 5**). This is the first work to examine modeling surface coverages ranging from dilute limit to the saturated limit.
- This is the first work to examine modeling Zn and Se surface diffusion on CdTe(111) and the effect of binary pair interactions regarding surface diffusion of Cd, Zn, Te, and Se on CdTe(111) (**Figure 6**).
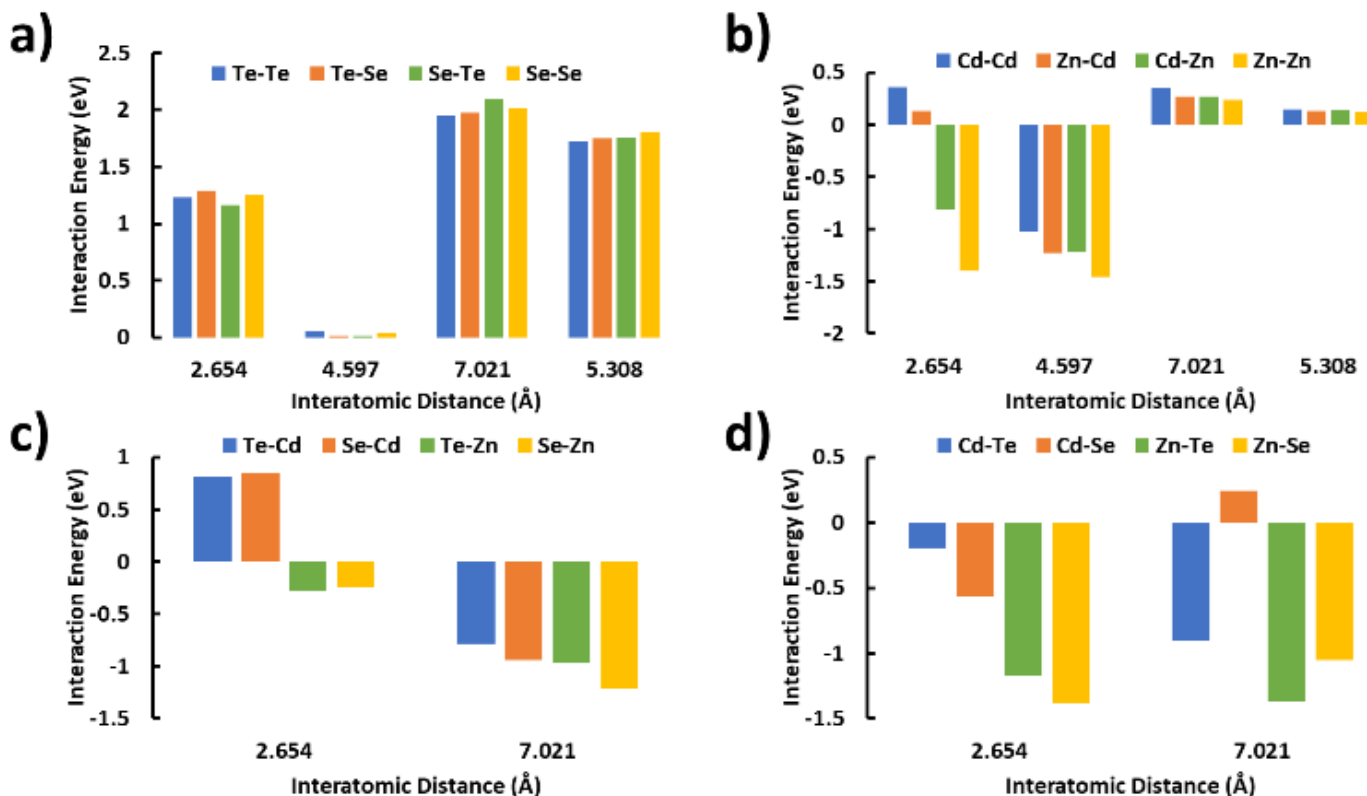
Figure 3. Interaction energies (in eV) for a) the Cd-Terminated (111) surface for A-site elements only (*e.g.*, Te and Se), b) the Te-Terminated (111) surface for B-site elements only (*e.g.*, Cd and Zn), c) the Cd-Terminated (111) surface for mixed A-site and B-site elements, and d) the Te-Terminated (111) surface for mixed A-site and B-site elements. The described pair interactions are (0-0'), (0-1), (0-1'), and (0-2), respectively.
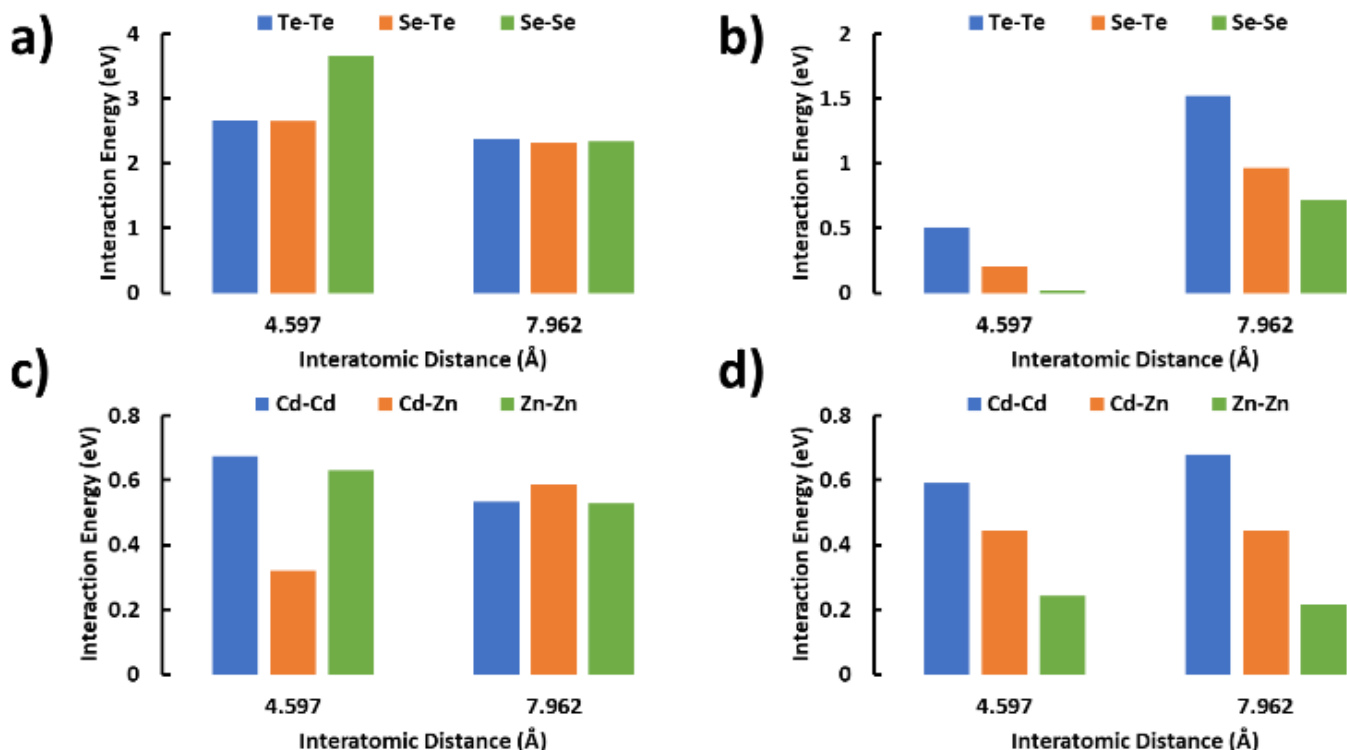
Figure 4. Interaction energies (in eV) for a) the Cd-Terminated (111) surface for A-site elements only (e.g., Te and Se), b) the Te-Terminated (111) surface for B-site elements only (e.g., Cd and Zn), c) the Cd-Terminated (111) surface for mixed A-site and B-site elements, and d) the Te-Terminated (111) surface for mixed A-site and B-site elements. The described pair interactions are (0'-1') and (0'-2'), respectively, as displayed in Figure 1.
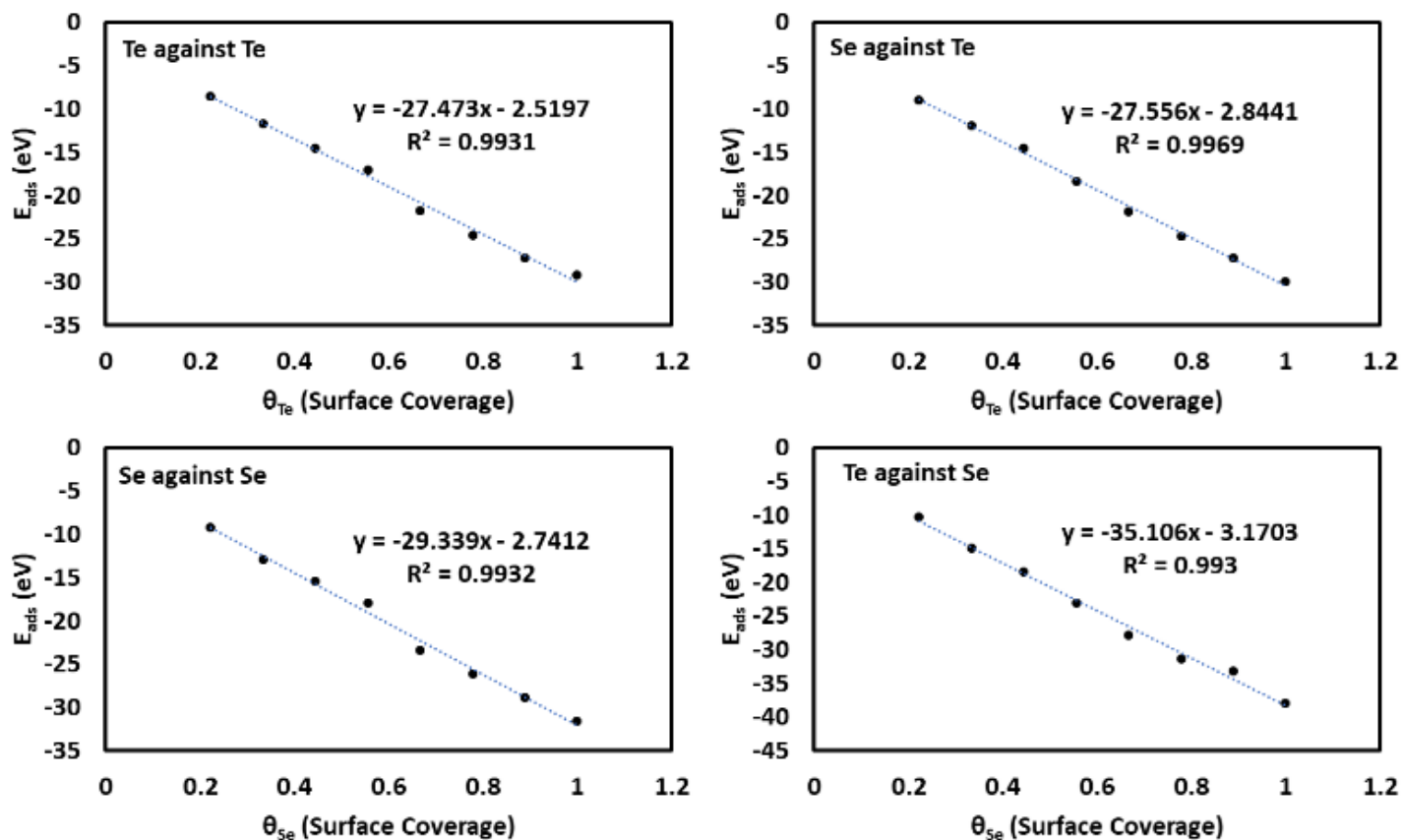
Figure 5. Adsorption energies (E_{ads}) referenced to monoatomic Te and Se on the Cd-Terminated (111) A-site with respect to increasing Te or Se surface coverage.
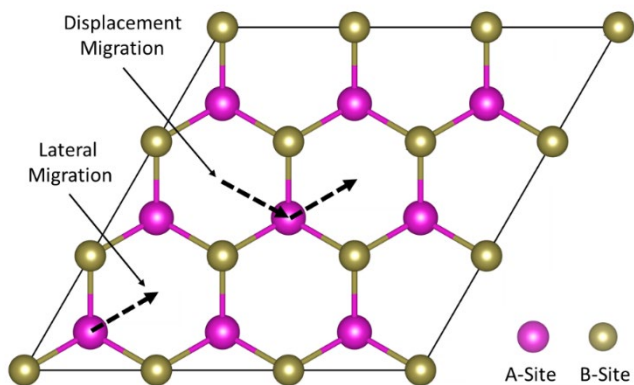
Figure 6. Possible diffusion paths for Cd, Te, Se, and Zn adatoms.

Peer-reviewed Publications

- Szaro N.A., Baker J.N., A first principles study of the adsorbate interactions on the CdTe(111) surface with Cd, Zn, Te, and Se adatoms and their effect on early growth behavior. *In Preparation*.

Team Member

Nicholas Szaro*

Laboratory Director's Postdoctoral Research Fellow

References

1. Precedence Research Report 2339. *Solar Cell Market – Global Industry Analysis, Size, Share, Growth, Trends, Regional Outlook, and Forecast 2024-2034*. Precedence Research. 2023. https://www.precedenceresearch.com/solar-cell-market (accessed 2024-08-29).
2. Peng, J., Lu, L., & Yang, H. Review on life cycle assessment of energy payback and greenhouse gas emission of solar photovoltaic systems. *Renew. Sustain. Energy Rev.* **2013**, *19*, 255-274. DOI: 10.1016/j.rser.2012.11.035
3. Fthenakis, V., & Kim, H. C. Life-cycle uses of water in US electricity generation. *Renew. Sustain. Energy Rev.* **2010**. *14* (7), 2039-2048. DOI: 10.1016/j.rser.2010.03.008
4. Zheng, X., Kuciauskas, D., Moseley, J., Colegrove, E., Albin, D. S., Moutinho H., Duenow J.N., Ablekim T., Harvey S.P., Ferguson A., & Metzger, W. K. Recombination and bandgap engineering in CdSeTe/CdTe solar cells. *APL Mater.* **2019**, *7* (7), 071112. DOI: 10.1063/1.5098459
5. Chungh M. & Ranganathan M. Adsorbate interactions on the GaN(0001) surface and their effect on diffusion barriers and growth morphology. *Phys. Chem. Chem. Phys.* **2016**, *19*, 2111-2123. DOI: 10.1039/C6CP07254B
6. Chungh M. & Ranganathan M. Lattice kinetic Monte Carlo simulation study of the early stages of epitaxial GaN(0001) growth. *App. Surf. Sci.* **2017**, *422*, 1120-1128. DOI: 10.1016/j.apsusc.2017.06.067
7. Naderi, E., Nanvati S., Majumder C., & Ghaisas S.V. Diffusion of Cd and Te adatoms on CdTe(111) surfaces: A computational study using density functional theory. *AIP Adv.* **2015**, *5* (1), 017134. DOI: 10.1063/1.4906794

Additive Manufacturing of Deuterated Polymers for Rheological Model Verification

Camden A. Chatham

In polymer 3D printing, the extent to which neighboring layers fuse together dictates the strength of printed objects. This work experimentally validates modelled predictions of layer fusion through deuterium labelling and neutron imaging, which directly captures molecular movement from one layer into another resulting from various manufacturing conditions.

Introduction

The additive manufacturing (AM) layerwise paradigm enables geometric flexibility during fabrication, but results in performance properties governed by layer interfaces. Therefore, interlayer penetration (i.e., molecular diffusion) and bonding are critical to ensure adequate performance of end-use parts. Understanding and predicting part performance from printing conditions is highly desired by those intending to use AM for end-use part fabrication. Rheological models, including the Upper-convected Maxwell and Rolie-poly models, have been shown in published literature to estimate molecular diffusion across layer interfaces for given printing conditions, which correlates with interfacial strength. However, direct measurement of interlayer diffusion is challenging and unreported. Neutron imaging/scattering can directly measure molecular diffusion if deposited in alternating protonated/deuterated layers (**Figure 1**). Deuterium labelling provides contrast for imaging without significantly altering polymer behavior from the typical protonated material.
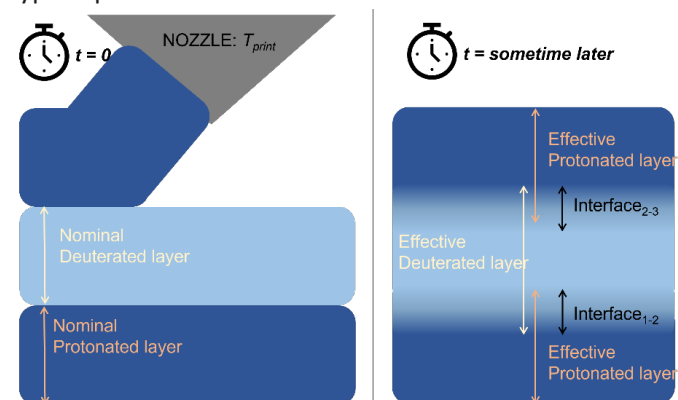
Figure 1. Graphical depiction of alternating layer deposition immediately after deposition (left) and after some elapsed time (right). Interlayer penetration is directly determined from the ratio of measured effective layer height (right) to the nominally deposited layer height (left).

The present, work both calculates extent of coalescence through converting previously published models into Python scripts and compares model results against experimental results. Generating model predictions requires measuring several intrinsic polymer properties governing flow behavior at elevated temperatures; such datasets are invaluable for informing any sort of computational materials engineering effort.

Deuterium labelling for polymer research is underutilized due to high cost of commercial product. This project explored deuteration of four polymers leveraging unique-to-SRNL capabilities. Three did not preserve molecular weight; one reaction progresses slowly. Additionally, FY24 has focused on coding predictive models and generating the relevant polymer property libraries. Key properties have been measured for eight polymers with fourteen targeted manufacturing conditions (**Table 1**).

Polymer	Mw & Mn [g/mol]	Rg [Å]
Polystyrene	293,000 & 89,800	150
PMMA	98,465 & 44,940	38
*D-PMMA	132,851 & 103,000	296
PC	46,085 & 16,900	38
PVOH	-	87
*PETG	615,000 & 34,000	54
PLA	91,000 & 52,000	53

Table 1. Molecular weight and radius of gyration (Rg) for the studied polymers of interest. Molecular weight determined via size exclusion chromatography in tetrahydrofuran (THF) compared against polystyrene standards. Rg determined via small angle x-ray scattering (SAXS) and the polymer excluded volume model. Polymers marked with * may not have fully dissolved resulting in a false high Rg. Measurements by University of Tennessee – Knoxville (UTK).

Approach

The project's primary objectives are (1) coding predictive models enhancing the study of structure-process-property relationships in the chosen AM modalities of Fused Filament Fabrication (FFF) and Powder Bed Fusion (PBF) and (2) evaluation of molecular diffusion across layer interfaces through deuterium labelling and neutron contrast imaging and fracture toughness.

The chosen predictive models (Upper-convected Maxwell for PBF and Rolie-poly for FFF) require temperature-dependent measurements of several key thermal, rheological, and mechanical polymer properties in addition to the thermal environment characteristic of the corresponding AM modality. Temperature profiles corresponding to several chosen process parameter sets (temperature, speed, time between layers) were collected in FY24 via in situ thermal camera for both PBF and FFF (**Figure 2**). Temperature-dependent properties were measured in FY24 for the common polymers in **Table 2**.

Design of Experiments Table				
Sample ID	Nozzle Temp [°C]	Parts per Build	Layer Height [mm]	Print Speed [mm/s]
1	Low	One	Low	Low
2	Low	One	Low	Default
3	Low	Multiple	Default	Low
4	Low	Multiple	Default	Default
5	Default	One	Default	Low
6	Default	One	Default	Default
7	Default	Multiple	Low	Low
8	Default	Multiple	Low	Default
9	Low	Multiple	High	High
10	Default	One	Default	High
11	Default	Multiple	High	Low
12	High	One	High	Default
13	High	Multiple	High	High
14	High	Multiple	Default	Low

Table 2. Statistical design of experimental printing conditions for specimen fabrication.

The target models predict (1) extent of coalescence and (2) fracture toughness. Experimental evaluation correlates (1) neutron contrast-mapping resultant locations of deuterium-labelled polymer chains with predicted extent of coalescence and (2) experimental fracture toughness with predicted fracture toughness. In-house deuterium labelling was attempted for several polymers; however, the process was deemed viable for only polypropylene (PP). Deuterated poly(methyl methacrylate) (D-PMMA) was purchased from a commercial source. Filament from D-PMMA was prepared for FFF printing in FY24. Powder from deuterated-PP (D-PP) for PBF printing and post-print neutron imaging will occur in FY25.

Fracture toughness was characterized for chosen polymers at several printing conditions according to the design of experiments in **Table 1** in FY24. These results will be compared against model predictions in FY25.

Accomplishments

- Subcontract with University of Tennessee put into place June 2024.
- University of Tennessee – Knoxville (UTK) measured radius of gyration (Rg) for seven polymers for use in predictive models (**Table 1**)
- Functional Python codes written to describe both two-particle coalescence in the Powder Bed Fusion (PBF) additive manufacturing (AM) context (Upper-convected Maxwell model) and molecular diffusion across the layer interface in the Fused Filament Fabrication (FFF) AM context. Molecular diffusion and entanglements have been previously shown in the literature as correlating with fracture toughness (Rolie-poly model), which is also a predictive calculation made in SRNL Python scripts.
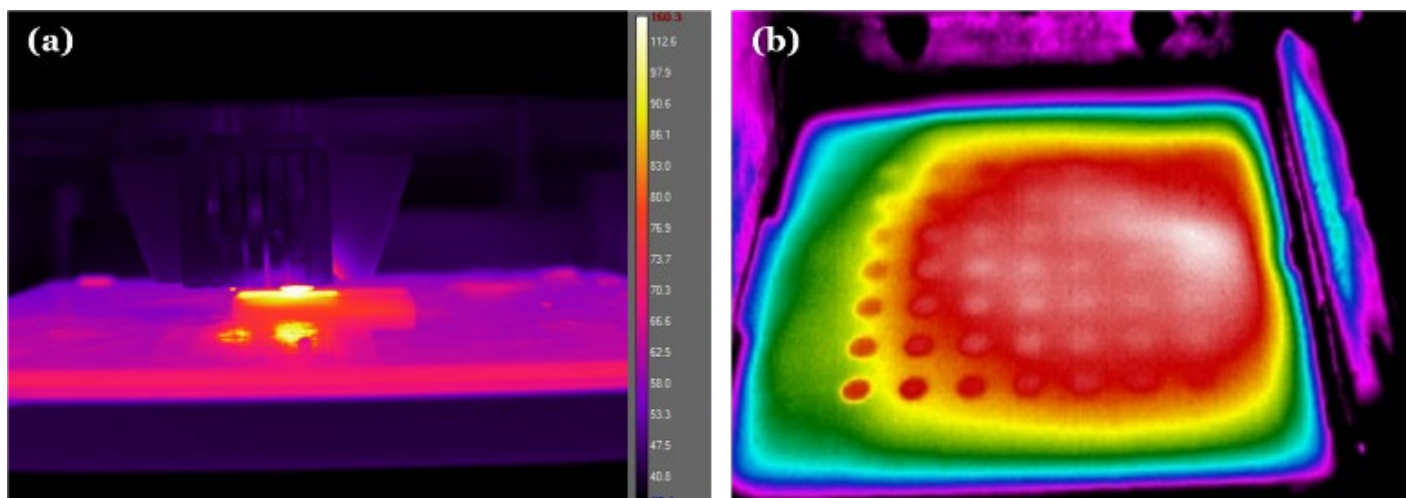

Figure 2. Infrared camera image representing single set of manufacturing conditions in (a) Fused Filament Fabrication (FFF) and (b) Powder Bed Fusion (PBF) additive manufacturing.

- The material libraries containing all pertinent thermal and rheological properties for the predictive calculations have been collected for the following polymers: polycarbonate (PC), poly(methyl methacrylate) (PMMA), polystyrene (PS), polypropylene (PP), polyamide 12 (PA12; nylon 12), poly(lactic acid) (PLA), poly(vinyl alcohol) (PVOH), poly(ethylene-co-glycol terephthalate) (PETG). The libraries include the following properties: relaxation time, zero-shear viscosity, melt temperature, glass transition temperature, specific heat capacity, and crystallization kinetics .
- Fracture toughness measurements for specimens printed according to the statistical design of experiments presented in **Table 3** have been collected for PETG. Additionally, fracture samples have been prepared from PP and PVOH for testing in FY25.
- Deuterium labelling through isotope exchange was attempted on commercially available pellets of PS, PETG, PLA, and PP. Macroscopic indicators of molecular weight degradation, such as color change and change from solid to gel-like state, were observed for PS, PETG, and PLA.
- Thirty-seven% deuterium exchange was observed on PP after 21 days of reaction (**Figure 3b**). This is significantly slower than expected. Fifty wt% PP filament (Braskem) and 50 wt% mineral oil (LVO500) were mixed under gentle argon flow at 220°C using overhead stirring. Once homogeneous, 2 wt% platinum on carbon (Tanaka) was added to the reaction vessel. Once homogeneous, 25 sccm deuterium (D_2) gas was bubbled into the reaction mixture via a cannula. The reaction proceeded for 14 days. After 14 days, the reaction mixture was heated to 240°C to increase reaction speed. The reaction proceeded another seven days.
- Deuterated PMMA (D-PMMA) was purchased from a commercial vendor and made into six inches of 3D printable filament. A novel short length melt casting and splicing method was used to efficiently convert the as-received flake feedstock formfactor into filament suitable for printing (**Figure 3b**).
- Printer hardware and process modifications were made to enable FFF printing of brittle filament, such as PMMA. **Figure 4** shows the direct-drive hardware modification made to the Ultimaker S3 removing the imposed radius of curvature between drive mechanism and heated deposition nozzle. The stock radius of curvature was observed to cause strain resulting in filament fracture (and therefore print failure) for brittle polymers like PMMA.

Fracture Toughness Results				
	PETG	PMMA	PVOH	PP
Sample ID	**KIc** $Mpa*m^{1/2}$	**KIc** $Mpa*m^{1/2}$	**KIc** $Mpa*m^{1/2}$	**KIc** $Mpa*m^{1/2}$
1	1.27	--	X	X
2	1.17	--	--	X
3	--	--	--	--
4	X	--	--	--
5	1.59	--	--	--
6	0.78	--	--	--
7	1.36	--	--	--
8	0.98	--	--	--
9	0.76	--	X	X
10	--	--	--	--
11	--	--	--	--
12	X	--	--	--
13	--	--	--	X
14	--	--	--	--

Table 3. Fracture toughness results corresponding to varying print conditions for several materials studied. 'X' indicates samples have been printed but not yet tested. '-' indicates samples are not yet printed.

Team Members

E. Cade Willis, Andrew Rhodes, Haley Jones*, Anastasia Mullins, Nicholas Issa, Alexander Vitale, Tyler Guin, Tim Novajosky[a][**], Mark Dadmun[b], Mrinalini Kolaprath [b][**]

[a]University of Georgia
[b]University of Tennessee - Knoxville
[*]Postdoctoral Researcher
[**]Student Researcher
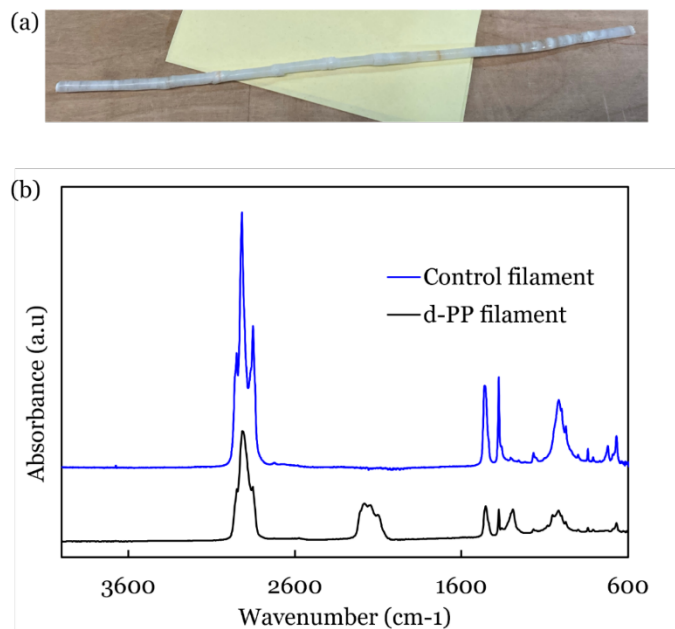
Figure 2. (a) Image of melt cast filament made from deuterated poly(methyl methacrylate) (D-PMMA). (b) Comparison of Fourier-transform infrared (FT-IR) spectra of polypropylene (PP) before and after deuteration reaction indicating 37% deuteration of PP after 21 days of constant reaction.
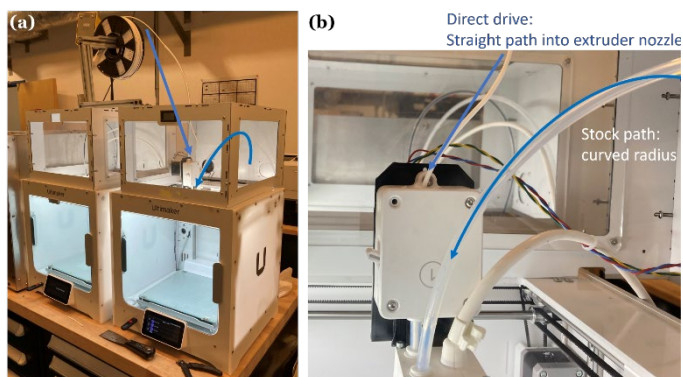
Figure 3. Direct drive hardware modification for Ultimaker S3 Fused Filament Fabrication (FFF) printer enabling printing of brittle filament (like PMMA). (a) Depicts stock and updated filament paths from overall system view. (b) Depicts stock and updated system paths close-up.

High Entropy Alloy Nanoparticles for Catalysis

Matt Craps

High entropy alloys are an exciting class of new catalysts composed of five or more elements in roughly equal amounts. These alloys often outperform even the best monometallic catalysts. This project is using a microwave route to synthesize high entropy alloy nanoparticles directly onto a carbon support suitable for catalysis.

Introduction

Advanced research to develop novel catalysts is necessary to improve their performance and lessen the use of expensive and rare metals. High entropy alloys (HEAs) have been demonstrated to show remarkable catalytic performance with lower cost materials. HEAs are solid solutions composed of five or more elements in roughly equal amounts (**Figure 1a**). Often, HEAs outperform the sum of their individual components due to synergistic effects. This is caused, in part, by the different sizes of each element. These differences lead to lattice distortion (**Figure 1b**), creating a strained and reactive catalytic surface. The co-location of different elements on the surface also leads to a wide mix of active sites with unique binding energies and electronics. The varied binding energy differences are especially key for multistep reactions where a monometallic catalyst would only have active sites designed for a specific elementary step. Despite their impressive catalytic properties, a substantive problem in the HEA field is the vast compositional space that HEAs occupy. While there are only 66 naturally occurring metals to choose from and test, the number of combinations quickly ballons to over a billion for systems of five metals. Therefore, rational decision making in alloy composition and high-throughput testing are key.
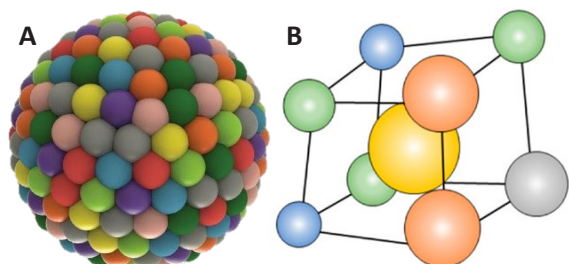
Figure 1. (a) High entropy alloy (HEA) particle with each color representing a different element. (b) HEA crystal structure displaying lattice distortion from varying atomic sizes

Approach

Due to the vast number of elemental combinations that can be made, high-throughput testing is advantageous. In the lab, high-throughput microwave synthesis was used to induce nanoparticle formation.[1] Metal salts are dried onto a graphene oxide support, which is then microwaved for a few seconds (**Figure 2**).
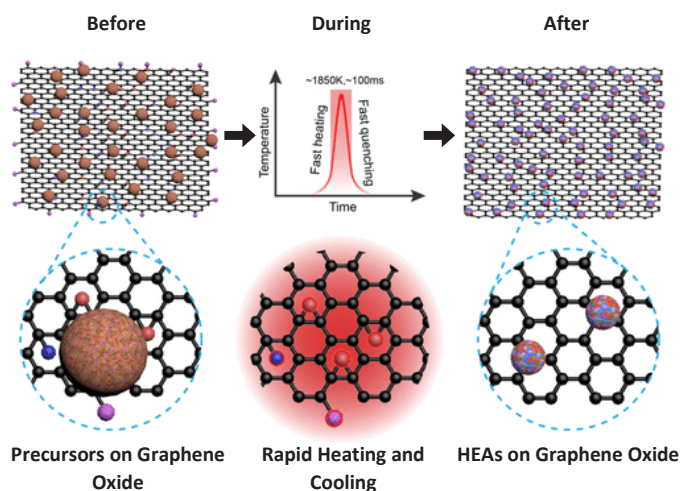
Figure 2. Synthesis scheme of high entropy alloys, showing the state before (left), during (center), and after (right) microwave heating.[1]

The microwave energy causes rapid heating of the salt precursors, causing metal reduction and alloy formation. The localized heating results in hot spots where particles form. The HEA nanoparticles, synthesized directly on a carbon support, can be further characterized and tested as catalysts. Scanning electron microscopy is used to image the nanoparticles and determine size, shape, distribution, etc. (**Figure 3**). Energy dispersive X-ray spectroscopy allows for elemental composition determination and locations of each element. Powder X-ray diffraction gives crystal phase information, ensuring it is a one-phase alloy system. Catalytic testing is currently

conducted for the conversion of ethane to ethylene (oxidative dehydrogenation of ethane). Other gaseous reactions are possible and are being planned. The microwave synthesis method allows for a variety of metals to be utilized. Current alloying elements include noble metals (e.g., gold, palladium, and platinum), first row transition metals (e.g., iron, cobalt, and nickel), main group metals (e.g., aluminum and tin) and refractory metals (e.g., tungsten and molybdenum).

Figure 3. Scanning electron microscope image of AuPdCuZnGa nanoparticles (top left) and corresponding energy dispersive X-ray spectroscopy maps of the various elements. Gold is shown in yellow, palladium in purple, copper in green, zinc in red, and gallium in blue. Scale bar at bottom right applies to all images.

Accomplishments

- Hazard analysis and work documents drafted and implemented.
- Explored multiple synthetic techniques, ultimately deciding on microwave synthesis.
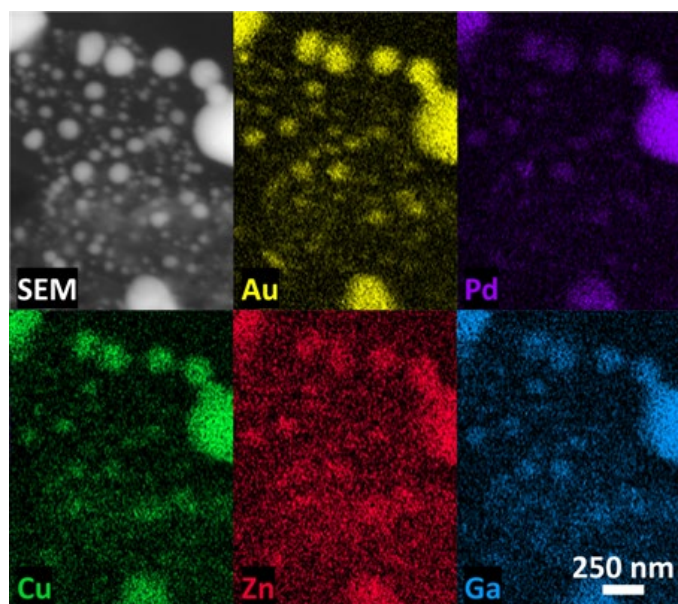- Installed flow cell reactor to allow microwaving under inert gas flow.
- Synthesized various target HEA compositions including PtPdFeCoNi, PtPdVFeCe, AuPdCuZnGa.
- Trained and utilized various instrumentation across SRNL to support project.
- Explored the effect of oxidation from pure graphene to graphene oxide.
- Initial unoptimized oxidative dehydrogenation of ethane catalysis results show promising data (76% ethane conversion and 71% selectivity for ethylene at 700 °C).
- Determined how to synthesize HEAs on a carbon support fixed on an induction susceptor.

- Contract to obtain atomic resolution transmission electron microscopy characterization with North Carolina State University's Analytical Instrumentation Facility is in process.
- First manuscript planned and outlined.
- Mentored two summer interns who learned about this project, Peter Woodell (Clemson, SULI program) and Harry Carrion (Polytechnic University of Puerto Rico).
- Matt Craps received 'Excellence in Research Advising' Award.
- Matt Gordon won the People's Choice award at the 2024 SRNL Research Slam Finals presenting about this project.
- Presented five posters: SRNL Day at Georgia Institute of Technology, Postdoc Poster Session, Summer intern Poster Session (two posters), and LDRD Poster Session.
- Presenting three posters in early FY25: SERMACS conference, AIChE conference, and SRNL University Partnership Day at USC.

Team Member

Matt Gordon*

*Laboratory Director's Postdoctoral Research Fellow

Reference

1. Qiao, H.; Saray, M. T.; Wang, X.; Xu, S.; Chen, G.; Huang, Z.; Chen, C.; Zhong, G.; Dong, Q.; Hong, M.; Xie, H.; Shahbazian-Yassar, R.; Hu, L. Scalable Synthesis of High Entropy Alloy Nanoparticles by Microwave Heating. *ACS Nano* **2021**, *15*, 14928–14937.

Accelerated Discovery of W-Re-Ta-Mo Refractory Medium Entropy Alloy for Extreme Conditions

Guru Dinda

This report summarizes the methodology developed for the accelerated discovery of W–Re–Ta–Mo refractory medium entropy alloys for harsh service conditions, specifically for hydrogen and low-carbon fuel turbines, liquid rocket engines, space nuclear propulsion systems, hypersonic vehicle applications, and advanced, next-generation nuclear reactors.

Introduction

Extreme-environment applications require components that must have elevated temperature oxidation and corrosion resistance, strength, toughness, and plasma and neutron irradiation resistance, all of which are rarely found in a single material. Refractory alloys such as tungsten- (W) and molybdenum- (Mo)based alloys can withstand high operating temperatures. However, refractory alloys exhibit intrinsic brittleness and oxidation-susceptibility, which remains a significant challenge for their processing and application in harsh service conditions. There have been ever-increasing demands for structural materials that can withstand corrosive/oxidizing environments, severe mechanical loading, nuclear environments, and extreme temperatures. However, traditional alloy design and alloy selection are practically restricted by "one alloy at a time" concept. Given the vast universe of potential alloys that can be created by combining various elements, the conventional method of synthesizing and testing samples one at a time is too slow for exploring the broad range of novel materials. To overcome the limitations of the current refractory materials, we have developed a high-throughput alloy development technique based on the laser-based, directed energy deposition principle coupled with integrated computational modeling and high-throughput materials synthesis and screening to dramatically reduce the time to discover new W-Rhenium (Re)-Tantalum(Ta)-Mo refractory medium entropy alloy for extreme environment applications. It is expected that the proposed high-throughput alloy development technique will be used extensively to explore various alloy libraries and be established as a mainstream rapid alloy development tool for the discovery of many new high-performance materials for structural and functional applications.

Approach

To demonstrate the proposed accelerated alloy discovery concept, we have developed a laser based directed energy deposition (DED) system based on a 3-kW diode laser, six-axis robotic arm integrated with two-axis positioner, four powder feeders, and a coaxial deposition nozzle with a potential for process monitoring and feedback control. In pursuit of the proposed goal, the research plan is divided into two interconnected research aims: (1) Design W–Re–Ta–Mo refractory medium entropy alloy composition space via CALPHAD-based solidification modeling, and (2) Establish a high-throughput alloy synthesis and screening procedure via laser-based DED process. We have employed an equilibrium solidification model to simulate the phase composition, entropy, density, thermal conductivity, and electrical conductivity in the W-Re-Ta-Mo quaternary alloy system. The primary objective of this task is to determine the solid solution phase boundary in the W-Re-Ta-Mo composition space. The second objective of the CALPHAD simulation is to establish the composition window of the W-Re-Ta-Mo alloys with solidus temperature > 3000 K. Laser-based directed energy deposition is an additive manufacturing technique where the powder is fed into the melt pool created by a high-power laser beam to form an overlay layer of material, as shown in **Figure 1**. Since one can control the powder feed rate over time, delivering multiple powders from different powder feeders with different feed rates can produce discrete as well as compositional gradient samples. This offers a unique possibility for rapid preparation of a complete spectrum of materials with wide variety of compositions.
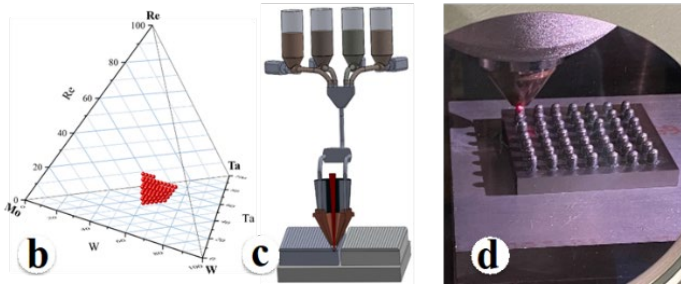
Figure 1: (a) Directed energy deposition (DED) system developed at SRNL, (b) CALPHAD predicted composition space of W-Re-Ta-Mo refractory medium entropy alloys, (c) Schematics of the multi-material DED process, (d) As-deposited W-Re-Ta-Mo refractory medium entropy alloy coupons on a single substrate.

Accomplishments

- Equilibrium phase composition, entropy, density, thermal conductivity, and electrical conductivity of 600 W-Re-Ta-Mo discrete alloy compositions have been calculated by CALPHAD simulations and the solid solutions phase boundary in this quaternary alloy systems have been identified.

- Laser deposition process parameters of W, Re, Ta, and Mo and combination of these elements have been developed for the deposition of coupons with density >99.9%.

- More than 200 W-Re-Ta-Mo alloy coupons have been deposited with optimized process parameters for microstructural investigation and mechanical testing.

Team Members

Rajiv Mishra ,Nathan Wyeth, Raden Gustinvil

Postdoctoral Researcher

Chemical Vapor Transport for the Preparation of Single Crystals of Actinide Complexes

Rosalie Greer

This project aims to develop the synthesis and characterization of transition metal and actinide-based materials with promising applications in electronics and quantum computing. Incorporation of actinides such as uranium into materials shows potential in developing valuable material properties that are difficult or impossible to achieve with lighter elements.

Introduction

Transition metal chalcogenides are compelling materials that, due to their tendency to form van der Waals layers, often have strong anisotropic characteristics and some form topological materials. For instance, WTe_2 has been shown to be a topological semimetal with "titanic" magnetoresistance, wherein electrical resistance changes with an applied magnetic field,[1, 2] an attractive property for spintronics and memory devices. While p-type doping of WTe_2 has shown to increase magnetoresistance,[3] some n-type dopants decrease magnetoresistance.[4] This project established chemical vapor transport (CVT) synthetic capabilities and began work on WTe_2 doping to explore transition metal chalcogenide properties.

Uranium-based chalcogenides, as heavy-fermion two-dimensional materials, are attractive for their potential applications in quantum information science and as magnetic materials.[5,6] Although UTe_2 has received particularly intense research interest, UTe_3 and its analogs have been largely overlooked. In order to resolve UTe_3's longstanding problem of contradictory reports of both paramagnetic[7, 8] and antiferromagnetic ordering[9] in UTe_3, SRNL performed magnetic characterization and the first single-crystal neutron diffraction analysis of this species. Using samples prepared with unprecedented polymorph control between α- and β-UTe_3, the project began to determine their magnetic structures, de-conflicted earlier reports, and observed initial indications of hidden magnetic order. The project also developed synthetic methods and established capabilities at SRNL to produce the first examples of ^{235}U-enriched UTe_2 in order to explore possible isotopic effects on quantum properties.

Approach

Tungsten ditelluride and uranium tellurides (UTe_x) were initially targeted, with investigation later expanded to USe_3 and $ThTe_3$. To generate these complexes as high-quality single crystals, chemical vapor transport (CVT) and molten salt flux (MSF) synthetic techniques were employed. For CVT, a chemical vapor transport agent (CVTA) reacts with elemental precursors in a vacuum-sealed quartz ampoule within a temperature gradient to form volatile complexes. These complexes are transported across the gradient (both low-to-high and high-to-low are possible) over several days and deposited as single-crystals of the target compound (**Figure 1A**). In contrast, MSF uses an excess of a eutectic salt flux such as NaCl/KCl to act as a molten reaction medium for the elemental precursors at high temperatures. Slow cooling of the flux over days allows the growth of low-defect, low-impurity single crystals of the target compound (**Figure 1B**).

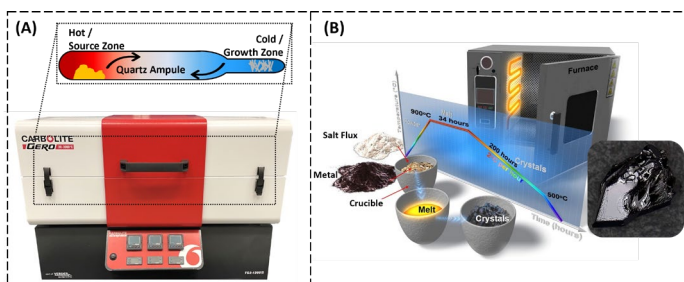**Figure 1.** Illustration of chemical vapor transport (A) and molten salt flux (B) growth methods.

Tuning of CVTA selection, precursor stoichiometry, and temperature gradients and profiles enable the synthesis of various materials and allow for polymorph control. In FY24 SRNL focused on establishing crystal growth capabilities and safety protocols to enable future synthesis of isotopically-enriched U-based crystals,

optimizing WTe_2 growth and doping studies, and coordinated external characterization of crystal, magnetic, and electrical properties. Collaborators in the Salguero group at the University of Georgia (UGA) performed recipe development and optimization of dU syntheses, and supplied materials for the external characterizations. External characterization was performed in coordination with Idaho National Laboratory (INL) and with the $WAND^2$ team at the Oak Ridge National Laboratory (ORNL) High-Flux Isotope Reactor (HFIR).

Accomplishments

- Established new CVT and MSF growth capabilities at SRNL.
- Demonstrated and optimized CVT growth of WTe_2 at SRNL, identity confirmed *via* single-crystal X-ray diffraction (SC-XRD) (**Figure 2E**)
- CVT and MSF growth recipes for UTe_2 were optimized at UGA on the same equipment as is in place at SRNL in anticipation of SRNL ^{235}U synthetic work
- Optimization of UTe_3 growth was completed through CVTA testing (Br_2, $TeBr_4$, I_2, or mixtures of these) and use of carbon-coated ampoules to minimize oxidation
- First-of-its-kind polymorph control capability for UTe_3 developed
- No prior literature documenting the ability to produce solely α-UTe_3 or β-UTe_3

- Temperature tuning allows synthesis of polymorph-pure UTe_3 of either polymorph (**Figure 2A**)
- Polymorphs characterized structurally and first observation of color difference between polymorphs reported (**Figures 2A-C**)
- Analysis of α-UTe_3 and β-UTe_3 *via* vibrating sample magnetometry (VSM) allowed demonstration of paramagnetic properties in the former, two magnetic ordering temperatures in the latter
- Second β-UTe_3 ordering not previously reported
- Higher-quality crystals and measurement than previous reports
- First-ever single-crystal neutron diffraction on α-UTe_3 and β-UTe_3 performed at ORNL HFIR
- Prior powder neutron diffraction found no magnetic ordering
- Paramagnetism found in α-UTe_3 as expected (**Figure 2D**) with constrained lattice parameters at 1.5 K
- Lack of magnetic ordering in β-UTe_3 observed in contradiction to VSM results, possibly indicative of hidden magnetic order
- Data processing and analysis of neutron diffraction results is ongoing
- Demonstrated synthesis of α-$ThTe_3$ and USe_3
- Identities confirmed *via* SC-XRD and imaged *via* scanning transmission electron microscopy (STEM) (**Figure 2F, G**)
- Intended for use in future magnetic and electrical studies
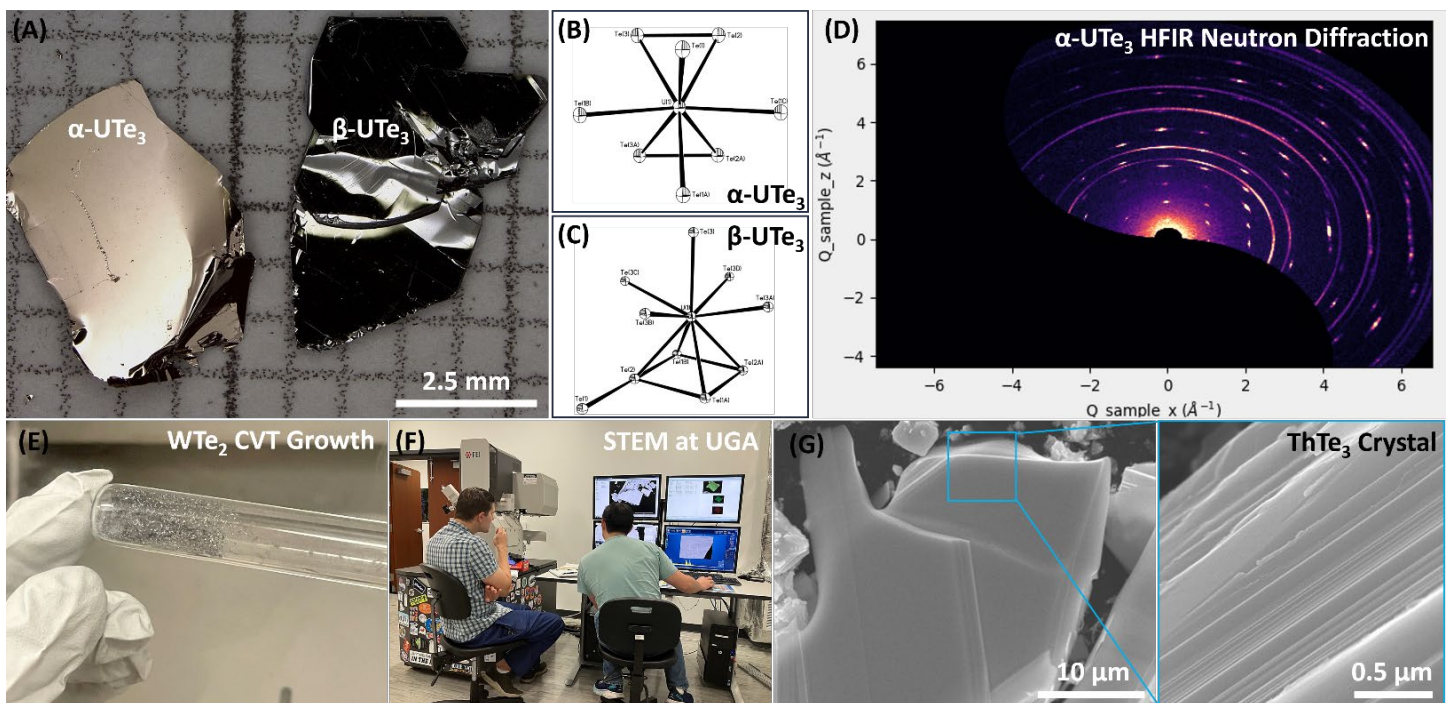
Figure 2. Single crystals of α-UTe3 and β-UTe3¬ grown through CVT (A), SC-XRD of α-UTe3 (B) and β-UTe3 (C), neutron diffraction showing crystal lattice parameters of α-UTe3 at 1.5 K (D), WTe2 grown through CVT (E), Nicholas Sessing (UGA) and Matthew Simmers (SRNL) examining crystals with STEM (F), and STEM imaging of a ThTe3 crystal demonstrating van der Waals layers (G).

Peer-reviewed Publication

- Magnetic Order Variation and Discrepancies in UTe_3 Polymorphs (under preparation)

Team Members

Binod Rai, Matthew Simmers, Lorianne Shultz-Johnson[*], Tina Salguero[b], Nicholas Sesingb[b*] Krysztof Gofryk[c], Volodymyr Buturlim[c*], Matthias Frontzek[c], Athena Chen[c], Jie Xing[c].

[b]University of Georgia
[b]Idaho National Laboratory
[c]Oak Ridge National Laboratory
[*]Postdoctoral Researcher

References

1. Yu, P.; Fu, W.; Zeng, Q.; Lin, J.; Yan, C.; Lai, Z.; Tang, B.; Suenaga, K.; Zhang, H.; Liu, Z. Controllable synthesis of atomically thin type-II Weyl semimetal WTe2 nanosheets: an advanced electrode material for all-solid-state flexible supercapacitors. *Advanced Materials* **2017**, *29* (34), 1701909.

2. Tian, W.; Yu, W.; Liu, X.; Wang, Y.; Shi, J. A Review of the Characteristics, Synthesis, and Thermodynamics of Type-II Weyl Semimetal WTe2. *Materials* **2018**, *11* (7), 1185.

3. Lin, E.-C.; Lin, Y.-T.; Chou, C.-T.; Chen, C.-A.; Wu, Y.-J.; Chen, P.-H.; Lee, S.-F.; Chang, C.-S.; Chen, Y.-F.; Lee, Y.-H. Enhanced Magnetoresistance of Doped WTe2 Single Crystals. *ACS Applied Electronic Materials* **2022**, *4* (9), 4540-4546.

4. Singh, A.; Sasmal, S.; Iyer, K. K.; Thamizhavel, A.; Maiti, K. Extremely large magnetoresistance (XMR) in Ni-doped WTe2. In *AIP Conference Proceedings*, 2024; AIP Publishing: Vol. 2995.

5. Giustino, F.; Lee, J. H.; Trier, F.; Bibes, M.; Winter, S. M.; Valentí, R.; Son, Y.-W.; Taillefer, L.; Heil, C.; Figueroa, A. I. The 2021 quantum materials roadmap. *Journal of Physics: Materials* **2021**, *3* (4), 042006.

6. Ran, S.; Eckberg, C.; Ding, Q.-P.; Furukawa, Y.; Metz, T.; Saha, S. R.; Liu, I.-L.; Zic, M.; Kim, H.; Paglione, J. Nearly ferromagnetic spin-triplet superconductivity. *Science* **2019**, *365* (6454), 684-687.

7. Nouvel, G.; Zwick, A.; Renucci, M.; Lockwood, D.; Noël, H. Magnetic ordering and Raman scattering from electronic excitations and phonons in uranium trichalcogenides. *Journal of Physics C: Solid State Physics* **1987**, *20* (12), 1881.

8. Suski, W. Magnetic properties of the uranium trichalcogenides and UTesub (3. 38). *Bull. Acad. Pol. Sci., Ser. Sci. Chim.;(Poland)* **1976**, *24* (1).

9. Noël, H. Magnetic susceptibility of the uranium trichalcogenides US3, USe3 AND UTe3. *Journal of the Less Common Metals* **1986**, *121*, 265-270.

Tritium and Radiation-resistant Silicone Membranes through Tailored Phenyl Content

Tyler Guin

The lack of tritium-compatible elastomers complicates tritium processing and is a technology barrier for fusion power. This project explores phenyl silicone elastomers as potential tritium-resistant elastomers. This project demonstrated a novel silicone synthesis that resulted in radiation stability of >6.2 MGy gamma radiation dose in air.

Introduction

Prior work at SRNL has demonstrated that polymers perform poorly in contact with tritium, either turning into "goo" from chain scission or brittle char from crosslinking. Conventional inert polymers, such as PTFE, are not resistant to tritium, as the activation energy induced by the beta decay is orders of magnitude higher than conventional chemical bond energy. While most polymers are not resistant to tritium, SRNL has demonstrated that highly aromatic polymers such as polyimides have relatively good tritium resistance. However, polyimides are not useful for many barrier applications as they are inflexible and difficult to process.

SRNL has explored the use of phenyl-silicone oils for use in high-rad environments, and these oils demonstrated exceptional resistance to gamma irradiation and deuterium isotope exchange. In contrast to traditional methyl silicones, phenyl silicone oil contains 89 wt% phenyl content, which provides exceptional radiation stability. Importantly, it is possible to synthesize longer chain polymers with equivalent chemical structures through organo-silane chemistry.

SRNL has also explored the gamma radiation resistance of phenyl silicones, focusing on changes in thermomechanical properties. As expected, phenyl content positively correlates with radiation stability. However, the viability of phenyl silicones in this application is unknown as there are significant gaps in the available literature:

1) All prior work has utilized carbon-carbon crosslinking chemistry.
2) The gas permeation has not been explored as a function of radiation exposure.
3) All prior work retained the original catalyst, which lowered the radiation stability.

Approach

Silicone elastomers are traditionally synthesized as an oligomeric oil, terminated with cross-linkable vinyl moieties. These vinyl moieties convert to C-C bonds, which represent radiological weaknesses in the molecular structure. However, without these groups, the crosslinking occurs through removal of water, which must permeate through the elastomer during curing. This can induce voids and defects. Therefore, the first step of the project was to develop a tunable synthesis methodology that enables crosslinking without vinyl groups. In FY23, a novel synthesis method was developed in which silanol precursors were reacted with a volatile tin catalyst to generate the phenyl silicone elastomers with no residual C-C crosslinks or residual catalyst (**Figure 1**).

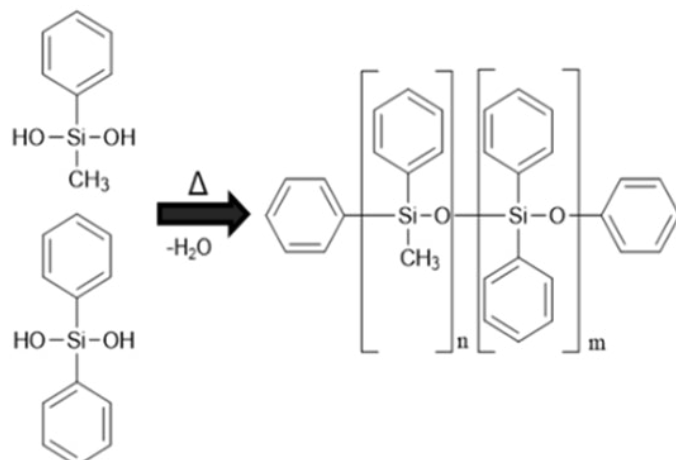**Figure 1.** Synthesis of phenyl silicone elastomer. Catalyst is a volatile organic tin salt.

In FY24, a series of phenyl silicone elastomers with varying crosslinker and phenyl contents were prepared. It was discovered that 2 mol% crosslinking enabled elastomers with 33-75 mol% phenyl content. These samples were cut into strips (for mechanical testing) and disks (for permeation testing), then exposed to extremely

high doses of gamma radiation in air (photographs shown in **Figure 2**). Initial exposures in FY23 demonstrated that 1 MGy exposures did not induce any changes in test samples, so extremely high doses were required in FY24, causing significant delays.

Samples were irradiated up to 6.2 MGy via a Co-60 source in air. After irradiation, the control and irradiated samples were characterized via dynamic mechanical analysis (DMA), dynamic scanning calorimetry (DSC), FTIR spectroscopy, gel fraction in acetone, and tensile testing (**Figures 3-6**). Additionally, the hydrogen permeability of the samples was measured in an SRNL custom-built permeation manifold (**Table 1**).

Figure 2. Photograph of 75 mol% phenyl silicone elastomer, unexposed and after 6.2 MGy of gamma radiation in air. The change in color is likely due to oxidation.
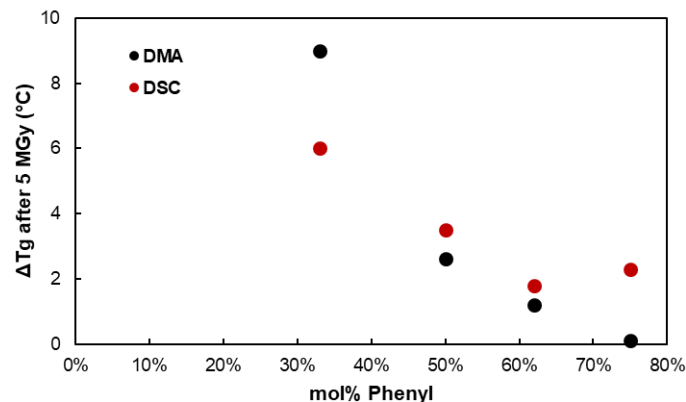
Figure 4. Change in glass transition temperature of phenyl silicone elastomers after 5 MGy gamma irradiation as measured by the inflection of heat flow in DSC and the peak of the tan delta in DMA. 75% phenyl DMA is taken at the second peak in DMA.

Sample Name	Argon Permeability	
50% Control	1.51E-10	*mol/m*s*MPa*
50% after 6.2 MGy	8.59E-11	*mol/m*s*MPa*
% Difference	*43%*	
62% Control	1.51E-10	*mol/m*s*MPa*
62% after 5 MGy	1.45E-10	*mol/m*s*MPa*
% Difference	*4%*	
75% Control	3.85E-11	*mol/m*s*MPa*
75% After 5 MGy	5.01E-11	*mol/m*s*MPa*
% Difference	*-30%*	

Table 1. Argon permeability of phenyl silicone elastomers after gamma irradiation.

Figure 3. FTIR spectra of phenyl silicone elastomers (33-75 mol%) before and after 6.2 MGy of gamma radiation. Spectra are offset.

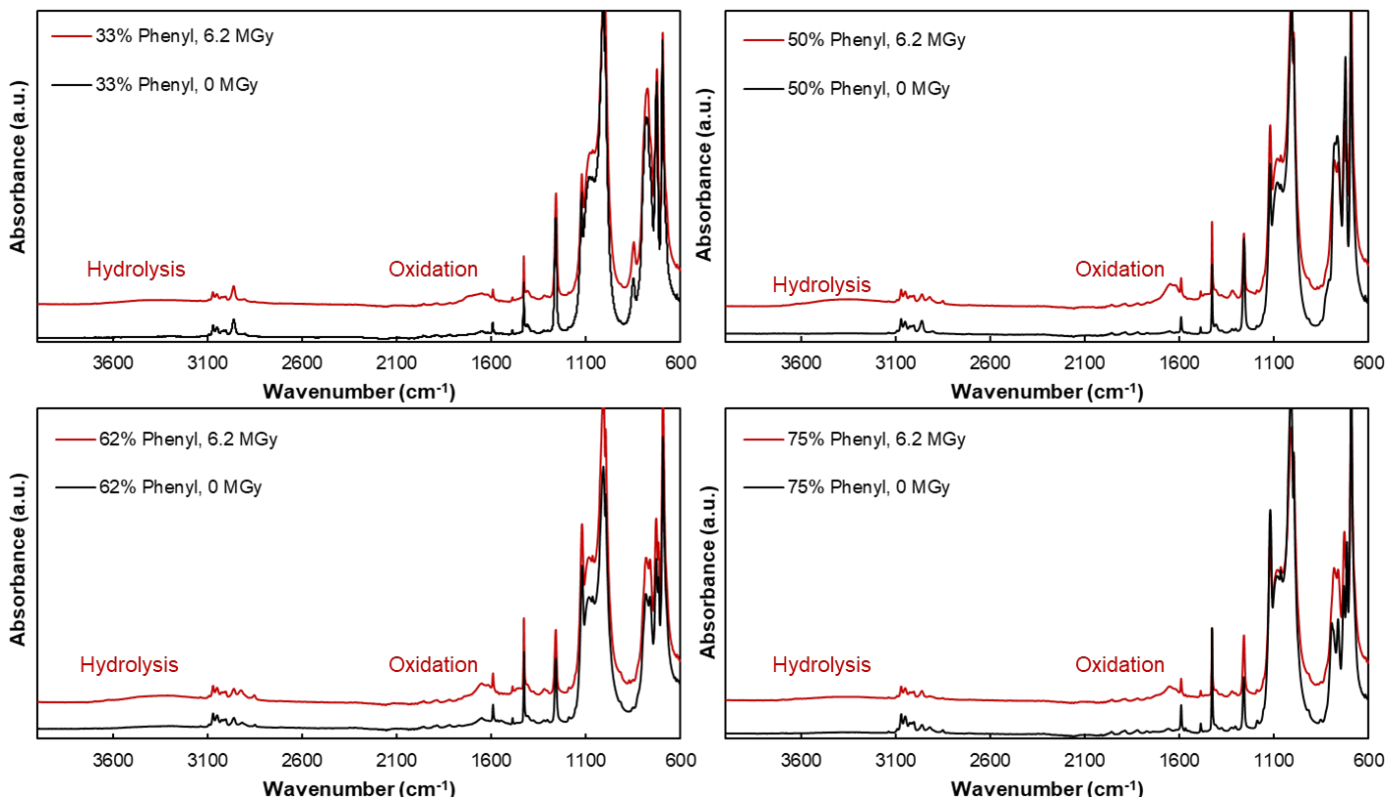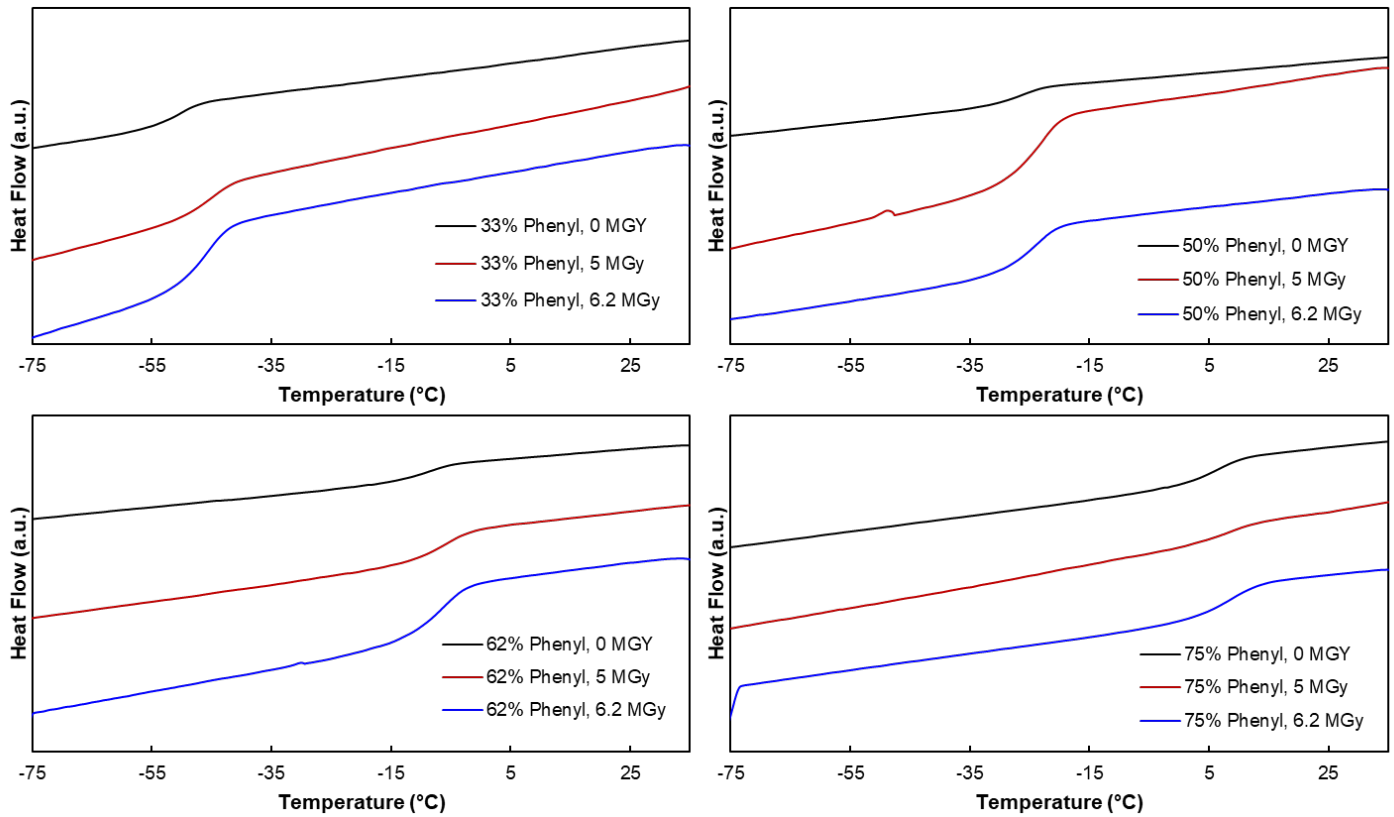**Figure 5.** DSC traces of phenyl silicone elastomers before and after 5 and 6.2 MGy of gamma radiation
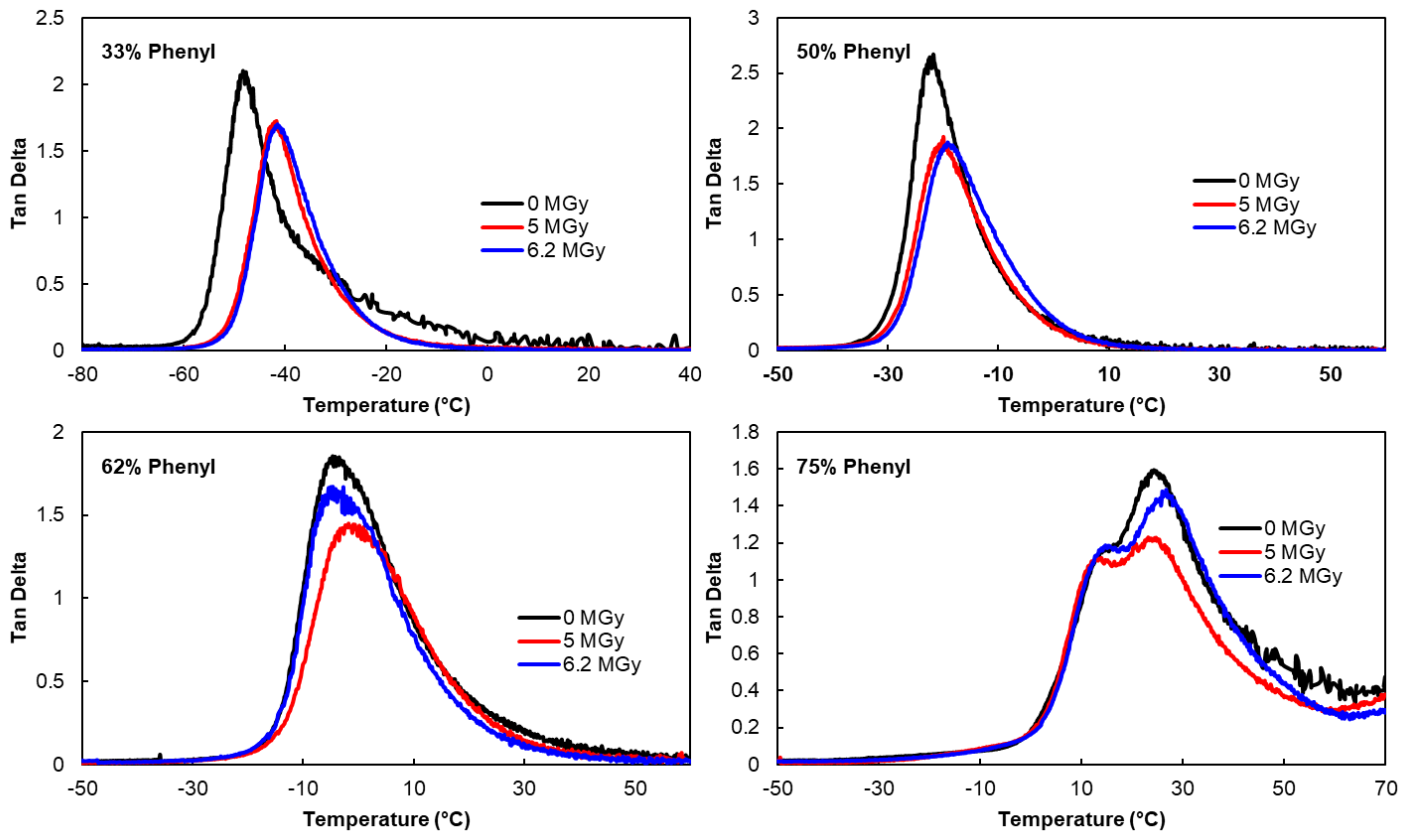

Figure 6. Tan delta (ratio of loss to storage modulus) as a function of temperature, as measured by DMA, of phenyl silicone elastomers before and after 5 and 6.2 MGy of gamma radiation.

Accomplishments

- Synthesized phenyl silicone elastomers of varying crosslinker content and phenyl content from silanol monomers.
- Exposed three sets of phenyl silicones elastomers to high doses of gamma radiation (up to 6.2 MGy)
- Performed wide variety of thermomechanical analysis on samples.
- Increasing phenyl content correlated with greater radiation resistance, as measured by DMA and DSC.
- The glass transition temperature increased with increasing radiation dosage. However, the 62 mol% and 75% mol phenyl elastomers showed very little thermomechanical change after a 6.2 MGy irradiation.
- SRNL hypothesizes that the elastomers oxidized during gamma radiation, both from the color change and from the appearance of a peak at 1680 cm^{-1} in FTIR.
- Performed argon and hydrogen permeation testing on samples.
- H_2 and argon permeation of samples was modified by gamma irradiation. Lower phenyl content resulted in increased argon permeability after exposure. High phenyl content resulted in decreased argon permeability after exposure.

- Phenyl silicone elastomers have much lower hydrogen permeability than conventional silicones (5.0×10^{-9} vs 120×10^{-9} mol/(m s MPa) for 62% phenyl vs 0% phenyl).
- Permeability testing is ongoing.
- Demonstrated that these elastomers are highly radiation tolerant compared to traditional radiation tolerant elastomers.
- Commercial unfilled elastomers never rated above 1 MGy.
- Filed invention disclosure and provisional patent on novel synthesis.
-

Intellectual Property

Invention Disclosures
- SRS-23-001

Patent Applications
- US Patent Application 63/500,743

Team Members

Lauren Hanna, Chris Verst, George Larsen, Dale Hitchcock, Anastasia Mullins, Gavin Mattingly

References

1. Clark, E.A., Shanahan, K. L. . Effects of Tritium on UHMW-PE, PTFE, and Vespel [registered trademark] Polyimide. *Fusion Sci. Technol.* **2007,** *52,* 1007-1011.
2. Palsule, A. S., Clarson, S. J. & Widenhouse, C. W. Gamma irradiation of silicones. *J. Inorg. Organomet. Polym. Mater.* **2008,** *29,* 207-221.
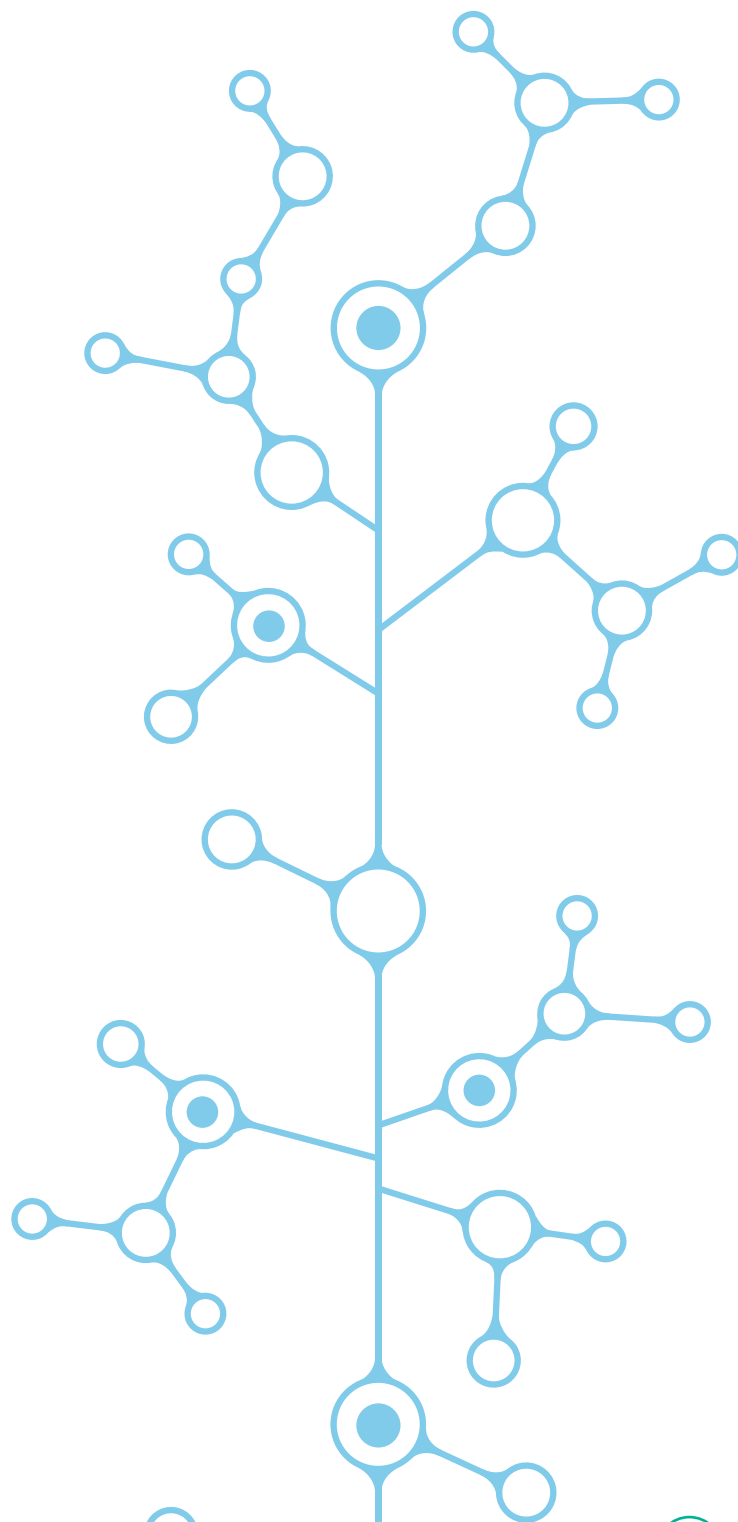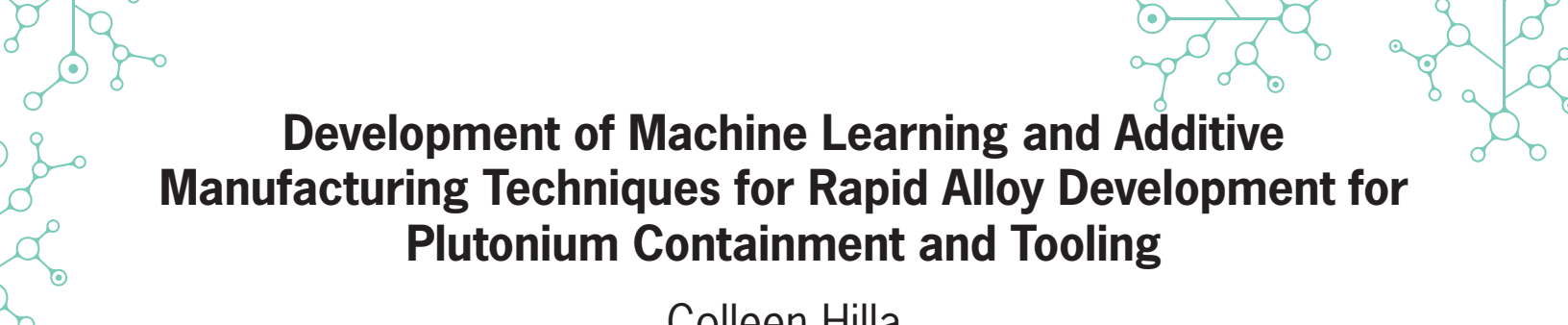
Development of Machine Learning and Additive Manufacturing Techniques for Rapid Alloy Development for Plutonium Containment and Tooling

Colleen Hilla

This project is developing and testing a framework that allows evaluation of new materials much more efficiently both in terms of time and cost by coupling machine learning with 3D printing methods. This process will enable the fabrication of parts with reduced lead times and superior mechanical and chemical properties.

Introduction

Refractory materials, such as tungsten and tantalum, have a high melting temperature and high tensile strength, which is ideal for high temperature and harsh environment applications. However, they can be difficult to manufacture both in terms of welding and machining. This makes them an interesting candidate for additive manufacturing (AM) through which the processing steps are reduced. Additionally, poor ductility, corrosion and oxidation behavior is seen in many refractory materials. Alloy development may allow for materials with comparable strength and thermal behavior with improved toughness and chemical behavior. Laser directed energy deposition (DED) is an AM method that can utilize multiple powder hoppers. This allows for location-specific compositional changes and subsequently multiple different alloys to be produced and tested in a single build. This is a promising tool for high-throughput material development. However, this can still be an expensive process. Therefore, material modeling is employed to down select possible compositions and allow for the testing of materials with a high likelihood of success. Initial modeling data were used to screen for potential alloy candidates for the first round of testing. Various novel alloys were fabricated. These alloys have promising characteristics for various applications, the primary focus being nuclear material processing. Printed alloys have also been used for model validation and resultant data will be used for training of a neural network to create a responsive alloy development loop. This will allow for more rapid alloy development for refractory materials for this and future applications.

Approach

The overall approach of this work had two tenants. The first was a printing effort that focuses on parameter development and alloy testing. The second tenant was modeling, which focused on material selection. Initial parameter development was completed on pure tantalum, which provided a baseline parameter set for alloy printing. The pure tantalum also provided a point of comparison for alloy analysis and testing. Forty-two parameter sets were tested across two DED machines to develop a machine agnostic processing window. Laser power, scan speed, and powder flow rate were varied. Initial material modeling utilized a Calphad materials modeling approach coupled with first principle models. Using these varied approaches, 15 properties were compiled ranging from microstructure to mechanical behavior. Modeling data were used for alloy screening and selection. The effect of alloying elements on melting temperature is shown in **figure 1**. Twelve alloys were selected for the initial round of alloy testing, based on composition, melting temperature, and corrosion behavior. Sample composition, oxidation behavior, and hardness were analyzed for all samples. Composition and property data were used for model validation and were collected for future machine learning work. These experimental data were compiled with calibrated model data and literature data. This larger data set includes 3000 refractory alloys that have provided the initial training sets for a neural network that will employ supervised learning. Additional corrosion and mechanical behaviors are being tested. These properties will be included in a subsequent iteration of the neural network.
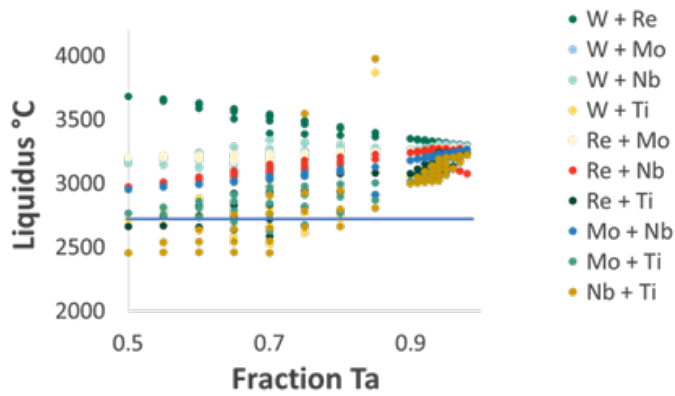
Figure 1. Effect of alloying of Tantalum on melting temperature

Accomplishments

- Parameter processing window was mapped through the testing of 42 processing parameters across two DED systems. Optimal parameters were identified for tantalum and tantalum heavy alloys.
- Material modeling was completed for 885 alloys, from which 39 were selected as candidate alloys.
- Twelve of the candidate alloys were fabricated and tested for microstructure, oxidation behavior and hardness. Seven showed minimal cracking, increased hardness compared to pure tantalum and a reduction in oxide precipitation. Example microstructures are shown in **figure 2**.
- Alloy data for 3000 refractory materials were compiled for machine learning.

Peer-reviewed Publication

- Hilla, C.; Ayers, T.; Dinda, G.; Mcclane, D. Effect of Directed Energy Deposition Process Parameter on Build Quality of Tantalum. *Prog Addit Manuf, Submitted May 29, 2024*

Team Members

Tatiana Ayers, Guru Dinda

Figure 2. Alloy microstructures

Evaluation of Electromagnetic Pulse Shielding Polymers from First Principles

Joshua Kleppinger

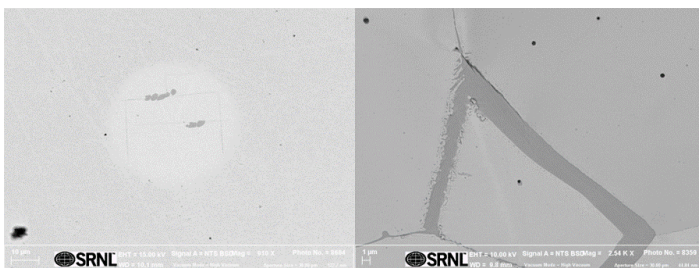Polymer materials are of growing interest for electromagnetic shielding applications due to their flexibility, ease of processing, high corrosion resistance, and low weight. This work developed simulation models to evaluate the shielding capabilities of select polymers as a first step towards developing polymer shielding at SRNL.

Introduction

Electromagnetic pulses (EMPs) are a specific class of high-power electromagnetic interference (EMI) that can damage sensitive electronics. EMI can be easily blocked with bulky metal enclosures, but these can be prohibitively expensive to manufacture and degrade over time due to corrosion, limiting their use predominantly to military and government applications. For these reasons, there has been growing interest in developing electromagnetic interference (EMI) shields based on polymer materials due to their inherent flexibility, low weight, high corrosion-resistance, and ease to process compared to traditional metal-based enclosures.[1]

As shown in **Figure 1 (a)**, EMI can be shielded through two mechanisms: reflection and absorption (as heat). Good conductors excel at reflection and absorption over the entire energy spectrum but will also block non-EMP frequencies. For a more tailored approach, an option worth considering is ferroelectric materials such as polyvinylidene fluoride (PVDF) polymers, which have been shown to demonstrate substantial dielectric loss in the 1-100 MHz range (a similar range to the E1 pulse).[2, 3] These materials have internal polarization and a semicrystalline structure that allow for a slow acting dipolar component to the dielectric function, producing a spike in lossy-ness well below the typical THz and UV-Vis range (**Figure 1 (b)**).
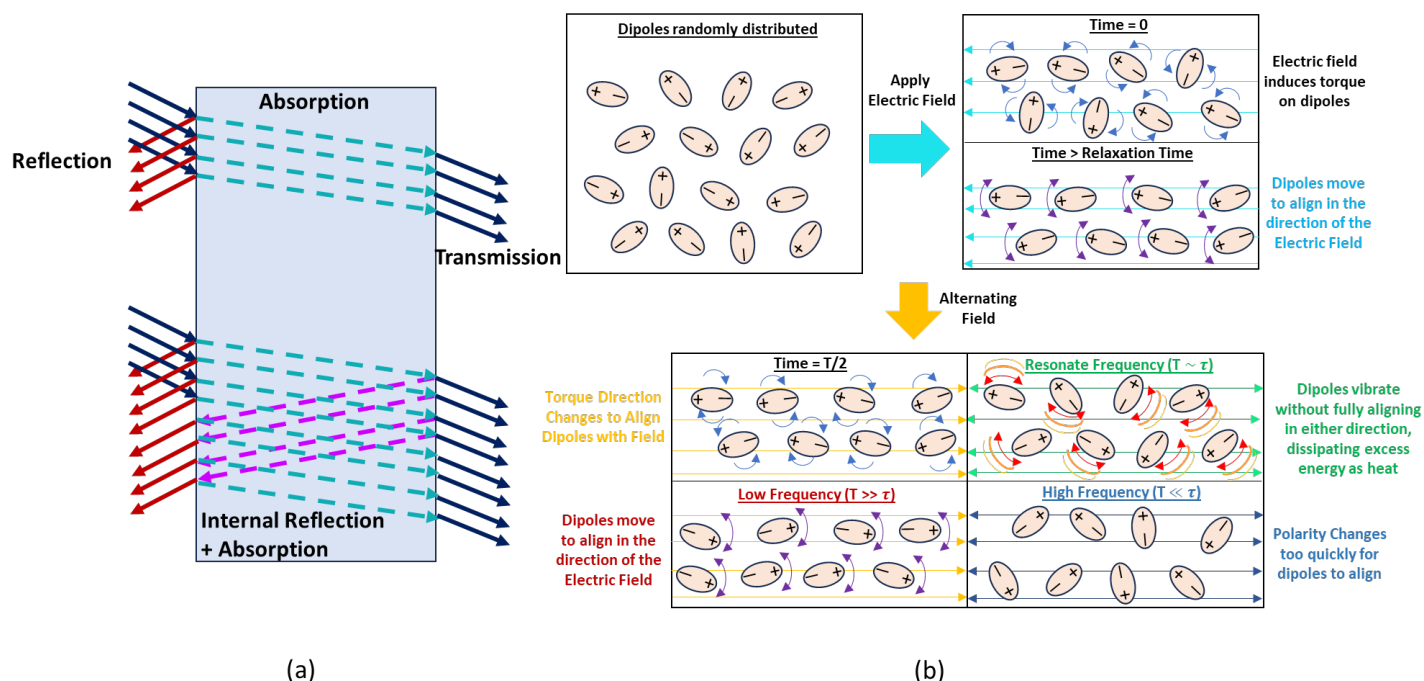
Figure 1. (a) Diagram demonstrating the shielding mechanisms of conductors and lossy dielectrics. Electromagnetic waves can be blocked by reflecting them off the surface, absorbing them as heat internally, or some combination with multiple internal reflections. (b) Schematic of spontaneous polarization in materials with fixed dipole moments. The electric field induces a torque on individual dipoles, forcing them to rotate to align with the electric field; however, the rate at which they can align is limited by their moment of inertia, causing them to become unresponsive at high frequencies.

This work developed a proof-of-concept simulation model based on density functional theory for evaluating the EMP shielding potential of both conductive and ferroelectric polymers and applied these models to well established polymer/polymer families that could be used for evaluating and identifying new materials in the future.

Approach

The project first selected two families of polymers for both categories of electronic medium—Polypyrrole (PPy) (**Figure 2 (a)**) and Polyaniline (PANI) for conductive polymers and Polytetrafluoroethylene (PTFE) and PVDF (**Fig. 3 (a)**) for ferroelectric polymers—and modelled their structure and their crystal phases as infinite chains along the c-axis. For medium, hybrid density functional theory (DFT) calculations were performed using HSE06 pseudopotentials in VASP to relax the geometry and calculate the high frequency (>THz) ionic (via DFPT) and electronic (conduction band states method) components

of the dielectric functions. For conductive polymers, the dielectric functions were then augmented by introducing the conductivity obtained simultaneously via hybrid functional DFT with the electronic dielectric functions and extended to low frequencies via Drude model (**Figures 2 (b) and (c)**).

By ferroelectric polymers, the fixed transverse dipole moment was first calculated for an individual chain based on the modern theory of polarization in VASP.[4] To predict how a collection of randomly distributed transverse dipoles may react to an electric field, 10,000 rotations of the polymer chains and dipole moments were generated in cartesian space such that the average dipole moment summed to zero. As shown in **Figure 3 (b)**, a sinusoidal time was simulated varying electric field in the x-direction, inducing a chain axis torque on the fixed dipoles causing them to rotate. The dielectric functions were then calculated from ratio between the electric field amplitude and average polarization amplitudes. The imaginary part was determined from the polarization power loss.
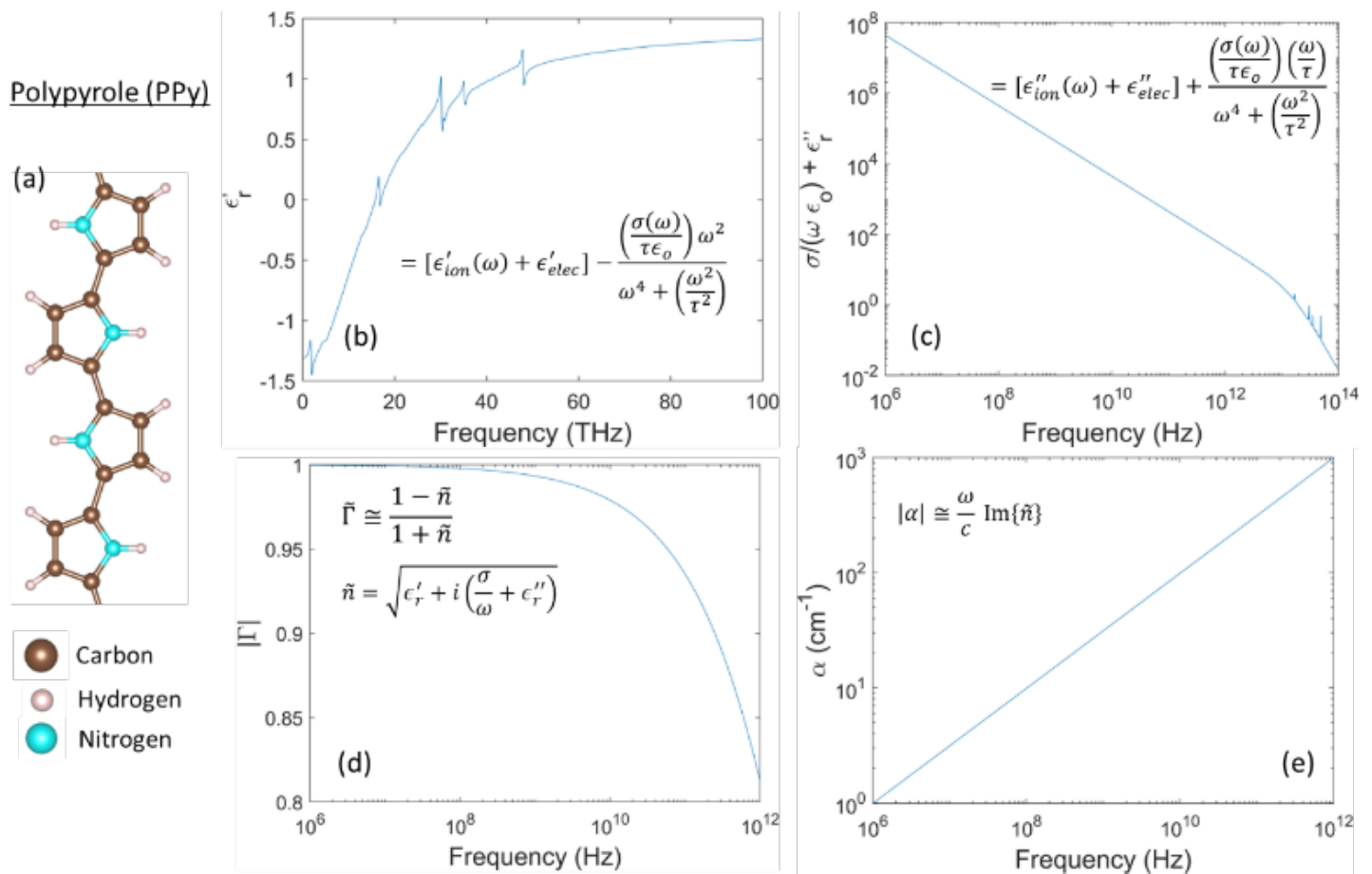
Figure 2. (a) Crystalline structure of an infinite PPy chain and its (b) real and (c) imaginary dielectric functions. The real and imaginary parts are modified from the DFPT ionic and HSE06 electronic dielectric functions to incorporate the Drude model's conductivity correction. The electron scattering time τ is set to a typical value of 10^{-14} sec. (d) Reflection coefficient for normal incidence and (e) attenuation coefficients as functions of wave frequency.
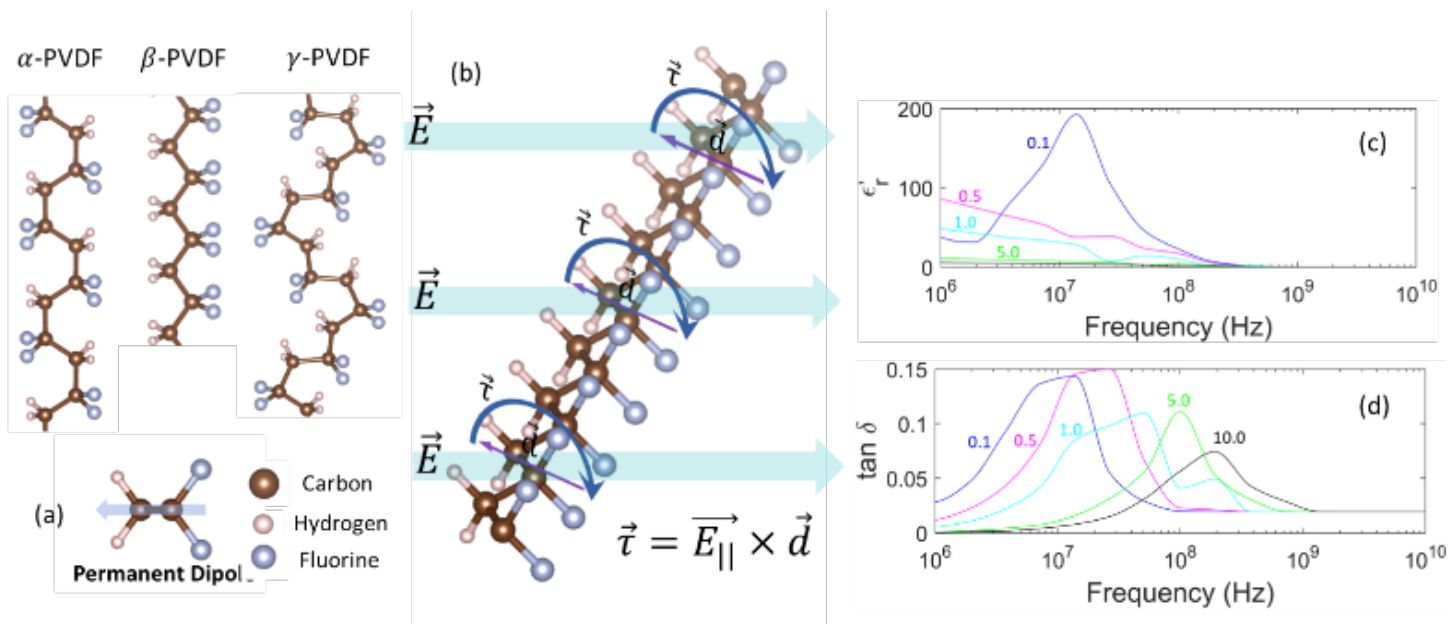
Figure 3. (a) Crystalline structure of a PVDF chains in the α, β, and γ phase. The ferroelectric β phase exhibits a strong transverse dipole moment orientated from the C-F to C-H dimers. (b) Schematic demonstrating how the electric field induces a rotation along the chain length for an individual polymer chain. (c) Real part of the dielectric function and (d) loss tangent as a function of frequency at fixed electric field magnitudes (given in V/cm). Note that the dielectric functions are scaled such that only a portion of segments have free movement to respond to an electric field and that the magnitude of the permittivity highly depends on the phase composition and orientation of the chains during manufacturing.

Accomplishments

- Developed models for evaluating the low frequency (<THz) reflectivity and absorption coefficients for conductive polymers based on density functional theory calculations and evaluated them using PPy and PANI polymers.
- Undoped PPy maintains high reflectivity ($\Gamma \cong 1$) up until 100 MHz (**Fig. 2 (d)**). The absorption length of non-reflected waves is on the order of cm-mm until the GHz frequency range.
- Developed a model for predicting the dielectric properties of ferroelectric polymers with fixed orientational dipole moments and evaluated it using PVDF and PTFE polymers at varying frequencies and amplitudes of incident waves. In general, amplitude is something that is not considered in experimental evaluation of the dielectric properties but is inherent in the torque induced on the fixed dipoles.
- (**Figure 3 (c)**) Simulations show that for β-PVDF, the real dielectric function is suppressed at higher amplitudes. This is an overshooting effect where the force is strong enough to cause dipoles to spin rather than oscillate.
- (**Figure 3 (d)**) The position of the peak $\tan \delta$ for 0.1 and 0.5 V/cm matches with the position of the experimental loss peaks in PVDF.[2, 3] At higher amplitudes, the peak shifts to the right indicating that the material can be used to filter waveforms based on both amplitude and frequency.

References

1. Maruthi, N.; Faisal, M.; Raghavendra, N. Conducting polymer based composites as efficient EMI shielding materials: A comprehensive review and future prospects. *Synthetic Metals* **2021**, *272*, 116664. DOI: https://doi.org/10.1016/j.synthmet.2020.116664.
2. Khanchaitit, P.; Han, K.; Gadinski, M. R.; Li, Q.; Wang, Q. Ferroelectric polymer networks with high energy density and improved discharged efficiency for dielectric energy storage. *Nature Communications* **2013**, *4* (1), 2845. DOI: 10.1038/ncomms3845.
3. Meng, N.; Ren, X.; Zhu, X.; Wu, J.; Yang, B.; Gao, F.; Zhang, H.; Liao, Y.; Bilotti, E.; Reece, M. J.; et al. Multiscale understanding of electric polarization in poly(vinylidene fluoride)-based ferroelectric polymers. *Journal of Materials Chemistry C* **2020**, *8* (46), 16436-16442, 10.1039/D0TC04310A. DOI: 10.1039/D0TC04310A.
4. Spaldin, N. A. A beginner's guide to the modern theory of polarization. *Journal of Solid State Chemistry* **2012**, *195*, 2-10. DOI: https://doi.org/10.1016/j.jssc.2012.05.010.

Synthesizing, Compounding, and Characterizing a Heat Labile Foam

Mark Kranjc

A novel azo diol and polycarbonate polyols were synthesized and mixed as a part A (isocyanate component) and part B (polyol component also containing water as a foaming agent, and a silicone surfactant) to form rigid polyurethane foams with densities of approximately 160 kg/m³ (10 lbs/ft³).

Introduction

Shipment of certain Low Level Waste (LLW) items occurs in standard cargo containers. [1], [2] Workers wearing the proper protective clothing are expected to secure the load by closely packing items, use of strapping, or in a few cases building scaffolding to hold in place. The latter is shown in **Figure 1**.

Figure 1. Scaffolding holding in place a container containing low level waste items within a shipping cargo container.

This project would develop a polyurethane (PU) foam that could be injected into the closed container from outside the container using Foam-In-Place techniques. Once the shipping container reaches the destination the foam would be removed by heating to temperatures around 100° C. The foam will decompose from a solid to mostly gaseous reaction products due to novel polyol components that have been synthesized and used to form the solid PU foam.

This work initially began with a short-term (10 week) Visiting Faculty Program (VFP) in 2021; the idea was

presented to the IP Committee, and a US Patent Application Publication was generated. [3] The review process with the USPTO is pending. The primary objectives for this project are to attain As Low As Reasonably Achievable (ALARA, DOE Policy [4]) levels of radioactivity as well as potentially reduce cost. Instead of operators securing the load from within the cargo container, operators secure the load by pumping and mixing a part A and part B while outside the cargo container. The part A and part B will react and Foam-In-Place within the container. The cargo container provides shielding that reduces radiation exposure to zero outside the container walls.

Approach

The general approach taken in Year 1 (FY2024) was to synthesize novel polyols as well as purchase off the shelf polyols that were used as a part B component to react with the isocyanate of a part A component and create rigid PU foams. The general chemical reactions that occurred while generating the foam are shown in **Figure 2**.
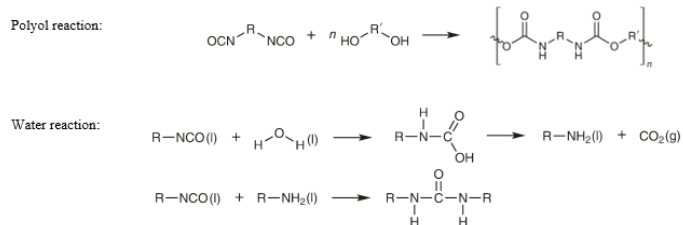

Figure 2. General reactions of isocyanate in part A with polyol and water in part B.

The objective is to produce a PU foam that will convert from solid to mostly gas (<15% by weight solids remaining) when heated at temperatures around 100°C upon arrival at the destination. In addition, test methods were developed for characterization. These tests include

impact strength testing (ASTM D1596) using a newly purchased Instron Model 9450 Impact System, TGA testing using a Mettler Toledo TGA 2, and 3D Imaging of thin sample cross sections to confirm closed cell structure (ASTM D3576) of foam with the Keyence VHX-6000 Digital Microscope. Finite Element Analysis (FEA) was also performed in Year 1 to determine what the criterion would be for the minimum impact strength of these foams.

SRNL has been accumulating chemical structures of potential components of the part A and part B using CAS #s. Moving forward in Year 2, chemical structure – physical property relationships can be determined that would assist in selecting and formulating components of the Foam-In-Place PU that would meet and exceed requirements. Examples include synthesize additional moieties in those polyols already synthesized that make them more susceptible to catalyzed degradation reactions and increasing or decreasing crosslink density to obtain maximum impact strength.

Accomplishments

- Two versions of polypropylene carbonate (PPC) were purchased, an azo containing diol (AZO) were synthesized, and polycarbonate polyols (PC) were synthesized; the chemical structures are shown in **Figure 3**. Details of the synthesis performed are given in the paper cited in the Peer-reviewed Publications section.
- Samples of these polyols were mixed in a part B compound along with a foaming agent (water) and silicone surfactant (Gelest silicone). The part A isocyanate used was from an off the shelf rigid PU foam available (Foam-iT) that contains two isocyanates: MDI and a branched PMDI; the chemical structures are shown in **Figure 4**. The part A and part B were mixed to form the rigid polyurethane foams, one sample is shown in **Figure 5**.
- FEA was completed and has established that the minimum impact strength requirement for the foam to secure loads in a cargo container should be in the range of 0.30 to 0.75 MPa. [5] The following conditions apply:
- Design was per Code of Federal Regulations, 49 CFR 393.102, 2024.
- Analysis done for worst case scenario of large length/weight ratio and high internal density of 7.85 g/cm^3 (steel). See **Figure 6**.
- Targeted foam density range is 48 to 80 kg/m^3 (3 to 5 lbs/ft^3, pcf). These low densities can provide a cost savings.

- Gravitational (G) Force requirements are 8G in the forward direction, 0.5G in the lateral direction and 1G between items in the cargo container.
- This was the first time BSRA/SRNL/USC Aiken has synthesized polyols and formulated part A and part B components to produce a rigid polyurethane foam for potential use at the Savannah River Site and other sites in the DOE complex. These science and engineering methodologies could be used for creating other polyurethane foams with unique properties in future applications (e.g., decontamination and decommissioning).
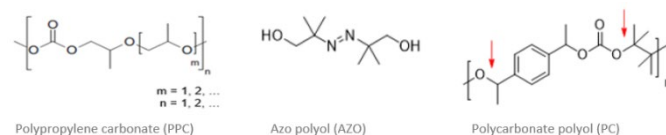

Figure 3. Polyols used in the part B portion of a foam in place rigid PU foam. The PPC was purchased off the shelf and the AZO and PC were synthesized in FY24.
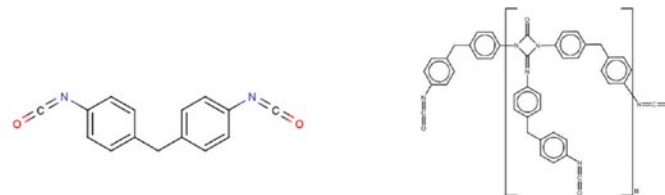
Figure 4. Part B isocyanates used to create foam with synthesized novel polyols in Year 1. On the left is MDI (4,4'-Methylenediphenyl diisocyanate or 4,4' MDI, CAS #101-68-8) and on the right is a branched version of PMDI (Benzene, 1,1'-methylenebis[4-isocyanato-] homopolymer or Polymeric MDI, CAS #325686-28-6)

Peer-reviewed Publication

- Kranjc, M.; Marshall N.; McKeel C.; Murrell, C.; Osborne M. Synthesizing, Compounding, and Characterizing a Heat Labile Polyurethane Foam. In 2024 Center for the Polyurethane Industry (CPI) Polyurethane Technical Conference Proceedings, Atlanta, USA, September 30 – October 2, 2024.

Intellectual Property

Patent Application

- Ketuskey, E.; Kranjc, M.; Shuler, J.; Marshall, N. Heat Labile Foam-In-Place Polyurethane Foam. US Patent Application Publication, No. US2024/0141127 A1. May 2, 2024.

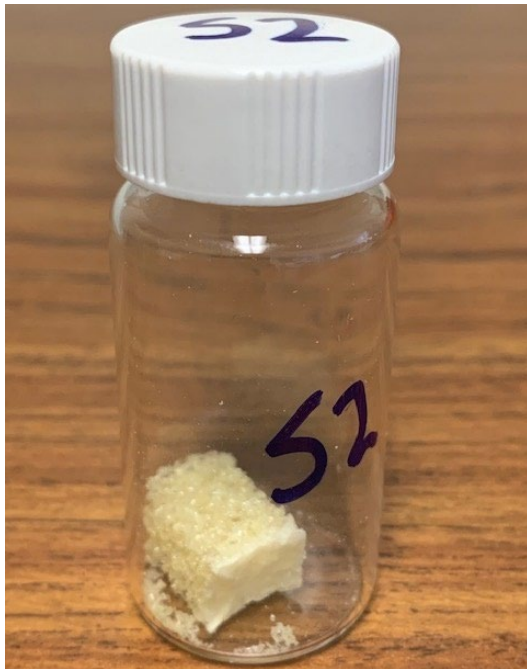**Figure 5.** Rigid PU foam created from polyols synthesized in FY24. Polyols were compounded into a part A component consisting of polyol, foaming agent (water), and surfactant (silicone). The part B isocyanate came from a typical off the shelf rigid polyurethane foam (FOAM-iT)

Team Members

Nicholas Marshall[a], Connor Murrell, Charles McKeel, Matthew Osborne, Matthew Hamm, Larry Fuetral, Camden Chatham, Cade Willis, Haley Jones[*]

[a] University of South Carolina, Aiken
[*] Postdoctoral Researcher

References

1. 49 CFR 173.433, 2024.
2. 49 CFR 173.435, 2024.
3. US Patent Application Publication No. 2024/0141127 A1, published May 2, 2024.
4. DOE-HDBK-1215-2014, *Optimizing Radiation Protection of the Public and the Environment*, for use with DOE O 458.1, ALARA Requirements, 2022
5. McKeel, C.; *Structural Performance of Container Securements using Foam-In-Place Methods*, Calculation M-CLC-A-00768, 2024.
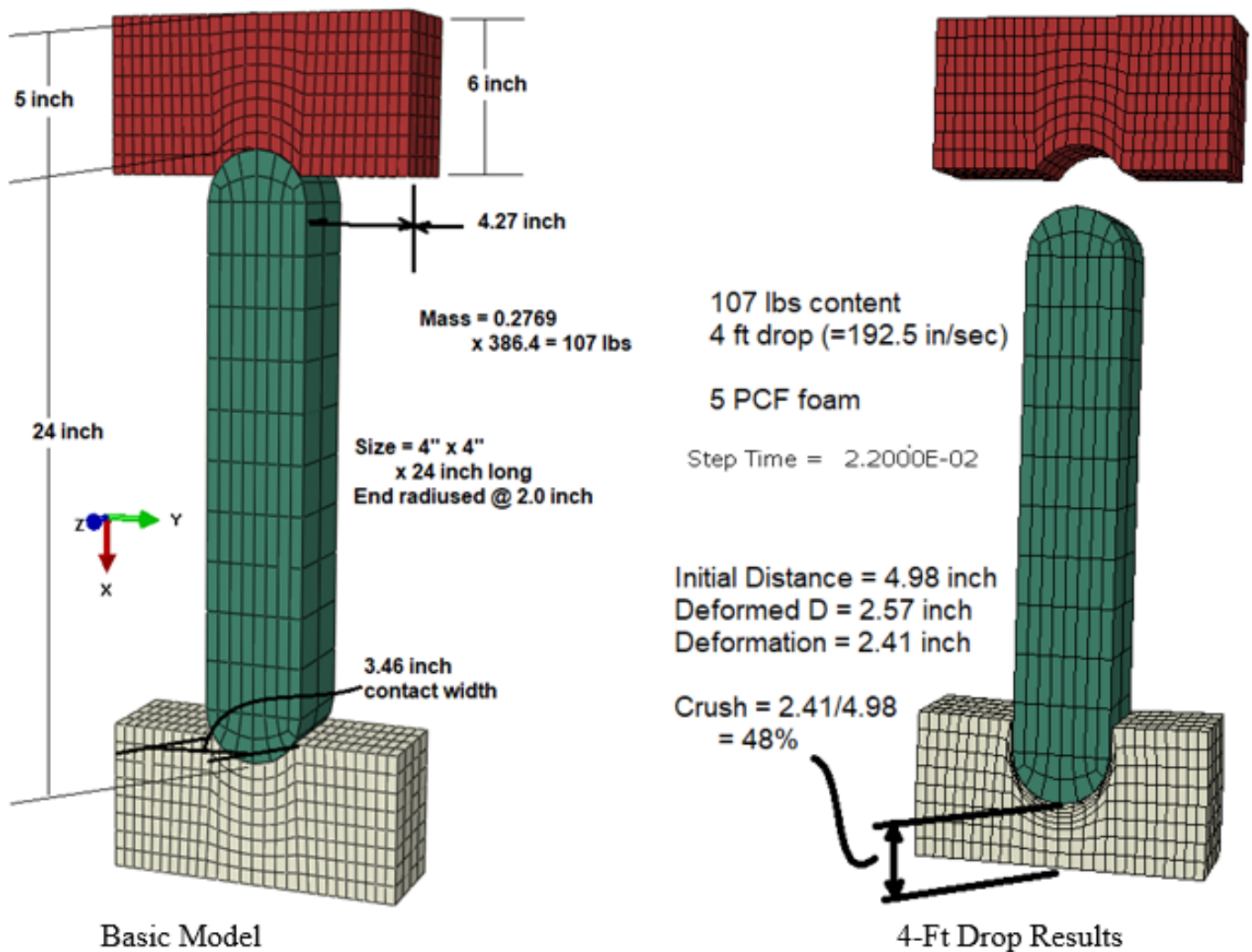
Figure 6. Finite Element Model of Foam-In-Place Content Securement Used for Shipping Container Drop Conditions.

Upgrading Landfill Produced Biogas Using Microbial Electrolysis Cell

Nathaniel Losey

Methane produced from the landfills can be utilized as a renewable energy source for electricity generation and heating. This process is driven by the decomposition of organic matter by oxygen-sensitive microorganisms. The objective of this project was to investigate mechanisms for stimulating electroactive microorganisms involved in methane production from landfill leachate.

Introduction

Landfills produce large amounts of methane from the breakdown of organic material by microbially-driven anaerobic decomposition. Landfills will either flare this methane to prevent its release as a potent greenhouse gas, or in other cases will collect the methane as a component of landfill gas and distribute it for industrial uses such as heating or electricity generation.[1] A major challenge in this process is the cleanup and removal of contaminant gases from this landfill gas. Landfill gas with a higher percentage of methane may be more amenable to cleanup and suitable for transport and downstream industrial purposes.

This project investigated strategies shown to enhance microbially-driven anaerobic decomposition in other settings such as in wastewater treatment plants or using anaerobic digestor sludge. Specifically, strategies related to enhancing the microbial activity of electroactive microorganisms that engage in direct interspecies electron transfer. Studies have shown that addition of semi-conductive materials such as granular activated charcoal, iron minerals (magnetite) or reduced carbon materials (such as carbon fiber or carbon nanotubes) can result in markedly higher methane production rates and concentrations.[2] Alternatively, microbial electrolysis cells have also demonstrated increases in methane production rates and yields. Successful demonstration of lab-scale processes for increasing methane production rates and yields could serve as the basis for designing large-scale units for enhancing methane production from landfill leachate.

Approach

Landfill leachate was collected from the Three Rivers Landfill located on the Savannah River Site in coordination with the Three Rivers Solid Waste Authority (**Figure 1**). Microorganisms involved in anaerobic decomposition in the landfill environment are extremely oxygen sensitive and require experimental setups that exclude oxygen. An Anaerobic Coy Chamber was employed to provide an oxygen-free environment for experimental manipulations (**Figure 2**). The experimental approach was to employ techniques to enhance growth of electroactive microorganisms by addition of semi-conductive materials and, in future testing, electrolysis cells of varying scale. Small bottles with butyl rubber stoppers were filled with small amounts of sediment and landfill leachate and were incubated in the presence of semiconductive materials including granular activated charcoal and iron minerals. Methane concentrations were determined after a four-week period using a photoacoustic spectrometer.

Figure 1. Leachate Collection Basin, Three Rivers Landfill.

Figure 2. Testing Setup for Landfill Leachate. Left, Anaerobic Coy chamber for anoxic manipulations of microbes. Top right, Incubations of Landfill leachate with granular activated charcoal. Bottom right, electrolysis cell for future testing.

Accomplishments

- Landfill leachate was collected from the Three Rivers Landfill and briefly characterized.
- To facilitate cultivation of anaerobic microorganisms a Coy Anaerobic Chamber was set up and cleared for use. An initial base case run was performed using landfill leachate with and without amendments of granular activated charcoal over a four-week period.

Team Member

Junhua Jiang

References

1. US-EPA *AN OVERVIEW OF RENEWABLE NATURAL GAS FROM BIOGAS*; 2020, 2020.
2. Cheng, Q.; Call, D. F., Hardwiring microbes via direct interspecies electron transfer: mechanisms and applications. *Environmental Science: Processes & Impacts* **2016,** *18* (8), 968-980.
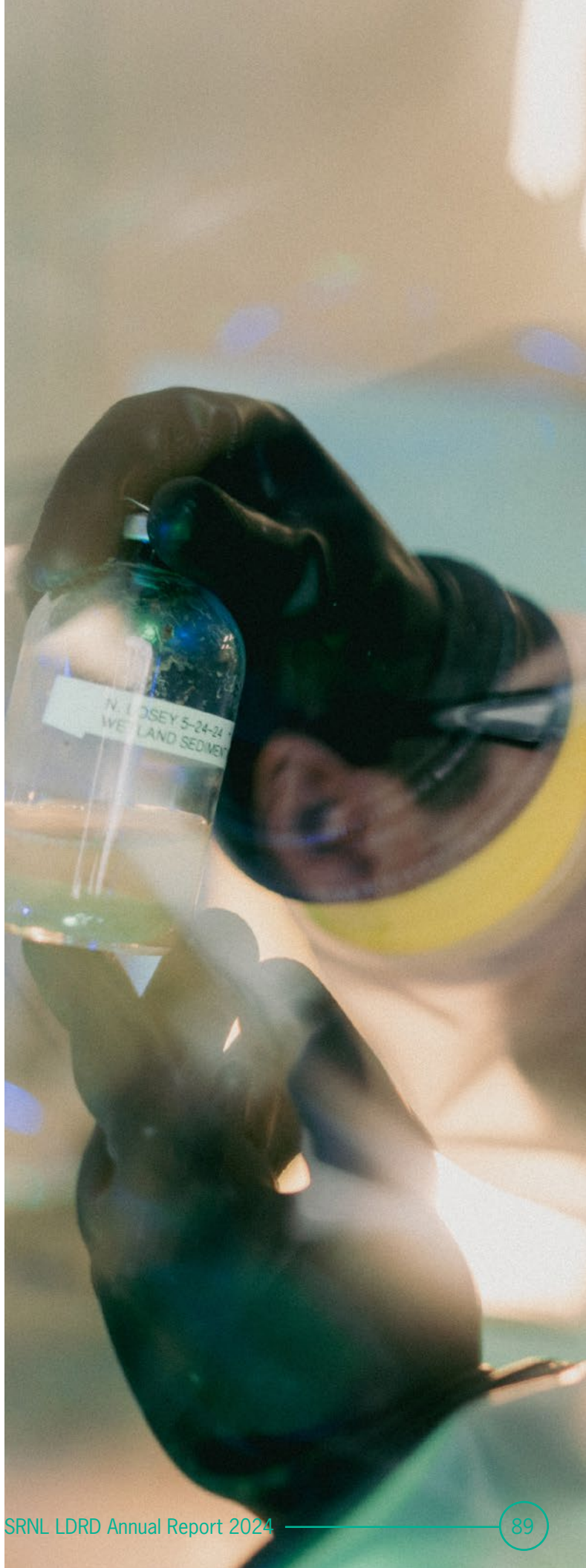
Synthesis and Characterization of Critical Material Free Permanent Magnets

Binod Rai

The goal of this proposal is to develop Critical Material-Free Permanent Magnets (CM-FPM) with high coercivity, remanence, and maximum energy product ((BH)max). By synthesizing and characterizing candidate materials, we aim to address the current challenges associated with critical material dependence.

Introduction

Permanent magnets are materials that generate their own magnetic fields, with the strongest known examples being "rare earth" magnets, such as neodymium magnets. Although these magnets contain only a small amount of the rare earth element neodymium, they are predominantly made of iron. Neodymium magnets are renowned for their exceptional field strength, which has led to their widespread use in the automotive, biomedical, defense, aerospace, and consumer electronics industries. However, the heavy reliance on neodymium has resulted in global shortages and significant price increases. This dependence on a critical material, predominantly mined in China, poses a serious risk to the U.S. economy, competitiveness, and technological advancement. China controls 61% of global rare earth element production, including neodymium. This proposal seeks to reduce our reliance on neodymium and other critical materials by developing and characterizing new CM-FPMs, thereby decreasing our dependence on foreign resources.
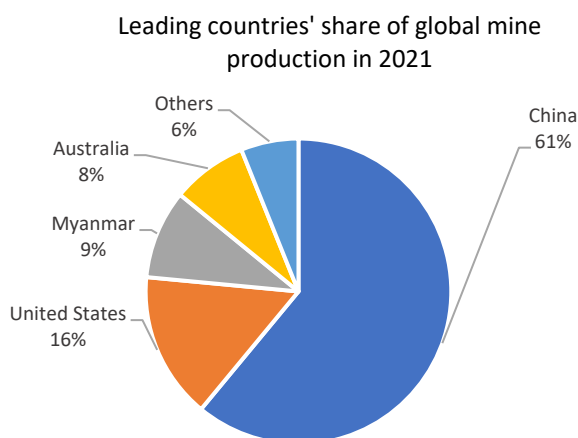

Figure 1. China dominates the rare earth mining industry, controlling nearly 61% of global mine production.

Approach

The approach focuses on identifying and synthesizing materials with high magnetocrystalline anisotropy and remanence, which are crucial for achieving an improved (BH)max in CM-FPMs. Coercivity will be optimized by tuning magnetocrystalline anisotropy, as well as by controlling particle and grain sizes. Additionally, aligning grains along the magnetic easy axis will enhance remanence. This proposal also seeks to discover ternary CM-FPMs with high coercivity, remanence, and (BH)max.

The design and development of new CM-FPMs will involve magnetic characterization using the Quantum Design Dynacool PPMS at SRNL. This capability allows us to synthesize and characterize magnetic samples entirely in-house.

Accomplishments

One manuscript draft in review, six presentations completed in FY24, and four summer interns mentored. The details are provided below:

- Alex Bretaña presented at the Citizens for Nuclear Technology Awareness Up and Atom Event on Oct. 3
- Alex Bretaña presented a poster at the 69th Annual American Vacuum Society Meeting
- Alex Bretaña attended and presented a poster at the 2024 6th US School on Total Scattering Analysis at Oak Ridge National Laboratory
- Alex Bretaña presented a poster at the 2024 SRNL Day at Georgia Tech
- Alex Bretaña presented a presentation at the L3330 Group Meeting – September 4, 2024
- Presented a poster at the 2024 LDRD Poster Session

- Procured new Thermogravimetric analyzer and remeasured the transition temperature of Yttrium substituted $Ce_2Fe_{14}B$ samples here at SRNL (see **Figure 2**)
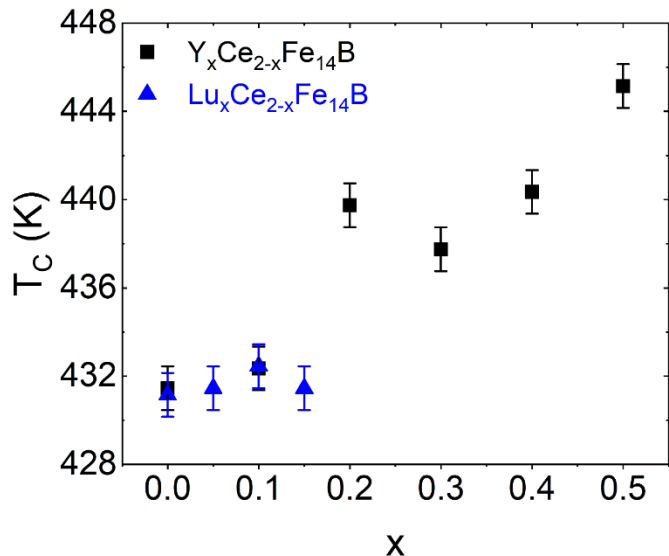

Figure 2. Curie temperatures as determined by TGA for annealed $Ce_2Fe_{14}B$, $(Lu_xCe_{2-x})Fe_{14}B$ (x=0.05, 0.1, 0.15), and $(Y_xCe_{2-x})Fe_{14}B$ (x=0.1, 0.2, 0.3, 0.4, 0.5) alloys.

- Alex Bretaña and Ben Conner visited collaborators at the University of South Carolina – Columbia and taught them how to prepare samples for anisotropic magnetic measurements
- Completed anisotropic magnetic measurements on Yttrium substituted $Ce_2Fe_{14}B$ samples (see **Figures 3 and 4**)
- Manuscript currently in review at the Journal of Allows and Compounds - on Lutetium and Yttrium – "Enhanced thermal stability and magnetic properties in Y substituted $Ce_2Fe_{14}B$"

Peer-reviewed Publications

- Bretaña, A., Housley, C., Ajo, H., Koenig, T., Conner, B. S., Ward, P. A., Greer, R., Morrison, G., zur Loye, H.C., Rai, B., Enhanced thermal stability and magnetic properties in Y substituted $Ce_2Fe_{14}B$, J. of Alloys and Compounds, D-24-17340 (In Review, 2024)

Team Members

Alex Bretaña[*], Catherine Housley, Henry Ajo, Tucker Koenig, Chandra Lamberth, Patrick Ward, Ben Conner, Greg Morrison[a*], Hano zur Loye[a]

[a] University of South Carolina – Columbia
[*] Postdoctoral Researcher

Figure 3. Field dependent magnetization measurements on aligned powder with the magnetic field applied along the easy direction for annealed Ce2Fe14B and $(YxCe2-x)Fe_{14}B$ (x=0.1, 0.2, 0.3, 0.4, 0.5) alloys.
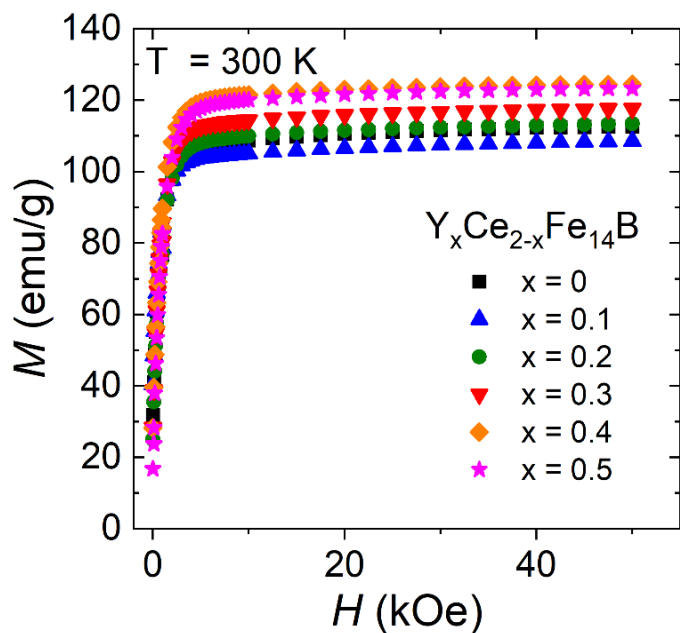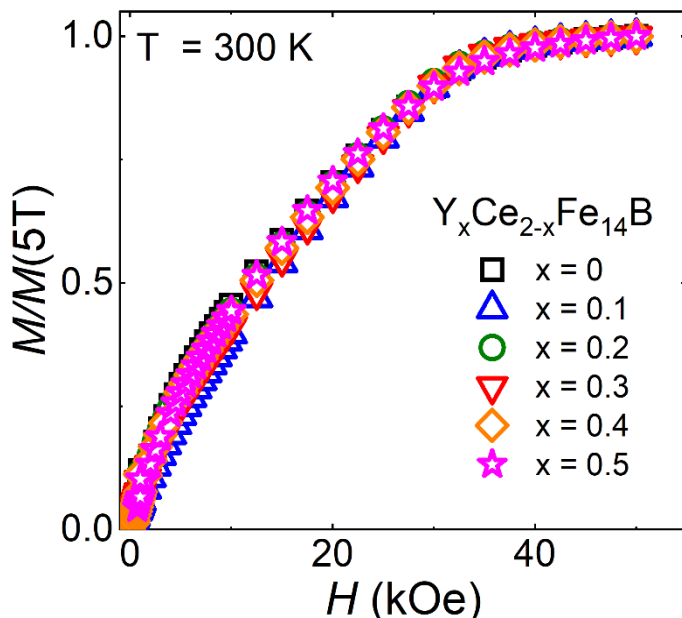

Figure 4. Field dependent magnetization measurements on aligned powder with the magnetic field applied along the hard direction for annealed $Ce_2Fe_{14}B$ and $(Y_xCe_{2-x})Fe_{14}B$ (x=0.1, 0.2, 0.3, 0.4, 0.5) alloys.

FY24 PROJECTS

CORE COMPETENCY:

Assuring production and supply of strategic materials and components

Surface Modification to Reduce Tantalum Attack by Chlorine in Molten Salt

Tatiana Ayers

Plutonium production requires inert materials for very harsh conditions (e.g., molten salt under chlorine/oxygen gas mixture at elevated temperatures). A treatment that provides a more inert surface than the carburization treatment of tantalum would benefit the plutonium manufacturing enterprise by reducing operator exposure, lowering production costs, and improving product quality.

Introduction

The project objective is to explore surface treatments to reduce the corrosion of tantalum in chlorine/oxygen gas mixtures. Tantalum chloride gasses result from exposure of tantalum to chlorine gas, which leads to extensive material loss. Untreated tantalum parts fail prematurely under these conditions. Chemical surface modifications of tantalum were explored in the 1990s, which provided modest performance improvements in molten salt and in chlorine gas.[1-3] Carburizing treatments on tantalum parts were adopted despite offering only limited improvements in chlorine/oxygen gas mixtures. Since then, a variety of novel surface treatments have been invented but the performance of such treatments in chlorine/oxygen gas has only been studied minimally.[4] Alternative treatments may provide a more substantial diffusion/interaction barrier to protect the tantalum part from the gas phase.

A literature review was conducted to identify coatings and surface treatments to be applied to tantalum to increase its corrosion resistance in a high-temperature molten salt environment sparged with chlorine gas. Surface treatment and coating providers were identified and contracted to apply the selected surface treatments and coatings to tantalum coupons. In many cases, this is the first time these surface treatments and coatings have been applied to a tantalum substrate. Additively manufactured tantalum coupon alloys were also tested. The experimental matrix/design for corrosion testing the tantalum coupons was finalized. The corrosion testing will take place in a glovebox with a furnace capable of heating molten salts to high temperatures while sparging with chlorine gas.

Approach

Tantalum was obtained from lab excess and a third-party vendor for making the coupons for corrosion testing. Coupons were sent to a nitriding vendor for an exploratory study of nitriding tantalum. During the testing process it was found that the nitriding process was inhibited by a layer of carbon and oxygen on the surface of the tantalum coupons. Nitradd solution was utilized to clean the tantalum coupons at 150 °C, after which the coupons were rinsed in water and ethanol. Electron dispersive x-ray spectroscopy (EDS) was used to analyze carbon and oxygen levels for uncleaned and cleaned tantalum coupons after each cleaning cycle. **Figure 1** shows the weight loss vs. oxygen weight percent reported by EDS. The correlation indicated that tantalum coupons that experienced a weight loss of greater than 30 mg were likely to have an EDS oxygen weight percent of less than 1%. These coupons were deemed ready to be shipped to the surface treatment and coating providers.
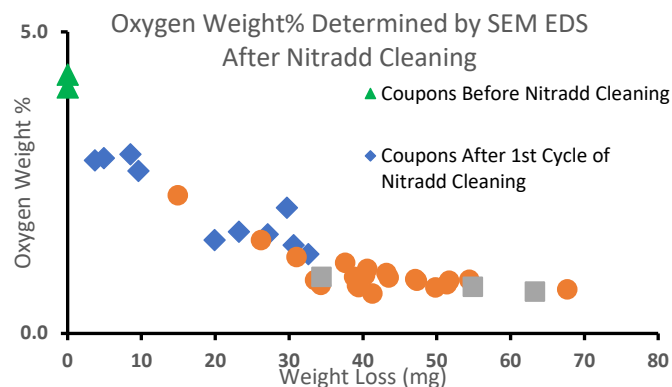

Figure 1. Oxygen weight percent determined by EDS vs. measured weight loss after different cycles of Nitradd cleaning. Coupons that had greater than 30 mg of weight loss and less than one weight percent oxygen as determined by EDS were deemed ready for shipping.

Figure 2 shows scanning electron microscopy (SEM) images of tantalum coupons before and after cleaning with the Nitradd solution. The EDS maps of these images are also included in Figure 2. The dark spots that are more prevalent on the SEM images of the tantalum coupons before cleaning had higher carbon and oxygen content than the lighter areas. Despite inconsistent weight loss for the tantalum coupons during the first cycle of Nitradd cleaning, EDS was used to evaluate coupon readiness for shipping based on the determined oxygen weight percent.
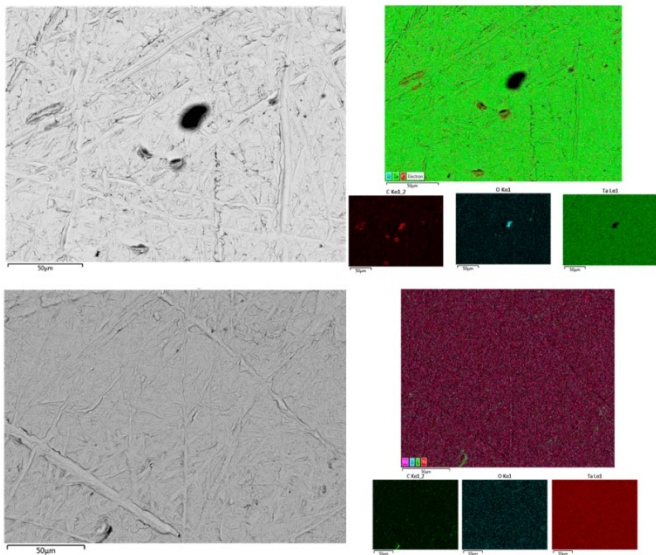

Figure 2. SEM images of coupons before and after Nitradd cleaning with the accompanying EDS mappings showing that cleaned coupons had fewer dark areas of concentrated carbon and oxygen. Top Left: SEM image of tantalum coupon before Nitradd cleaning. Top Right: EDS map of tantalum coupon before Nitradd cleaning. Bottom Left: SEM image of tantalum coupon after Nitradd cleaning. Bottom Right: EDS map of tantalum coupon after Nitradd cleaning.

Accomplishments

- Four surface treatments, three coatings, and three additively manufactured alloys were identified for corrosion testing. Three companies were contracted to complete the surface treatments and coatings for testing.
- Eighty coupons were Nitradd cleaned before shipping to vendors. Sixty of the coupons were sent to vendors for treatment while the remaining 20 coupons will be tested in the corrosive environment without treatment to set a baseline.
- Fifty coupons were obtained from a third-party vendor. Forty-five of these coupons will receive surface treatments while the remaining five coupons will be tested without treatment to set a baseline.
- Sixty coupons have returned from receiving coatings and surface treatments and are receiving preliminary evaluations on the Keyence optical microscope and

SEM. Four of the coupons (one of each type of coating/surface treatment) were cut and polished to perform EDS. The preliminary evaluations will be used to compare the condition of the as-received coupons with the conditions of the coupons after testing.

Team Members

Gregory Chipman*, Colleen Hilla**

*Laboratory Director's Postdoctoral Research Fellow
**Eisenhower Postdoctoral Research Fellow

References

1. Axler, K.M., *Engineered Materials for Application in Severe Metallurgical Environments: Tantalum-Carbon Alloy Development LA-12876-T*. 1995, Colorado School of Mines: Los Alamos National Lab
2. Rense, C.E.C., et al., *Materials Compatibility During the Chlorination of Molten $CaCl_2$ CaO Salts*. 1987, Los Alamos National Laboratory
3. McLaughlin, D.F., C.E. Sessions, and J.E. Marra, *Corrosion Behavior of Silicon Nitride, Magnesium Oxide, and Several Metals in Molten Calcium Chloride with Chlorine.* Nuclear Technology, 1992. **99**: p. 242-251
4. Takeuchi, M., et al., *Corrosion resistance of ceramic materials in pyrochemical reprocessing condition by using molten salt for spent nuclear oxide fuel.* Journal of Physics and Chemistry of Solids, 2005. **66**(2-4): p. 521-525
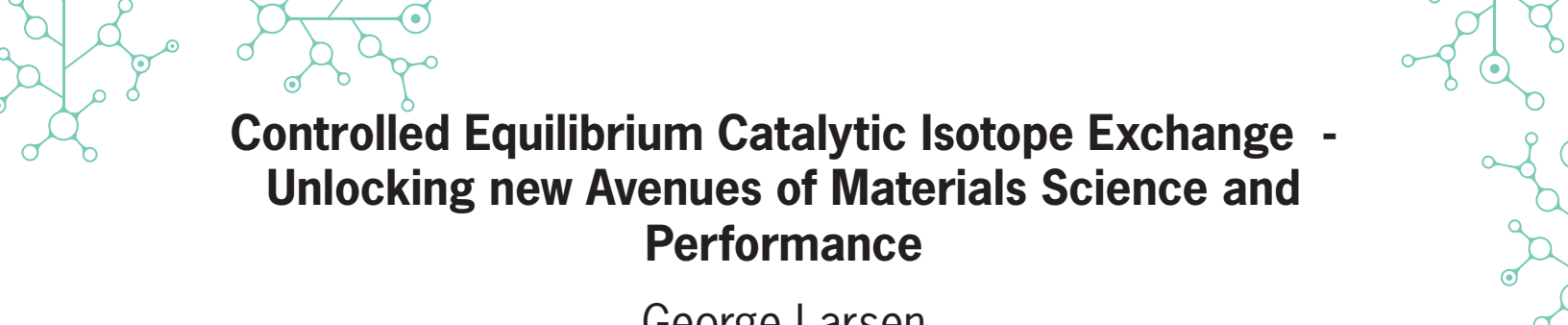
Controlled Equilibrium Catalytic Isotope Exchange - Unlocking new Avenues of Materials Science and Performance

George Larsen

Deuterated materials are desirable for many applications but are rare or extremely expensive. By harnessing our competency in hydrogen processing, SRNL can disrupt the traditional process and create new avenues of research and applications. The primary goal is to develop a unique resource for the deuteration of materials and apply it toward research in strategic areas.

Introduction

Deuterated materials, such as polymers, have unique properties compared to normal, protiated materials. This is because protium (H) and deuterium (D) have the largest relative mass ratios of any isotopes, which significantly affects kinetics (kinetic isotope effect), and the C-D bond has improved stability compared to the C-H bond. However, deuterated organics are extremely expensive and only available in small quantities, if available at all. This is because traditional methods for deuterated organic syntheses rely on D_2O chemistry to build up larger molecules from precursors and monomers – an expensive and laborious process that is constrained by known chemical pathways.

Catalytic hydrogen isotope exchange is a promising approach to synthesize new and existing deuterated materials to shortcut the traditional process. However, catalytic exchange is a slow, equilibrium-driven process. Thus, the vast majority of deuterium that enters the reactor passes through unreacted. To make the catalytic process cost-efficient and scalable, the unreacted deuterium needs to be separated from protium and other impurities in the effluent stream and recycled – this is the basis of the controlled equilibrium catalytic isotope exchange (CECIE) process. It is worth noting that these requirements are analogous to those of a deuterium-tritium fusion fuel cycle, and SRNL is recognized as the world leader in developing and deploying hydrogen processing technologies. The goal of this project is to develop a unique resource at SRNL for the deuteration of materials and apply it toward research in strategic areas: batteries, novel optical materials, fusion energy, polymer recycling, and basic materials science.

Approach

The crux of making CECIE relevant to science and industry is the combination of hydrogen isotope exchange reactions with subsequent hydrogen processing, including impurity removal and isotope separation. The most efficient way to couple these two processes is to create a recirculation loop through the catalytic reactor. This recirculating loop is connected to an impurity trap and an isotope separation system through valves and control volumes. The loop is initially charged with deuterium, which is circulated through the heated catalytic reactor. As hydrogen isotopes exchange in the target molecule, the protium level in the loop increases, and the deuterium level correspondingly decreases. The isotope separation system needs to be connected to the recirculation loop in such a manner as to enable dynamic control of the loop protium concentration. With an in-loop binary gas analyzer for monitoring, the valves can be controlled and operated to bleed out protium/deuterium and feed pure deuterium back in from the external and recycled supplies. The isotope separation system is the heart of the hydrogen processing system, and the project employs SRNL's Thermal Cycling Absorption Process (TCAP) for this task. Specifically, a micro-TCAP system is being utilized for the project. To maximize the impact of SRNL's CECIE process, the project will produce several classes of deuterated materials that are currently cost-prohibitive for intensive research. These materials will be investigated internally and through external collaborations for applications in batteries, fusion energy, polymer recycling, and neutron detection.

Accomplishments

- Designed, assembled, and used catalytic reactor recirculation loop - integration with the micro-TCAP will be completed at the end of FY24 (**Figure 1**).
- Produced a multigram batch of deuterated neutron detection material, P2 (**Figure 2**).
- Harnessed the CECIE recirculating loop to produce highly deuterated ethylene glycol, an important precursor to many materials such as those used in Li ion batteries.
- Investigated the effect of molecular chain length on the deuteration of carboxylic acids, which are used to produce polymers, pharmaceuticals, solvents, and liquid crystals (**Figure 3**).
- Utilized CECIE loop to support other SRNL efforts, including a DOE Early Career Award.
- Presented results at International Isotope Society Meeting.

Intellectual Property

Invention Disclosure

- Deuterated Polymers for Battery Separators

Team Members

Tyler Guin, Kori McDonald, Collin Malone, Houston Smith*,

*Postdoctoral Researcher
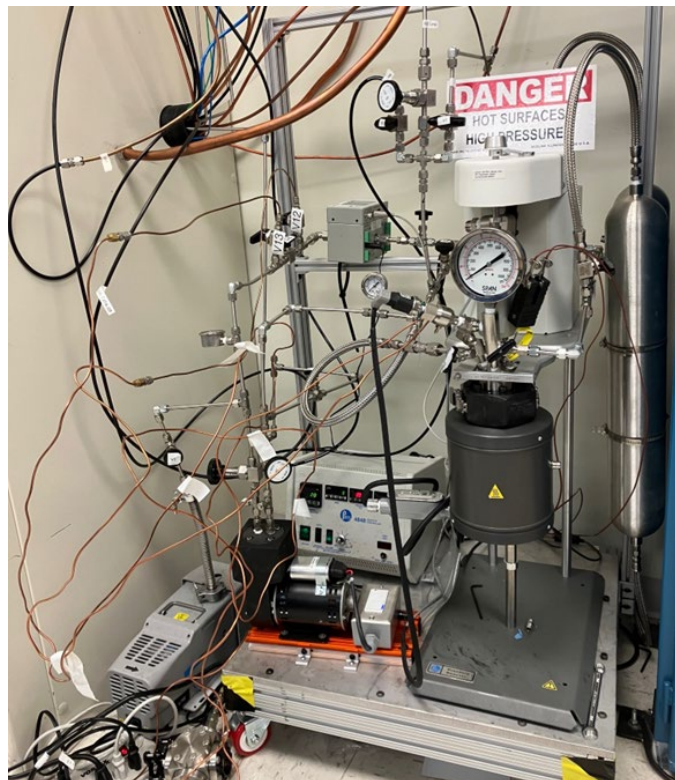
Figure 1 Completed CECIE catalytic reactor recirculation loop.
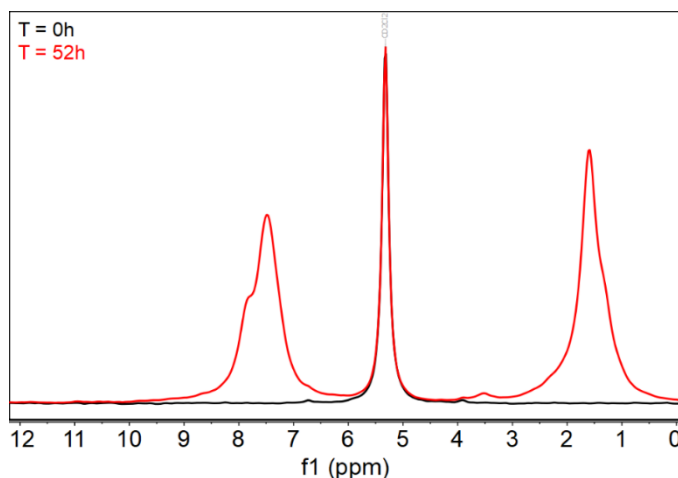
Figure 2. ^{2}H nuclear magnetic resonance (NMR) spectra showing the deuterium incorporation in the methyl and aromatic groups in the P2 neutron detection material.
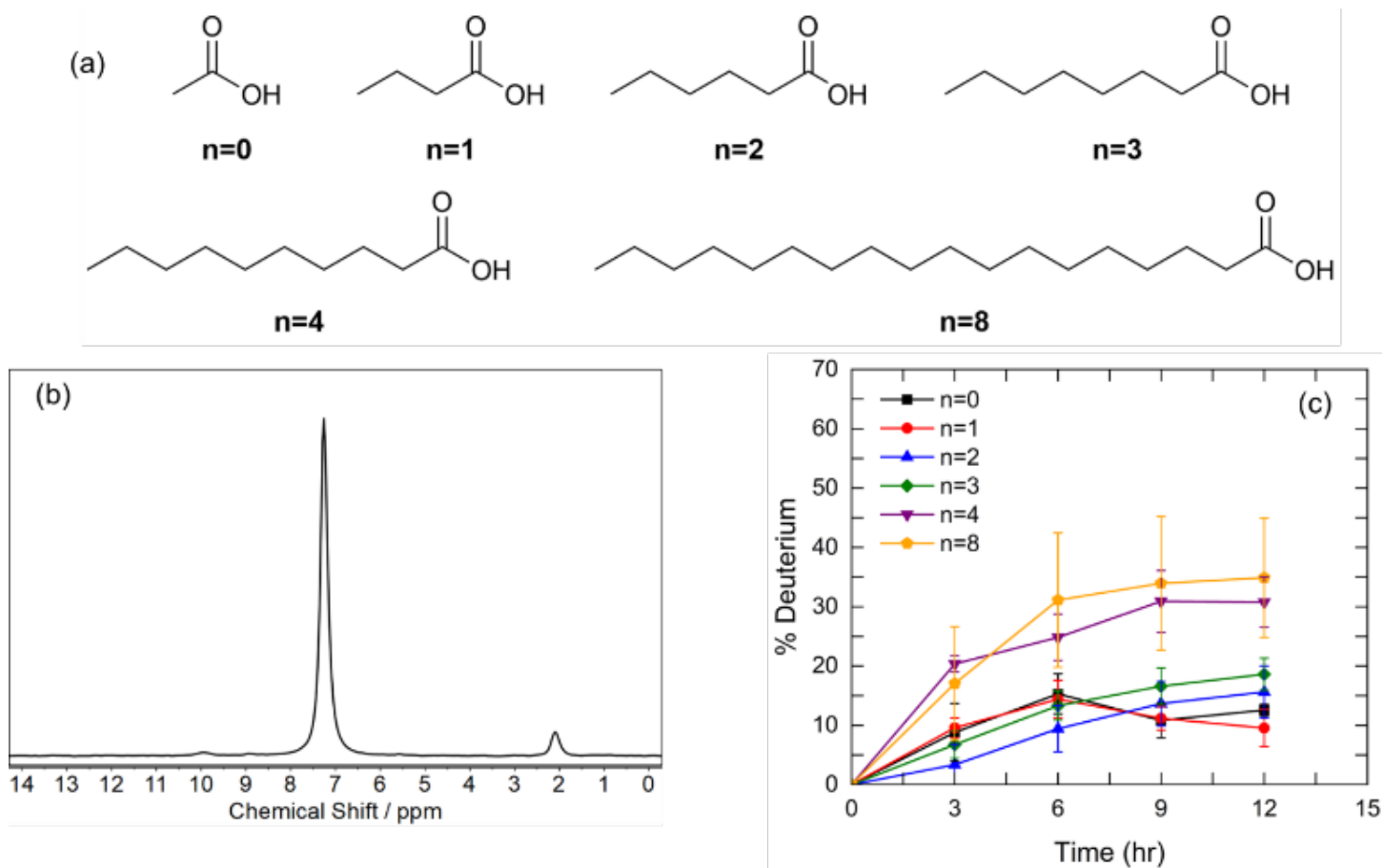
Figure 3. (a) Molecular structures of carboxylic acids under investigation. (b) Nuclear magnetic resonance (NMR) data showing the exchange of hydrogen with deuterium in carboxylic acid. (c) Catalytic deuterium incorporation versus time for carboxylic acids with chain lengths n = 0 – 8.

FY24 PROJECTS

CORE COMPETENCY:

Sensing, characterizing, assessing, and deterring nuclear proliferation

Mass Spectrometer Accuracy with Unmanned Aircraft Systems Integration

Nabra Asgedom

This project studied the effects of drone flight on gas sample concentrations and collection utilizing an onboard mobile mass spectrometer. As gas sampling technology becomes more efficient and lightweight, the ability to use drones for collection must be further characterized in order to gather accurate results. This approach compares in-flight data collection to data collection on the ground to quantify the effects of drone mobile mass spectrometer deployment.

Introduction

Mass spectrometers are used to determine the structure and chemical properties of molecules, identify unknown compounds by determination of molecular weight, and quantify known compounds in an air or gas sample. In recent years, mass spectrometers have been integrated onto Unmanned Aircraft Systems (UASs), commonly known as drones, for data collection in dangerous or complex environments. Mobile mass spectrometers can be used to locate dangerous chemicals and byproducts of interest for government entities. Unlike traditional gas sensors, Residual Gas Analyzers (RGAs) are smaller, more rugged mass spectrometers capable of sensing a wide range of elements and compounds. UAS integration creates an abnormal gas sampling environment for RGA applications because Unmanned Aerial Vehicles (UAVs) disturb airflow and cause additional vibrations on the system. During typical RGA mass spectrometer operations, the sensor must receive an appropriate amount of airflow and the electronics/sensor filament must not experience amplified vibrations. Results from this study characterized and determined the reliability of UAV data collection when various elements and compounds are analyzed from the air.

Approach

Before the UAV flight, RGA telemetry was verified, and parameters were modified to ensure an adequate range of data was collected (**Figure 1**). A gas generator was placed with markers at 5-meter intervals from one another as shown in **Figure 2**. UAV flights were performed at three different altitudes per marker; hovering at each altitude for 20 seconds to ensure sufficient samples were taken (**Figure 3**). After UAV flights, the RGA was staged

above all markers at multiple elevations for comparison of gas concentration without UAV effects (**Figure 4**).

Figure 1. Telemetry Verification and Power Supply for RGA Initialization.

Figure 2. Experiment set-up with markers.

Figure 3. Mid-flight data collection following the flight path.

Figure 4. Stationary RGA Data Collection.

The data collected during the experiment targeted multiple exhaust gasses from the generator to the closest amu (atomic mass unit); butane (58.167 amu), benzene (78.167 amu), and toluene (91.167 amu). The particle data collected during each flight was recorded and averaged in **Table 1**. The analyzed data range for each exhaust gas was +/- 0.5 amu. The averaged flight data were compared to the averaged stationary data and expressed as a percent difference (**Table 2**). All targeted exhaust gasses had a partial pressure 24-29% higher during flight tests compared to static tests. **Figures 5 & 6** show benzene concentrations throughout flight and static testing. All other targeted gases followed the same overall trends. The flight data collection showed an approximately horizontal trendline with a slope of 1E-15. The static test had a negative linear trendline with a slope of –5E-15, showing that as the RGA was moved to further markers, the gas concentration decreased while the in-flight concentration stayed the same.

	Flight 1 Partial Pressure (Torr)	Flight 2 Partial Pressure (Torr)	Flight 3 Partial Pressure (Torr)	Average Partial Pressure (Torr)
Butane (58.167 amu)	1.92E-11	1.69E-11	1.46E-11	1.69E-11
Benzene (78.167 amu)	1.88E-11	1.65E-11	1.48E-11	1.67E-11
Toluene (91.167 amu)	1.58E-11	1.38E-11	1.22E-11	1.39E-11

Table 1. Flight Data Collection.

	Partial Pressure (Torr) (flight tests averages)	Partial Pressure (Torr) (static tests averages)	% Increase
Butane (58.167 amu)	1.69E-11	1.32E-11	28%
Benzene (78.167 amu)	1.67E-11	1.29E-11	29%
Toluene (91.167 amu)	1.39E-11	1.12E-11	24%

Table 2. Flight vs. Stationary Data Comparison.

Accomplishments

- Established a property loan agreement with Augusta University allowing SRNL access to an Alta X UAV and Extrel RGA.
- SRNL's first time flying an RGA mass spectrometer for sample collection on a UAS platform (**Figure 3**).
- SRNL's first time collecting real-time gas analysis feedback from an aerial collection source (**Figure 1**).
- Found a significant increase of 24-29% between all targeted particles during flight collection versus stationary collection.
- At further markers, the flight data collection stayed constant while the static test data decreased.

Team Members

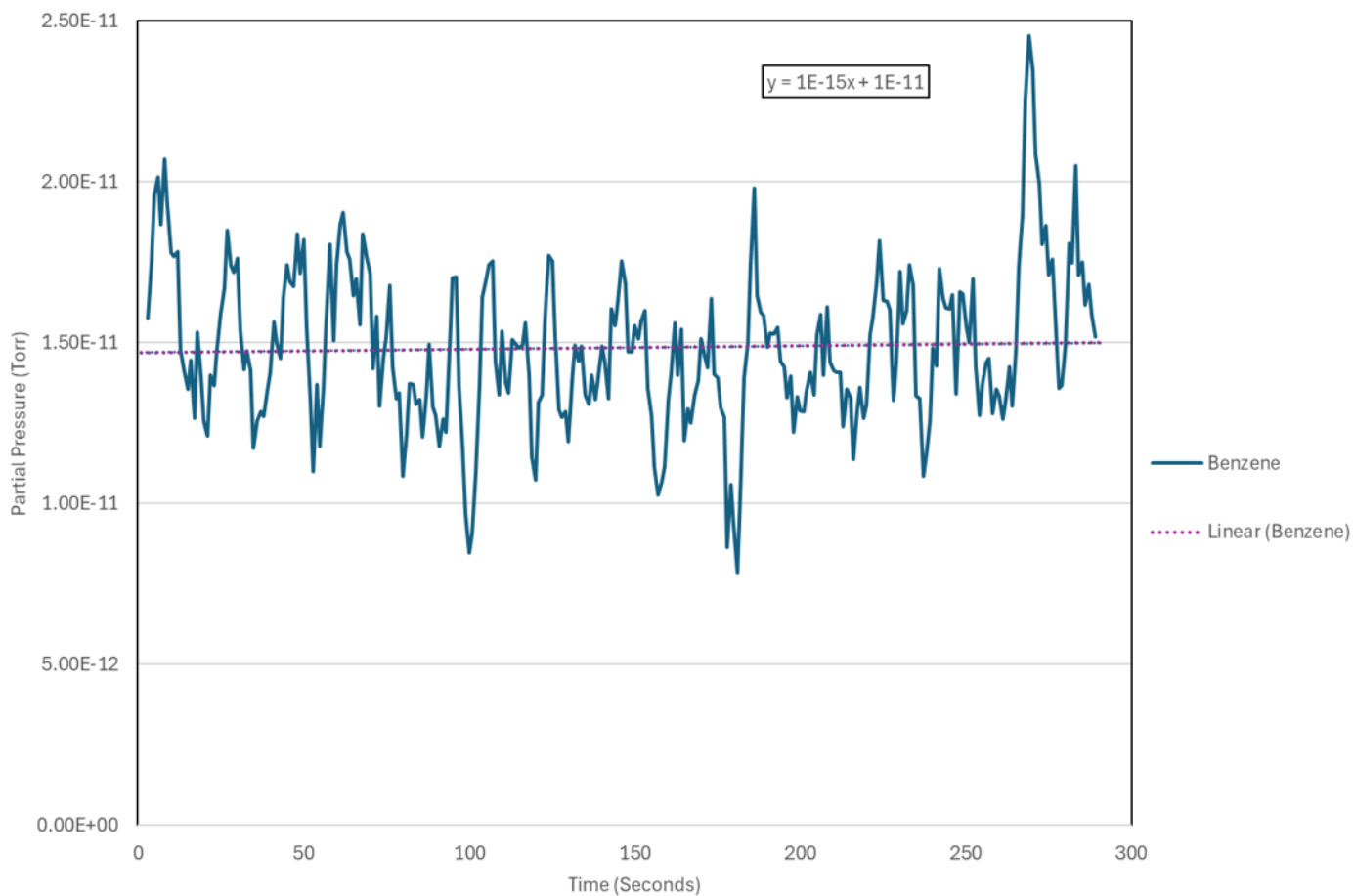Troy Lorier, Jeffrey Steedley, Dr. Guido Verbeck [a]

[a] Augusta University

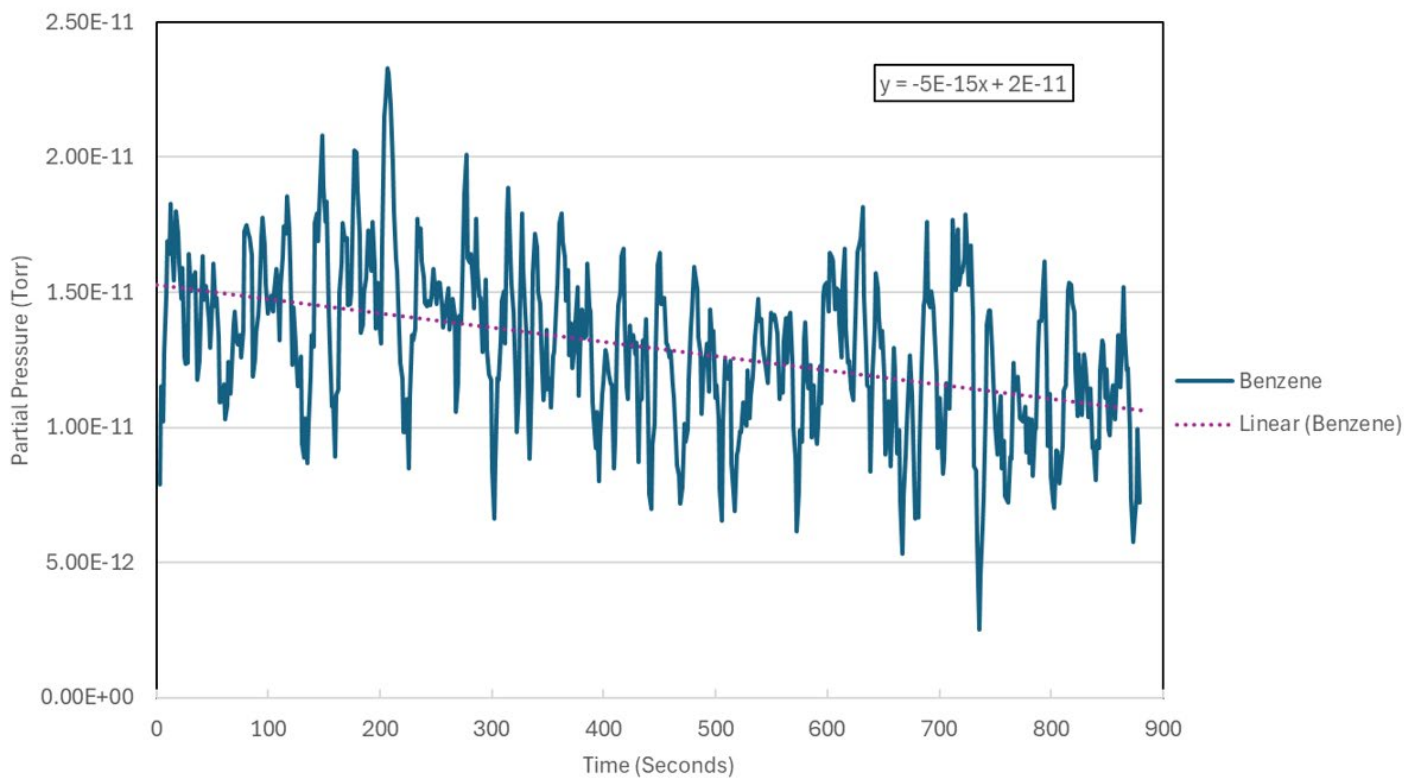**Figure 5.** Flight 3 Benzene Data Collection Example.

Figure 6. Static Test Benzene Data Collection Example.

Mercury Loading and Source Trends from Isotopic Records of SRS Environmental Matrices

Heather Brant

Mercury is a toxic element that is found both naturally and as an introduced contaminant in most Savannah River Site environments. This work focused on determining mercury isotope composition of SRS environmental media as a utility to trace mercury contamination sources over space and time.

Introduction

Mercury (Hg) is a toxic element that occurs both naturally and as an introduced contaminant in many Savannah River Site (SRS) environments and across the DOE complex. Extensive research has documented Hg within environmental matrices of the SRS[1]. There are numerous possible sources of mercury contamination to the SRS environment, including legacy operations of the SRS, offsite point sources, and atmospheric deposition. The contributions and roles of these sources to legacy Hg observations within the SRS environment remain uncertain. Recent advances in multicollector–inductively coupled plasma–mass spectrometry (MC-ICP-MS) have enabled highly precise measurements required to detect subtle differences in the isotopic composition of heavy elements, including Hg. Determination of stable Hg isotope ratios in various environmental media proves useful to trace Hg source(s) and processes involved in the transfer of Hg into the environment.[2] This study aimed to (1) optimize SRNL's existing MC-ICP-MS capabilities to include Hg isotopes (2) develop a novel, rapid method for simultaneous total Hg concentration determination and sample preparation for Hg isotopic analysis (**Figure 1**), (3) determine the concentration and stable isotopic composition of Hg in various SRS environmental matrices (**Figure 2, 3**), and (4) investigate the relationship of possible sources and trends of Hg loading in the SRS environment over past decades (**Figure 3**).

Approach

The goal of this study is to determine if Hg isotopic compositions within SRS environmental matrices preserve signatures of local and regional sources. Pursuit of this goal coincides with strategic sampling and analytical method development. Hg contamination of the SRS environment is well documented.[1,3] Data from these documents were reviewed to provide insight on selection of regional sampling sites that received legacy Hg discharges from different sources, including background. Environmental matrices considered for sampling included tree bore wood cores, sediment, and soil. Literature suggests dendrochronology and stratigraphy coupled with Hg isotope ratios provide a natural archive of Hg source exposure.[4,5] Recent and archived sediment and tree core samples were utilized to develop and validate parameters associated with the novel, rapid method of simultaneous total Hg concentration analysis and preparation for Hg isotopic measurements. Analytical parameters determined during this study included optimal sample weights, concentration ranges, detection limits, trapping solutions, and instrument criterion for Hg concentration and isotope analysis. Several field trips allowed for the collection of 34 tree cores from three locations (**Figure 4**). Age dating and sectioning methods were developed for the cores. Initial determinations indicate Hg concentrations fluctuate with temporal growth of the sampled trees (**Figure 3**). Sediment total Hg concentrations were determined from 27 locations both on and off SRS. Concentration and isotope ratios of the sediments indicate spatial differences between and within sampling locations (**Figure 2**). These initial data from the sediment and tree cores provide insightful information that will be used to inform future sampling strategies and additional method development.
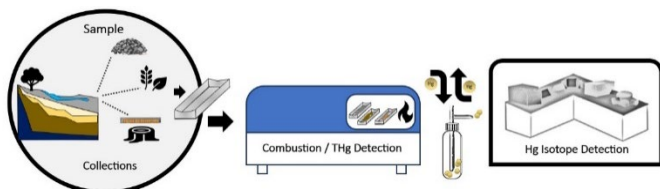
Figure 1. Simplified illustration of rapid detection method. Environmental media loaded directly into autosampler, combusted, total mercury (THg) detection by atomic absorbance, while off gas collected into trapping solution. Trapping solution then introduced through cold vapor system of multi collector-inductively coupled plasma- mass spectrometer for mercury isotope determinations.
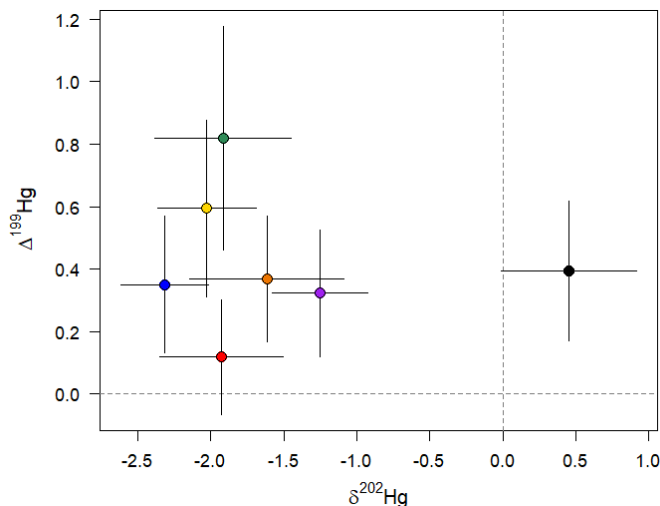

Figure 2. δ^{202}Hg (MDF) versus Δ^{199}Hg (MIF) in sediment from locations on and off-site of the Savannah River Site (SRS). Uncertainties are 2 standard deviations (2σ) and represent measurements early in method development. Orange and red circles represent two locations in Upper Three Runs (UTR) stream; above Burial Grounds and beneath Burial Grounds, respectively. Purple circle indicates flood plain drainage from TNX area into the Savannah River. Blue circle represents Steed Pond of Tims Branch. Green circle represents drainage from S-Area. Black circle represents industry upstream of SRS collected within the Savannah River. Yellow circle represents Crouch Branch near H-Area. Dotted black lines indicate natural values.
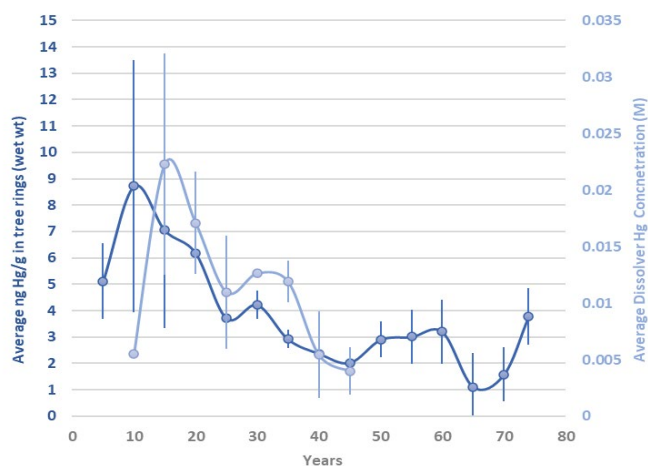

Figure 3. Radial pattern of Hg concentration in bore wood of a pine tree near F- and H-Area at SRS (in blue). Each blue circle represents a five-year average Hg concentration (ng/g ± 1σ). Bore wood core growth dates from 1950 (year 0) to 2024 (year 74). Each orange circle on the secondary axis represents a five-year average Hg concentration (M ± 1σ) as reported for the SRS Separation Areas dissolvers (F- and H-areas)[3]. Secondary axis data (in orange) is sparse and limited to years 1959-1994.

Figure 4. Bore wood core collection from a pine tree. Radial pattern (light/dark) within the core indicates annual increment growth. Hg concentration can be determined on each year (one ring), averaged though years, or as several years analyzed together (several rings). Analysis of Hg isotopes may require combining rings (spanning several years) to meet quality control requirements of the MC-ICP-MS instrument.

Accomplishments

- Acquired and installed a Milestone Direct Mercury Analyzer (DMA-80).
- Acquired cold vapor sample introduction system, reagents, and standards required for analysis.
- Installed the cold vapor system with the existing MC-ICP-MS.
- Determined optimal operating conditions for all systems.
- Determined isotope ratio precision and reproducibility for method.
- Collected initial environmental media to assist with method development.
- Determined total mercury concentrations for recent collection and archived media. Total mercury concentrations will assist with the selection of sampling sites and for development of the analytical parameters associated with isotopic characterization.
- Determined mercury isotope ratios within recently collected and archived collected environmental media. Isotope ratios will quantify SRS spatiotemporal trends of environmental media.
- Alexis Riche gave oral presentation at 2024 annual Goldschmidt Conference.
- Riche, A.T., H. Brant, S. Bowden, K. Samperton, W. Kuhne, and A. Swindle. 2024. Determining mercury loading and source trends from new and historical concentration and isotopic records of Savannah River Site environmental matrices, Goldschmidt Annual Conference, Chicago, UL, abstract 23860.

Team Members

Shelby Bowden[*], Haley Cole, Wendy Kuhne, Alexis Riche[*], Kyle Samperton, and Ashlee Swindle

[*]*Postdoctoral Researcher*

References

1. Halverson, N. (2008). Final Report on the Aquatic Mercury Assessment Study. doi:10.2172/939852.
2. Blum, J. D., L. S. Sherman, and M. W. Johnson (2014), Mercury isotopes in Earth and environmental sciences, Annu. Rev. Earth Planrt. Sci., 42, 249– 269.
3. Pickett, C.E, T.G. Campbell, and W.E. Harris. 1989. Mercury Requirement for Separation Processes, OPS-STH-890145, Westinghouse Savannah River Company, Aiken , SC.
4. Scanlon, T. M., Riscassi, A. L., Demers, J. D., Camper, T. D., Lee, T. R., & Druckenbrod, D. L. (2020). Mercury accumulation in tree rings: Observed trends in quantity and isotopic composition in Shenandoah National Park, Virginia. Journal of Geophysical Research: Biogeosciences, 125. https://doi.org/10.1029/2019JG005445.
5.   Meixnerová J, Blum JD, Johnson MW, Stüeken EE, Kipp MA, Anbar AD, Buick R. Mercury abundance and isotopic composition indicate subaerial volcanism prior to the end-Archean "whiff" of oxygen. Proc Natl Acad Sci U S A. 2021 Aug 17;118(33). doi: 10.1073/pnas.2107511118.

Multivariate Optimization for Sampling Instrumentation

Stephanie Gamble

This work introduces an approach for multivariate, multi-objective optimization with Karush-Kuhn-Tucker conditions to optimize method parameters of an instrument, including both continuous and categorical parameters. An example case has been conducted for optimization of gas chromatography – mass spectrometry sample analysis.

Introduction

In fields involving sampling, optimization of instrument parameters is a common practice as the data output (e.g., peak shape in gas chromatography – mass spectrometry (GC-MS)) from samples is highly dependent on the instrument's method parameters. There is a need to employ a generalized strategy suitable for almost any analytical instrumentation/sample preparation/analysis scheme. Trial-and-error is the typical method optimization technique, which is time consuming and inaccurate when dealing with multiple parameters. The solution is utilizing multivariate Lagrangian optimization. In addition, a novel concept is proposed to broaden the options for the quantities to be optimized, for example, simultaneously optimizing height and width rather than only peak area. Multi-objective optimization with Karush-Kuhn-Tucker conditions limits the optimization space to real-world or realistic solutions that are bounded by physical limitations of the instrument or process. If categorical parameters are considered as well, as these cannot be represented by a value, these must be represented by a binary vector and optimized discretely.

These optimization methods are relevant to analytical systems/samplers/sample preparation methods used by government agencies, nuclear nonproliferation offices, and food industries. The resulting procedure will reduce time invested in optimizing analytical methods compared to traditional univariate trial-and-error optimization and potentially improve the sensitivity of current techniques. This methodology could serve to reduce the cost of developing and optimizing future systems and instruments.

Approach

Modern, accurate optimization theory applied to the context of method optimization led to the development of a technique for optimizing the method parameters for a sampler or analytical instrument, such as a GC-MS analysis instrument (e.g., **Figure 1**).

Figure 1. A gas chromatography – mass spectrometry (GC-MS) instrument for analyzing air or liquid samples.

The techniques defined allow for the capability to simultaneously optimize multiple objective quantities [1], use of Lagrangian optimization as opposed to trial-and-error, inclusion of Karush-Kuhn-Tucker (KKT) conditions[2,3] to constrain the parameters based on physical limitations, and consider the Pareto Optimal front[4] to define optimality for a multi-objective problem. A technique has also been developed for considering both continuous parameters and categorical parameters. See **Figure 2** for the definition of the equation required to solve for the optimal parameter values (X^*, Y^*).

$$\nabla_X \mathcal{L}(X_Y^*, Y) = \nabla_X[O(X_Y^*, Y) + \sum \mu_i g_i(X_Y^*) + \sum \lambda_j h_j(X_Y^*)] = \vec{0}$$

where: $g_i(X_Y^*) \leq 0$, for all i

$h_j(X_Y^*) = 0$, for all j

$\mu_i \geq 0$, for all i

$\mu_i g_i(X_Y^*) = 0$, for all i

$\lambda_j \in \mathbb{R}$, for all j

$$O(X^*, Y^*) = \min_Y O(X_Y^*, Y)$$

Figure 2. Lagrangian equation with KKT conditions. $O(X)$ denotes the overall objective function (weighted linear combinator of individual objectives to be simultaneously optimized). g_i functions denote inequality constraints, where the physical range limitations for each parameter are included in the optimization. h_j functions denote any additional equality constraints that may relate the parameters.

An example case was conducted for a GC-MS sample containing eleven iodinated alkane compounds with the goal of both maximizing the height of the intensity peaks and minimizing their width. A fractional factorial screening design[5] with analysis of variance[6] determined the parameters of significance for the objectives. Then, surface response experiments, conducted via a Box-Behnken experimental design[7], provided data to fit the objectives to a second order approximation to be optimized. The categorical parameter considered (liner shape) is treated as a binary vector and optimized discretely.[8,9] The equation in **Figure 2** was solved to find the optimal parameter values for the GC-MS instrument method. Data collected at approximately these optimal values is shown in **Figure 3**. The Pareto optimal front for the two objectives is given in **Figure 4**.
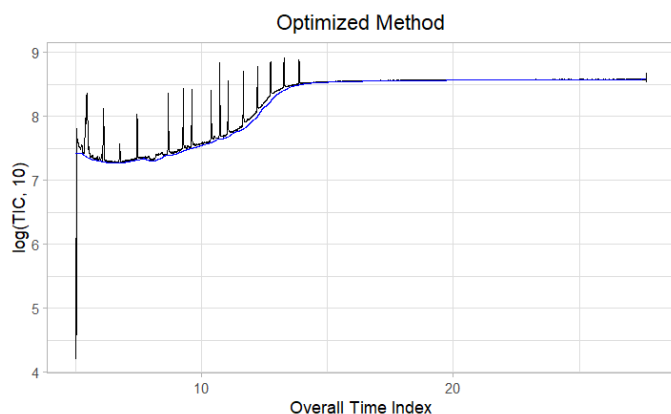

Figure 3. Data collected from analysis conducted at approximately the optimal method parameters for the GC-MS instrument. The inlet liner shape is a straight liner with wool, the split ratio is 200, the gas carrier flow rate is 1.4 mL/minute, the oven temperature ramp rate is 28 °C/minute, and the column film thickness is 1 μm. (The largest column film thickness available on hand was 1 μm thick. Larger thicknesses can be purchased on special order. For this example, the largest standard film thickness available was used)
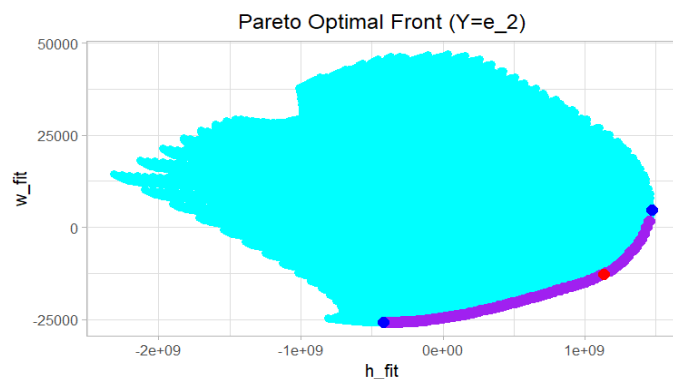

Figure 4. The Pareto optimal front of the fitted average peak height vs fitted average peak width in purple. The red point is the solved optimal point, based on weights chosen to normalize the two objectives, $O(X, e_2) = -\frac{1}{max(h)} O_h(X, e_2) + \frac{1}{max(w)} O_w(X, e_2)$. The space of admissible parameters is given in cyan. $Y = e_2$ refers to the second option of the categorical parameter, liner shape, which was the straight liner with wool.

Accomplishments

- A new optimization technique for method optimization for sampling and analytical instruments was developed using modern and accurate optimization theory, improving results compared to a trial-and-error optimization technique. Improvement in objective values may be up to two orders of magnitude in the example of optimizing the peak height in GC-MS.
- The inclusion of experimental designs in this optimization technique saves researchers up to 2^(N-3) experiments to conduct, where N is the number of parameters. This would be approximately 30 minutes – one hour per experiment, saving researchers hours and providing further improvement over trial-and-error with no definite conclusion.
- The new technique improves accuracy of optimal values compared to using trial-and-error or unbounded optimization where the parameters are later restricted individually rather than incorporating physical constraints during the optimization.
- The expansion to new objective quantities allows for improved results based on the needs of individual projects this technique will be applied to.
- Optimization technique has been expanded to include ability to optimize both continuous and categorical parameters.
- A journal article was published in Analytical Chemistry that describes the full optimization technique for continuous parameters and provides an example application.

- A second journal article is in preparation to be submitted to Analytical Chemistry that describes the full optimization technique considering both continuous and categorical parameters.
- A GUI was developed to assist scientists with the optimization technique and perform the optimization calculations (for continuous parameters only). This includes constructing a fractional factorial screening experiment, ANOVA, constructing a Box-Behnken response surface experiment, and performing the optimization. The GUI has been written as an R-package, "MethodOpt", which has been granted a copyright. It is in the process of being prepared for public release on CRAN (Comprehensive R Archive Network).
- A publication has been prepared describing the use of the GUI "MethodOpt," which will be submitted to Analytical Chemistry once the package has been released on CRAN.

Peer-reviewed Publications

- Gamble, S. N.; Granger, C. O.; & Mannion, J. M. Advanced Method Optimization for Sampling and Analysis Instrumentation. *Analytical Chemistry*. **2024**, 96 (29), 11666-11672. DOI: 10.1021/acs.analchem.3c05763
- Luke, B.; Gamble, S. N. MethodOpt: a Shiny-based graphical user interface for multivariate instrument method optimization. *in preparation to submit to Analytical Chemistry*.
- Gamble, S. N.; Granger, C. O.; & Mannion, J. M. Advanced Method Optimization with Categorical Parameters. *in preparation to submit to Analytical Chemistry*.

Intellectual Property

Copyright Disclosures
- MethodOpt

Team Members

Stephanie Gamble, Caroline Granger[*], Joseph Mannion, Mohammad Khan[*], Tatiyanna Singleton[+], Benjamin Luke[+]

[*]*Postdoctoral Researcher*
[+]*Post-Bachelor's Intern*

References

1. K. Miettinen. Nonlinear Multiobjective Optimization. *Springer Science & Business Media*. 1998.
2. M. Abouhawwash & K. Deb. Karush-Kuhn-Tucker Proximity Measure for Multi-Objective Optimization Based on Numerical Gradients. Technical Report COIN Report No. 2016005. Department of Electrical and Computer Engineering, Michigan State University, East Lansing, USA. 2016.
3. G. Giorgi, B. Jiménez, & V. Novo. Approximate Karush-Kuhn-Tucker Condition in Multiobjective Optimization. *J Optim Theory Appl*. 2016. 171:70-89.
4. R. T. Marler, & J. S. Arora. Survey of multi-objective optimization methods for engineering. *Structural and Multidisciplinary Optimization*. 2004. 26:6, 369–395.
5. D. C. Montgomery. Design and Analysis of Experiments (9th ed.) *John Wiley & Sons, Inc.* 2017.
6. R. A. Fisher. Statistical Methods for Research Workers (14th ed.) *Oliver & Boyd*. 1970.
7. G. Box & D. Behnken. Some new three level designs for the study of quantitative variables. *Technometrics*. 1960. 2:455-475.
8. Hernandez, H. Categorical optimization. ForsChem Research Reports. 2022. DOI:10.13140/RG.2.2.28486.96328
9. Vanaret, C. A global method for mixed categorical optimization with catalogs. arXiv preprint arXiv:2104.03652. 2021. URL https://www.researchgate.net/publication/350663194_A_global_method_for_mixed_categorical_optimization_with_catalogs, accessed 2 August, 2024.

Instrument Feasibility Assessment of Commercial Off-the-Shelf Portable Mass Spectrometers with Ambient Ionization Sources for In-Facility Analysis of Uranium Isotopes

Caroline Granger

The objective of this seedling study was to generate a report identifying portable, commercial off-the-shelf mass spectrometers with ambient ionization sources to be utilized by International Atomic Energy Agency inspectors during safeguards inspections. This technology will enable inspectors to quickly determine if samples contain enriched uranium at levels exceeding treaty guidelines.

Introduction

Uranium isotopic analysis is a key safeguard activity of the International Atomic Energy Agency (IAEA) to ensure treaty compliance (i.e., detection of undeclared material or nuclear material exceeding uranium enrichment values). In 2022, the IAEA conducted approximately 3000 in-field verification activities at roughly 1300 nuclear facilities in 188 States.[1] Traditional in-field analytical techniques used by the IAEA for uranium isotopic analysis are time consuming, expensive, and require the expertise of a highly trained IAEA inspector.[2-4] As such, the IAEA has expressed interest in other methods/instrumentation that can overcome many of the limitations associated with traditional in-field analytical techniques that will significantly increase their sample throughput and ability to quickly identify noncompliance at nuclear facilities (e.g., production of highly enriched uranium (HEU) at a low enriched uranium (LEU) enrichment facility).

The research team chose to investigate portable mass spectrometers compatible with ambient ionization sources because they significantly reduce the sample preparation and instrument vacuum requirements while also being user-friendly and accurate. Ambient ionization sources are easily interchangeable based on the need of the inspection, thus making them compatible with various sample types that an IAEA inspector may encounter. To identify the most suitable instrument for this application, the research team performed an extensive literature search to identify commercial off-the-shelf (COTS) portable mass spectrometers that would be easy to implement into current IAEA sampling protocols while also providing high-quality data to uphold the IAEA's reputation as the nuclear inspectorate.

Approach

This feasibility study was conducted by assessing available COTS instruments based on three categories: (1) portability, (2) instrument operation and maintenance, and (3) mass spectrometer performance metrics. The first step of this study focused on identifying all commercially available portable mass spectrometers with ambient ionization sources. Once suitable instruments were identified, a scoring rubric was generated based on an in-depth literature search of portable mass spectrometers and previous studies generated by the IAEA, SRNL, LANL, and PNNL for in-field uranium isotopic analysis via mass spectrometry.[5-7] The scoring rubric consists of seven different metrics: portability, user experience and maintenance, data interpretation and management, power requirements, sensitivity, mass resolution, and mass scan range. Each instrument was assigned a number between one (does not meet criteria) and 10 (fully meets criteria) based on how well it met the criteria, and each category was totaled to give an overall score. Results from this study indicate that the most promising instrument was the Continuity™ (BaySpec, San Jose, CA).

Accomplishments

- The report is the most comprehensive study of portable, COTS mass spectrometers with ambient ionization sources for the in-field analysis of uranium isotopes throughout the nuclear fuel cycle.
- Results from this study identify the Continuity™ (BaySpec, San Jose, CA) as the mass spectrometer most suitable for this application. Future laboratory studies are required to verify its performance analyzing uranium-bearing samples.

Team Members

Danielle Mannion, Holly Rebuck, Mark Goldy, Amie McElroy, KateLyn Smith, Haley Cole, Joseph Mannion

References

1. Mutluer, A. *IAEA Draws Safeguards Conclusions for 188 States - Safeguards Implementation Report 2022.* International Atomic Energy Agency, Department of Safeguards: Vienna, Austria, 2023. https://www.iaea.org/newscenter/news/iaea-draws-safeguards-conclusions-for-188-states-safeguards-implementation-report-2022 (accessed 2024-07-09).

2. Erdmann, N.; Amador, P.; Arboré, P.; Eberle, H.; Lützenkirchen, K.; Ottmar, H.; Schorlé, H.; van Belle, P.; Lipcsei, F.; Schwalbach, P.; Gunnink, R. COMPUCEA: A High- Performance Analysis Procedure for Timely On-site Uranium Accountancy Verification in LEU Fuel Fabrication Plants, *ESARDA Bulletin*, **2009**, 43 (5), 30-39.

3. *Development and Implementation Support Programme for Nuclear Verification.* STR-382; International Atomic Energy Agency, Department of Safeguards: Vienna, Austria, 2016. https://www.iaea.org/sites/default/files/16/05/development_and_implementation_support_programme_for_nuclear_verificatio.pdf (accessed 2024-06-04).

4. Chan, C.Y.G.; Valentine, J.D.; Russo, R.E. *Scoping study to expedite development of a field deployable and portable instrument for UF6 enrichment assay*. LBNL-2001050; Lawrence Berkeley National Laboratory: Berkley, CA, 2017. https://escholarship.org/uc/item/6k47p04z (accessed 2024-07-15).

5. Sexton, L.T.; Ticknor, B.W. *Concept of Operations (ConOps) for the Use of In-Field Mass Spectrometry During IAEA Safeguards Inspections*. SRNL-STI-2013-00062-Rev 0; Savannah River National Laboratory: Aiken, SC, 2013.

6. Hart, G.L.; Barinaga, C.J.; Hager, G.J.; Duckworth, D.C. *Market Research Survey of Commercial Off-The-Shelf (COTS) Portable MS Systems for IAEA Safeguards Applications*. PNNL-22237. Pacific Northwest National Laboratory Richland, Washington, 2013. https://www.pnnl.gov/main/publications/external/technical_reports/PNNL-22237.pdf (accessed 2024-07-15).

7. Yoshida, T.M.; Leibman, C.P.; Stark, P.C.; Hart, G.L.; Barinaga, C.J.; Hager, G.J.; Duckworth, D.C.; Ticknor, B.W.; Sexton, L.T. *In-Field Mass Spectrometry for Safeguards Applications – Gap Analysis Report*. LA-UR-13-23696, PNNL-22497, SRNL-STI-2013-00304; Savannah River National Laboratory: Aiken, SC, 2013.
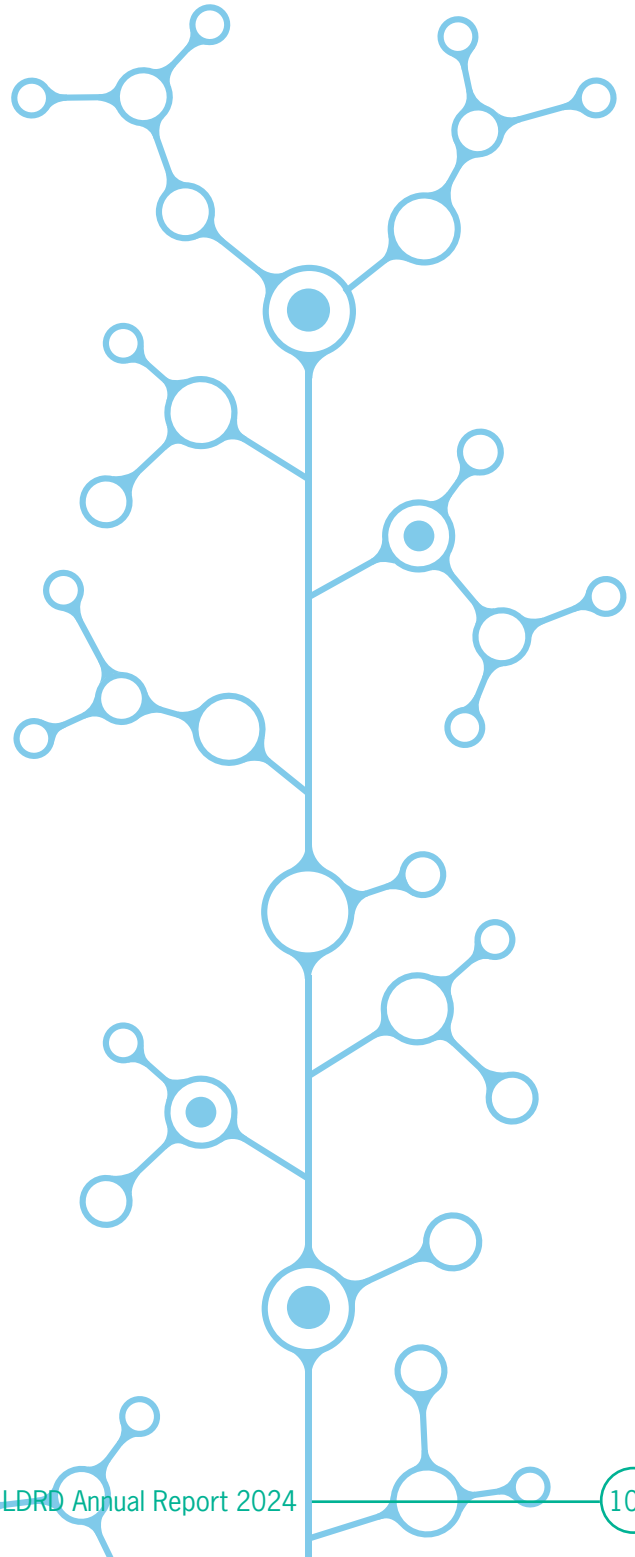
Characterizing Microstructural Evolution of Tritium Processing and the Effects of Gaseous or Surface Impurities on Getter and Cladding Elements

John T. Kelly

This research unravels the molecular fingerprinting of impurities that are relevant to the production and separation of the hydrogen isotope tritium (3H or T). The work demonstrates the real-time detection of impurities in operando chemical reactions. This approach monitors the onset of reactivity between the surface and gaseous impurities.

Introduction

The focus of this work is characterizing the adsorption, decomposition, and recombination of hydrogen isotopes to describe an event like the Watts Bar nuclear plant reactor 1 Cycle 16, which raised concerns about a possible breached TPBAR. In this study, pure and alloys of metal-based samples were exposed to ammonia, methane, and water to simulate conditions that would result in a stained outer surface on cladding tubes and ring-like features on the inner surface of cladding tubes. This scope of work combines previously demonstrated elemental analyses (mass spectrometry) with molecular fingerprinting the isotopic exchange at the surface with high resolution infrared signatures. The work with high resolution experiments has demonstrated the detection of trace levels of ammonia and isotopic exchange *in operando* reactions. As a goal for this research, elemental and molecular spectroscopic data provided a novel method of monitoring the onset of surface impurities. The work is non-radiological and surrogate materials were used for all experimental research.

Approach

High-resolution mass spectrometry and infrared spectroscopy monitors gaseous impurities to determine concentrations for each isotopologue of the constituent gaseous environment and transient intermediates trapped in isolation. An exhaustive database was generated for determining the concentration of the three water isotopologues (^1H_2O, $^1HO^2H$, and ^2H_2O) and four ammonia isotopologues (N^1H_3, $N^1H_2{}^2H$, $N^1H^2H_2$, and N^2H_3) in concert with chemometric pre-processing and calibration modeling. The primary goal of this research is the development of an analytical methodology for disentangling contributions and effects of gaseous or surface impurities by adsorption, decomposition, and recombination of hydrogen isotopes. The project leveraged a continuous sampling strategy, reduced pressure data acquisition, and sample transfer from infrared to mass-to-charge analyses. **Figure 1** shows the experimental design and example data set from the research performed as a graduate student research project.
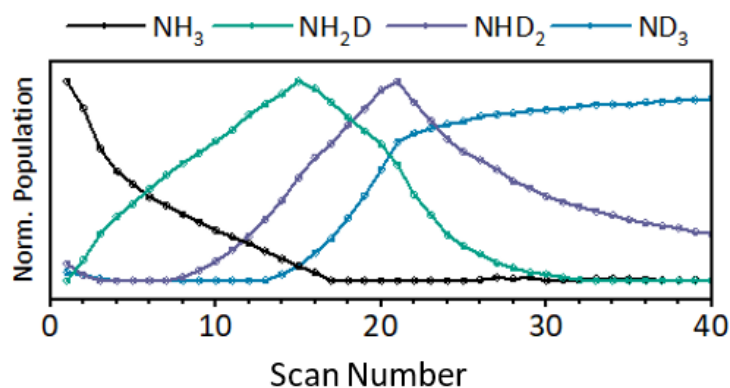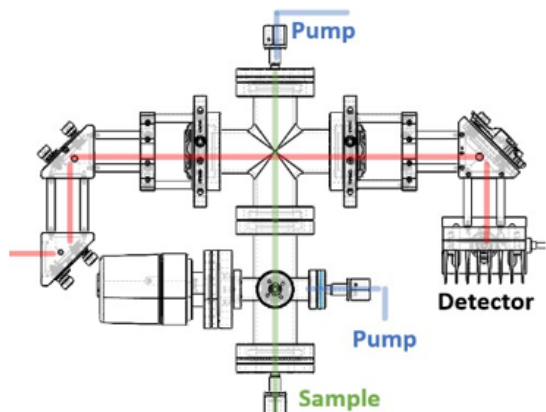

Figure 1. The figure to the left illustrates the design of actively sampling through a capillary tubing while keeping the probed volume under vacuum. Sample is pumped to a mass spectrometer for primary analysis of reactants, intermediates, and products. The trace in the figure to the right is isotopologue profile across an isotope exchange experiment.

This work demonstrates the feasibility of a novel approach to determine the effect of gaseous or surface impurities on tritium processing by gaseous or surface impurities, but the application is considered targeted (well-described analyte) due to the nature of an under-defined background or matrix with unforeseen interferences. The uncertainty of this approach can only by overcome by an exhaustive assessment of the impurities (reactant, intermediates, and products) beyond the known carbon, carbon monoxide, carbon dioxide, methane, water, and ammonia. The next evolution of this work complexes the infrared spectral acquisition by employing an intelligent acquisition of data by (1) automating background exclusion, (2) baseline components assessment, (3) iterative precursor inclusion, and (4) track-and-trend analytics. This concept leads to a robust, reproducible, and reliable profiling, identification, and pathway analysis in a deployed or radiological environment.

Accomplishments

- Construction of continuous sampling apparatus for gaseous impurities with optical access and gas transfer for mass- to-charge analysis.
- Automated 5-point calibration by mass flow-controlled dilution scheme for wavelength and concentration dependencies.
- Orthogonal measurements across high resolution mass spectrometry and direct absorption spectroscopy.
- Trained graduate student in fundamental signal processing, optical alignment practices, and batch-based data manipulation.
- Provided iterative revisions on manuscript and invention disclosure for technology developed in this project.

Peer-reviewed Publication

- J. T. Kelly, H. M. Sabatini, L. E. McNamara, C. J. Koch, C. D. Chouinard, A. G. Watrous, R. C. Fortenberry, and T. Guin "Infrared Signature of Ammonia Cracking by High-Resolution Absorption Spectroscopy", Analytical Chemistry (Internal Review)

Intellectual Property

Invention Disclosure

- Real-time Concentrations of Isotopologues by Enhancement Apparatus

Team Members

Heidi B. Sabatini[a+], Louis E. McNamara, Christopher J. Koch,[*] Christopher D. Chouinard[a], Alexandria G. Watrous[b], Ryan C. Fortenberry[b], and Tyler Guin

[a]Clemson University
[b]University of Mississippi
[*]Postdoctoral Researcher
[+]Graduate Student

References

1. Harilal, Sivanandan S*., et al.* "Detection of Tritium using Ultrafast Laser-Induced Breakdown Spectroscopy." Journal of Analytical Atomic Spectrometry 39.3 (2024): 699-703.
2. Kautz, Elizabeth J., et al. "Enhancing Analytical Merits of Laser-Induced Breakdown Spectroscopy of Hydrogen Isotopes Using an Orthogonal Double-Pulsing Scheme." Spectrochimica Acta Part B: Atomic Spectroscopy (2024): 106952.
3. Cooper, Adam, et al. "Determining Aqueous Deuterium Detection Limits via Infrared Spectroscopy to Understand its capabilities for Real-time Monitoring of Tritiated Water." Fusion Engineering and Design 207 (2024): 114647.
4. Hermann, Valentin, et al. "Observation and Assignment of a High-Resolution FTIR-Spectrum of $T_2^{16}O$, $DT^{16}O$ and $HT^{16}O$ in the Range of 4300 to 4700 cm^{-1}." Journal of Molecular Spectroscopy 398 (2023): 111859.
5. Heung, L. Kit. "Tritiated Ammonia Formation." Fusion Technology 28.3P2 (1995): 1188-1193.

Development of Transuranic Stimuli-Responsive Metal-Organic Frameworks

Corey Martin

Optoelectronic devices based on f-element-containing metal-organic frameworks are an emergent area of research due to interest in a new generation of semiconducting materials. Tailoring materials properties using photochromic moieties is a powerful approach to tune optoelectronic properties and requires a fundamental understanding of cooperativity between f-elements and integrated switchable molecules.

Introduction

Demands in emerging technologies in the field of optoelectronics attract significant attention toward lanthanide-based materials, and in particular, lanthanide-based metal-organic frameworks (MOFs) due to their applications as diode materials, optical and magnetic sensors, fluorescent probes, and ratiometric thermometers.[1–3] Interest in the area of lanthanide-containing materials is partly driven by the fundamental chemical properties of lanthanides and actinides as a class, including the fact that they can possess metal centers exhibiting both luminescence and magnetic properties, enabling the design of multifunctional devices (e.g., platforms for biomedical imaging and diagnostics based on magnetic and fluorescent properties).[4,5] Further, the development of materials with intriguing electronic structures and properties can be promoted through the high spin-orbit coupling typically observed for lanthanides and actinides.[6,7] At the same time, forbidden f-f transitions give rise to peculiar optical properties such as hypersensitive and narrow emission profiles that can cover a large range of the electromagnetic spectrum (400 to 1600 nm).[7,8]

Understanding the electronic, magnetic, and photophysical properties of lanthanide- and actinide-containing MOFs is essential to determining their unrevealed potential (**Figure 1**). This project merges the area of f-element-containing MOFs with photochromic molecules to provide on-demand modularity of embedded photoswitchable moieties and, thus, tunable materials properties. An established correlation between dynamic photophysical response under light and optoelectronic properties enables the creation of the next-generation optoelectronic and magneto-optical devices.
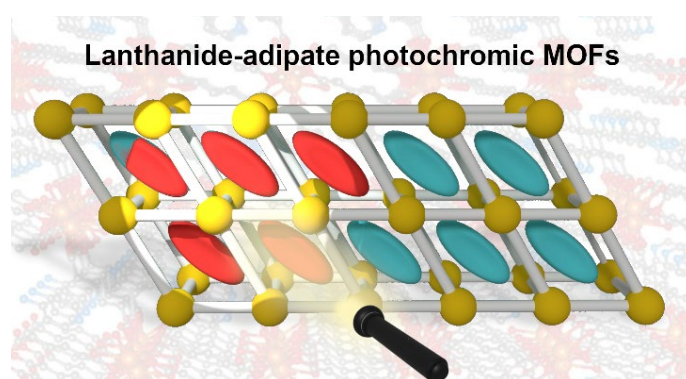

Lanthanide-adipate photochromic MOFs

Figure 1. Lanthanide-adipate metal–organic frameworks are in the spotlight as a platform for embedding photochromic molecules in lanthanide-containing frameworks and harnessing the combinatorial power of f-electrons and stimuli-responsive molecules.

Approach

The incorporation of photochromic molecules within MOFs is a promising approach to probe possible interactions between f-element-based metal centers and light-responsive components, which could be used to tune the optical and electronic properties of the bulk material with high spatiotemporal control using light as a noninvasive stimulus.[9–11] The reversible interconversion between photoisomers leads to distinct and on-demand properties (e.g., absorption and emission profiles, magneto-optical response, polarization, and dielectric constants). The overall goal of this research is to merge the areas of f-element chemistry and photochromic molecules using MOFs as a platform to control and understand the unique properties of f-elements (e.g., spin-orbit coupling, relativistic effects, narrow emission profiles).

The incorporation of photochromic azo compounds (i.e., organic molecules with diazenyl (R–N=N–R') functional

groups) in MOFs is an attractive strategy to impart light-based response since photoresponsive azobenzene derivatives integrated in bulk materials have already been applied as actuators due to significant changes in their molecular confirmations, polarity, and light absorption upon their photoisomerization. Furthermore, azobenzene derivatives have been used to control liquid crystal domains or photophysical properties of nonlinear optical materials and sensors due to their long thermal lifetimes, large extinction coefficients, high photoisomerization quantum yields, and excellent fatigue resistance.[11,12]

This project combined diffuse reflectance, ^{1}H nuclear magnetic resonance, Fourier-transform infrared, and energy-dispersive spectroscopy to understand optical properties and materials characterization (**Figure 2**). Photoisomerization kinetics were determined using time-resolved diffuse reflectance (**Figure 3**). Powder- and single-crystal X-ray diffraction were used to characterize the MOFs' structure and understand metal-ligand distances, angles, and first-principle interactions.
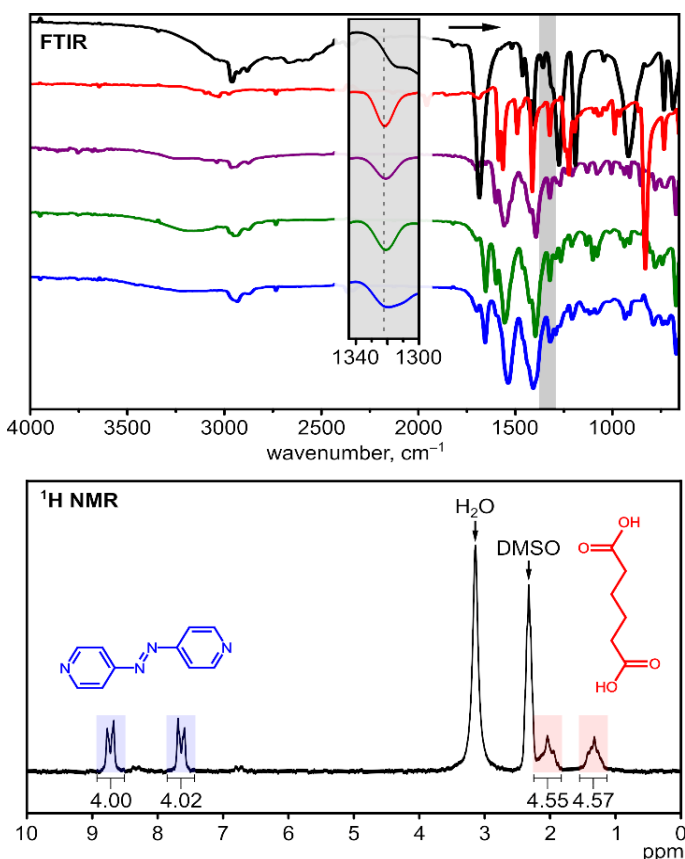
Figure 2. (Top) FTIR spectra of (blue) Azo@Ce-MOF, (green) Azo@Pr-MOF, (purple) Azo@Nd-MOF, (red) 4,4'-azopyridine, and (black) adipic acid. The inset shows δ(C–H: in-plane bend) coupled to ν(C–C: stretch) at 1322 cm^{-1} in 4,4'-azopyridine and MOFs containing 4,4'-azopyridine. (Bottom) ^{1}H NMR spectrum of digested Azo@Pr-MOF in dimethyl sulfoxide-d$_6$. The resonances corresponding to 4,4'-azopyridine and adipic acid are colored blue and red, respectively.
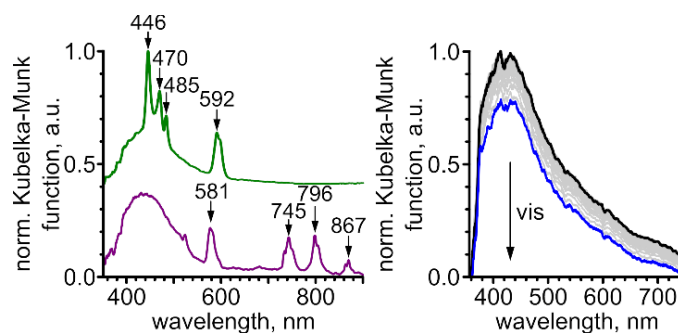
Figure 3. (Left) Normalized diffuse reflectance spectra of Azo@Pr-MOF (green) and Azo@Nd-MOF (purple). The wavelengths of the sharp absorption features in Pr- and Nd-containing samples are marked. (Right) Normalized diffuse reflectance spectra of Azo@Ce-MOF after 30 s of 300 nm irradiation (black) followed by attenuation under visible light (blue).

Accomplishments

- Reported the first photoisomerization studies for Ce, Pr, and Nd-MOFs containing azobenzene molecules.
- Established first-order rate kinetics for azobenzene-containing lanthanide MOFs (Azo@Pr-MOF, Azo@Ce-MOF, and Azo@Nd-MOF) that showed a more rapid photoisomerization than azobenzene in solution (e.g., 4.3-fold faster photoisomerization kinetics in Azo@Pr-MOF compared to free 4,4'-azopyridine).
- Confirmed photochromic retention of azobenzene in photoswitch-embedded lanthanide frameworks. Measured in solution and embedded in a MOF (solid-state) for photoisomerization rate comparison.
- Successfully cycled photoisomerization of azobenzene within Azo@Pr-MOF to show fatigue resistance of installed photochromic molecules as well as reversible photoisomerization.
- Prepared novel Azo@Am-, Pu-, and Np-MOFs that are to be included in an upcoming publication comparing lanthanide MOFs with actinide MOFs.

Peer-reviewed Publications

- Martin, C. R.; Thaggard, G. C.; Lehman-Andino, I.; Mollinedo, E.; Rai, B. K.; Page, M. A.; Taylor-Pashow, K.; Shustova, N. B. Photochromic Ln-MOFs: A Platform for Metal-Photoswitch Cooperativity *Inorg. Chem.*, **2024**, *63*, 12810–12817.

Team Members

Ingrid Lehman-Andino,[a] Eduardo Mollinedo,[a]* Binod K. Rai,[a] Matthew A. Page,[a] Kathryn Taylor-Pashow,[a] Grace C. Thaggard[b†], Natalia B. Shustova

[a]*Savannah River National Laboratory*
[b]*University of South Carolina*
Postdoctoral Researcher
†*Graduate Student Researcher*

References

1. Islamoglu, T.; Ray, D.; Li, P.; Majewski, M. B.; Akpinar, I.; Zhang, X.; Cramer, C. J.; Gagliardi, L.; Farha, O. K. From Transition Metals to Lanthanides to Actinides: Metal-Mediated Tuning of Electronic Properties of Isostructural Metal-Organic Frameworks. *Inorg. Chem.*, **2018**, *57*, 13246–13251, DOI: 10.1021/acs.inorgchem.8b01748

2. Karmakar, A.; Li, J. Luminescent MOFs (LMOFs): recent advancement towards a greener WLED technology. *Chem. Commun.* **2022**, *58*, 10768–10788, DOI: 10.1039/d2cc03330e

3. Wang, X.; Zhang, X.; Li, P.; Otake, K. I.; Cui, Y.; Lyu, J.; Krzyaniak, M. D.; Zhang, Y.; Li, Z.; Liu, J.; Buru, C. T.; Islamoglu, T.; Wasielewski, M. R.; Li, Z.; Farha, O. K. Vanadium Catalyst on Isostructural Transition Metal, Lanthanide, and Actinide Based Metal-Organic Frameworks for Alcohol Oxidation. *J. Am. Chem. Soc.* **2019**, *141*, 8306– 8314, DOI: 10.1021/jacs.9b02603

4. Roy, S.; Chakraborty, A.; Maji, T. K. Lanthanide-organic frameworks for gas storage and as magneto-luminescent materials. *Coord. Chem. Rev.* **2014**, *273-274*, 139–164, DOI: 10.1016/j.ccr.2014.03.035

5. Black, C. A.; Costa, J. S.; Fu, W. T.; Massera, C.; Roubeau, O.; Teat, S. J.; Aromí, G.; Gamez, P.; Reedijk, J. 3-D Lanthanide Metal-Organic Frameworks: Structure, Photoluminescence, and Magnetism. *Inorg. Chem.* **2009**, *48*, 1062–1068, DOI: 10.1021/ic8017826

6. Bünzli, J.-C.; Eliseeva, S. V. Intriguing aspects of lanthanide luminescence. *Chem. Sci.* **2013**, *4*, 1939–1949, DOI: 10.1039/c3sc22126a

7. Fang, Y.; Xing, C.; Zhan, S.; Zhao, M.; Li, M.; Liu, H.; Wang, C. Multifunctional Magnetic-Fluorescent Nanoparticle: Fabrication, Bioimaging, and Potential Antibacterial Applications. *ACS Biomater. Sci. Eng.* **2019**, *5*, 6779–6793, DOI: 10.1021/acsbiomaterials.9b01332

8. Jankowski, R.; Wyczasany, M.; Chorazy, S. Multifunctionality of luminescent molecular nanomagnets based on lanthanide complexes. *Chem. Commun.* **2023**, *59*, 5961–5986,DOI: 10.1039/D3CC00342F

9. Thaggard, G. C.; Maldeni; Kankanamalage, B. K. P.; Park, K. C.; Haimerl, J.; Fischer, R. A.; Shustova, N. B. Switching in Harmony: Tailoring the Properties of Functional Materials with Orthogonal Stimuli. *Chem. Phys. Rev.* **2024**, *5*, 011305, DOI: 10.1063/5.0189069

10. Mehlana, G.; Bourne, S. A. Unravelling chromism in metal-organic frameworks. *CrystEngComm* **2017**, *19*, 4238–4259, DOI: 10.1039/C7CE00710H

11. Rice, A. M.; Martin, C. R.; Galitskiy, V. A.; Berseneva, A. A.; Leith, G. A.; Shustova, N. B. Photophysics Modulation in Photoswitchable Metal-Organic Frameworks. *Chem. Rev.* **2020**, *120*, 8790–8813, DOI: 10.1021/acs.chemrev.9b00350

12. Russew, M.-M.; Hecht, S. Photoswitches: From Molecules to Materials. *Adv. Mater.* **2010**, *22*, 3348–3360,DOI: 10.1002/adma.200904102
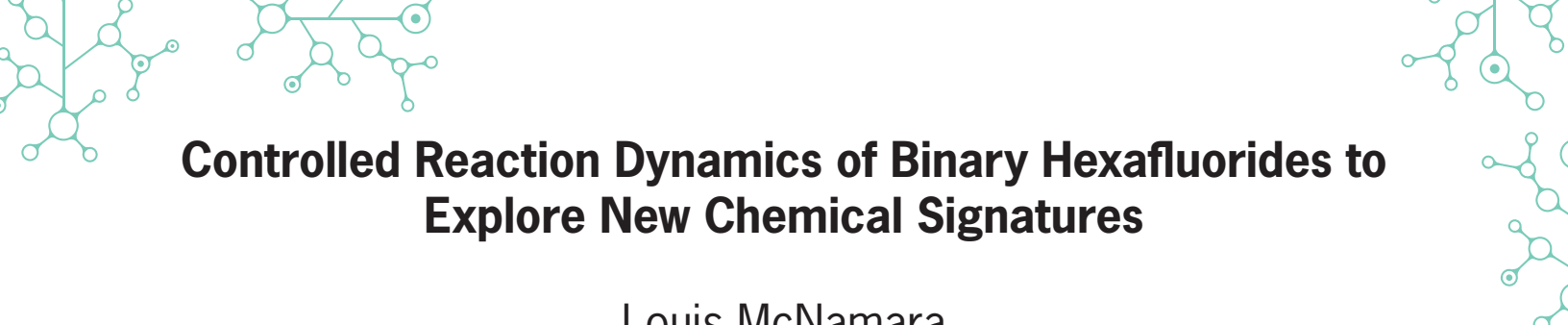
Controlled Reaction Dynamics of Binary Hexafluorides to Explore New Chemical Signatures

Louis McNamara

The goal of this project is to better understand the fundamental chemistry governing binary hexafluorides - molecules containing six fluorine atoms bound to a central atom. Specifically, an improved understanding of uranium hexafluoride chemistry is targeted because it plays a critical role in nuclear safeguards and nonproliferation.

Introduction

The hydrolysis of uranium hexafluoride (UF_6) plays a crucial role in the generation of material effluents relevant to nuclear safeguards and nonproliferation. The uranyl fluoride (UO_2F_2) hydrolysis products are generated in ambient conditions via reaction with atmospheric water. The reaction products are a key signature for destructive analysis methods and environmental sampling. Unfortunately, the mechanism of this reaction remains unresolved despite numerous experimental and theoretical studies over the past several decades. This knowledge gap has direct negative consequences for nuclear safeguards methods and their development. A fundamental scientific understanding of UF_6 hydrolysis thermodynamics and kinetics will be valuable to multiple Defense Nuclear Nonproliferation (DNN) R&D roadmap objectives. Both experimental and theoretical studies have shown the reaction mechanism is dependent on the starting conditions (e.g., reagent relative ratios, temperature, pressure) but there are no proposed mechanisms for the dependence on these conditions. Previous work at SRNL illustrated the viability of using a custom-built vacuum chamber and cryostat interfaced with an FTIR spectrometer to observe intermediate formation in situ. We intend to expand on this work by improving the experimental design, studying other binary hexafluorides, and looking at reactions beyond the simple hydrolysis. All of this information will lead to new signatures through the improved understanding of signature propagation of UF_6.

Approach

Prior work performed at SRNL was successful at obtaining spectra of the cryogenically-slowed UF_6 hydrolysis reaction.[1] The initial work done at SRNL was not designed for this type of experiment, so a new cryogenic vacuum chamber was designed (**Figure 1**) to facilitate the proposed research. The new chamber will achieve a lower and more stable vacuum, provide superior control over the temperature, and use diamond windows to facilitate the application of multiple spectroscopic techniques. Multiple binary hexafluorides besides UF_6 - such as tungsten and osmium hexafluoride - will be studied using the new chamber while the methodology is refined in a non-radiological laboratory. Each binary hexafluoride is reactive with water, but they will not all react to form the same intermediates and products. Comparison of the intermediate spectra from these dissimilar reactions will yield valuable information regarding the reaction pathways and allow for a higher level of confidence in the peak assignments of the observed UF_6 intermediates. After the new system has demonstrated the required capabilities, work with UF_6 will begin. Additionally, for each of the binary hexafluoride, reaction beyond hydrolysis will be considered. In particular, reactions with common industrial effluents and emissions, such as NO_x, will be considered. The reactions will also be halted at varying points along the reaction coordinate by re-lowering the temperature of the cold finger, preventing any further reaction of the intermediates. At this stage, other reactants can be introduced to generate new signatures.

Accomplishments

- Hired and began training new postdoc.
- Completed the design of the sample chamber to be made of entirely COTS components that yields an ultra-high vacuum chamber and a temperature controlled cold finger capable of reaching 80 K.
- Engaged with university partners to acquire data that complement the results from experiments performed

at SRNL that may lead to future grant submissions under NA-22.

- Successfully acquired FTIR spectra of ammonia-water ices (**Figure 2**) to help train postdoc before moving to work with the more corrosive binary hexafluorides.
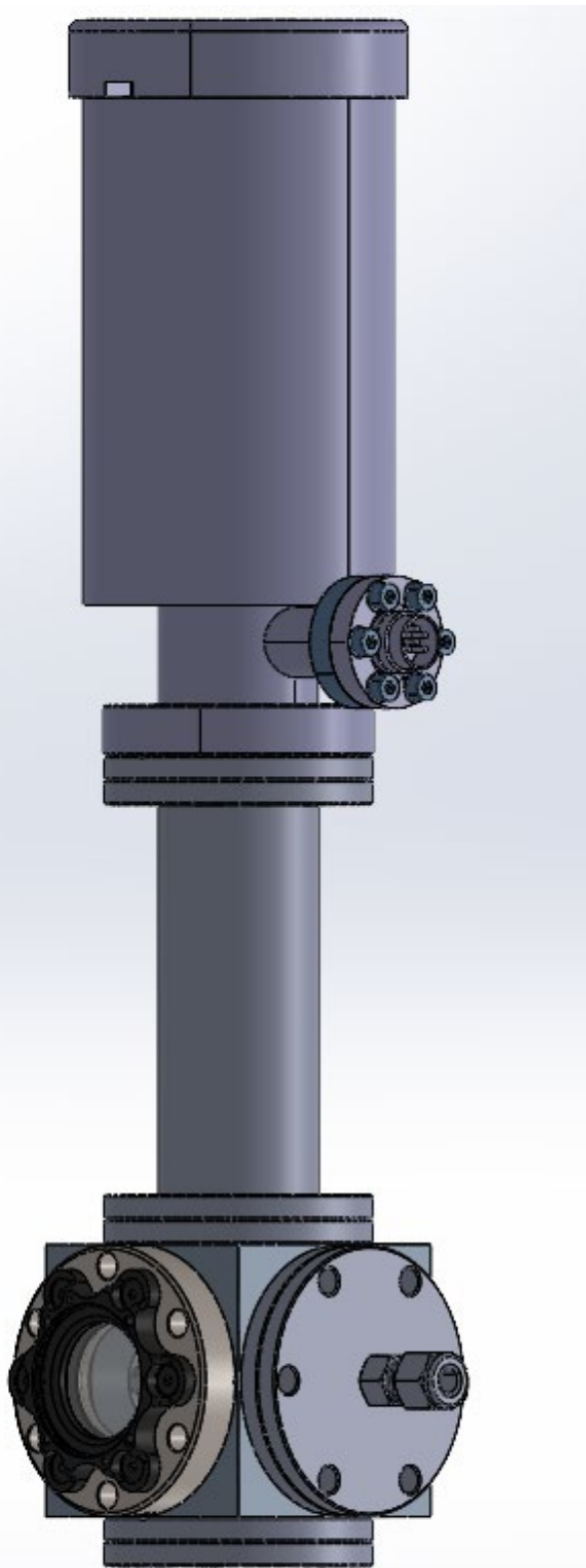

Figure 1. Model of new cryo-cell system consisting of COTS components. The new cell reaches ultrahigh vacuum and the cold finger is temperature controlled down to 80 K.
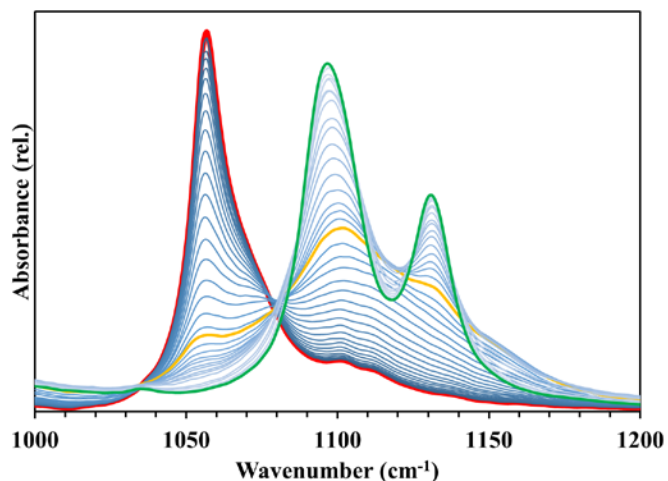

Figure 2. Graph of ammonia (NH_3) mixing with water (H_2O) at cryogenic temperatures. The initial ammonia band is highlighted in red and shifts dramatically as it mixes with water. By controlling the temperature of the cell, we can form the ammonia monohydrate ($NH_3 \bullet H_2O$) highlighted in green. The transition form pure NH_3 to $NH_3 \bullet H_2O$ can be monitored, and an intermediate structure is highlighted in yellow.

Team Members

Abigail Waldron, Austin Dorris[*], Kyle Hartig[a]

[a]University of Florida
[*]Laboratory Director's Postdoctoral Research Fellow

Reference

1. Louis E. McNamara, Abigail M. Waldron, John T. Kelly, Samuel Uba, Eliel Villa-Aleman, and K. Alicia Strange Fessler "Monitoring the reaction dynamics of UF6 by cryogenic layering and FTIR spectroscopy", Proc. SPIE 13056, Chemical, Biological, Radiological, Nuclear, and Explosives (CBRNE) Sensing XXV, 130560R (7 June 2024). DOI: 10.1117/12.3013311

Rapid, rigorous, reproducible data analysis software for high-precision mass spectrometry

Kyle Samperton and Elizabeth LaBone (Co-PIs)

Mass spectrometers are specialized instruments used by U.S. National Laboratories to precisely measure nuclear and non-nuclear materials. In this project, our team developed a comprehensive data analytics software package to address a critical lack of advanced computer programs required to process data collected by these cutting-edge scientific tools.

Introduction

High-precision mass spectrometry is a key technology in enabling all Savannah River National Laboratory (SRNL) mission organizations and advancing SRNL's Core Competency of *Sensing, Characterizing, Assessing, and Deterring Nuclear Proliferation* for domestic and international customers. Despite the centrality of precision mass spectrometry to SRNL projects and organizations, no software currently exists with either basic or advanced data analysis tools and data interactivity functions necessitated by modern high-precision methods, including thermal ionization mass spectrometry (TIMS) and multicollector–inductively coupled plasma–mass spectrometry (MC-ICP-MS). The lack of such software presents the greatest limitation in being able to maximize the scientific and technical potential of these "gold standard" analytical technologies, both at SRNL and beyond. The objective of this project was to develop a comprehensive data analytics software package and Graphical User Interface (GUI) for SRNL's diverse high-precision mass spectrometric capabilities. Efforts were focused on developing statistically mature, "frequentist" data analysis tools and the main GUI framework. This new software is compatible with and supports diverse SRNL high-precision mass spectrometry capabilities and will help to establish SRNL as a leader in precision data analytics for such technologies.

Approach

To build a mass spectrometry data analysis software suite, this project leveraged the power of R, a popular, free, open-source programming language and environment for statistical computing. R functionality can be augmented by freely downloading any of the >19,000 user-contributed packages on the online Comprehensive R Archive Network (CRAN) repository. One such package is Shiny, which provides tools for convenient development and customization of "point-and-click" Graphical User Interfaces within the R environment. Integrating R-based data analytics with Shiny-enabled data interactivity offers an attractive route for analysts to take advantage of R's statistical and computational power, allowing researchers without any programming experience to harness its considerable data analysis and visualization capabilities. In addition to Shiny, this project implemented Golem, a framework for production-grade Shiny applications that includes software documentation, structure, and testing standardization. These elements were integrated with team subject matter expertise in mass spectrometry, data analysis, and mathematics/statistics to develop **PRISMS** (**PR**ecision **IS**otopic **M**ass **S**pectrometry), a software package for importing, processing, visualizing, and reporting high-precision mass spectrometry information that addresses critical shortcomings of current commercial and open-source software. The software codifies best practices in the data analysis and technical literature, yielding a "frequentist", Monte Carlo method-based statistical package and GUI framework. In addition, PRISMS incorporates pertinent quality assurance and control components, including establishing metrological traceability of analytical results to specified reference materials and applying rigorous uncertainty propagation and analysis techniques. Screenshots of the PRISMS outputs are given below in **Figures 1**.
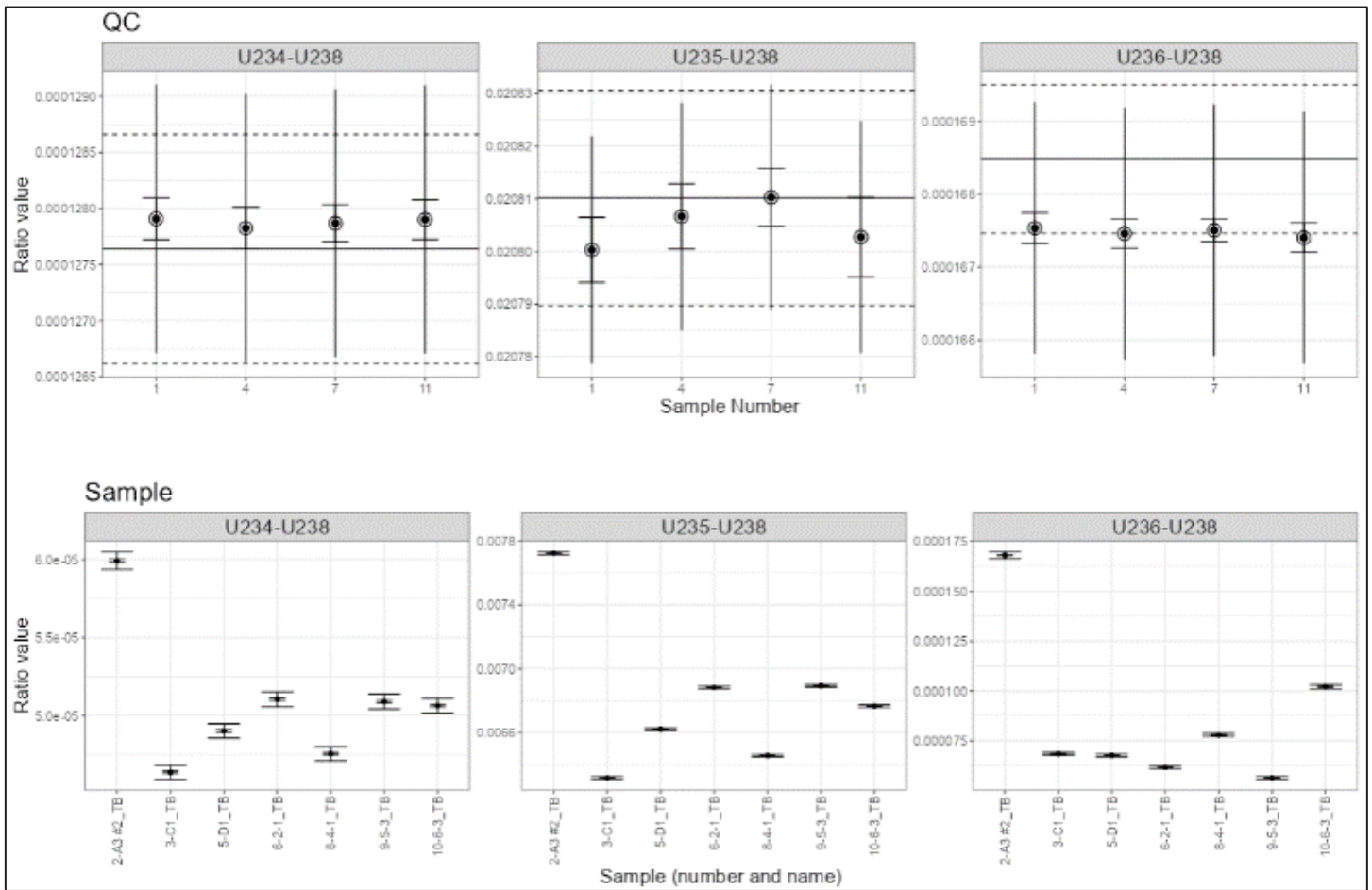
Figure 1. Software output showing plotted summary results of automated batch processing of MC-ICP-MS uranium isotopic data, including charts of Quality Control (QC) secondary standard analyses and sample results.

Accomplishments

- Recruited and hired an on-site Graduate Student Intern, Ellis McLarty (Graduate Student in the School of Mathematical and Statistical Sciences at Clemson University), to support software development tasks.
- Developed an operationalized, flexible, "point-and-click" Graphical User Interface for importing, processing, visualizing, and reporting mass spectrometry analytical results generated at SRNL.
- Adapted, functionalized, and incorporated "base R", command line-type data processing code into the Graphical User Interface framework.
- Established Method Editor software module to accommodate data produced by different mass spectrometer types and manufacturers.
- Presented project results at the Goldschmidt geochemistry/mass spectrometry research conference in August 2024.
- Graduate Student Intern presented on Bayesian statistical techniques being developed for this project at the SRNL Summer Intern Research Poster Session (July 2024) and SRNL Georgia Tech Day in Atlanta (September 2024).

Intellectual Property

Copyright Disclosures

- PRecision ISotopic Mass Spectrometry (PRISMS) computer software
- PRecision ISotopic Mass Spectrometry Graphical User Interface (PRISMS.GUI) computer software

Team Members

Kyle Samperton, Elizabeth LaBone, Shelby Bowden[*], Alexis Riche[*], Ellis McLarty[a]

[a]*Clemson University*
[*]*Postdoctoral Researcher*

Simulating Potential Adsorption and Desorption Capabilities of Nuclear Materials onto Microplastics

Vivian Turner

Microplastics have been successfully simulated in the in-house model, ALGE. Characteristics of a microplastic polyethylene were simulated to look at absorption capabilities of dissolved U-232, U-235, Cs-137, Tritium, and Sr-90 in water. Desorption capabilities were simulated for Cs-137, and all results were plotted as a time series.

Introduction

Microplastics (MPs) are an emergent and ubiquitous contaminant capable of adsorbing heavy metals and hazardous material and leaching the material downstream in aqueous systems. MPs can serve as carriers of pollutants and therefore could serve as an indicator or proxy for use in tracking material within the nuclear fuel cycle. Research related to MPs has a large gap in understanding adsorption and desorption capabilities, especially for nuclear materials such as Cs-137, Sr-90, Tritium, U-235. This work begins to explore those gaps through the utilization of existing literature and an in-house aqueous model, ALGE. ALGE has been used for a variety of releases (thermal, dissolved, and particulate), with previous work including simulations of Cl gas deposition into nearby ponds[1] and an accidental release of tritium at the Savannah River Site[2]. Combining literature coefficients and ALGE physics-based simulations will enable quantification of potential interactions of radionuclides with MPs.

Approach

To simulate MPs in ALGE, the properties to simulate silt (density, diameter, etc.) were substituted for MP properties, specifically polyethylene (PE) (**Table 1**). The half-life and absorption coefficients for U-232, U-235, Sr-90, and Cs-137 were used for the transport simulations (**Table 1**). Absorption coefficients are based on existing literature of experiments related to absorption of radionuclides onto MPs[3,4,5,6] or to soil where coefficients of absorption onto MPs were not found[7,8]. Desorption capabilities were limited to Cs-137. The desorption coefficients or rate for Cs-137 are based on radionuclides desorbing off soil[7]. A run for each radionuclide was simulated over a 48-hour period with initial concentrations of 10 kg/m³ of dissolved radionuclides and MPs, and 5 kg/m³ of dissolved radionuclides initially absorbed onto MPs released over the first 24 hours. Simulations were first performed incorporating the absorption coefficient and the second set of simulations were performed for Cs-137 with both the absorption coefficient and desorption rate. The sample location used was the Chesapeake Bay where tidal forces and meteorological data were considered. A time series of MP concentrations and absorbed MPs near the source of the release were produced to compare absorption capabilities of radionuclides to polyethylene (**See figs. 1-6**).

Radio/plastic	Plastic diameter (m)	Plastic density (kg/m^3)	Absorption coeff (K_d)	Decay constant (lambda)
PE U 232	4e-5	1390	3.4482758 [4]	6.118668e-06
PE U 235	4e-5	1390	0.8[7]	3.11936E-17
PE Sr 90	4e-5	1390	40,000[6]	2.82400826472387 34e-06
PE Cs 137	4e-5	1390	80000 [5]	2.63574104707561 5e-06
PE H3	4e-5	1390	100 [3]	6.32577851298147 6e-06

Table 1. List of Microplastic and radionuclide parameters for ALGE experiments.
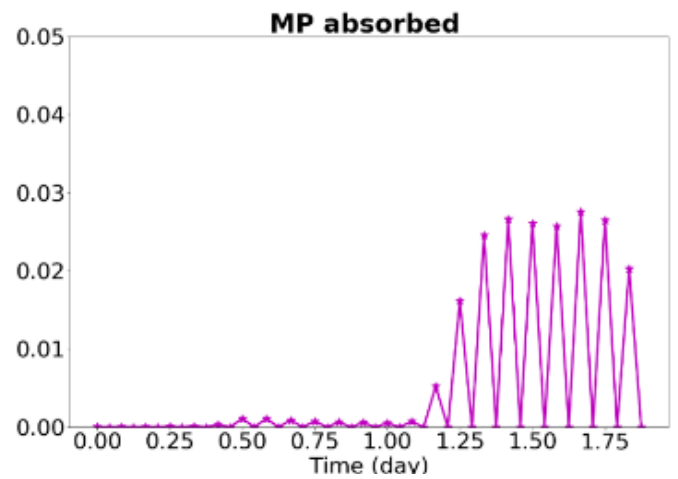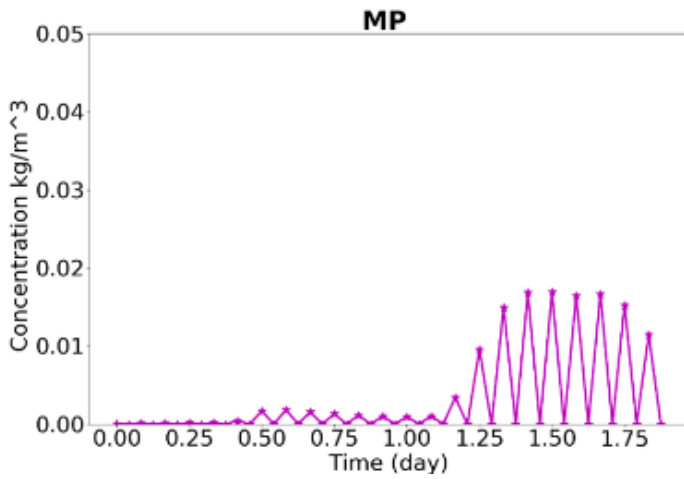
Figure 1. Concentrations of a.) Microplastics and b.) Microplastics with absorbed Cs137. No desorption rate was considered.
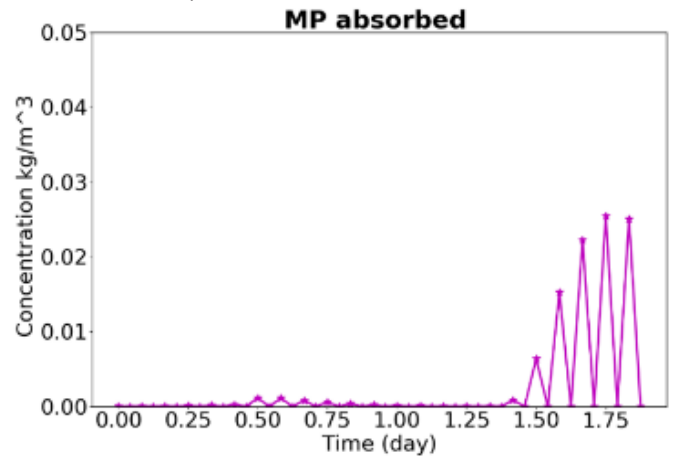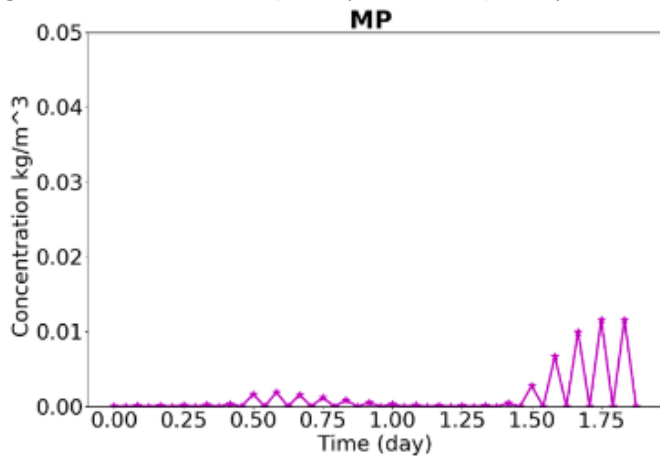

Figure 2. Concentrations of a.) Microplastics and b.) Microplastics with absorbed Cs137. A desorption rate of 4.45e-7 1/s was considered.
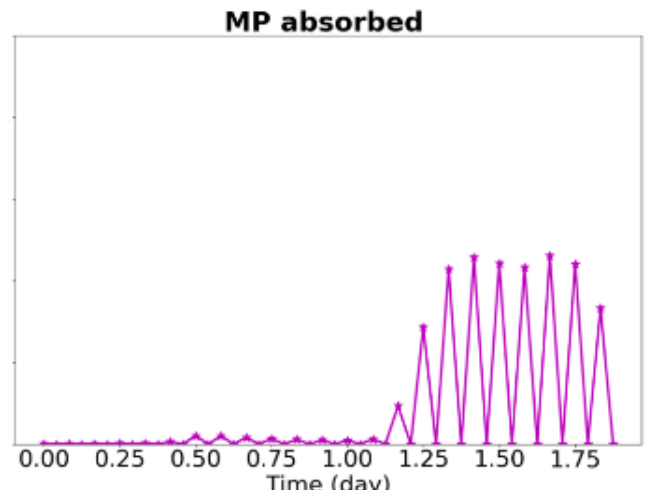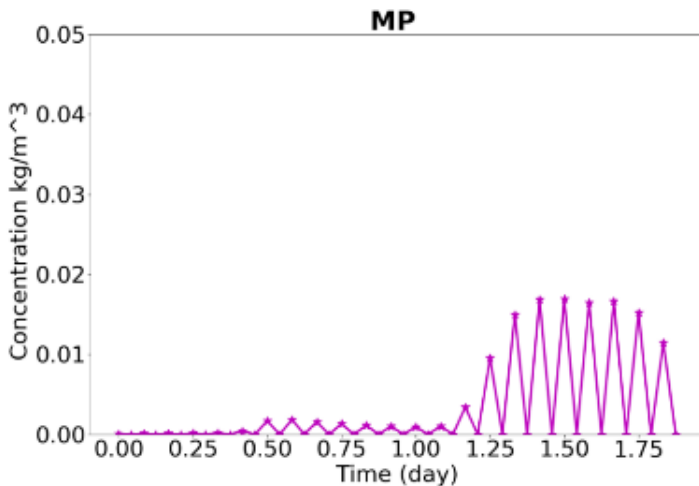

Figure 3. Concentrations of a.) Microplastics and b.) Microplastics with absorbed U-232.

Accomplishments

- Discovered that ALGE is capable of simulating MPs and MPs ability to absorb nuclear material by simulating several radionuclides interacting with polyethylene.
- Peak absorbed MP concentrations occurred after ~1.5 days at a location close to the source of the release.
- Peak absorbed MP concentration occurred after 1.7 days for Cs-137 when the desorption rate was included.

- Determined a large gap exists in experimental data for desorption of nuclear radionuclides based on literature review. ALGE simulations can be used to inform future laboratory investigations.
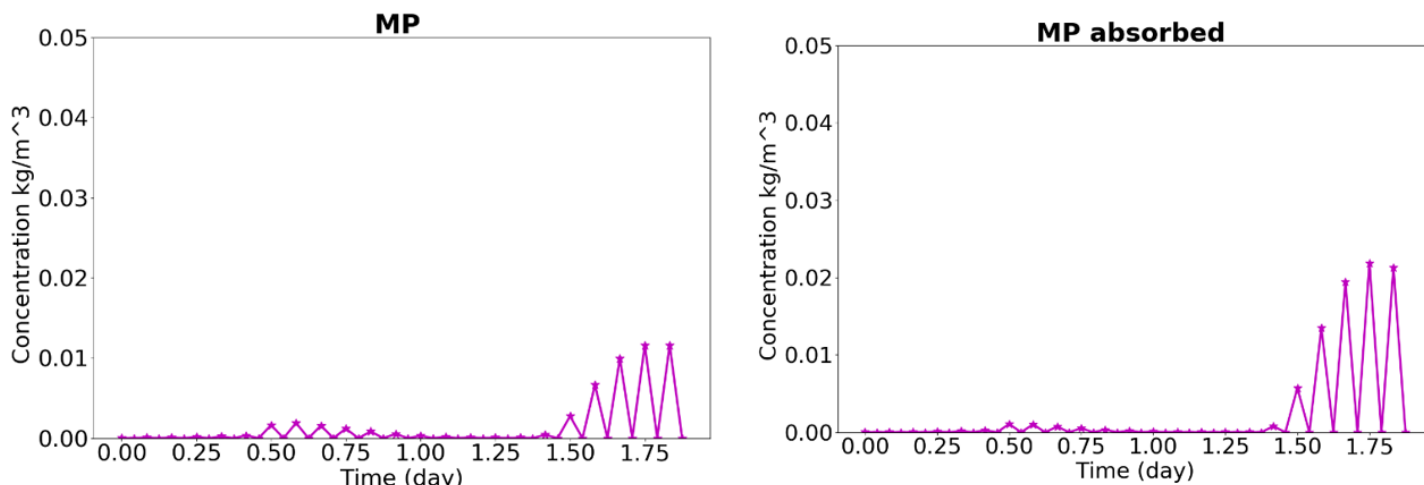- Created a baseline for MP absorption capabilities for potential nuclear nonproliferation activities.

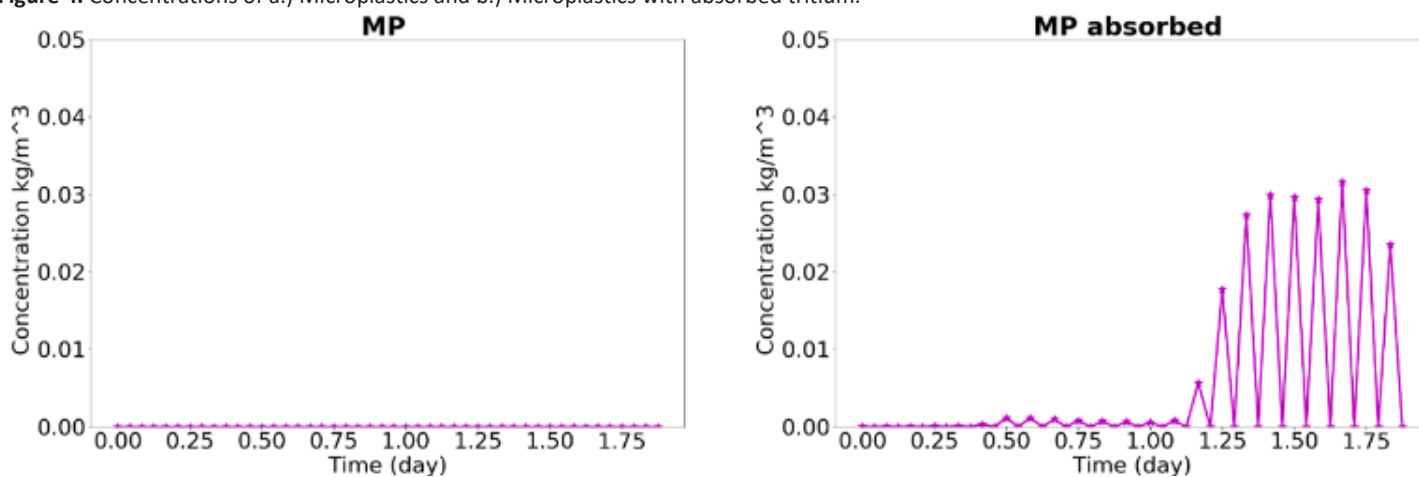**Figure 4.** Concentrations of a.) Microplastics and b.) Microplastics with absorbed tritium.

Figure 5. Concentrations of a.) Microplastics and b.) absorbed U-235 onto microplastics.
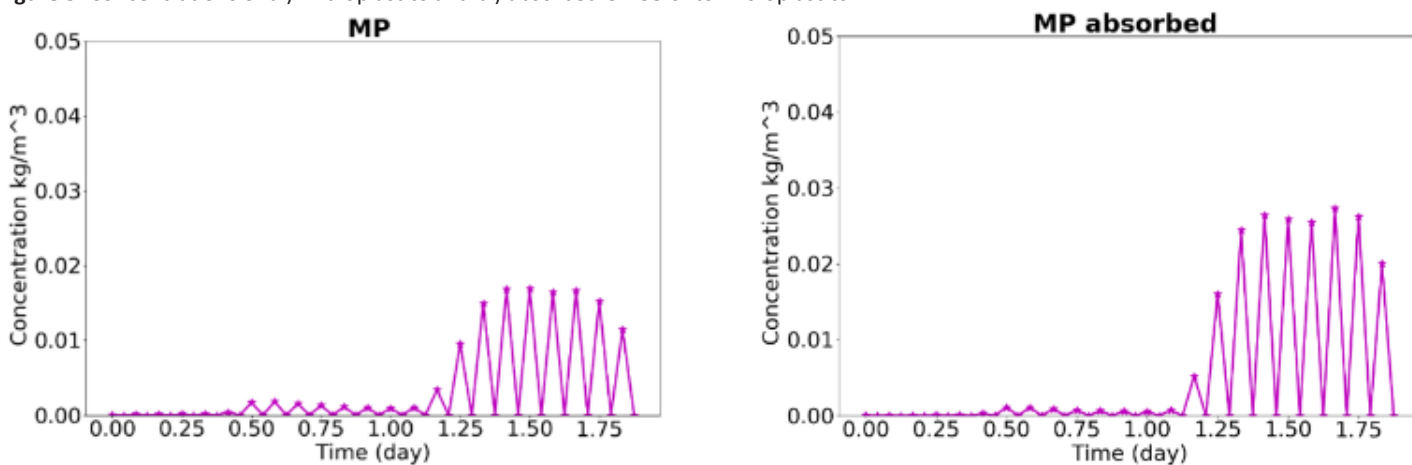

Figure 6. Concentrations of a.) Microplastics and b.) Microplastics with absorbed Sr-90.

References

1. Buckley, R. L., Hunter, C. H., Werth, D. W., Whiteside, M. T., Chen, K.-F., and Mazzola, C. A. (2012). A case study of chlorine transport and fate following a large accidental release. *Atmospheric Environment*, **62**, 184.198.
2. Blanton, J.O., Garrett, A., Bollinger, J. S., and Hayes, D. W. (2009). Transport and Dispersion of a Conservative Tracer in Coastal Waters with Large Intertidal Areas. *Estuaries and Coasts,* **32** (3): 573-592
3. EPA, U. UNDERSTANDING VARIATION IN PARTITION COEFFICIENT, kd, VALUES Volume II: Review of Geochamistry and Available kd Values for Cadmium, Cesium, Chromium, Lead, Plutonium, Radon, Strontium, Thorium,Tritium(3H), and Uranium. Agency, *United States Environ. Prot.* **1999**, 341.

4. Ioannidis, I.; Anastopoulos, I.; Pashalidis,I. Microplastics as radionuclide (U-232) carriers. *J. Mol. Liquids.***2022,** 351, ISSN 0167-7322, https://doi.org/10.1016/j.molliq.2022.118641.

5. Ioannidis, I., Kinigopoulou, V., Giannakoudakis, D.A., Arkas, M., Anastopoulos, I., Triantafyllidis, K.S. Pashalidis, I. Microplastics and disposable face masks as "Trojan Horse" for radionuclides pollution in water bodies – A review with emphasis on the involved interactions *Sus. Chem. Env.***2023,** 2949-8392.

6. Yadav, S., Rout, S., Joshi, V., Pulhani, V., Kumar, A.V. Unfolding the interaction of radioactive Cs and Sr

7. with polyethylene-derived microplastics in marine environment. *Disc. Oceans.***2024,** https://doi.org/10.1007/s44289-024-00015-8

8. Kasar,S.;, Mishra, S.; Sahoo,S.K.; Kavasi,N.; Omori, Y.; Arae, H.; Sorimachi,A.; Aono,T.; Sorption-desorption coefficients of uranium in contaminated soils collected around Fukushima Daiichi Nuclear Power Station *J.Env. Radioact*. **2021,** 106617.

9. Topcuoglu,S.; Gungor,N., Kirbasoglu. Distribution coefficients (Kd) and desorption rates of 137Cs and 241Am in Black Sea sediments. *Chemosphere*. **2002,** 1367-1373.

FY24 PROJECTS

CORE COMPETENCY:

Securing connected control systems and associated data
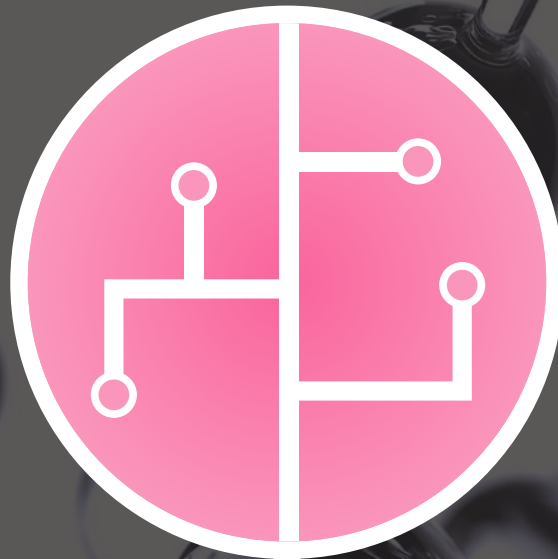
Reverse Engineering of Medical Devices for Innovation and Advancement in Healthcare

David Baldwin

The medical field has garnered significant attention in the realm of technology and cybersecurity. With its rapid expanse, the increased use of wireless technology and potentially vulnerable components is inevitable. This project will prevent current and future medical technology from being manipulated by threat actors.

Introduction

Medical cybersecurity research addresses the critical intersection of healthcare and digital security. As medical device use expands and becomes increasingly interconnected, the healthcare sector is poised to become a primary target for cyber warfare. This project aims to mitigate the risks in a field that often underestimates the importance of cybersecurity. To effectively simulate real-world conditions, a testing environment was developed that mimics the various types of networks encountered by embedded and field-operated devices (**Figure 1**). Additionally, a controlled environment was created to conduct preliminary analysis and testing without external communication interference. Specifically, testing has been conducted on medical ultrasound devices that have undergone CT scanning (**Figures 2 and 3**), as well as software analysis utilizing reverse engineering tools to understand their functionality.
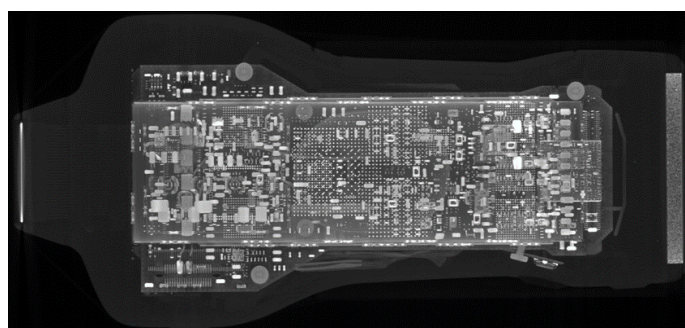

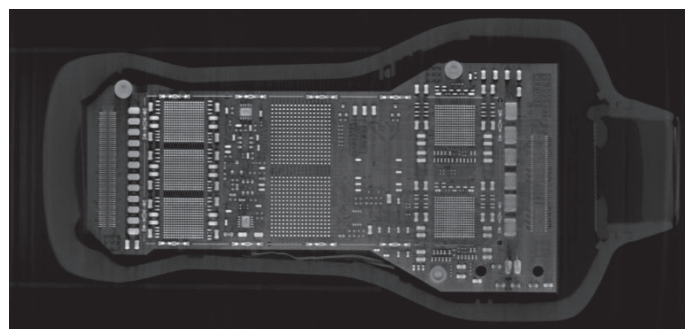**Figure 2.** Initial CT scan of VScan Air ultrasound device.

Figure 3. CT scan of ultrasound device isolated to a single layer of the Printed Circuit Board (PCB).
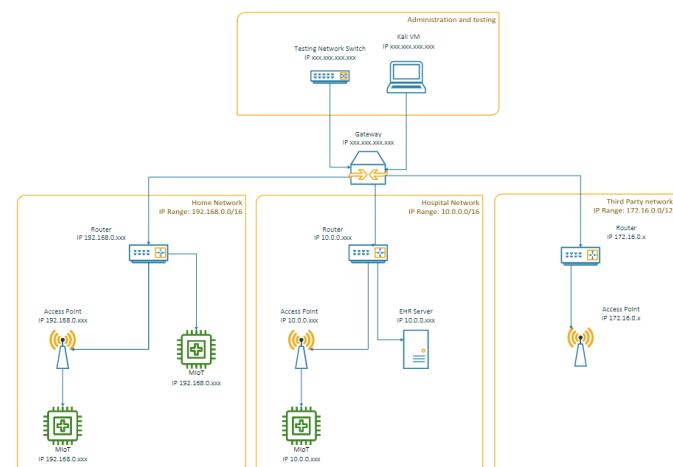

Figure 1. Testing environment network diagram, each section in orange highlights different networks medical devices interact with, including the general internet, personal network, the hospital, and third-party records storage.

Approach

The research approach commenced with open-source reconnaissance to identify medical devices employing vulnerable technologies and their utilization of network connectivity (**Figure 4**). Subsequently, a comprehensive testing network was established to encompass all relevant elements these devices encounter in real-world environments.

Each device underwent thorough investigation, including hardware analysis, to understand design intricacies and identify potential supply chain subversions. For medical devices interfacing with tablets and mobile phones, the associated software was reverse engineered (**Figure 5**).
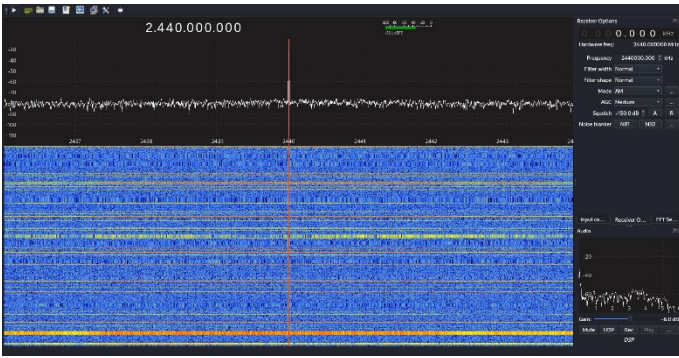
Figure 4. Analysis of wireless frequencies emitted by wireless medical device being tested.

This process examined the embedded technologies including Bluetooth, Wi-Fi, Cellular, and GPS to determine their integration into downstream medical devices, which was crucial for identifying potential weaknesses.

Analysis of communications between devices and upstream components is critical since these interactions harbor significant risk vectors. To ensure a sterile testing environment, networked devices were placed in a faraday enclosure certified to isolate their wireless signals. This provided engineers with comprehensive insights into device functionalities and shortcomings, enabling simulations of malicious intent to validate vulnerabilities.

Following extensive research, collaboration with vendors will address identified vulnerabilities, ensuring preemptive mitigation to protect patients and healthcare providers from potential medical exploits.

Accomplishments

- Created fully functional testing environment capable of simulating real-world situations for testing medical devices.
- Generated report SRNL-STI-2024-00225 analyzing various mobile ultrasound devices, highlighting hardware vulnerabilities native to the devices.
- Invitational presentation to the SCCS research board
- Discovered code snippets through reverse engineering that can present medical personnel with potentially life-threatening scenarios.
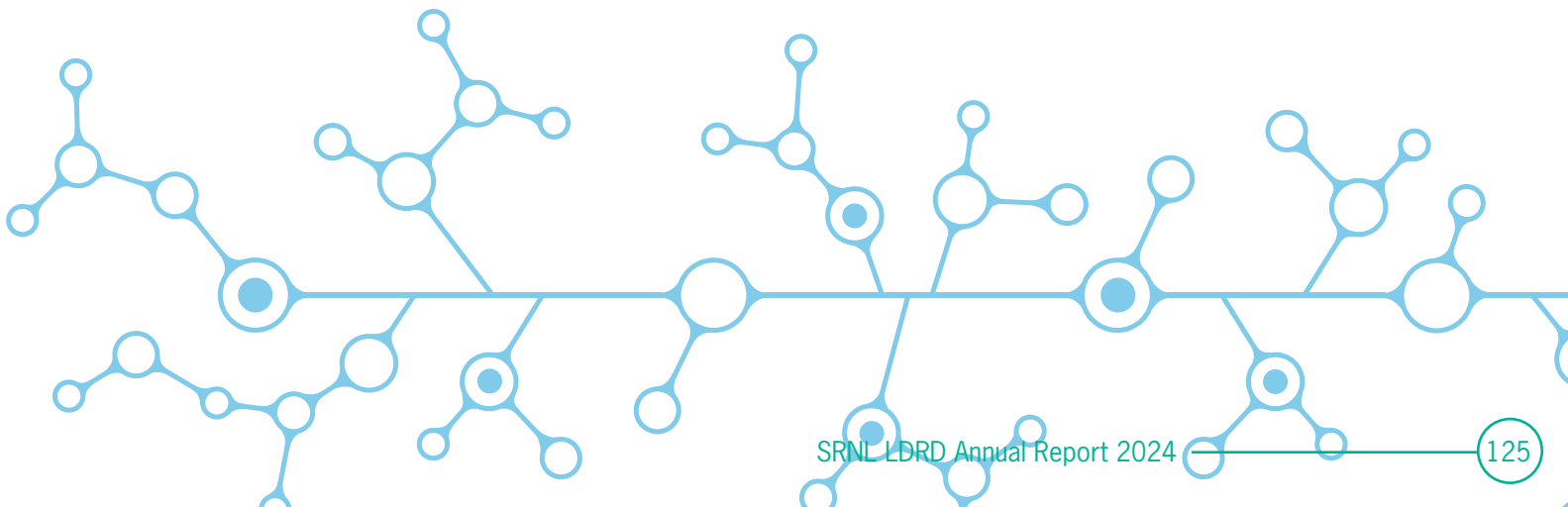
Peer-reviewed Publication

- Tauscher, D.; Nowatkowski, M.; Morris, J. D.; Baldwin, D. Medical Devices: Reverse Engineering for Innovation and Advancement in Healthcare. IEEE SoutheastCon 2024, pp. 860-862, doi: 10.1109/SoutheastCon52093.2024.10500213

Team Members

Michael Nowatkowski[a], Jeffrey Morris[a], Dillon Tauscher, Justin Carney, Mitchell Jordan

[a]Augusta State University

```
4524    public void setGpsInfo(Location location) {
4525        if (location == null) {
4526            return;
4527        }
4528        setAttribute(TAG_GPS_PROCESSING_METHOD, location.getProvider());
4529        setLatLong(location.getLatitude(), location.getLongitude());
4530        setAltitude(location.getAltitude());
4531        setAttribute(TAG_GPS_SPEED_REF, "K");
4532        setAttribute(TAG_GPS_SPEED, new Rational((location.getSpeed() * ((float) TimeUnit.HOURS.toSeconds(1L))) / 1000.0f).toString());
4533        String[] split = sFormatterPrimary.format(new Date(location.getTime())).split("\\s+", -1);
4534        setAttribute(TAG_GPS_DATESTAMP, split[0]);
4535        setAttribute(TAG_GPS_TIMESTAMP, split[1]);
4536    }
```

Figure 5. Module of code that checks exact location of tablet or phone within an application interacting with wireless ultrasound device. (Snippet from open source, dependent library)

Threat Hunting Representations for Embedded-system Anomaly Tracking

Glenn Fink

This work applies large language models to cybersecurity data enabling automatic characterization of machines and connections at line speeds. This year the focus was on identifying data, establishing partnerships, and building initial data pipelines. A data set was generated and others are in process, and a core competency workshop was conducted.

Introduction

This work represents a strategic direction in cyber and artificial intelligence at SRNL in alignment with and support of the SRNL strategic plan. The central scope will develop effective cyber analysis tools to assist threat hunters in identifying malicious cyber activity in electric grid cyber infrastructure. Additionally, nominal investments in key growth areas will create opportunities for similar, additional research. These investments include purchase of institutional computing updates, collaborating with our BSRA educational partners for workforce development and hiring pipelines, connecting our data visualization and cyber capabilities, establishment of data stewardship, and development of strategic and business development partnerships. These efforts will lay the groundwork for future, related investments. The primary tool to be developed is called Threat Hunting Representations for Embedded-system Anomaly Tracking (THREAT), which employs natural language processing (NLP) and visualization to enable threat hunting over behaviors found in computer log files. The ultimate outcome of the technical scope will be a more secure power grid. In the larger picture, THREAT will lead the way by encouraging investments in the focal areas of employing AI to solve cyber problems and human analyst cognitive augmentation through AI and visualization. The project focuses on rapid development of initial capabilities in the first year to demonstrate value to key potential sponsors.

Approach

In FY24, the approach was to procure equipment, collect data, and develop partnerships to be able to accomplish most of the work in FY26. The project purchased a GPU machine and negotiated a new network boundary that will enable its access to needed internet resources. The requirements for cyber network data were defined and several test data sets were acquired to use with our models. The project obtained tools such as VMWare, Wireshark, Zeek, and Suricata to analyze this data and transform them into data usable for training. The project team is working with the SRNL General Counsel on data transfer and use agreements intended to facilitate sharing operational data for research purposes. The project engaged DOE-EM threat hunters as a user community for requirements elicitation and evaluation of our results and conducted a workforce development workshop for cyber and AI as part of the workforce development thrust.

Accomplishments

- Conducted a workshop on workforce development in cyber and AI with 160 attending from 30 organizations in seven states and two countries.
- Collected data from the Mobile Melt-Consolidate (MMC) project for ingestion into the eventual model.
- Worked with local farms and the SC government to collect cyber data from robotic farms in the area.
- Created a draft data sharing agreement with the SRNL General Counsel preliminary for sharing data from SRMC.
- Procured a GPU machine with eight H100 GPUs for LDRD projects that wish to do AI and cyber research.
- Established strategic direction for an open science network segment at SRNL that would allow access to Internet-resident tools and data that are not available under the SRNS network constraints.
- Created partnerships with Army Cyber, DefenseWerk's Cyber Fusion Innovation Center

(CFIC), Augusta University, Booz Allen Hamilton of Augusta, and others.

- Follow-on work applied the general research of this project to two others generated two new funded projects and $500K of new funding. This will enable the project to hire a developer.

Peer-reviewed Publication

- Cyber Log Embeddings paper in draft. To be completed Sept. 15, 2024.

Team Members

Rachel Jones, Luke Gosink, Tom Danielson, Alaric Hartsock[a], Chris North[b]

[a] *Pacific Northwest National Laboratory*
[b] *Virginia Polytechnic and State University*

Defining Qubit Properties in Pa^{4+} Complexes

Lindsay Roy

This research seeks to develop a detailed understanding of the chemical and electronic properties of protactinium (Pa) complexes in the hopes of controlling its spin-orbit and crystal electric field effects with potential as an actinide qubit. FY24 activities focused on results of a hydrothermal synthesis and the first single-crystal analysis of a novel protactinium sulfate complex, $(PaO)_2(SO_4)_3(H_2O)_2$.

Introduction

Quantum materials are at the forefront of scientific discovery because their exotic electronic properties will enable new applications in computing, information, sensing, and other related applications. The f-elements have shown exceptional promise as new quantum materials, particularly as relativistic effects to enable phenomena such as quantum wells and quantum tunneling. The energetics of the actinide series are interesting because the 5f and 6d orbitals change across the periodic table, enabling a rich and complex chemistry wherein control of quantum bit (qubit) could be possible. Protactinium is of particular interest because of near degeneracy of the 6d/5f orbitals, making it behave more like a transition metal. This work delineates the chemical engineering of high-valent 5f^1 protactinium complexes as qubits by evaluating how its unique atomic properties, including spin-orbit coupling (SOC), crystal electric field (CEF), and nuclear spin, can be exploited through coordination chemistry to observe long-lived coherence times. The research leverages both experimental and theoretical findings to generate a set of features to enhance quantum coherences in actinide molecules.

Approach

Our research has two overarching objectives: Purification, synthesis, and characterization of Pa complexes; and development of first-principles derivation of spin-orbit coupling and crystal electric field parameters for Pa.

Purification, Synthesis and Characterization:

1. Purify: Develop a method to extract the materials from the source.
a. Dissolution: Finding a suitable acid/solvent to isolate the sample from the source.
b. Separation: Multiple elements and unwanted products could be removed from the source requiring separation using solvent, precipitation, or exchange resins.
2. Synthesis and Characterization: The synthesis makes use of hydrothermal methods using a PARR acid digestion vessel to create single crystals. The loaded vessel is placed in a muffle furnace and heated to ≤230 °C. Single crystals are identified using single crystal X-ray diffraction analysis.

Exploration of the Pa-Ligand chemical space:

1. Exploration: Theoretical calculations of $(PaO)_2(SO_4)_3(H_2O)_2$.
2. Spin-Phonon Coupling: Establish a methodology to quantify the intensity as well as mechanisms and processes for relaxation pathways in actinide qubit complexes.

Accomplishments

As mentioned earlier, project work was divided into four tasks to show progress in all areas, outlined below along with their milestones. Results and accomplishments are presented under each milestone.

Task 1: Purification of ~80 mg legacy protactinium (Pa) material.
M1: Identified purification method for ^{231}Pa (August 2022)

The protactinium-bearing sealed source (**Figure 1**) was isolated in a 250 mL Nalgene bottle in preparation for leaching/dissolution. Initially 10 mL of a 5 M HF solution was added to the vessel and allowed to digest for 10 minutes before isolating a brown solution through filtration. To this solution, a 5x stoichiometric amount of ammonium hydroxide was added to form an off white/tan precipitate expected to be Pa(OH)$_5$. This

precipitate was then dissolved in 3 M sulfuric acid (H_2SO_4) due to the known stability of Pa in a sulfate solution. The solution was analyzed by gamma spectroscopy and determined to contain the bulk of the [231]Pa present in the original sample.

Task 2: Synthesis and characterization of Pa complexes.
M2: Determination of new Pa complexes (August 2024)

Single crystal XRD analysis of a crystalline sample revealed a monoclinic cell with a C2/c space group, density of 4.6640 g/cm3, and an empirical formula of Pa2S3H4O16. Lattice constants for the unit cell were determined to be the following: a = 22.2345(4) Å, b = 6.6587(1) Å, c = 7.9279(1) Å and α = γ = 90o, β = 96.894(2)o. As depicted in **Figure 2**, eight-coordinate Pa centers adopted a distorted bicapped trigonal prismatic geometry where the ligand vertices are arranged by two distorted bi-augmented triangular prisms with 10 triangle faces and one square face, also referred to as a Johnson 50 solid. The empirical formula indicated a Pa(V) center, which has been noted to be the most stable state for Pa.

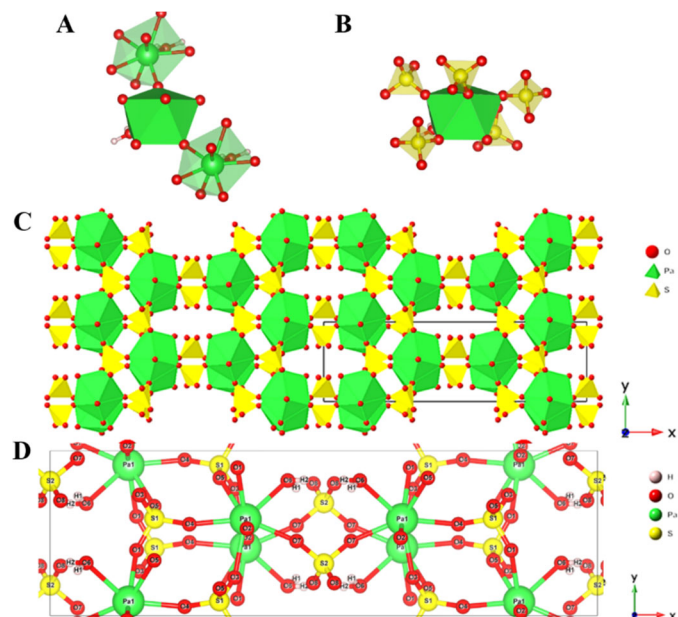**Figure 1.** Sample of lead contained Pa-231, legacy material at SRNL.

Figure 2. XRD crystal structure of the distorted bicapped trigonal prismatic geometry of the eight-coordinated protactinium atom is depicted in multiple visual representations for readability. The atom colors are as follows - Pa: green, S: yellow, O: red, and H: white. (A) Two oxygen ligands bond with nearest neighbor protactinium atoms. (B) Five oxygen ligands bond with the sulfur in the sulfate ions. (C) Perspective viewed along the z-axis of multiple unit cells of $(PaO)_2(SO_4)_3(H_2O)_2$. (D) Ball and stick view of a unit cell.

FIB-SEM and elemental compositions were quantified by Energy-Dispersive X-ray Spectroscopy (EDS) and indicated Pa, O, and S were well distributed throughout all four samples (**Figure 3**). The calculated S:Pa ratio from the elemental compositions indicated Pa:S ratios between 1.5-1.7.
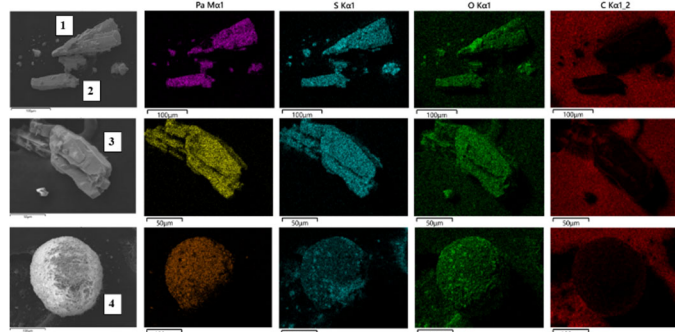

Figure 3. SEM-FIB images of Sample 1-4 with EDS analysis. Selected elements (Pa, S, O, and C) were visualized.

Task 3: Exploration of the Pa-Ligand chemical space.
M3: Validation of theoretical methods via experiment of known Pa complexes (August 2024)

Calculation of the density of states confidently indicated a Pa(V) center (**Figure 4**). A charge-transfer insulator with a band gap of 3.5 eV separated the conduction and valence bands. Hybridized O *2s* and *2p* atomic orbitals constituted the inner valence molecular *orbitals* and the outer valence molecular orbitals, respectively. The hybridization of the S 3p and O 2s/2p atomic orbitals

occurred around -10.5 to -9.1 eV while most of the Pa 6d and 5f atomic orbitals resided in the conduction band and supported a Pa(V) center. Given the stability of a Pa(V) state and the oxidizing conditions of a hydrothermal synthesis, the density of states data dos not deviate from our expectations and supported the proposed empirical formula.

M4: Derivation of spin-phonon coupling in $5f^1$ single ion magnets (August 2023)

Spin-phonon coupling calculations using the ORCA software began in Q4 FY22. Calculations focused on computing the magnetic properties of the early actinide chlorides and metallocene complexes.
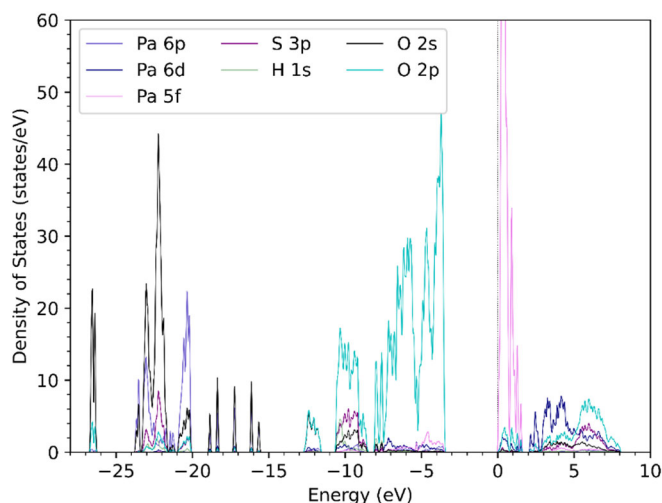

Figure 4. Electronic density of states for $(PaO)_2(SO_4)_3(H_2O)_2$.

Peer-reviewed Publications

- "Defining qubit properties in early actinide complexes," Stephanie Gamble, Lindsay Roy, Pete La Pierre, Julie Niklas, Tom Shehee and Garret Gotthelf, MRS Spring Conference, May 2022. (oral presentation)
- "Defining qubit properties in Pa^{4+} complexes," Stephanie Gamble, Lindsay Roy, Pete La Pierre, Julie Niklas, Tom Shehee and Garret Gotthelf, Rare Earth Research Conference, July 2022. (poster presentation)
- Megan Hoover, Theory Frontiers in Actinide Science Chemistry and Materials, February 2023. (oral presentation)
- "Defining Qubit Properties in High-Valent Actinide Complexes", Megan Hoover, Stephanie Gamble, Lindsay Roy, Pete La Pierre, Julie Niklas, Tom Shehee and Garret Gotthelf, MRS Spring Conference, April 2023. (poster presentation)
- Megan Hoover, 2023 Nuclear Waste Educators Workshop, July 2023. (oral presentation)
- Vinh Nguyen, 2024 Actinide Separations Conference, May 2024. (poster presentation)
- "How Novel is Protactinium: Insights into the Structure and Properties of $(PaO)_2(SO_4)_3(H_2O)_2$," Jarrod M. Gogolski, Garret Gotthelf, Megan E. Hoover, Vinh T. Nguyen, Binod Rai, Lindsay E. Roy*, Thomas C. Shehee, manuscript submitted for publication.

Team Members

Stephanie Gamble*, Jarrod M. Gogolski, Garret Gotthelf*, Megan E. Hoover*, Henry La Pierre[a], Julie Niklas[a*], Vinh T. Nguyen*, Binod Rai, Thomas C. Shehee

[a]*Georgia Tech*
Postdoctoral Researcher

**Savannah River
National Laboratory** ®